Investigation of the electrochemical properties of layered double hydroxides : operando advanced analysis of ionic transfer mechanisms

Elise Duquesne

Sorbonne Université

Ecole doctorale 388 – Chimie Physique et Chimie Analytique de Paris Centre

Laboratoire Interfaces et Systèmes Electrochimiques – UMR 8235

Bureau de Recherches Géologiques et Minières

Investigation of the electrochemical properties of layered double hydroxides: *operando* advanced analyses of ionic transfer mechanisms

Par Elise Duquesne

Thèse de doctorat

Dirigée par Catherine Debiemme-Chouvy

Soutenue publiquement le 30 septembre 2019 devant la commission d'examen composée de :

Mme Sophie PEULON	Chargée de Recherche CNRS-HDR	Rapporteur
M. Cédric CARTERET	Professeur	Rapporteur
Mme Stéphanie BETELU	Ingénieure de Recherche BRGM	Examinatrice
M. Hubert PERROT	Directeur de Recherche CNRS	Président
M. Emmanuel TERTRE	Professeur	Examinateur
Mme Catherine DEBIEMME-CHOUVY	Directrice de Recherche CNRS	Directrice de thèse
Mme Ozlem SEL	Chargée de Recherche CNRS	Invitée
M. Alain SERON	Ingénieur de Recherche BRGM	Invité
M. Michel Goldmann	Professeur	Invité

Remerciements

Les travaux de recherche présentés dans cette thèse ont débuté au sein du laboratoire LISE et du BRGM. En premier lieu, j'adresse un remerciement particulier au Labex Matisse et au BRGM qui ont cofinancé ce travail, et m'ont permis de côtoyer deux structures, l'une plus fondamentale, et l'autre, plus appliquée, et deux modes d'organisation au sein de la recherche.

Je tiens ensuite à tout particulièrement remercier les personnes qui ont initié ce projet de thèse, et qui ont apporté par leurs relectures de mon manuscrit un regard critique essentiel. Je tiens à exprimer toute ma gratitude à ma directrice de thèse, Catherine Debiemme-Chouvy (LISE), pour m'avoir soutenue et aiguillée, ainsi que pour ses conseils avisés, sa disponibilité et son humanité. Je suis également profondément reconnaissante à l'égard de Stéphanie Bételu, Ioannis Ignatiadis et Alain Seron (BRGM) qui m'ont éclairée sur mes questionnements et aidée sans relâche sur les analyses. J'adresse toute ma reconnaissance à Hubert Perrot et à Ozlem Sel (LISE) pour m'avoir accompagnée jusqu'à l'aboutissement de ce travail, et en particulier au sujet de l'*ac*-électrogravimétrie. Mes remerciements vont également à Hubert Cachet (LISE) qui m'a adressé de nombreux conseils pendant cette thèse et qui a relu avec attention mon manuscrit.

Pendant cette thèse, j'ai eu également l'opportunité d'utiliser le rayonnement synchrotron pour des études électrochimiques *operando*, ce qui a été pour moi une expérience à la fois humaine, scientifique et technique inestimable. L'intérêt d'une telle expérience au synchrotron a permis une collaboration avec l'INSP. Je remercie ainsi de tout cœur Michel Goldmann (INSP) pour sa confiance en notre projet ainsi que ses conseils et son aide précieuse tout au long de cette expérience. J'adresse aussi ma profonde reconnaissance à l'égard de Denis Limagne (INSP), Christophe Rafaillac (INSP) et Damien Bricault (LISE) pour leur aide irremplaçable dans l'élaboration de la cellule électrochimique et sa fabrication. Enfin, l'équipe de la ligne SIXS (synchrotron SOLEIL, France) constituée d'Alina Vlad, Andrea Resta et Alessandro Coati a été formidable pour sa disponibilité pendant et après les runs. Cette expérience au synchrotron n'aurait pas été possible sans un travail expérimental mené en amont avec Cyrille Bazin (LISE), pour mener à bien notre démonstration de variation de structure du matériau sous polarisation.

Je tiens également à remercier les rapporteurs de mon jury, M. Cédric Carteret (LCPME, Université de Lorraine) ainsi que Mme Sophie Peulon (LAMBE, Université d'Evry), pour le temps qu'ils ont accordé à ce travail, ainsi que d'avoir accepté la tâche de juger ce travail de recherche. Je remercie également M. Emmanuel Tertre (IC2MP, Université de Poitiers) qui a accepté d'être examinateur de mon jury.

Mes remerciements vont à tous les membres, passés et présents, des deux laboratoires d'accueil, qui ont constitué un cadre propice à mon épanouissement scientifique et personnel. En particulier, je remercie Isabelle et Martine, secrétaires du LISE, dont l'enthousiasme ne fait jamais défaut, Françoise, Stéphanie, Florence et Daniel pour leur disponibilité au niveau de l'instrumentation et leur gentillesse. J'ai également apprécié les conversations passionnantes avec Aziz, Cyprien, Damien, Hélène et Tony, qui ont alimenté mes réflexions. Je n'oublie pas les nombreux doctorants et post-doctorants qui m'ont apporté leur soutien et leur bonne humeur : Abdessadk, Aja, Alice, Antonin, Blanca, David, El Mahdi,

Elise M., Gabriel, Guillaume, Inès, Rafik, Simon, Sophie, Tabibian, Manel, Nesrine, Oumaïma, Thomas, Wanli et Zakaria du LISE, ainsi que Jordan, Myriam, Romain, Sheriff et Vivien du BRGM.

Enfin, toute ma reconnaissance va à mes proches ainsi qu'aux rencontres imprévues, qui ont contribué, par une parole marquante, un acte ou une aide altruiste, à me diriger progressivement sur la voie captivante de la recherche. J'adresse mes remerciements à mes amis, dont l'affection, les conseils judicieux et la considération m'ont portée. Je remercie infiniment mes parents et ma grand-mère pour leur soutien et leur amour indéfectible depuis toujours, et sans qui rien n'aurait été concevable. Je leur redis encore ma reconnaissance et mon affection.

Abstract

In the past decades, layered double hydroxides (LDHs) attracted increasing interest for their abilities of ion entrapment, containment and controlled release, with the potential to generate promising applications like energy storage, drug delivery and water treatment. For a conceivable employment of LDH, the understanding of ion transfers mechanisms between the material and the electrolyte is essential however poorly studied, and was further investigated in this PhD thesis. Also, the regeneration property of the material was prospected to test its sustainability.

The properties of the LDH derive from its specific bidimensional structure. It consists in a stacking of positively charged brucite-type layers due to the substitution of some divalent cations by trivalent cations. For electroneutrality reasons, the excess of positive charges is compensated in the interlayer space by the presence of hydrated anions weakly bound to the structure. This particularity confers a high potential for anionic exchange between the LDH and environment and for porosity. Another feature of the material concerns its specific pH value of the point of zero net charge (pH_{PZNC}), *i.e.* the pH value that depends on the chemical composition of the material and that corresponds to the equilibrium of charges resulting from protonation/deprotonation of –OH groups onto the external surface. A high pH value of the electrolyte compared to pH_{PZNC} provokes cation adsorption onto the surface.

It is suspected that both ionic transfers phenomena described above can be simultaneously controlled by electrochemistry in a reversible manner. A reversible anion transfer has already been evidenced for the LDHs composed of redox-active transition metals (ex: Co^{3+}/Co^{2+}, Ni^{3+}/Ni^{2+}, Fe^{3+}/Fe^{2+} etc…) by tuning the oxidation state of the metallic sites to reversibly modify the positive charge excess within the layers, however with no evaluation on kinetics and concentration of exchanged species. Also, a simultaneous modification of interfacial pH by electrogenerated H^+ or OH^- could modify the adsorption properties of cations onto the surface.

This Ph.D. thesis aims at deepening the understanding of the mechanisms and kinetics related to the reversible ion/solvent transfer between the electrolyte and the LDH under cyclic polarization by means of *operando* coupled electrogravimetric and crystallographic techniques. The Ni/Fe-LDH 6/2 was chosen for its specific properties of electronic conductivity and faradaic behavior that enhance ion transfer. Investigations were conducted on both the chemically synthesized and assisted electrosynthesized Ni/Fe-LDHs to compare the impact of their specific properties of crystallinity, porosity and charge transfer on the mechanism of species transfer.

A conventional technique coupling electrochemical and gravimetric measurements (EQCM) as well as a non-conventional technique, specifically the electrochemical impedance spectroscopy (EIS) coupled to fast quartz crystal microbalance (QCM) also called *ac*-electrogravimetry, enable to study the ion transfer phenomena located at the electrode/electrolyte. From *ac*-electrogravimetry, many information can be obtained: (i) separation of the different contributions related to the charged and non-charged species involved in the electrochemical processes, (ii) nature and kinetics of species transferred between the electrode and the electrolyte, and (iii) variation of the relative concentrations of the species inside the examined

material. It led to demonstrate the Ni/Fe-LDH pseudo-capacitance properties of mix cation (K^+) and anion (OH^-) exchanger and the H_2O molecule transfer during the reversible redox reaction. The specific sites of transfer of each of these species were also identified by EDX/XPS analyses and an *in situ* XRD technique coupled with electrochemistry under constant potential that was developed at the laboratory during this thesis. For the first time, developing and coupling *operando* XRD to gravimetric and current measurements under cycling potential at synchrotron (Saclay, France) underlined non reversible catalyzed oxygen evolution reaction (OER) that play a role in the interlayer spacing. Cation electroadsorption/desorption onto the external surface was further evidenced by electrochemical control of the pH at the coated interface, via OER above the pH_{PZNC}.

Keywords: Layered Double Hydroxides (LDHs), Electrogravimetry, *Ac*-electrogravimetry, Grazing-Incidence Wide-Angle X-Ray Scattering (GIWAXS), cationic transfer, anionic transfer, dehydration

Table of contents

General introduction

Layered double hydroxide (LDH) materials consist of a stacking of positively charged brucite-like layers,[2,3] due to the substitution of some divalent cations M(II) by trivalent cations N(III). For electroneutrality reasons, the excess of positive charges is compensated by the presence of exchangeable hydrated anions in the interlayer space. Their general formula is $[M^{II}_{1-y}N^{III}_{y}(OH)_2^{y+}][A^{m-}_{y/m}]^{y-}$, zH_2O. The interest of the layered double hydroxide material principally lies in its bidimensional structure conferring a high capacity for cation and anion adsorption, anionic exchange and porosity. It offers the possibility to access a high diversity of particles with various morphologies by varying the modification of the synthesis route, the chemical composition of the layers, the chemical or structural modification of the interlayered space.

The easiness of the chemical LDH synthesis as well as an easy control of the composition and physico-chemical properties is also of particular interest for varied industrial applications. For the last decades, the number of publications related to layered double hydroxides and its related electrochemical properties has dramatically increased for wide applications. Notably, it is a promising catalyst in electrochemical water oxidation as an alternative to some costly and scarce noble-metal oxides such as RuO_2 and IrO_2, for an essential role in various energy conversion and storage systems[4] (water splitting,[5] fuel cell and metal-air batteries[6]). LDH is also studied as a promising supercapacitor electrode[7,8] for high energy density storage systems. On one hand, the morphology, the chemical composition and the large specific area of the LDH favor the property of electrical double layer capacitance. On the other hand, a degree of redox reaction at the surface also provides a Faraday pseudocapacitance. Finally, another application is water treatment by intercalation of toxic, strategic or expendable anions like arsenates, vanadates, nitrates or sulfates.

It is highly significant to meticulously study, understand and control the electrochemical mechanism related to the ionic transfer between the material and the electrolyte which constitutes an important part of the operating principle of these applications. One of the LDH properties that limits the applications mentioned above is the low electronic conductivity of the LDHs. It can be promoted by preparing thin films of LDHs coated on a working electrode surface. Particularly, the presence of redox-active transition metals[9] (ex : Co^{3+}/Co^{2+}, Ni^{3+}/Ni^{2+}, Fe^{3+}/Fe^{2+}, etc…) within the brucitic structure of the LDHs enables both the amelioration of the conductivity and the reversible tuning of the oxidation state by cyclic polarization through an electron hopping mechanism. This action permits a reversible modification of the positive charge excess within the layers. The ionic and free water molecule transfers related to the tuning of the redox-active transition metals are known to occur,[10] however their identification (in terms of molar mass), kinetics and transferred concentrations were poorly investigated.

This Ph.D. thesis aims at refining the understanding of the different ions and solvent transfer mechanisms and kinetics between the electrolyte and the LDHs, related to the reversible redox reactions of the electroactive sites of the LDHs. Under cyclic polarization, the reversible tuning of the oxidation state is possible and observable through electrochemical measurements. With *in situ* polarization of an electrode coated with LDH, a non-conventional coupled electrochemical and gravimetric method, specifically the electrochemical impedance spectroscopy (EIS) coupled to a fast quartz crystal microbalance (QCM) also called *ac*-electrogravimetry methodology[11,12, 13,14] appears to be an attractive tool to study the nature and the concentration of the ionic species and solvent molecules transferred at the electrode/electrolyte interface. This methodology was successfully used for in depth characterization of reversible redox reactions involved in Prussian Blue or lamellar structures such as birnessite as well as the associated mass transfer.

In this work, *ac*-electrogravimetry allowed the determination of the electrochemical mechanisms and kinetics associated to the redox active transition elements within the layers of Layered Double Hydroxides. A special attention was paid on Ni/Fe-LDH 6/2 that is known to be one of the most conductive LDH and whose electroactive Ni can be reversibly switched to the (+II) and (+III) oxidation states under polarization. Nano-Ni/Fe-LDH 6/2 were investigated to enhance the number of the transfer sites (*i.e* intercalation sites and adsorption sites onto both edge and basal surfaces). Nano-Ni/Fe-LDH were either obtained by chemical and electrochemically assisted syntheses. For a better insight in the associated transferred species (anions, cations and water molecules), experiments were conducted in different supporting electrolytes (LiOH, KOH and CsOH) whose pH value was higher than Ni/Fe-LDH 6/2 pH of zero point of net charge (Ni/Fe-LDH 6/2 pH_{PZNC} equal to 8).

Highly relevant information was obtained: (i) kinetics and identification of species transferred between the electrode and the electrolyte, (ii) separation of the different contributions related to the charged and non-charged species involved in the electrochemical processes, and (iii) variation of the relative concentrations of the species inside the examined material. To corroborate the results and to localize the sites of interests where the different species transfers take place, XRD measurements were coupled to electrochemical and electrogravimetrical measurements under *operando* polarization at synchrotron SOLEIL (France). It also enabled to determine non reversible oxygen evolution reaction (OER) catalysis reactions that play a role in the interlayer spacing and in the species transfer at the interface of the investigated LDH.

The manuscript is divided into five chapters (chapters 3 to 5 are issued from submitted or future papers). The first chapter reports on the state of the art of the current knowledge in the electrochemical and electrogravimetrical studies of LDH materials.

The second chapter aims to describe the experiments that were conducted to synthesize the LDH by chemical and electrochemically assisted routes, as well as the characterization techniques of the synthesized material, the

electrochemical and electrogravimetrical techniques, and the *operando* coupling of the electrochemical, electrogravimetrical and XRD measurements under polarization at synchrotron Soleil.

The third chapter investigates the synthesis of the electrochemically assisted route of the Ni/Fe-LDH 6/2 in KOH 1 mol/L that is known to have an enhanced conductivity compared to the chemically synthesized LDH. The reversible ionic and water transfer between the LDH and the electrolyte are studied by EQCM and *ac*-electrogravimetry. The nature and kinetics of each transferred species are determined. The low crystallinity of the material prevents the continuation with further advanced analyses.

The fourth chapter aims to describe the electrochemical properties of the chemically synthesized Ni/Fe-LDH 6/2 in KOH 1 mol/L that is known to have a much higher crystallinity compared to the electrochemically assisted route. By tuning the oxidation state of redox-active Ni(II) and by varying the pH at the interface of the coated electrode, the mechanisms and kinetics of the reversible ionic transfers between the LDH and the electrolyte are studied by EQCM and *ac*-electrogravimetry. The results are corroborated with *in situ* XRD and EDX/XPS analyses. The effect of the oxygen evolution reaction onto the ionic transfer is highlighted.

The fifth chapter describes further the mechanisms and kinetics of the chemically synthesized Ni/Fe-LDH by varying the cation of the supporting aqueous electrolyte (Cs^+, K^+, Li^+). By *operando* XRD, electrochemical and electrogravimetrical under potential cycling conducted, for the first time, at synchrotron, new indications bring out the catalysis of interlayered water molecules by interfacial pH control.

Chapter I

Ionic transfers into LDH with electrochemistry: a bibliographical study

Chapter 1 starts with a comprehensive literature review of the electrochemical properties of LDHs. More details are given on the advances in the knowledge of mass transfer between the electrolyte and the material in basic solutions, in which the structure of the LDH is stable. Finally, the scope and objectives, starting from the state of the art of the present Ph.D. thesis are introduced

1.1 Chemical and structural composition of the LDHs

1.1.1 Chemical composition of the layers

Layered Double Hydroxides (LDHs) are solids constituted of brucite-like layers[2,3] in which some divalent cations, M^{II}, are isomorphically substituted by trivalent cations, N^{III}. Such substitution induces an excess of positive charges within the layers, M and N being the species that may have the same atomic number or may be different.

To respect electroneutrality, the excess in net positive charge is compensated by the charge of weakly bound intercalated anions, A^{m-}, in the interlayer space, usually surrounded by water molecules. Depending on the interaction with the layer, anions can be more or less easily exchanged by other anions, thus LDH are also referred as anionic clays, for their high anionic exchange properties. The substitution ratio, y, between M^{II} and N^{III} can be controlled during the synthesis. It has an effect on the number of anions intercalated within the interlayer space. The general formula of LDH can be written as follows:

$$[M^{II}_{1-y}N^{III}_{y}(OH)_2{}^{y+}][A^{m-}_{y/m}]^{y-}, zH_2O \quad (1.1)$$

From now, the composition of the LDH is noted with the abbreviation M^{II}/N^{III}-(A^{m-})-LDH (1-y)/y or M^{II}/N^{III}-LDH (1-y)/y for convenience. A scheme of this material is represented in figure 1.1.

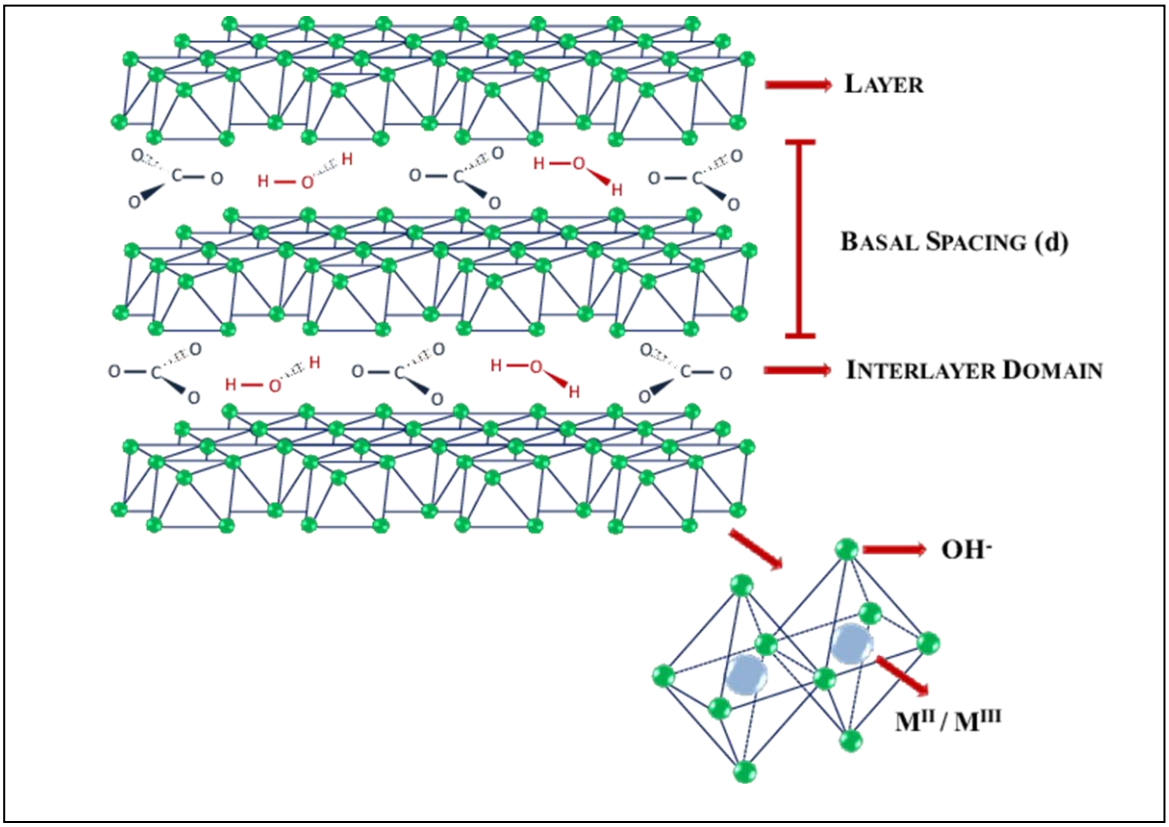

Figure 1.1: Structure of the LDHs[15]

A few LDHs exist in limited amounts in the environment as minerals like hydrotalcite $Mg_6Al_2(OH)_{16}(CO_3),4H_2O$, pyroaurite $Mg_6Fe_2(OH)_{16}(CO_3)$, zH_2O,[16] or Iron(II)-iron(III) hydroxy-salts (also called green rusts) as byproducts of metabolism of certain bacteria, and also unintentionally in man-made contexts such as the products of corrosion of metal objects. Moreover, intentional synthesis can be performed to obtain LDH of varied compositions within the layers and the interlayer spacing to modulate the intrinsic ionic capture properties of those materials. Performing synthesis, a great number of cations can be introduced in the lamellar structure: the more common divalent cations are Ca^{II}, Mn^{II}, Mg^{II}, Zn^{II}, Cu^{II}, Co^{II}, Ni^{II}, and the more common trivalent cations are Al^{III}, Fe^{III}, Cr^{III}.[16,17] Some publications report the synthesis of LDHs with monovalent and trivalent metals like Li^{I}/Al^{III}-LDH[18] and LDH with divalent and quadrivalent metals like Zn^{II}/Ti^{IV}-LDH[19] and Ni^{II}/Ti^{IV}-LDH.[20] Also, it is possible to synthesize LDH whose cationic composition is made of many divalent or trivalent cations like $Mg^{II}/Al^{III}/Fe^{III}$-LDH.[21] They are called mixed LDH.

1.1.2 Chemical composition of the interlayer space

The interlayer space is composed of water molecules and anions. Various anionic species can participate in the charge compensation inside the interlayer space.[22] They can be monovalent or have several charges, be organic ($C_6H_5SO_3^-$, CH_3COO^-), inorganic (NO_3^-, CO_3^{2-}, SO_4^{2-}, Cl^-), charged polymers (polyacrylate, polystyrène

sulfonate), or electro-active molecules (redox mediator). In the case of organic species, the obtained materials are inorganic/organic hybrid materials in which the intercalated species may be strongly bounded to the layers (ionic, physical or covalent interaction). The variety of combinations (cations/anions) confers a diversity of physico-chemical properties that can be modulated for various targeted application of anionic capture like water treatment[23,24,25] support for catalyzer,[26,27,28] reactive charges inside the polymers or for anionic release like energy storage devices,[7,6] or drug release.[29,30,31,32,33]

1.1.3 Structure of the LDH phase

The crystallites of the LDH are constituted of a stacking of $M^{II}(OH)_6$ and $N^{III}(OH)_6$ edge-sharing octahedra layers similar to the $Mg(OH)_2$ brucite structure. Each octahedron contains a metallic cation at its center surrounded by 6 hydroxyl groups at its summits. The stacking can be a 3R stacking (*i.e.* rhomboedric ABCABC) or a 2H stacking (ABABAB hexagonal).[17] Thus, the space group is classically R-3m. The a parameter is directly related to the distance between two metallic cations within the layer which is the double of the distance between two (110) planes according to $a = 2.d_{110}$. The c parameter is related to the basal distance d of the material according to $c = 3.d(003)$. This distance is a marker of the nature of the intercalated anion as each intercalated anion has a specific diameter and induces a particular strength of attraction with regard to the cationic layer.[34,35] It is also a marker of the hydration and M(II)/N(III) ratio. These crystallographic parameters are determined by X-ray diffraction. The XRD pattern of such materials can be separated into three regions:

1. The region below 30° (2θ) contains the diffraction peaks following the (00l) planes
2. The region above 55° (2θ) contains the (hk0) and (hkl) planes related to the metal hydroxide planes,
3. The intermediary region between 30° and 55° (2θ) contains the (h0l) and (0kl) planes whose positions depend on the polytype (3R or 2H).

In a larger scale, crystallites are aggregated and form interstices, which causes textural porosity. Even though the pore size distribution obtained thereby is broad and the pores are not well-organized, textural pores can increase surface area and enhance the accessibility to crystal surface.[36] The level of textural porosity depends on the different synthesis routes,[37] that are described below.

1.2 Species exchange between the LDH and aqueous media (without electrochemical polarization)

Once the LDH is immersed in solution, different mechanisms of transfer of anions, cations and water have been evidenced between the electrolyte and the material. Three mechanisms of anionic capture are known:[38] surface adsorption, anionic exchange and LDH reconstruction after thermal treatment at moderate temperature (memory effect). Capture after thermal treatment is not discussed in this thesis as the structure of the material is affected.

Different mechanisms of cationic capture are also known[39] although they are less explored than anionic capture, and the selected cations are mainly heavy metal ions such as Pb^{2+}, Cd^{2+}, Hg^{2+} and Cu^{2+}, Zn^{2+} and radiochemistry metal ions such as Co^{2+}, Ni^{2+} and Sr^{2+}. The affinity for cations ranges between 0.01 $mmol.g^{-1}$ and $4mmol.g^{-1}$. Their capture mechanisms are divided into four categories: precipitation of metal hydroxides onto the LDH surface, adsorption through the bonding with surface hydroxyl groups of LDHs, isomorphic substitution (more likely at the layers edge)[40,41] and chelation with the interlayer anionic functional ligand in the interlayer. Solvent transfer mechanisms are also reported into the interlayer space. The number of water molecules depends on the available space and anion species.[42]

1.2.1 Anionic intercalation/adsorption by switching the transition metal oxidation state

Anionic intercalation is another reversible mechanism of anionic capture and is defined as the transfer of anions from the aqueous medium to the interlayer space. The intercalation is principally influenced by the charge balancing of the anions into the interlayer space for the compensation of the positive net charge density within the layers by coulombian interaction. The anion intercalation reaches an optimal capacity for a M^{II}/N^{III} ratio of 3.[43] Furthermore, the intercalation increases with crystallinity: a best crystalline LDH material is obtained generally with a M^{II}/M^{III} ratio of 3/1.

1.2.1.1 Competition between anions - anionic exchange

LDH has a better affinity towards anions that have more than one charge. For example, Miyata[44] observed that for hydrotalcite (Mg/Al-LDH), the affinity scale of the LDH towards the anions is the following: $CO_3^{2-} > SO_4^{2-} > OH^- > F^- > Cl^- > Br^- > NO_3^- > I^-$. For Costa,[45] the order of exchange selectivity based on computational simulation with Zn/Al-LDH is: $CO_3^{2-} > OH^- > F^- > Cl^- > Br^- > NO_3^-$. In general, LDH with different cationic compositions have a great affinity for carbonate ions (CO_3^{2-}) that are present in alkaline solutions. These anions are also present in high quantity during the chemical synthesis of LDH (co-precipitation method) in the alkaline solution during the co-precipitation of cations. For this reason, LDH often contains carbonate ions in their interlayer space. This intercalation can be prevented in controlled atmosphere (deaeration of the solution or glove box).

The intercalation capacity for a specific anionic species can be modified and is maximal when the interlayer spacing has the same dimension as the diameter of anionic species of interest[43]. This interlayer spacing may be adjusted by varying the composition of the cationic layers as this distance decreases with the increase in the radius of the cations within the layers. Tuning the cationic composition ratio M^{II}/M^{III} also plays a role on the affinity of LDH towards specific anions.[43] Some studies have been made on the release of nitrates for environmental purposes. In mixed $Mg^{II}/Fe^{III}/Al^{III}$-LDH, the authors[21] have demonstrated that the nitrate adsorption increases as the aluminium content decreases in favor of the Fe content. After exchange, the Mg/Al-

LDH 4/2 structure is composed of 90 % carbonates and 10 % sulfates, whereas the Mg/Fe-LDH 4/2 structure is composed of 89 % carbonates, 7 % sulfates, and 4 % nitrates. These results are consistent with those of Delorme *et al.*[46] who showed that carbonate ions fully displace nitrate anions from the LDH structure in Mg/Al-LDH 4/2, and Tezuka *et al.*[47,48] who showed a stronger affinity for nitrates and a lower affinity for sulfates in Mg/Fe-LDH compared with Mg/Al-LDH. In Mg/Al-LDH,[49] it was noticed that when the Mg/Al ratio increases, the selectivity for sulfate and fluoride decreases, while that for nitrate increases (despite the fact that the diameter of the F^- ion is slightly smaller than the thickness of a flat-oriented NO_3^- anion). It was proved that the ion sieve effect is not the only factor that affects selectivity. There may be also involvement of other factors, such as the interaction with the interlayer surface of host layers and interlayered water in the case of nitrate selectivity.

The competition between anions may also vary according to the already intercalated ions.[50] For anionic species from As(III), As(V), B, Cr(VI) and Se(IV), the order of removal performance is as follow: Mg/Al-NO_3-LDH > Mg/Al-Cl-LDH >> Mg/Al-SO_4-LDH > Mg/Al-CO_3-LDH, suggesting the stability of the divalent anions like SO_4^{2-} and CO_3^{2-} in the LDH structure and thus their poor exchange properties. The Mg-Al-NO_3-LDH demonstrated an excellent ability to remove dilute concentrations of anionic species from As(V), Se(IV) and Cr(VI) with the following order; As(V) > Se(IV) > Cr(VI) > As(III) > B.

1.2.1.2 Ionic exchange method – Choice for the anionic species within the interlayer spacing

As previously mentioned, during the chemical synthesis/precipitation of the material in basic solutions, the anions initially present in the solution are intercalated into the interlayer spacing of the LDH. The synthesis in ambient air provokes the CO_2 dissolution and the elaboration of a high amount of carbonates in the basic solution. Carbonates having a high affinity compared to monovalent anions are consequently prevalent in the interlayer spacing. To prepare LDH composed of other anions (more commonly Cl^-, NO_3^-, SO_4^{2-}), it is necessary to avoid the contamination of carbonates by controlling the atmosphere (glove box) during the synthesis and by preparing a solution with the specific anions. In the interlayer spacing, a complete anion exchange is possible if the anion to incorporate has a higher affinity than the anions still present into the LDH. The direct exchange method stands for the anionic exchange mechanism to exchange the anions of the interlayer spacing of a LDH that contains initially anions with a low affinity (nitrates, chlorides….) with another anionic species in excess in a solution and which has a higher affinity. The LDH slurry is immersed into a solution containing an excess of anions that are to be intercalated. The time needed for the anionic exchange depends on temperature, pH, nature of the species in excess and the composition of the LDH.[38]

1.2.2 Adsorption of anions and cations by external surface modification

In aqueous media, **the anion adsorption** onto the surface of the LDH is an adhesion process of ions attracted by the external charged surface of the particles. The efficiency of this capture mechanism can be enhanced by

increasing the specific area of the material using the appropriate synthesis route. Many kinetic models analyze the adsorption of oxyanions by LDH (first order and pseudo first order kinetics, controlled diffusion, homogeneous diffusion and shrinking core models…).[38] Initially, adsorption is a fast mechanism (from one hour to one day). However, the final equilibrium state is slow to obtain (from some hours to several days). Different factors modify the adsorption of oxyanions onto the LDHs: pH, competition between anions, adsorbents concentration, temperature and morphology of the LDH.[38]

The **cationic sorption** (by precipitation or surface complexation) also depends on pH, temperature and ionic strength. Second and first order kinetics are the most widely used to model cation sorption process.[51, 52] Heavy metal precipitation can be produced either as part of LDH structure or in a separate phase. For example, the LDH interfacial pH allow cation chemical precipitation (as hydroxide phase) onto the external surfaces.[53]

In these conditions and in the absence of carbonate and sulfate ions (which are known to precipitate Pb(II) from near to neutral pH[54] in the investigated electrolyte, the spontaneous precipitation of $Pb(OH)_2$ (and adsorption of $Pb(OH)^+$) takes place in the pH range from 7 to 10.[55] Isomorphic substitution is another way to contain (replace) cations with conservation of the LDH structure. The atoms must have the same size and total ionic charge as those replaced.[56] Mg^{2+} was substituted by Co^{2+}, Ni^{2+} or Zn^{2+} in freshly prepared Mg/Al-Cl-LDH 2/1 when immersed in aqueous solution.

Heavy metals can also react with the anionic functional ligand in the interlayer space.[57] For example, in Zn/Al-EDTA-LDH, Zn^{2+} reacts with EDTA to form $[Zn(EDTA)]^{2-}$ complex which causes the intercalation of zinc cations in LDH.

In this thesis, the aim is to tune the oxidation state of the metallic cations within the brucitic layers and to understand the related direct consequences on adsorption. Thus, the precipitation, chelation and isomorphic substitution are not experimented; that is why the involved processes are not detailed. In solutions, the used cations (K^+) cannot be precipitated in the experimental conditions or isomorphically substituted. The chelation with anions is also not possible in the LDH as the anions are chosen to be CO_3^{2-} and OH^- 0.5M and 1M respectively.

The transfer of cations and anions between the electrolyte and the LHD depends on the morphology, pH of the electrolyte and temperature. Their effects are detailed in the following.

1.2.2.1 LDH morphology

LDH morphology is one of the key parameters in this study; it is responsible for the kinetics of both faradaic redox reactions and ion transfer rate. The formation of nanometric structures significantly increases the surface-to-volume ratio, thus the specific area is enhanced. Several synthesis routes design specific forms, *i.e.* sand rose composed of many thin wires, nanoplatelets, 3D hierarchical structures… some of them improve the porosity of

the material, which aims to obtain increased exchanges with the solution and a small aggregation state for electrochemical exposition reasons.[37] Several synthesis routes will be detailed in chapter 1.3 and the respective porosity will be detailed.

1.2.2.2 pH

The pH value is also one of the key parameters in this study because both cation and anion adsorptions are sensitive to the pH value. First of all, pH (and complexing agents) is/are responsible for ion speciation in solution.[58,59] In agreement with Miyata[44] affinity scale, the ion speciation should be responsible for the anionic exchange properties. In addition, the pH of the zero point of net charge,[60] pH_{PZNC} (pH resulting from the cancellation of the positive charge originating from the chemical composition of the LDH and the variable charge resulting from the protonation/deprotonation of the LDH layers) should play a key role on the adsorption processes. The pH_{PZNC} is an intrinsic property of the LDH and it depends on its composition.

The reactivity of the external surfaces should strongly be influenced by the net proton surface charge, which depends on pH and ionic strength, with respect to Brønsted–Lowry acid-base theory, through the following reactions:

$$\equiv M\text{-}OH + H^+ + A^- \Leftrightarrow \equiv M\text{-}OH_2^+(A^-) \quad (1.2)$$

$$\equiv M\text{-}OH + C^+ \Leftrightarrow \equiv M\text{-}O^-(C^+) + H^+ \quad (1.3)$$

where M is a metal cation constituting the layered sheets and consequently the external surfaces of LDH and A- or C+ are anions or cations. It implies the sorption of both cations and anions onto edge surfaces depending on the pH at the clay interface.

For example, pH_{PZNC} equals 8.16[61] for Ni/Fe-LDH 6/2 and equals 10.6[60] for Mg/Fe-LDH 4/2. If the pH of a suspension of LDH is more than pH_{PZNC}, it enhances the deprotonation of the Metal-OH function of the external layers of the LDH particles. The resulting charge of the external layer is negative, which provokes the adsorption of cations from the aqueous solution and the desorption of anions. If the pH of the solution is less than pH_{PZNC}, it enhances the protonation of the Metal-OH function of the external layer of the LDH. Thus the resulting charge is positive, which provokes the desorption of cations and the adsorption of anions. In the case of $pH << pH_{PZNC}$, the structure of the LDH is deteriorated, also inducing a drop in the adsorption of the anions.

The dependence of the adsorption of anions onto LDH is thus sensitive to changes in pH.[62,63] For example, in Li/Al-Cl-LDH, As(V) adsorption is sensitive to changes in pH between 4 and 7.[62] Sorption of arsenate on Li/Al LDH-Cl displayed a pH-sensitive behavior from pH 4.0 to 7.0, but it was insensitive to pH above pH 7.0 (up to

9), approaching to the pH_{PZNC} of Li/Al LDH-Cl (7.22). Two types of reaction sites within Li/Al LDH-Cl were envisaged to participate in LDH arsenate sorption process. This result is in agreement with:

- the anionic exchange properties according to the permanent positive basal surfaces arising from isomorphic cationic substitutions,
- the variable proton surface charge arising from hydroxyl functional groups coming from the external layers, leading to the enhancement of anion sorption with the pH decrease.

It is worth highlighting that above pH_{PZNC}, the insensitivity to anionic exchange properties can be explained by arsenate speciation in solution. Indeed, in the absence of any complexing agents, the only one bivalent form (predominant) existing in the pH range 7-9 is $HAsO_4^{2-}$. This bivalent form exists up to 11.8. Above 11.8, the predominant specie (AsO_4^{3-}) is trivalent. The anionic exchange process should thus be influenced by the pH value in the range 9-14. Indeed, experiments conducted with calcinated Mg/Al-LDH, in the pH range 2-12, in the absence of any complexing agents, showed the adsorption sensitivity of As(V) and Se(IV) versus pH[63]. For Se(IV), data acquired are clearly influenced by both the Mg/Al-LDH pH_{PZNC} value (6.8-8.9)[64,65] and the As(V) speciation versus pH. Indeed, H_2SeO_3 predominates in the pH range 0-2.5; $HSeO_3^{2-}$ in the pH range 2.5-8.5 and SeO_3^{2-} in the pH range 8.5-14. The large increase of the As(V) sorbed amount in the pH range 2-4 can be explained by sorption and anion capture of $HSeO_3^-$. The sorbed amount remained then relatively constant versus pH. The "slight" increase in the pH range 8.5-11 can be explained by SeO_3^{2-} anion capture. For uncalcinated Mg/Al-LDH, the As(V) sorbed amount is rather influenced by the pH_{PZNC} value; probably due to the harder competition for anion exchange between As(V) and carbonate anion initially present in the interlayered sheets.[66]

1.2.2.3 Temperature

Usually, the sorption amounts of metal cations increases with increasing temperature due to the endothermic nature of the adsorption reaction.[67] For anions, usually the adsorption decreases with increasing temperature due to the exothermic nature of the simple adsorption reaction. For example, the As(V) and Se(IV) adsorption onto LDHs was reported as an exothermic process.[63,68] However, a number of studies have reported that the adsorption of oxyanions by LDHs is an endothermic process[69,70] and others reported no dependence on temperature.[66,63]

1.2.3 Exchange of water

In interlamellar space, LDHs include water molecules distributed around the hydration layer of the metal hydroxide layer and the hydration spheres of the intercalated anion. As shown by TG analysis,[42] in hydrotalcite Mg/Al-LDH, water molecules are weakly bound to the metal hydroxide layer and are lost below 100°C. The degree of hydration of the metal hydroxide layer ranges between 2 and 5.84. Intercalated water molecules are more strongly bound when located into the hydration sphere of the anion and are lost at higher temperatures (100°C < T < 250°C). They are estimated to lie between 0.8 and 6 molecules.[42] The number of intercalated water molecules depends on the intercalated anion species: in carbonate-LDHs the greater proportion of water

molecules is associated with the anion, whereas in the nitrate and chloride containing LDHs, the greater proportion of the intercalated water is bound to the metal hydroxide layer. This trend is in keeping with the higher hydration enthalpy of the divalent anions compared to the monovalent anions.

Water diffusion has been studied within the interlayer domain. Molecular dynamics simulation[71] shows that in Mg/Al-Cl-LDH, a water molecule is mostly fixed in a hydroxyl group site, as an acceptor of two hydrogen bonds from the upper and lower hydroxyl groups of the layers. Water diffusion is largely contributed by a series of jump events: water molecules can jump to two hydroxyl groups in an adjacent site in 10^4 ps on average. Thus, the diffusion coefficient of water is calculated to be of the order of $10^{-9}cm^2/s$.

Except reference 36, a very few articles relate the mechanisms of water intercalation and water exchange of a LDH immersed in aqueous solution. However, a dense literature concerns the water intercalation into the better known clay minerals (*i.e.* cationic clays). The nature and strength of forces between water molecules and the clay mineral depend on the position of water molecules within the pore space of the clays.[72] In clay minerals, crystalline swelling is controlled by a balance between strong forces of attraction and repulsion[73,74] and is more easily modeled by considering potential energies of attraction and repulsion between charges.[75] The attraction potential energy is electrostatic and dominantly arises from the coulombian attraction between the negative surface of the layers and the positive charge of the interlayer cations. Van der Waals interactions between adjacent layers may also contribute to the total potential energy of attraction. The potential energy of repulsion comes from the partial hydration potential energy of the interlayer cations. All the intercalated water is generally found to be in the hydration sphere of the cations. The water molecules bond to each other, leading to the incorporation of water in excess. To a lesser extent, the potential energy of repulsion comes from the partial hydration potential energy of the negative surface charge sites. According to Lal and Shukla,[76]swelling due to diffused double-layer repulsion can be curtailed by strong adsorptive forces of polyvalent cations, e.g., the Coulombic attraction forces hold the two clay particles together against the double-layer repulsion.

For less known LDHs, by analogy, a similar however less important water swelling should be also observed in LDH with the increase of M^{III}/M^{II} ratio and water swelling will be discussed in chapter 5. Different hydration levels were already evidenced with XRD characterization[34,35] on various compositions of the layers. On Zn/Al-NO_3-LDH, Ni/Al-NO_3-LDH and Co/Al-NO_3-LDH, the same anion NO_3^- is intercalated into the interlayer space. A slight modification of the interlayer distance is observed with $d_{Zn/Al} > d_{Ni/Al} > d_{Co/Al}$ which seems to be due to different hydration levels.

1.2.4 Conclusion

Depending on their ionic or solvent nature, species transfer between the LDH and the electrolyte were not homogeneously studied. Anion transfer was largely investigated, however to our knowledge, there are a few articles on cationic adsorption, and even less publications in water transfer or hydration. For the enhancement of

all the species transfer, the increase in porosity of the material is of prime importance. Section 1.3 will detail the related synthesis routes and related porosity. Moreover, for studying of reversible modification of the oxidation state and following the transferred species, electrogravimetrical and electrochemical measurements have to be performed. The detail of the deposition of the LDH material onto an electrode is thus also explained in section 1.3.

1.3 Synthesis methods for the elaboration of modified electrode with LDH

This section emphasizes on the different methods of synthesis of the LDH. For each one the specific interests are developed and the choice of the optimal one for our investigations is of prime interest. For the study of simultaneous electrochemical and nanogravimetric measurements related to the mass transfer between the LDH and the electrolyte, an electrode that also plays the role of quartz crystal microbalance is needed. For this reason, a LDH thin film is deposited onto a quartz plate coated with gold at a resonant frequency of 9MHz. For the fabrication of such a coated electrode, the optimal criteria are:

- the synthesis of a pure and highly crystallized LDH,

- a high specific surface area,

- a facilitated charge transfer between the material and the electrode,

- a uniform coating onto the electrode,

- a fast fabrication,

- a conductive material.

All the known synthesis routes do not fulfill all these conditions. They are divided into two categories: the chemical synthesis and the electrochemically assisted synthesis.

1.3.1 Chemical syntheses of the LDH

1.3.1.1 Co-precipitation method with constant pH - separated nucleation and aging steps,[1] or with variable pH[21,77]

The pre-synthesized step of the chemical synthesis is generally the co-precipitation at constant pH (described by S. Miyata in 1975).[78] It is a chemical synthesis of LDH by precipitation of divalent and trivalent metal cations in a basic solution.

Metal salts are added into an aqueous basic solution with carbonate and hydroxyl ions with optimal pH value at which the precipitation occurs at relatively low temperature, below 100°C.[79, 80] Thermodynamic studies evidenced that LDH precipitation is favored due to their greater stability compared to the corresponding simple

hydroxides.[81] Another alkalization agent like urea can also be used for the coprecipitation reaction. The hydrolysis reaction of urea slowly liberates CO_3^{2-} anions which gives particles with higher dimensions, of the order of the micrometer.[82,83] The final slurry is centrifuged three times with deionized water to separate the LDH from the salt residues in the solution.

For the co-precipitation method with variable pH, an aqueous solution of metal salts is prepared, in which carbonate and hydroxyl ions are added dropwisely with a peristaltic pump, to reach an optimal pH value at which the precipitation occurs at relatively low temperature, below 100°C.

Synthesis by topochemical route proceeds to the oxydation of a part of the cations originally presents using solids like oxides or hydroxides. It enables the formation of monometallic LDHs. The oxidation may be possible thanks to oxygen from gaseous phase[84] or to oxidizing agent from liquids (H_2O_2, Br_2).[85]

1.3.1.2 Post-synthetic treatments

Several post-synthetic treatments can be applied to pre-synthesized LDHs to control the particle size, aggregation, and morphologies. The main mentioned treatments are hydrothermal treatment, solvothermal treatment, spray drying and soft templating.

Hydrothermal treatment enables the maturation of the pre-synthesized LDH at a temperature up to 140°C. It involves the re-activation of nucleation, crystal growth and aggregation. The high temperature increases the Brownian motion of LDH particles which prevents their aggregation for the fabrication of nanoparticles. The metal cations are also better distributed in the solution, thus forming a highly crystallized particle. However prolonged hydrothermal treatment or too high temperature causes re-aggregation due to the formation of large particles overcoming the electrostatic repulsion between particles.[86]

Solvothermal treatment proceeds to the use of chelating agents (organic additives) that also play an important role to improve the structural ordering, size and stability of each crystal as well as the stability of crystals. For example, some articles report on the preparation of LDH hollow microspheres by optimizing crystallization, dissolution and recrystallization of constituent crystals[87] using sonication and/or adding ethylene glycol and glycine as a chelating agent.[88]

For spray drying method, a few publications appear in the literature about this technique. A LDH colloidal suspension obtained by separated nucleation and aging steps[1] is sprayed to form an aerosol which leads upon solvent evaporation and the consolidation of LDH nanoparticles to spherical microspheres.[89, 90] There is no extensive study on the effect of process parameters on the properties of spray-dried agglomerates.

Soft-templating is also performed with LDH. Cooperative self-assembly between organic templates (micelles of amphiphilic organic molecules like surfactants and water soluble polymers) and inorganic precursors yield

organized architecture and subsequent removal of organic templates by extraction or calcination. Created structures have a well-defined porosity and are tuned by varying the surfactant and the composition of the starting mixture.[91] Micelles are colloidal dispersions with a particle size within 5-100 nm range.[92] Thus, building blocks of LDH must be small enough in nm range. For successful fabrication, nanobuilding blocks is indeed less than 4-6 nm.[93] For example, Gunawan et al. reported the fabrication of coral-like porous Mg/Al-LDH microspheres in ethylene glycol/ methanol/sodium dodecyl sulfate system (SDS)[94]. Zhang et al. and Sun *et al.*[95,96] synthesized flower-like Mg/Al-LDH porous microstructures with SDS. Shao et al. prepared Mg/Fe-LDH microspheres with the morphologies of hollow, yolk–shell and solid interior structure by a hydrothermal reaction in NaOH aqueous system with SDS additive.[97]

The chosen synthesis is the co-precipitation method of divalent and trivalent metal cations as the LDH is bimetallic. To obtain nanoparticles, the varying pH value method is used as well as hydrothermal treatment with a temperature of 80°C. The other post-synthetic treatments are excluded as other molecules are needed during the solvothermal treatment and soft-templating methods. Also, spray drying method is lowly studied.

1.3.1.3 Formation of thin films of LDH onto an electrode

Many different techniques of coating are found in literature like dropcasting, spin-coating, insertion of a support, layer-by-layer method.

For the coating of an electrode by dropcasting, the surface of the electrode is firstly polished and rinsed or sonificated with ethanol.[9] Then, a drop of LDH slurry is dropcasted onto the electrode and dried in air[98] or in a dessicator over silica gel[9] during 12 hours. The interactions between the film of LDH and the electrode are weak, which does not facilitate the electron transfer between the film of LDH and the electrode.[99]

The coating can be prepared by spin-coating[100] that allows a compact structure formed of oriented platelets, parallel to the surface of the substrate.[101]

LDH can be also inserted onto a support, like porous anodic alumina aluminum, MXene substrates and graphene oxide nanosheets supports for an *in situ* LDH growth[102, 103, 104] by simple immersion into a metal salt solution in the presence of precipitating agent (NaOH, NH_4OH, hexamethylenetetramine (HMT), urea…).

Assembling exfoliated LDH nanosheets is also a promising way to form textural porosity with a higher specific surface area. After co-precipitation, exfoliation can be for example achieved by vigorous shacking of Zn/Cr-LDH sample in formamide. Sandwiched multilayers and alternately deposited negative polyanions are deposited onto gold surface.[105] Platelets are observed to adopt a preferred orientation with their c axis perpendicular to the substrate surface.[101]

Dropcasting method is used in this thesis as an optimum technique for the study. For spin-coating method and assembling exfoliated LDH, due to the orientation of the platelets, the interlayer domain is not "evidenced" at the interface. The direct coating onto a support during coprecipitation, although of interest, is excluded as used electrodes are gold patterned quartz crystals.

1.3.2 LDH synthesis by assisted electrochemical synthesis onto an electrode

Some investigations have concerned the formation mechanism of the LDHs onto an electrode. Indira and Kamath in 1994[106] were the first authors who reported and described the synthesis of Co/Al and Ni/Al-LDHs 3/1 by the electrochemically assisted route. In an aqueous solution of nitrates as well as divalent and trivalent metals, the cathodic reduction of both nitrates and water produces hydroxide ions at the vicinity of the working electrode leading to the LDH precipitation. According to Scavetta *et al.*,[35] the following reactions (1)–(7) produce OH^- or consume H^+:

$H^+ + e^- \rightarrow H_{ads}$ (1.4)

$2H^+ + 2\,e^- \rightarrow H_2$ $E° = 0.000V/SHE$ (1.5)

$NO_3^- + 2H^+ + 2e^- \rightarrow NO_2^- + H_2O$ $E° = 0.934V/SHE$ (1.6)

$NO_3^- + 10H^+ + 8e^- \rightarrow NH_4^+ + 3H_2O$ (1.7)

The electrolysis of water is:

$2H_2O + 2e^- \rightarrow H_2 + 2OH^-$ $E° = -0.828V/SHE$ (1.8)

Anion reduction reactions are listed according to:

$NO_3^- + H_2O + 2e^- \rightarrow NO_2^- + 2OH^-$, $E° = 0.010V/SHE$ (1.9)

$NO_3^- + 7H_2O + 8e^- \rightarrow NH_4^+ + 10OH^-$ (1.10)

Reaction 1.7 can be decomposed in different steps in acidic media on copper disks Cu (111) and Cu(100) as follows:[107]

$HNO_3 + 2H^+ + 2e^- = HNO_2 + H_2O$ (1.11)

at 0.150V in Cu(100) and 0.100V in Cu(111) (versus reversible hydrogen electrode (RHE)[108]

$HNO_2 + 1H^+ + 1e^- = NO + H_2O$ (1.12)

$NO = NO_{ads}$ (1.13)

$NO_{ads} + 5e^- + 6H^+ = NH_4^+ + H_2O$, (1.14)

at 0.100V in Cu(100) and 0.100V in Cu(111) with diameter 6mm.

However, because of slow kinetics of heterogeneous electron transfer, the direct reduction of nitrates on bare metallic electrodes is difficult.[109,110,111] Some authors use the deposition of nanomaterials on electrode surface, *i.e.* copper nanoparticles modified gold electrodes, Cu/Pd bimetallic properties modified BDD (boron doped diamond), Cs (solid carbon) nanoparticles and PP (polypyrrole) nanowires modified gold electrodes which increases the sensitivity of the electrode response by maintaining a large and highly active surface area.[112]

According to Indira and Kamath in 1994,[106] the relative importance of the three classes of reactions for the electrogeneration of base is not known. In a study about the assisted electrodeposition of simple hydroxides $Mg(OH)_2$ and $Ni(OH)_2$, the yield of $Mg(OH)_2$ is much higher from a chloride bath when compared to a nitrate bath under all deposition conditions, and the yield of $Ni(OH)_2$ is equivalent in nitrate bath and chloride bath. It seems that the HER is the only reaction responsible for electrogeneration of base in a chloride bath and is therefore of importance.

On purely thermodynamic considerations, the reduction reaction with the most positive E° value is preferred over the others. Reactions (1.6) and (1.7) have a more positive E° value compared to most metal ion reduction reactions14 (except for those of Cu^{2+}, Ag^{+}, and Bi^{3+}) which provokes the precipitation of the metal instead of metal deposition. For the electrodeposition of copper or bismuth hydroxides, the cathodic reduction technique was extended to perchlorate baths as perchlorate reduction reactions have much higher E° values than the nitrate reduction reactions. However these experiments failed to yield hydroxide deposits. The authors believe that thermodynamic consideration is not the sole determining criterion for the success of this class of electrosynthetic reactions. Also unknown kinetic factor may play a crucial role. Complexation with the conterion in the electrolyte will be also investigated in chapter 3.

For the assisted electrodeposition of the LDH, it is assumed from literature that different routes are possible depending on the concentration in OH^- at the vicinity of the electrode.[34] If the production of OH^- is slow, the LDH should be synthesized onto the electrode in two steps: the first one is the precipitation of the cation, $N^{(III)}$, in $N(OH)_3$ and the second is the formation of the LDH from the reaction between $N(OH)_3$ and $M^{(II)}$. If the production of OH^- is fast, the LDH is formed in one step, with the concomitant precipitation of $M^{(II)}$ and $N^{(III)}$ metals in the stoechiometric proportions of the synthesis solution, like when the solution containing $N^{(III)}$ and $M^{(II)}$ is titrated with NaOH at constant pH value, which enables to obtain uniform films of LDH.

The assisted electrodeposition method fulfill most of the criteria listed for the LDH coated electrode. It enables a fast fabrication of electrode as the formation of a thin film of LDH onto an electrode is done in only one step and in a few seconds. The electrodeposition has been performed on different conductive materials, for example: ITO,[113] glassy carbon,[114] gold,[115] FeCrAlloy,[116] and Ni.[117] The coating onto the electrode also is claimed to be uniform. It is also claimed to the control both film thickness and morphology by tuning the potential and deposition time, as notified by Tonelli's group.[35] In 60 seconds, the electrode is fully covered with a thickness of

150 nm, and the film is homogeneous and dense with a nanoparticle size lower than 50 nm, connected in a gel-like manner in a sand rose morphology. If the electrodeposition time lasts more than 60 seconds, the particles have a larger size and a higher thickness. Another advantage compared to the chemical synthesis is that the assisted electrogenerated LDH film has a better adherence onto the electrode and consequently a better electron transfer between the electrodes and the LDH than the chemically synthesized LDH.[99] According to Tonelli's group,[35] the mechanical adhesion of the coating to a Pt electrode can be further enhanced with an electrochemical pretreatment of the surface in sulfuric acid which decreases the required surpotential for the nitrate reduction and enhances the production of OH^-.

Another advantages compared to the chemical synthesis is the intercalation of nitrates into the interlayer spacing without any controlled atmosphere. The reduction of nitrates in an acidic solution that contains metallic cations enables to exclusively intercalate nitrates into the interlayer spacing, because the carbonates are not present in acidic media. For Zn/Al-LDH, Ni/Al-LDH, Co/Al-LDH, XRD characterization evaluates the interlayer distance d that corresponds to the intercalation of nitrate anions between the layers.[34,35]

The main disadvantages of this technique are the low crystallinity of LDH and the presence of impurities. In the literature, the XRD pattern of the assisted electrodeposited material is characteristic of the LDH. The FWHM of the diffraction lines are larger than that observed for the chemical synthesis. That means a lower degree of crystallinity of the electrodeposited LDH.[34] The low intensity of the peaks is due to the small thickness of the thin film which also makes it difficult to characterize by XRD. A hint is to scratch the film of many samples to reap a higher quantity of powder for XRD characterization. According to Yarger *et al*.,[115] the deposition of pure and well-ordered Zn/Al-LDH requires an optimum potential, ratio of divalent/trivalent metals and initial pH. Increasing or decreasing the aluminum concentration in the plating solution resulted in the formation of aluminum or zinc containing impurities, respectively, instead of varying aluminum content incorporated into the LDH phase. A more negative potential provokes the deposition of zinc metal or zinc hydroxide, and a less negative potential provokes the deposition of zinc oxide. Increasing the pH destabilizes the formation of the LDH phase while decreasing pH promotes the deposition of other impurities.

The investigation of the electrogenerated coating is thus of prime interest to understand the occurrence of impurities and low crystallinity of the film. Also, it is important to understand the reduction reaction for the production of base that play a role in the synthesis of the LDH.

1.4 Electrochemical properties of LDHs

1.4.1 Electron transfer in electrochemistry

Within the material, the transport of electronic charge occurs through the LDH layers via an electron hopping mechanism between localized redox centers and ion motion across the pores and channels of the material to preserve the electroneutrality of the LDH structure[36, 118, 119].The electronic transfer within the LDH depends on the diffusion of the anions between the conducting elements. Two strategies promote the electron transfer within the LDHs and render the structure of the LDH electroactive: (1) the intercalation of redox active anions from the electrolyte into the interlayer spacing, and (2) the presence of transition metal cations with redox activity in aqueous solution within the layers of the LDH. Many articles from the literature describe the strategy (1) of intercalation of different redox active species of different sizes into the LDH interlayer, especially redox mediators that can relay electron within the structure for diverse applications like electrocatalytic detection process or the regeneration of the enzyme active sites in biosensors or biofuel cells.[120,121] For instance, some molecules like electroactive anions and metal complexes bearing anionic groups such as anthraquinone mono- and disulfonate (AQS),[122] 2,2′-azino-bis-3-ethylbenzothiazoline-6-sulfonate,[123] nitroxide,[124] and ferrocene derivatives[124] or porphyrins.[125] A limiting process is that only less than 10 percent (in mole) of these intercalated anions participate in the electrochemical reactions. EQCM measurements unveil a loss/gain of ions from the electrolyte as a charge balancing mechanism occuring during the electron transfer.[126] Those can be a sorption of cations onto external sheets during the reduction to compensate the negative charge within the interlayer spacing, or the deintercalation of anions during the reduction depending on the conditions. Another limiting process is the diffusion of other anion species whose LDHs affinity is more significant.[124,127]

This strategy is not developed in this thesis as we aim at reversibly intercalate/deintercalate anions that are not necessarily redox active. The strategy (2), discussed in the next section, is the synthesis of a LDH composed of transition metal cations within the layers of the LDH.

1.4.2 Use of transition metals with redox activity in aqueous solution

Generally, LDH has poor conductive properties and can even be insulating like in the case of Mg/Al-LDH[99] or Zn/Al-LDH[128] when the intercalated anions are not electroactive. For a reversible anionic capture, it is necessary to work with conducting materials and to reversibly modify the ratio of metals with +III oxidation state versus metals of +II oxidation state. Thus, the use of transition metals of d group with two different oxidation states +II and +III in aqueous solution that enhance the conductivity of the material is of prime interest.

With electrochemistry, the cyclic oxidation/reduction of the divalent/trivalent transition metal of d groups within the cationic layers of the LDH reversibly tunes the excess of positive charges within the layers. It has a

consequence on the mechanisms of intercalation/deintercalation of the charged and uncharged species and possibly on the structure of the LDH. Thus, this mechanism is investigated in the literature to pave the way towards enhanced and reversible capture/liberation of anions.

In the literature, the redox active Co, Ni, Mn and Fe are good candidates as they satisfy the conditions cited above *i.e*. they are transition metal of d group that have the +II and +III oxidation state and their standard redox potentials occur in the potential window between the water oxidation potential and the water reduction potential in aqueous media.

Table 1.1: Table of standard redox couples values

Redox couple	Redox couple E° (V/SHE)
O_2/H_2O	1.23 [Pourbaix]
Ni^{III}/Ni^{II}	0.48[129 130]
Co^{III}/Co^{II}	1.01[130]
Mn^{III}/Mn^{II}	0.59[130]
Fe^{III}/Fe^{II}	0.77[130]
H_2O/H_2	0 [Pourbaix]

The most commonly synthesized LDHs are composed of Ni^{II}/Al^{III}, Ni^{II}/Fe^{III}, Co^{II}/Fe^{III}, Co^{II}/Al^{III}, Mg^{II}/Fe^{III} in different ratios as well as monometallic LDH like Co^{II}/Co^{III}-LDH and green rusts Fe^{III}/Fe^{II}-LDH. The conductivity and transfer mechanism of each of them are investigated in the literature.

In general, the conductivity of the LDH material is studied in strongly basic media like KOH and NaOH by cyclic voltammetry and electrochemical impedance spectroscopy. The study of the charge transfer within the Ni/Al-LDH by electrochemical impedance spectroscopy shows semicircles whose shape is characteristic of a pseudocapacitive material. The redox mechanism is quite complex as it implies both an electron transfer for the oxidation/reduction of the metal within the layer, and the charge neutralization of the material by the insertion/deinsertion of ions, as confirmed by Vialat *et al.*[131] The electrochemical behavior results in both electronic and ionic contributions.[132] For an active M^{II} cation in strong alkaline solutions like Ni^{II} in Ni^{II}/Fe^{III}-LDH, the change in the M^{II}/N^{III} ratio starts with the oxidation reaction following the equation:

$$[M^{II}_{1-y}N^{III}_{y}(OH)_2]^{y+}\,[A^{m-}_{y/m}]^{y-},\ zH_2O + nOH^- \leftrightarrow [M^{II}_{1-y-n}M^{III}_{n}N^{III}_{y}(OH)_2^{(y+n)+}]\,[A^{m-}_{y/m}]^{y-}[OH]^{n-},\ zH_2O \qquad (1.15)$$

A two kinetic-limiting step may take place at the surface of the material: the kinetic-limiting step of the ions (due to the intercalation of anions) and the kinetic-limiting step of the electrons (due to the electron-hopping). From EIS data analyses of Ni/Al-LDH **and** from the calculation of the activation energy for the two processes,

the **kinetic-limiting step** of the overall electrochemical process is related to the electron hopping.[133] This fact explains the decrease of R_{et} from 7000 Ω for Ni/Al-NO_3 to 2000 Ω for GnS@Ni/Al-NO_3 composite, confirming the role of exfoliated graphene (GnS) as electron percolant.[134,135]

1.4.2.1 Electric charge transfer by hopping mechanism

The charge transfer occurs via a hopping mechanism and can be compared to an internal redox reaction between the reduced and oxidized forms of the M^{III}/N^{II} couple. Finding the equivalent circuit enables to deconvolute the contribution of the electrons and the OH^- ions to the overall conduction. In reference[133], the model is the following: an electron is released to oxidize Ni centers and the OH^- anions enters into the structure for electroneutrality. It was also proved that the electronic conductivity depends on the potential while the resistance related to the ionic charge transfer is almost potential independent. The ionic charge transfer depends on the desolvation and adsorption processes of OH^- anions. Increasing the pH increased the OH^- concentration which increased the overall conductivity of the material.

Two regions are distinguished at the interface between the LDH and the electrolyte:[131] the external LDH surface/electrolyte solution interface and the internal LDH layers/electrolyte interface located inside the pores, channels, and interlayer domains. The internal interface is more involved in the electrochemical process and it was demonstrated by extrapolation of the electrical charge Q at $v \to 0$ and $v \to \infty$. The extrapolation of Q at $v \to 0$ estimates Q_{tot}, *i.e.* the charge related to the internal and external interfaces. The extrapolation of Q at $v \to \infty$ is the estimation of the external charge Q_{out}.[136] For Ni/Al-LDH in 0.1M KOH, the electrochemical response is activated upon potential cycling. Q_{tot} and Q_{out} are respectively 7 and 0.1 C g^{-1} [135] leading to a contribution of the external surface of only 1.4 %. For Co/Al-LDH, no activation of the electrochemical response is observed upon potential cycling.[135] Q_{tot} and Q_{out} of 172 and 18 C.g^{-1} respectively are higher than the values found for Ni/Al-LDH. Thus, the overall electrochemical process in Co/Al-LDH is more efficient and faster than in Ni/Al-LDH and the percentage of external surface involved in the electrochemical process is significantly enhanced and equals 10%.

1.4.2.2 Capacitive behavior of the LDH: accumulation of anions at the interface

The concomitant migration of the anions inside the interlayer spacing compensates accumulated positive charges. It is found in literature that the electrochemical reaction is run by a diffusional regime of ions.[137]

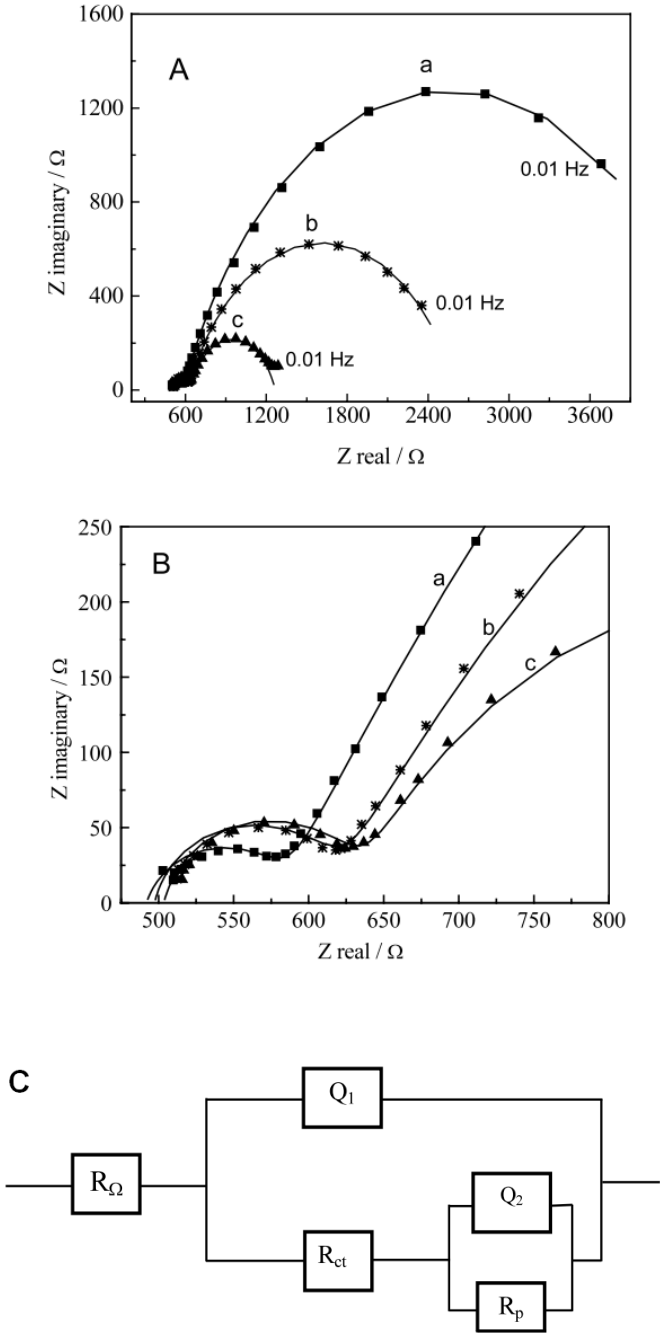

Figure 1.2: Nyquist plots of the impedance spectra of a Ni/Al-Cl film in pH 10 phosphate buffer (A) Frequency range 5 kHz to 10 mHz, (B) enlarged view of the high frequency from 5kHz to 5Hz. At open circuit, after 300s of oxidation at (a) 0.90 V, (b) 0.95 V, (c) 1.05V . Symbols are the experimental points and the solid lines are NLLS fit of the data to the equivalent circuit. (C) Equivalent electrical circuit used to fit the impedance data obtained for the Ni/Al-Cl films. R is the ohmic resistance, Rct the charge transfer resistance, R_p the resistive component of the mass transport impedance and Q_1 and Q_2 are constant phase

elements used to model the double layer capacitance and the capacitive component of the mass transport impedance, respectively.[137]

As a matter of fact, EIS data of partially oxidized Ni/Al-Cl films show a small depressed semicircle at high frequency corresponding to the charge transfer (Fig. 1.2B), followed by a second larger capacitive loop at lower frequency (Fig. 1.2A). The equivalent Randles type circuit is schemed in Figure 1.2C. At the rising portion of the second loop, the line makes an angle of nearly 45° with the real axis, as expected for a Warburg impedance.[138] The second loop corresponds to the mass transport of the charge balancing ions. Its radius decreases with the increase in the oxidation state of Ni. As a comparison, for unoxidized films, the Nyquist plot is a straight line characteristic of a passive layer with a high charge transfer resistance.[139]

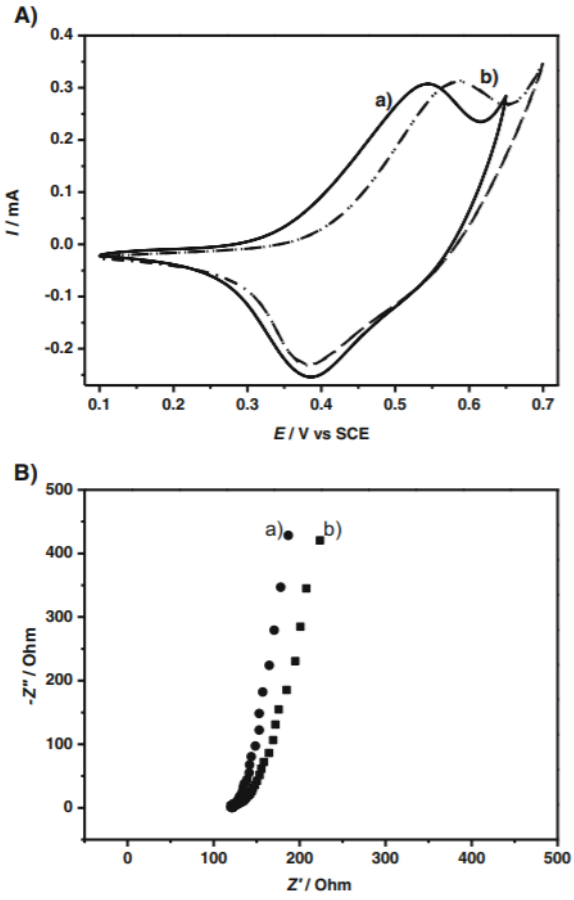

Figure 1.3 : (A) Cyclic voltammogramms ($v = 5$ mV s^{-1}) and (B) **Nyquist representation of electrochemical impedance spectroscopy data at open circuit potential after ten CV cycles (25 mHz–100 kHz, 10 mV) of Co_2Al-NO_3 (*a*) and Co_2Al-CO_3 (*b*). (Adapted from[135], copyright 2013, with permission from Elsevier Ltd.)** [131]

For partially oxidized films, the curving of the plots back toward the real axis at very low frequency indicates that the impedance is limited by convective steady state diffusion.[140] The diffusional regime of anions is related to a faster kinetics of the electron compared to the diffusion of anions. According to diffusion models proposed by Scholz *et al*. for redox reaction through microcrystals,[36,118,119] there is an accumulation of ions at the solid/electrolyte interface. Thus the faradic process is defined more like a pseudo-capacitive behavior. In the Randles type circuit, Warburg element is a subcircuit of a resistance (R_p) in parallel with a constant phase element (Q_2). The first constant phase element Q_1 models the double layer capacitance. From impedance analyses for Ni oxidation to 2.5+, the diffusion coefficient of ions, $D = 2\pi f_c l^{2}/[2\cos(n\pi/4)]^{2/n}$ where l is the thickness of the film and f_c is the characteristic frequency of the low frequency capacitive loops,[141] varies between 1 and 5.10^{-9} cm^2s^{-1}. The authors find similarities to values reported for proton diffusion in nickel hydroxide films.[139,141,142] The same diffusional regime is observed for Co/Al-LDH 2/1[131] with an apparent diffusion coefficient of $2.10^{-8}cm^2.s^{-1}$. EIS data (Fig. 1.3B) show a quasi-straight line at each potential. Consequently, only two constant phase components (CPE) are used in the equivalent circuit, suggesting that the two resistant components (R_{et} and R_d) vanished within the investigated frequency range.

The structural difference between Co/Al-LDH and Ni/Al-LDH explains the variation in the capacitive properties. From XRD, the a parameter (proportional to the interatomic distance between two metals) of the two materials[131] reveals a smaller interatomic distance for Co/Al-LDH than for Ni/Al-LDH. Consequently, the electronic transfer should be facilitated in cobalt-based LDH. This is confirmed with the charge transfer resistance (determined by EIS) that is lower for Co/Al-LDH 4/1 than for Ni/Al-LDH 4/1 with 0.4 $Ohm.cm^2$ and 14.1$Ohm.cm^2$ respectively.[143] Consequently, Co/Al-LDH is more capacitive than Ni/Al-LDH.[135] The oxidation of Ni/Al-LDH is governed by a faradaic process with low redox current density while the oxidation of Co/Al-LDH is governed by a multi-site pseudo-capacitive behavior. Thus, cobalt containing LDH have been investigated as electrode materials for supercapacitors,[7,8] and Ni containing LDH for batteries.[6]

Mixed LDH $Ni^{II}/Co^{II}/Al^{III}$-LDH composed of both Ni^{II} and Co^{II} as divalent cations with different ratios as well as Al^{III} were co-precipitated in the chemical route to mix the properties of both Ni-based LDH and Co-based LDH. Two different routes were used: the two mixed phases synthesized separately with $(Co/Al–NO_3\text{-LDH } 2/1)_{1-r}$ and $(Ni/Al–NO_3\text{-LDH } 2/1)_r$ with $r \leq 1$, and a single phase synthesized with Ni^{2+}, Co^{2+} and Al^{3+} altogether by coprecipitation method as $(Co_xNi_{1-x})/Al–NO_3$-LDH 2/1 phase with $x \leq 1$ where divalent metals are substituted at a local intralayer scale. For $x \geq 0.4$, the peak potential (E_{pa}) decreases and the a parameter decreases with a quasi-linear behavior versus x. For $x > 0.5$, R_{et} progressively decreases reaching a minimum value. Q_{tot} as function of the sample composition (x) evidences a cooperative effect of cobalt with a rapid increase of Q_{tot} when $x > 0.4$. The presence of amorphous phases in the samples ($x \leq 0.4$) has no effect on Q_{tot} of the coprecipitated phases. For the physical mixtures $(Co/Al–NO_3\text{-LDH } 2/1)_{1-r}$ and $(Ni/Al–NO_3\text{-LDH } 2/1)_r$, the potential is very close to that corresponding to the pure cobalt phase for $r > 0.2$ (most of the shift occurred for the first mixture $r = 0.1$).

Physical mixture presents more a percolation threshold behavior due to microscopic interface between both phases. This is even more pronounced when the charge variations are examined. Q_{tot} as function of r evidences a cooperative effect of cobalt only for r > 0.8. EIS spectra are very similar to that obtained for pure Co/Al-LDH with R_e close to 0 for all values of r.

For practical reasons and because we want to essentially study the Faradaic process, we focused on the preparation and study of the Ni-based LDH during the PhD work.

1.4.2.3 Tuning the electric charge transfer resistance

The electric charge transfer resistance can vary according to the cation element, M^{II}/M^{III} ratio, electrolyte, the synthesis route and electric percolants.

- **The electric charge transfer resistance depends on the M^{II}/N^{III} ratio**

The conductivity of the material varies with the stoichiometric composition in divalent and trivalent cations. For example, the increase in Ni/Al ratio from 1/1 to 2.4/1 provokes the increase in the peak currents and a shift of the peak potentials towards more cathodic values with the cyclic voltammetry technique (Figure 1.3a).[35] From EIS data, R_{et} decreases as the Ni/Al ratio increases (Figure 1.3b). It is probable that more Ni centers get closer to each other, which induces an easier electron hopping. For Ni/Al ratios comprised from 2.4/1 to 3.5/1, this effect is constant, perhaps because the electron-hopping rate cannot further increase.

- **The transfer resistance depends on the electrolyte**

The transfer resistance depends on the nature of the electrolyte as attested in the EIS spectrum. For Ni/Al-NO_3-LDH 2/1 after many cycles in KOH, LiOH and NaOH,[135] the EIS spectra simulations reveal a charge transfer resistance (R_{et}) that decreases from 7000 to 2600 and 32 Ohm in KOH, LiOH and NaOH, respectively. The electrolytic cation may have an effect on the electrochemical process and the electric charge transfer resistance. Upon cycling, the current signal increases in NaOH and LiOH solution until a maximum during the 10^{th} cycle. In KOH, the current remains constant. The reversibility is better for NaOH (peak separation 160 mV), followed by LiOH (180 mV) and KOH (230 mV). The electrochemical efficiency is higher in LiOH or NaOH than in KOH. In Ni/Al-NO_3, the electron transfer is governed by a diffusional process. It is confirmed by a peak current depending on the square root of the scan rate, and depends on the nature of the electrolyte cation. The slope is higher for Na^+ > Li^+ >K^+. This electrochemical behavior is still under investigation. A priori, these results tend to demonstrate that the cation coming from the supporting electrolyte should be responsible for this electrochemical behavior.

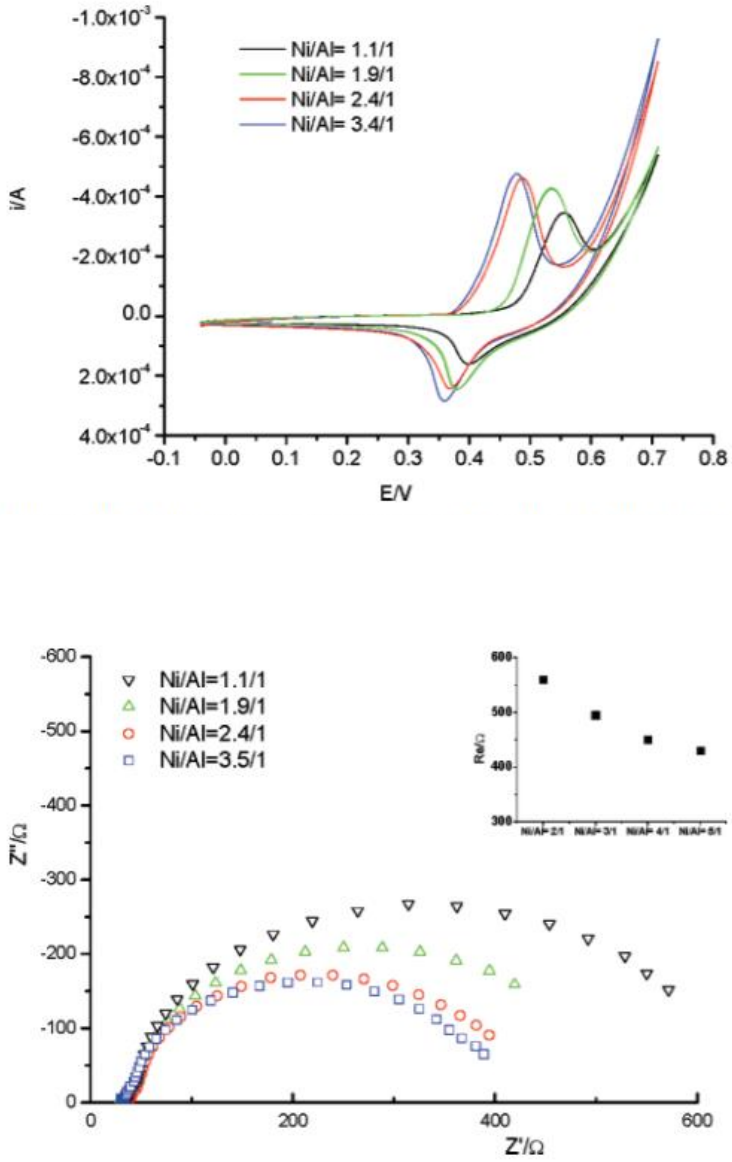

Figure 1.4: (a) Cyclic voltammogramms recorded in 0.1M NaOH at a Pt electrode modified with the films containing different Ni/Al ratios (b) Nyquist plots obtained for Pt electrodes modified with the films containing different Ni/Al ratios.[35]

From bibliography, the order of magnitude of the diffusion coefficients are established such as $Li^+ < Na^+ << K^+$ ($D_{bulk}Li^+$ $10 \pm 1 \times 10^{-10}$ m^2/s < $D_{bulk}Na^+$ $14 \pm 2 \times 10^{-10}$ m^2/s << $D_{bulk}K^+$ $22 \pm 1 \times 10^{-10}$ m^2/s)[144,145]. From the literature related to cationic clay minerals, it is known that cations such as K^+ preferably form internal sphere complexes[146,147] they are themselves directly retained in the adsorption sites on the surface. On the contrary, cations such as Li^+ generally form outer sphere complexes whose water molecules in the coordination sphere attach to the surface of the clay. But those behaviors are in agreement with cationic exchange properties according to the permanent negative basal surfaces of cationic clay minerals arising from isomorphic anionic

substitutions. In that case, absorption phenomena should be related to the variable proton surface charge of the LDH, arising from hydroxyl functional groups coming from the external layers.

Let us have in mind that for each investigated electrolyte, the activity coefficient is related to the electrolytic cation.[148] The pH value differs slightly from one electrolyte to another following $pH_{(KOH\ 1M)} > pH_{(LiOH\ 1M)}$ (calculated by the pHreeqC software using Thermoddem® database). Moreover, thin films of Ni/Fe-LDH probably underwent dozen of cycles of polarization in the aqueous electrolytes such as to enhance conductivity[149, 150,151,152] before current reached steady. Concomitantly, the increase in conductivity was assumably responsible for the increase in OER, and pH is not easily recorded at the LDH interface. This electrochemical behavior could be explained by the available OH^- concentration at the interface under the investigated experimental conditions (interfacial $[OH^-]_{NaOH}$ under the investigated conditions < interfacial $[OH^-]_{LiOH}$ under the investigated conditions < interfacial $[OH^-]_{KOH}$ under the investigated conditions).

This postulate is in agreement with the fact that the electric charge transfer resistance also depends on the concentration of ions in electrolyte. For Ni/Al–$NO_{3,}$[135] as previously reported by different authors[143,153,154] the increase in OH^- concentration induces a peak potential decrease and a current peak increase, which shows that OH^- anions are directly involved in the electro-oxidation process, and that their presence favors the oxidation. This electrochemical behavior was deeply investigated in this PhD work and reported in chapter 5.

- **Charge transfer improvement with Fe-based LDH**
  - **Mg/Fe-CO_3-LDH**

Until recently, Mg/Fe-CO_3 2/1 in KOH 0.1M was considered as a non-electroactive material.[99] The CV of Mg/Fe-LDH modified Pt electrode in 0.1M NaOH overlaps that recorded at the bare Pt. It does not display a Fe electrochemical signal in aqueous media, however the material catalyzes the oxygen evolution reaction (OER), actually iron oxyhydroxide is known to be an efficient electrocatalyst for OER in alkaline medium.[155] By enhancing the surface of the Mg/Fe-LDH with 3D hierarchical microspheres and a suitable mesopore distribution (−0.1 to 0.5 V vs. SCE) in 1M NaOH, Shao *et al.* have improved the mass transport of the electrolyte as well as the faradic redox global reaction, and could observe a reversible Fe redox current[97] (Fig. 1.5).

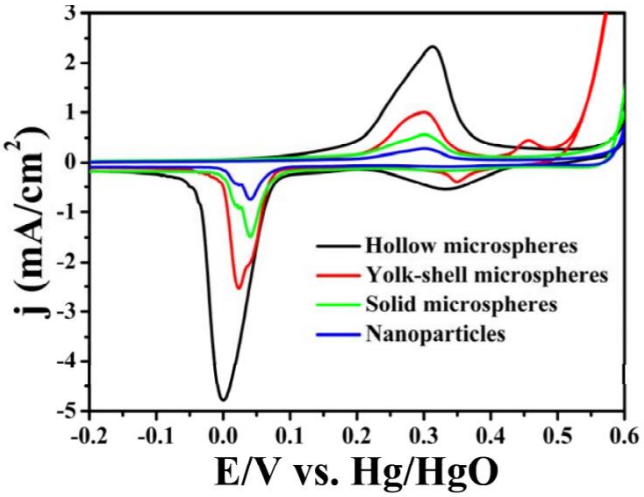

Figure 1.5: CV of the Mg/Fe-LDH microspheres (solid, yolk-shell and hollow) and LDH nanoparticles modified electrodes in 1 M NaOH solution at 50mV/s[97]

This result suggests interesting perspectives for the development of green electrolysis processes for the capture and release of ions (energy storage, water treatment, industrial effluent treatment…). The electrogravimetric behavior of nano-Mg/Fe layered double hydroxide particles were investigated using an Electrochemical Quartz Crystal Microbalance. Preliminary results are presented in Annex A.

- **Ni/Fe-CO_3 2/1, compared with $Ni(OH)_2$ and Ni/Al-LDH**

Iron is a candidate to improve electrochemical properties of LDH. From EIS data,[99] Ni/Fe-LDH 2/1possesses a smaller charge-transfer resistance than beta-$Ni(OH)_2$, *i.e.* a faster electron transfer process indicating that the transfer is easier between Fe and Ni. Ni/Fe-LDH is highly active for OER in alkaline medium (KOH 1M). From Raman spectroscopy, Ni/Fe-LDH is known to possess a more disordered structure and more structural defects than beta-$Ni(OH)_2$, suggesting that this could be the reason for its better performance in the OER reaction than in beta-$Ni(OH)_2$. Qui and Villemure have shown that the position of the peak potential depends on the upper limit in potential used to record the voltammograms in phosphate buffer solution (pH 7.9).[149] Nevertheless, in agreement with the OER, an increase in the upper limit of the potential should be responsible for the pH decrease at the interface which could be responsible for the shift of the potential to more positive values. For Ni/Fe-LDH, an increase in the Ni oxidation current is observed while the Ni reduction current remains similar to that observed with the Ni/Al-LDH 2/1.[99] Oliver-Tolentino et al. compared the performances of Ni/Fe-LDHs and Ni/Al-LDH with different ratios.[156] The material with the highest percentage of Fe is the best OER catalyzer. Trotochaud *et al.*[157] explain this phenomenon as a partial-charge-transfer mechanism that activates Ni centers is induced by the presence of iron. This could be explained by the electron delocalization on the layer surface, due to the arrangement of Fe atoms in the lattice, which spins from a specific magnetic structure that favors the super-exchange interaction. This permits the improvement of electron hopping through the layers.

- **Co_2/Fe-CO_3-LDH, compared with Co/Al-CO_3-LDH**

For Co/Fe-LDH, the substitution of Al^{III} by Fe^{III} causes a negative shift of both anodic and cathodic peak potentials ($E_{1/2}$ = 0.145 V/SCE) but the current peak remains similar and from EIS, the resistance is less important for Co/Fe (than that of Co/Al-LDH). It confirms that Fe is responsible for the increase in the LDH apparent electronic conductivity even if it does not participate directly to the redox process. This is consistent with the values of the percentages of the electroactive Ni sites as the material is more conductive when more Ni centers are involved in the electron hopping process. The data confirm that Fe does not undergo a redox reaction in the range of applied potential, as proven by Friebel *et al.*,[5] but leads to a decrease of the resistance to the electronic transport, as hypothesized by Trotochaud *et al.*[157] Moreover, the results obtained in the latter work demonstrate also that the order degree of the LDH structure affects the conductivity of the material significantly, with the R_e values of the electrochemically synthesized LDHs being much lower than those displayed by the chemically prepared LDHs, especially when Fe is present as the trivalent metal in the brucite-like layers.

By EIS, the electrochemical behavior of iron-containing LDH is compared for Mg/Fe-LDH 2/1, Ni/Fe-LDH 2/1, and Co/Fe-LDH 2/1. The electron transfer resistance is the highest for Mg/Fe, followed by Ni/Fe-LDH and finally Co/Fe-LDH, underlining a better electron transfer between cobalt and iron (Fig. 1.6).

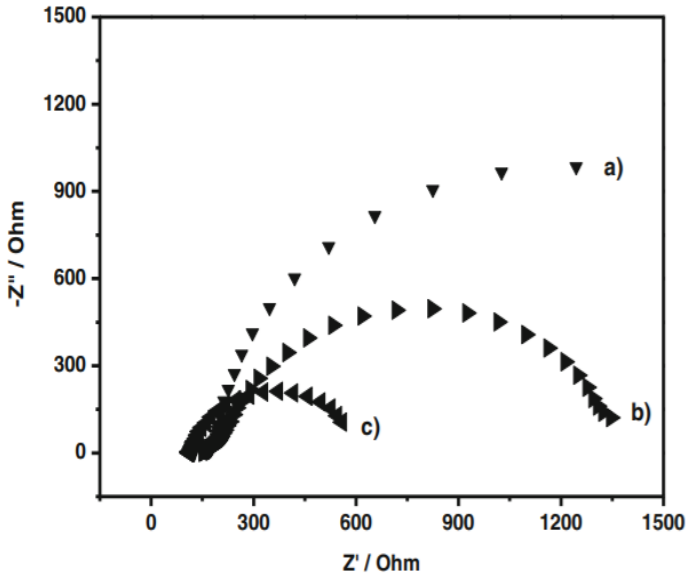

Figure 1.6: Nyquist representation of EIS data of (a) Mg/Fe-CO_3-LDH 2/1, (b) Ni/Fe-CO_3–LDH 2/1, and (c) Co/Fe-CO_3-LDH 2/1 at OCP after ten CV cycles in 0.1M KOH, 25 mHz-100kHZ, 10mV/s [131]

- **Future interests of manganese containing LDH**

Manganese is another interesting element as it has a large number of oxidation states ranging from -3 to +7. However the control of its oxidation state during the synthesis is the main problem and can cause the formation of impurity. Qiu and Villemure found an average oxidation state of +3.52 in Mg/Mn-CO_3-LDH sample, suggesting the presence $\mathbf{Mn^{IV}}$ in the LDH structure.[150] The voltammetric peaks observed between 0 and 0.4 V/SCE in 0.1KCl were attributed to $\mathbf{Mn^{III}/Mn^{IV}}$ redox couples. Reduction below 3+ did not occur even after several hours of electrolysis at negative potentials.

- **Monometallic LDHs**

Different monometallic LDHs are investigated in literature, mainly green rusts (Fe^{II}/Fe^{III}-LDH) and Co^{II}/Co^{III}-LDH. They present a higher redox flexibility compared to the LDH composed of different metal cations.

- **Redox properties of monometallic LDHs green rust (GR)**

$Fe^{II}/^{III}$ oxyhydroxycarbonate ($Fe^{II}_{6(1-x)}Fe^{III}_{6x}O_{12}H_{2(7-3x)}CO_3$) or GR-$CO_3$ with *in situ* redox flexibility ($1/3 \leq \times \leq 2/3$)[158] and GR-SO_4[159] have also been studied. Fe acts as both electron donor and acceptor with the possibility for a global one electron per Fe atom exchange.

Two redox transformations routes are determined. The first route is a dissolution/precipitation that may occur in three steps, during the oxidation. GR is (a) dissoluted to $Fe^{II}_2Fe^{III}_1$ complex, (b) followed by the oxidation of $Fe^{II}_2Fe^{III}_1$ complex to Fe^{III} and (c) the –FeO(OH) precipitation. The reduction is done via the release of Fe^{II} ions into solution by soluble Fe^{II}–Fe^{III} complexes acting as intermediate species. The second route is a solid-state reaction: the oxidation involves conversion of $Fe^{(II)}$ lattice into $Fe^{(III)}$ and deprotonation of OH groups in octahedra sheets. The reduction provokes the conversion of lattice into $Fe^{(II)}$ and protonation of OH groups. It implies the complete transformation of GR(CO_3) or GR(SO_4) to ferric exGRc-Fe(III) or exGRs-Fe(III), with the following formulas $Fe^{III}_6(OH)_{12-2y}(O)_{2+y}(H_2O)_yCO_3$ or $Fe^{III}_6(OH)_{12-2z}(O)_{2+z}(H_2O)_{6+z}SO_4$ with $0 \leq y$ or $z \leq 2$. The solid-state reduction gives ferrous exGRc-Fe(II) or exGRs-Fe(II), with chemical formulas $[Fe^{II}_6(OH)_{10}(H_2O)_2]\cdot[CO_3, 2H_2O]$ or $[Fe^{II}_6(OH)_{10}(H_2O)_2]\cdot[SO_4, 8H_2O]$. Lattice $Fe^{(III)}$ are completely conversed into lattice $Fe^{(II)}$. Simultaneously, maintaining electrical neutrality implies the protonation of a part of OH ions in the octahedra layers in agreement with LDH dihydroxylation and the resulting transformation to water molecules. The corresponding global solid-state reduction reaction should be written as $GR + 2H^+ + 2e^- = ExGR\text{-}Fe^{(II)}$. The solid-state route is favoured for (i) pH is quite alkaline (the pH must not be too high in order to avoid the formation of magnetite) and (ii) intercalated anion concentration increases.

The authors highlight the electrochemical restoration of green rust as the anodic charge of $Fe^{(II)}$ oxidation is equal to the cathodic charge of reduction. For GR(CO_3), decreasing the scan rate or increasing the temperature leads to

the appearance of two cathodic peaks because of the occurrence of an intermediate oxidized product, exGRc-Fe(III)* (Fig. 1.7).

The intermediate product undergoes a structural conversion into the more stable ferric compound, exGRc-Fe(III). For GR(SO_4), the voltammetric curve exhibits only one anodic peak and one cathodic peak, whatever the temperature or potential scan rate. However, the broadness of the cathodic peak may indicate a sum of several reduction processes. The initial mass is quasi-restored after the cathodic peak indicating the recovery of the green rust film at the end of the cyclic voltammogram and validates the oxidation of green rusts at pH 9.5 via a solid-state transformation (and not dissolution). The mass loss is related to the beginning of GR(CO_3) reduction (less than 1% of the initial mass of film).

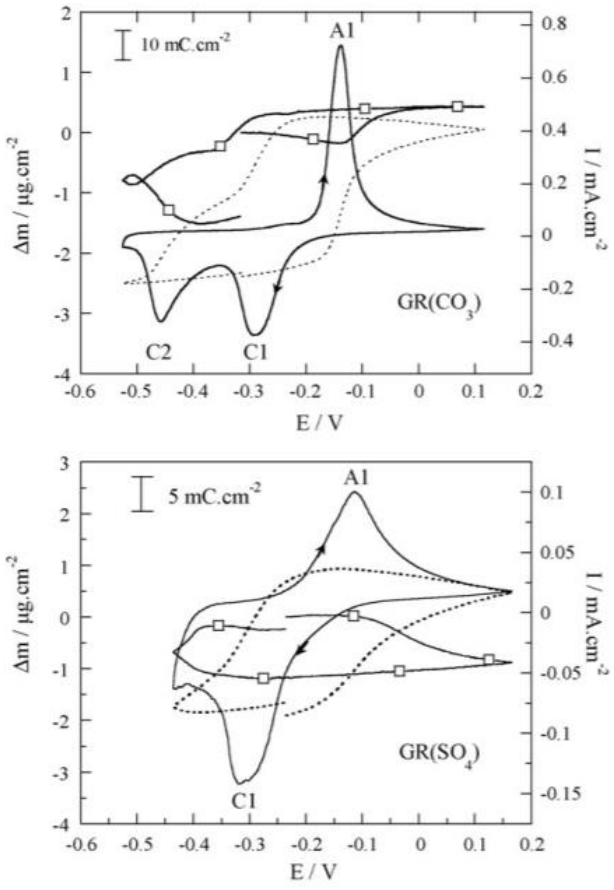

Figure 1.7: Cyclic voltammogramm (-), mass variation Δm (□) and coulombic charge Q (- - -) recorded with GR(CO_3) and GR(SO_4) [129]

- **<u>Co^{II}/Co^{III}-CO_3-LDH</u>**

These LDH have been studied by CV in 0.1M KOH.[160] The current peak at $E_{1/2}$=0.160 V vs. SCE is reversible with higher current than those observed for Co/Al-LDH 2/1 or Co/Fe-LDH 2/1. Before electrochemical oxidation,

the percentage of electroactive Co^{II} is estimated at 28 % mole for Co^{II}/Co^{III}-CO_3 and only 10 % mole for Co/Al-CO_3-LDH 2/1 or Co/Fe-CO_3-LDH 2/1. After the electrochemical oxidation, the mean amount of Co^{III} present in the LDH layer increased from 13 to 60 %. The net balance between half cycles, characteristic of the electrochemical efficiency results in an average value stabilized at 30 % of Co^{III} after reduction. This results in the usual ratio of 2 to 1 between divalent and trivalent cations in the LDH composition. The existence of a mixed oxidation state of Co^{II}/ Co^{III} is also found in these compounds with a ratio Co^{II}/Co^{III} close to 1.

1.4.2.4 Increased charge transfer in electrochemically synthesized LDH compared to chemically synthesized Ni-based LDH

For Ni-based LDH, the CV of electrochemically synthesized LDHs in 0.1M NaOH has more cathodic Ni peaks than for chemically synthesized LDH, since the shift of the peak potentials is enhanced in presence of Fe^{III}.[99] Impedance spectroscopy confirmed that the chemically synthesized LDHs possess a higher electronic transfer resistance than the analogous electrosynthesized materials. The electrochemical efficiency is higher for the electrosynthesized material and even more when Fe is present (increase of the peak current).

1.4.3 Conclusion

In section 1.4, the importance of electroactive metal cations in aqueous solution is explained for an active material. Co based LDH and Ni based LDH are of interest for a better conductivity. First approximations in terms of mass transfers by electrochemical analysis (EIS and CV) enable to estimate the contribution of the fastest process (*i.e.* transfer of electrons) and the lowest process(es) (one or several ion transfers). The interatomic distance in Co/Al-LDH is lower than in Ni/Al-LDH. Consequently, the electronic transfer via hopping mechanism is facilitated in cobalt based LDH. Co/Al-LDH is more capacitive than Ni/Al-LDH.[135] The oxidation of Ni/Al-LDH is governed by a faradic process with low redox current density while the oxidation of Co/Al-LDH is governed by a multi-site pseudo-capacitive behavior. Thus, cobalt containing LDH have been investigated as electrode materials for supercapacitors and Ni containing LDH for batteries. For a better understanding of the transfer of species during the redox reaction of the LDH, Ni-containing LDH is developed in this thesis as it is governed by one faradaic process with low redox current density, contrary to Co-containing LDH. Especially Ni/Fe-LDH is retained as the presence of Fe improves the charge transfer within the layer. The redox reaction was studied on Ni/Fe-LDH synthesized by the chemical route and by the electrochemically synthesized route. The former route has the particularity to be highly crystallized, while, for the latter route, the electronic transfer is enhanced between the LDH and the electrode. Also, the Mg/Fe-LDH was studied in this thesis as it is considered as an inactive film, although Fe should be oxidized and reduced. In the next section 1.5, the literature on the assumption about the transfer of ions, its nature and kinetics are reported during the electrochemical process.

1.5 Ionic transfers related to electrochemistry with electrogravimetric measurements

Section 1.4 shows that the understanding of the involved charge transfer mechanism and the corresponding mass transfer between the LDH and the electrolyte is not well understood. The conventional electrochemical methods, *i.e*. CV and EIS, provided information on the oxidation/reduction state of the active site and on the kinetics of electrons and ions. The electron transfer is more rapid than the ion transfer. However, CV and EIS alone do not provide information on the nature and kinetics of each involved species accompanying the electron transfer. In addition, no information is provided on the localization of the insertion in the material. It is therefore challenging to find eligible techniques for the *in situ* study of the mechanisms of transfer of the species and the specific sites of transfer. EQCM is a technique that monitors simultaneously changes in the current and in the mass of the deposited thin film while the latter is polarized, giving new information on the transferred species. With EQCM analysis, the calculus of the molar mass of the exchanged species versus potential may give information on the nature of a part or all of the transferred species. The state of the art of former studies of LDH with EQCM measurements is described in this section.

In the literature, a few articles reported the mass variation of LDH under a cyclic polarization with EQCM technique for LDH material. The reported literature in this section intends to detail the present knowledge on this phenomenon. Until now, for a better understanding on the ionic transfer mechanisms, only a few LDH were investigated with EQCM. In particular, green rusts and Co/Al-LDH.

The calculus of the mass per electron (MPE) is possible via $\frac{M(g.mol^{-1})}{e} = F.\frac{dm}{dq}$ with F is the Faraday constant. It gives the molar mass of transferred ion per transferred electron.

1.5.1 Cations play a role in the transfer

Two categories of ionic transfer between the electrolyte and the LDH are reported: ionic transfer in the case of anion electroactivity in the interlayer space of an inactive LDH when tuning the oxidation state, and the case of cationic electroactivity into the layers of the LDH and the related ion transfer. A study of interlayered electroactive anions in an inactive LDH revealed that different species play a role in the charge transfer depending on the film history. From QCM and electronic absorption spectroscopy measurements in hydrotalcite Mg/Al-X-LDH 3/1,[126] $[Fe(CN)_6]^{3-}$ in solution was incorporated as an ion-paired species as $Na[Fe(CN)_6]^{2-}$ for $X=Cl^-$ and $Na_2[Fe(CN)_6]^-$ for $X=SO_4^{2-}$ and CO_3^{2-}, respectively. During the film polarization, the $[Fe(CN)_6]^{3-}/[Fe(CN)_6]^{4-}$ couple underwent a reversible electron transfer in the interlayer space. EQCM measurements revealed a charge variation generated in a film and compensated by the leaching or incorporation of an ion-paired species. However, after ageing for 2 weeks in a 0.1 M Na_2SO_4 suspension, some fraction of

$[Fe(CN)_6]^{3-}$ interacted more strongly with the hydrotalcite surface. $[Fe(CN)_6]^{3-}$ ions did not leach during electrochemical reduction. Instead Na^+ ions were transferred for charge compensation.

In the case of tuning the oxidation state of electroactive cations within the layers by polarization, several models of ionic transfers are presented in the litterature. Reference [161] reports EQCM results of Ni/Al-NO_3-LDH in different electrolytes (KOH, LiOH and NaOH) at scan rates 5 and 50 mV/s (Fig. 1.8 and 1.9 respectively). The electrochemical efficiency depends on the electrolyte. It is low in KOH and NaOH (3 or 19%) and higher in LiOH (≈ 30%), suggesting again a strong dependence on the nature of the electrolytic cations of the redox reactions**.** The respective mass variations of each electrolyte (KOH, LiOH and NaOH) present different complex shapes during polarization, which highlights the transfer of more than one species. The mass variation also depends on the composition of the layers as the shape is different in Ni/Al-NO_3-LDH 2/1 and in Co/Al-NO_3-LDH 2/1 in the same electrolyte. For example, the current response of Co/Al−NO_3-LDH in KOH at 5 mV/s is similar in terms of shape while the mass response is magnified 20 times compared to Ni/Al−NO_3-LDH films. For each cycle, the Ni/Al−NO_3-LDH undergoes a mass depletion during anodic sweep (Ni oxidation) and a mass gain during cathodic sweep (Ni reduction). The assumption is that hydrated cations are expelled with a negligible counter flux of anions during Ni oxidation. The opposite is expected during the Ni reduction. The mass variation is the most important in KOH compared to NaOH and LiOH electrolytes. Another study demonstrates the competition between different cations involved in the transfer during polarization.[10] EQCM measurements during oxidation of Ni/Al-Cl-LDH in borate buffer pH 8 (Fig. 1.10) reveal that the presence of both sodium and potassium (0.004 M Na^+ + 0.05 M K^+, MPE = 19g/mol/e) decreases more the mass of the film than in the presence of only one cationic species (0.054 M K^+ MPE = 6 g/mol/e or 0.054 M Na^+, MPE = 11g/mol/e). According to the authors, the positively charged LDH are not expected to adsorb large amounts of cations. However, the incorporation of cation during the negative scan would have to be selective for sodium ions over potassium ions, since expulsion of cation was apparently not observed in buffers containing only potassium. This was confirmed with SEM/EDX analysis of a film immersed in a pH 8 borate buffer containing 4 mM Na^+ and 50 mM K^+ that showed a significant sodium content, over 4% (w/w) compared to less than 1% (w/w) for potassium. The small values of MPE should be explained by the fact that the molar mass of cations is probably balanced with a counterflux of anions or water.

For the tuning of the oxidation state of electroactive cations within the layers by polarization, other models of ionic transfers are presented in the literature. Zhang's group[162] suggests the possible insertion of lithium cations and hydroxyls as ion pairs into the lattice of Co/Al-LDH during electrochemical cycling in alkaline solutions.[153] Su *et al.*[163] suggest that small cations (Li^+ and Na^+) can be intercalated in the remaining interlayer octahedral $(OH)_6$ environments of the Co/Al-LDH structure for charge compensation following the electron transfer, with a probable competition with proton loss. During oxidation of Ni/Al-LDH[164] between 0.2V and 0.5V/AgAgCl NaCl 3M in potassium acetate, sodium acetate, and magnesium acetate, the MPE gives -23g/mol, -41 g/mol and -

14g/mol respectively (Mg^{2+} is doubly charged). The authors propose a model of a loss of cations from the LDH film for charge compensation, following the reaction:

$$[Ni/Al][C^+, Fe^{II}(CN)_6](s) \rightleftarrows [Ni/Al][Fe^{III}(CN)_6](s) + e^- + C^+(aq). \quad (1.16)$$

Results were similar with Ni/Al–Cl LDH films after the exchange with $[Mo(CN)_8]^{4-}$. Yao *et al.*[149] also attributed the decrease in mass during oxidation of the $[Fe(CN)_6]^{4-}$ in Mg/Al LDH films that had been aged for 2 weeks in sodium sulphate and sodium chloride solutions to the expulsion of Na^+ from the films.

1.5.2 Different transfer kinetics

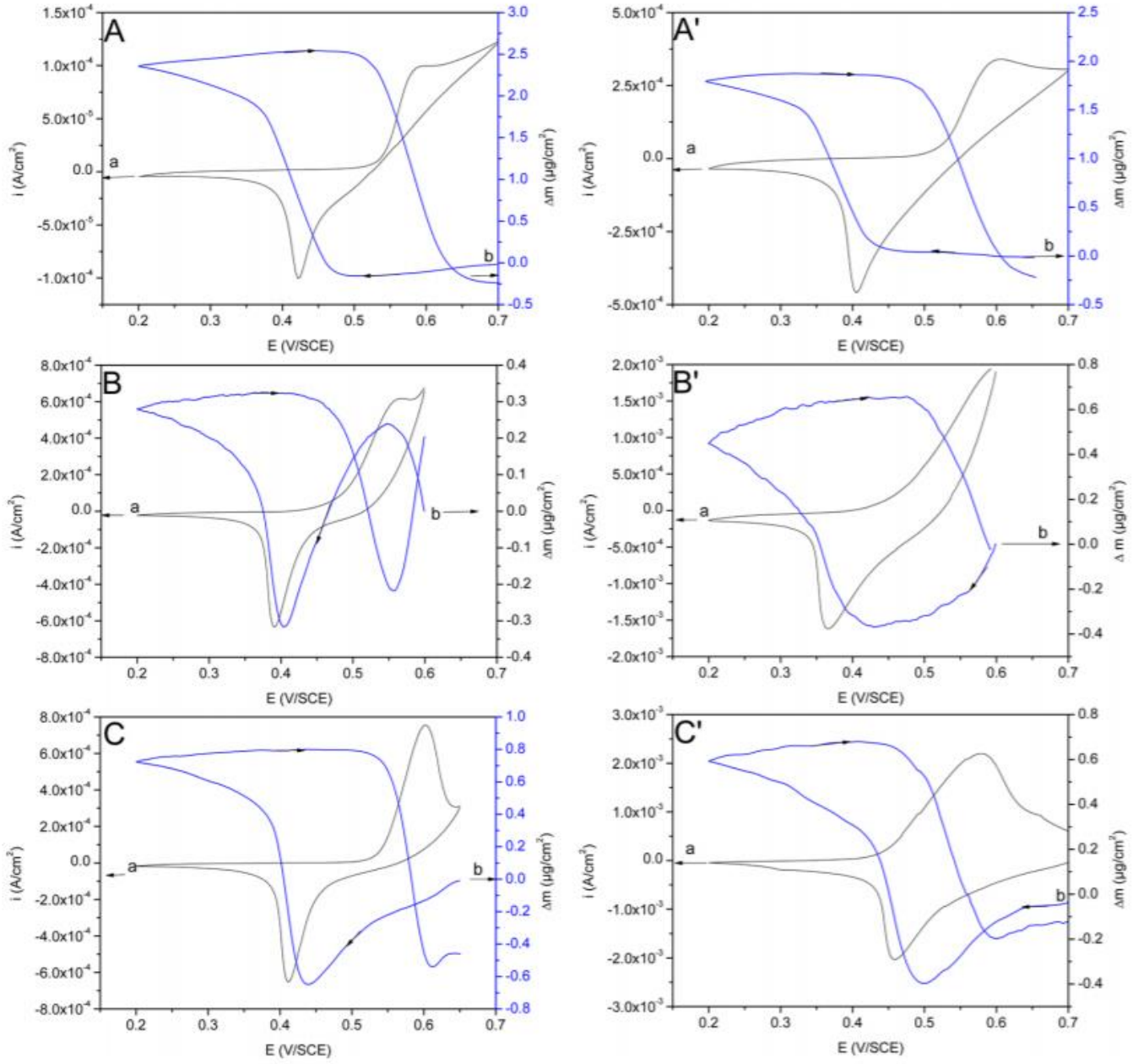

Figure 1.8: CV of Ni/Al-NO_3 films deposited on the gold electrode of the quartz resonator (black curve a) and the simultaneous mass changes (blue curve b) in 0.1M aqueous solution KOH (A, A'), NaOH (B, B') and LiOH (C, C') at v = 5 (A, B, C) and 50mV/s (A', B', C').[161]

With CV, the estimated efficiency of the electroactive metals within LDH shows that electroactive sites are more accessible in Co/Al-LDH (≈ 29% in all electrolytes KOH, LiOH and NaOH) than in Ni/Al-LDH (3% and 19% in

KOH and NaOH, and 30% in LiOH), suggesting a faster kinetics of the transfer (electronic and ionic) in Co/Al-LDH.[161]

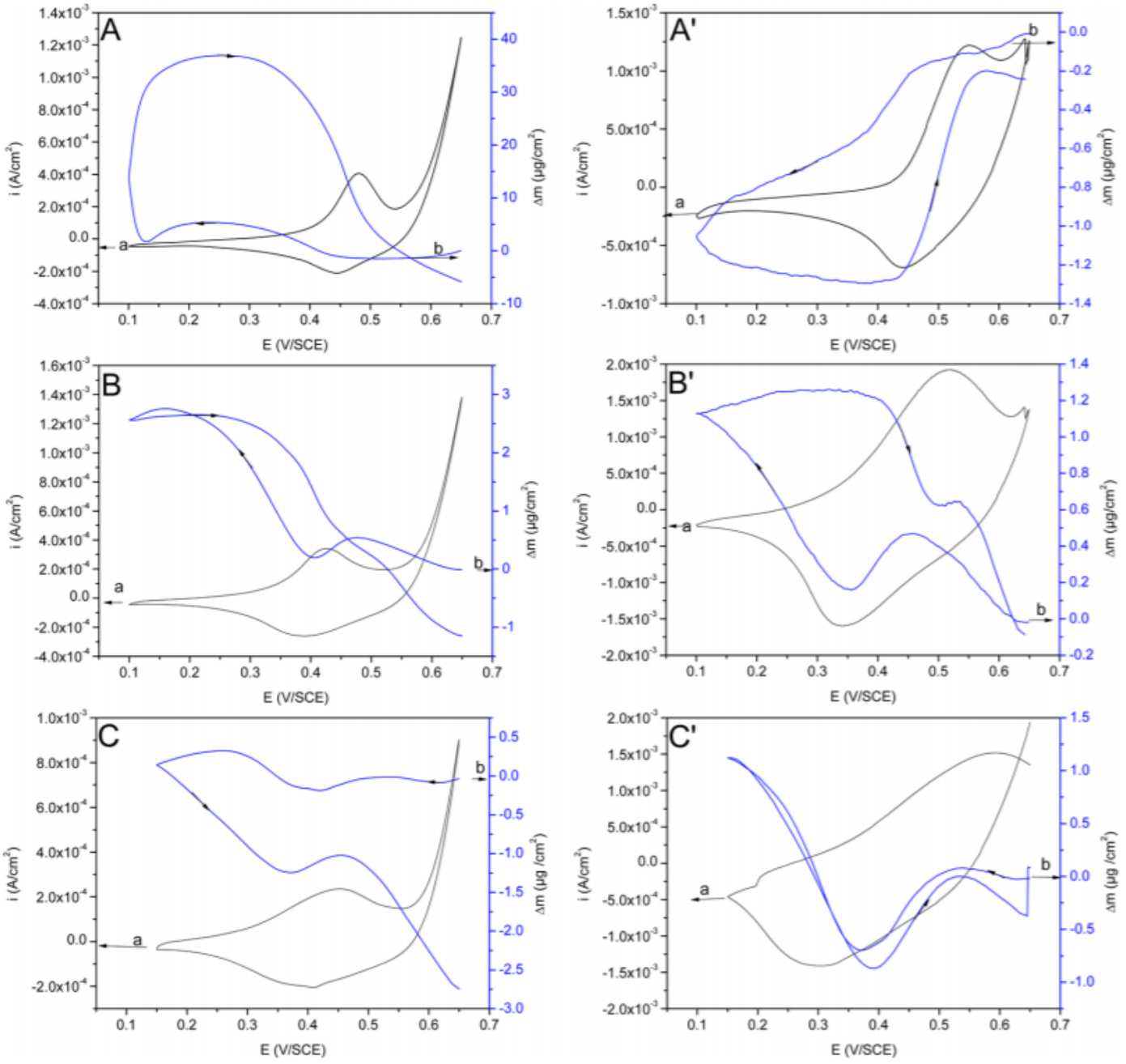

Figure 1.9: Cyclic voltammograms of Co/Al-NO_3 films deposited on the gold electrode of the quartz resonator (black curve a) and the simultaneous mass changes (blue curve b) in 0.1M aqueous solution KOH (A, A'), NaOH (B, B') and LiOH (C, C') at v = 5 (A, B, C) and 50mV/s (A', B', C').[161]

With EQCM, the transfer kinetics of different ions could be evidenced qualitatively when modifying the scan rate. For example, for Co/Al-NO_3-LDH in KOH[161] at low scan rate (5 mV/s), the fastest and lowest species "have time" to be transferred. The calculus of MPE corresponds to a pure potassium (+39 $g \cdot mol^{-1}$) insertion around the Co reduction peak potential. At more anodic potentials, lower and negative MPE values reveal charge compensation due to the association of a flux of potassium and a counterflux of solvent or anions. At higher scan rate (50mV/s), only the fastest species "have time" to be transferred. The MPE indicates an anion contribution associated with a counterflux of free solvent. Thus, it indicates a low kinetic transfer associated with cations and a fast kinetic transfer correlated to anions. Cation transfer is predominant in the three electrolytes except in KOH where, at high scan rate values, anion contribution emerges as the main input. The same trend is evidenced in LiOH and NaOH at low and higher scan rates. Cation transfer is predominant in the three electrolytes. The main major difference concerns the anion contribution that emerges as the main input in KOH at high scan rate values.[161] In NaOH 0.1mol/L, a cation contribution and a counterflux of anions are suspected. For the highest potentials, MPE present positive values indicating a partial contribution of the OH^- anions that decreases when the scan rate decreases. (Fast kinetics for anion)

The same statement was reported by Villemure *et al.* for Ni/Al−Cl-LDH thin films in potassium acetate and sodium acetate solutions.[10] The transfer was attributed to a simultaneous participation of at least two ions in the charge neutralization process, for instance insertion of Na^+ (23 $g \cdot mol^{-1}$) and expulsion of OH^- (17 $g \cdot mol^{-1}$). Finally, for 0.1 M LiOH at almost all scan rates, the MPE is close to Li. For the highest scan rate value (100 $mV \cdot s^{-1}$), MPE decreases but remains positive, showing a small anion contribution.

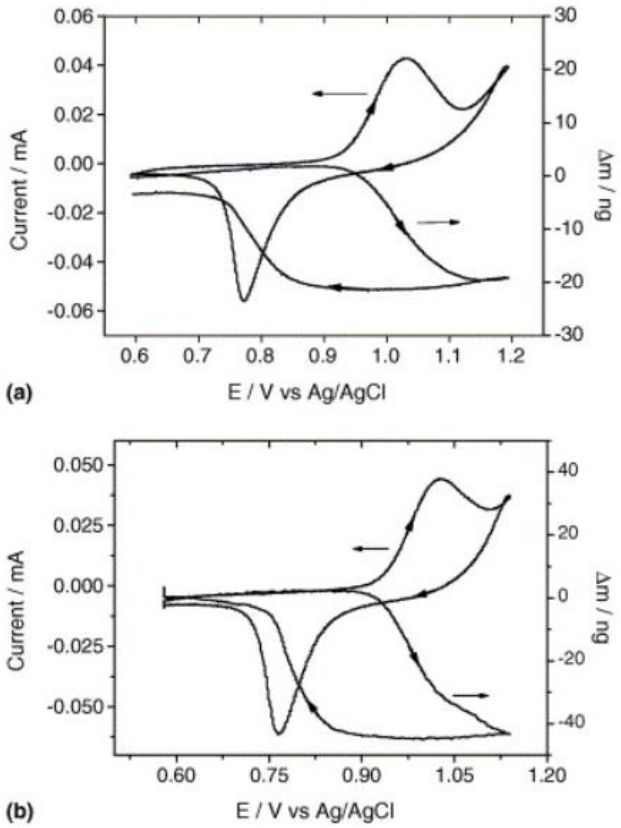

Figure 1.10: Mass change during potential scans for Ni/Al-Cl LDH films deposited on a gold coated quartz crystal in pH 8 borate buffers containing (a) 0.054mol/L potassium and (b) 0.05mol/L potassium and 0.004mol/L sodium (10th scan at 15 mV/s)[10]

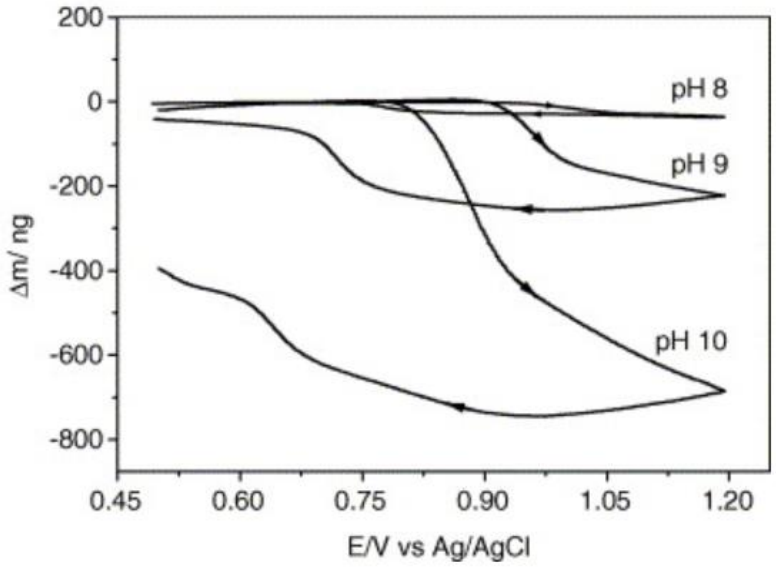

Figure 1.11: Mass versus potential recorded during voltammetric scans for different pH (8, 9 and 10)[10]

The transfer kinetics of ions also depends on pH. For Ni/Al-LDH in phosphate buffer solutions[10], the MPE increases with the increase in pH from 11g/mol in pH 8 to 35g/mol in pH 10 (figure 1.11). During the positive/negative sweep, the mass loss/gain is more cathodic which shows that the pH has an effect on the kinetics of the reaction. In addition, the mass variation decreases/increases in several steps, which also show that different species may play a role. In pH 8 potassium buffers, MPE is only equal to 4 g/mol. According to the authors, the simplest explanation is that charge compensation involves the loss of protons from the LDH lattice accompanied by some water from the LDH interlayer spaces according to:

$$[Ni_6Al_2(OH)_{16}][(Cl^-)_2.nH_2O]_{(s)} + OH^-{}_{(aq)} \rightarrow [Ni_6Al_2O(OH)_{15}][(Cl^-)_2.(n-x)H_2O]_{(s)} + (1+x)H_2O_{(l)} \quad (1.17)$$

At this stage, EQCM only provides an overview of the global transferred mass. It is nevertheless to be highlighted that the investigations were conducted using two different anions (OH^- versus HPO_4^-/PO_4^{2-} which mass molar differs significantly). In agreement with the charge compensation via OH^- and PO_4^{2-} intercalation/deintercalation (according to Miyata affinity scale [44]), the difference in the results can be explained by the low molar mass of OH^- in comparison with PO_4^{2-} balanced by both H_2O deintercalation/intercalation and cation transfer.

The authors make an analogy with the mass behavior of β-$Ni(OH)_2$ and α-$Ni(OH)_2$ in the same experimental conditions (polarization in alkaline solutions). In β-$Ni(OH)_2$, the mass variation follows the same trend and is assumed to result from the expulsion and insertion of protons and water molecules.[165,166] The dependence of the mass loss on the cation species cannot be explained with this equation and should be involved in the charge neutralization process. Intercalation and de-intercalation of cation is proposed to explain the mass changes observed in films of α-$Ni(OH)_2$.[165] Structurally, α-$Ni(OH)_2$ films are closely related to LDHs. Hydrated α-Ni(II) hydroxide films consist of parallel randomly oriented brucite-like $Ni(OH)_2$ layers separated by intercalated water molecules.[149] However, EQCM studies have shown that α-$Ni(OH)_2$ films usually gain mass on oxidation and lose mass on reduction[165,166] the opposite of what was observed here for Ni/Al-Cl-LDH films. According to the authors, the dependence of the MPE on the pH of the electrolyte is attributed to the instability of the Ni/Al-Cl-LDH when subjected to potential scans in basic solutions. However, the oxidation of water starts at the potential of oxidation of Ni and is more cathodic for higher pH. It could increase the expulsion of the produced H^+ and O_2. In the same way, the authors could have claimed the instability of the Ni/Al-LDH when subjected to potential scans in near to neutral solution in agreement with the progressive decrease in pH at the interface due OER even in a buffer solution and even if OERpH 8 < OERpH 10, depending in the cyclic scanning range and the number of investigated cycles.

1.5.3 Limits of the EQCM technique

The main limit of EQCM technique and the calculus of MPE is that the deconvolution between different species cannot be performed if transferred at the same potential. In the case when water contributes to the transfer, no

distinction is possible between the case of a simultaneous ion transfer with a flux of free water in the same direction. It is the same case for hydrated ions.

For example, for Ni/Al−NO_3-LDH 2/1 in KOH 0.1mol/L, the calculus of MPE reveals a hydrated K^+ contribution around the cathodic peak and the contribution of pure K^+ (39 g·mol^{-1}) below and above this potential[161]. The solvation effect increases with the scan rate (increase in MPE). It is nevertheless possible to envisage free water transfer in agreement with owing to conformational movements of electroactive film.[11]

1.5.4 Conclusion

The EQCM technique gives a global response on the transferred mass that is the consequence of a flux of different species and a counter flux of other species. All the previously cited articles on LDH based on EQCM experiments present hypotheses of the identity of the transferred species by means of the calculus of MPE, with some assumptions on their kinetics. Changing the scan potential rates allows to determine the faster species. However, the transfer of water molecules is unclear.

As mentioned, calculating MPE from EQCM data does not enable to separate the contribution of different species that play a role at the same potential range. To solve this problem, *ac*-electrogravimetry technique has been developed at LISE laboratory UMR8235.[11,12, 13,14] It enables to separate the contribution of the different uncharged and charged species by measuring the transfer function $\Delta q/\Delta E$ and $\Delta f/\Delta E$. It may bring new indications on the nature as well as the kinetics of the species transferred between the LDH and the electrolyte during the electrochemical process.

Before this thesis, this technique has not been applied to LDH films, however it has been helpful in polymer studies as an easy and fast identification methodology for cation and anion transfers involved in the charge compensation process as well as a noticeable informative method for kinetic study. In the next section, are presented some literature about *ac*-electrogravimetry.

1.6 *Ac*-electrogravimetry

The dynamic aspects of ions and solvent at the interface between electroactive films and an electrolyte remains a partially unsolved issue. *Ac*-electrogravimetry provides gravimetric and dynamic deconvolution of a global EQCM response by coupling fast quartz crystal microbalance and electrochemical impedance spectroscopy.[12] This technique measures the electrochemical impedance $\Delta E/\Delta I(\omega)$ and the mass variations of the film under a sinusoidal potential perturbation $\Delta m/\Delta E(\omega)$ simultaneously. *Ac*-electrogravimetry was employed for characterizing supercapacitive charge storage mechanisms[13,167] as well as faradaic mechanisms, and detects the contribution of the charged or uncharged species for the separation of anionic, cationic and free solvent contributions during the various electrochemical processes.

Ac-electrogravimetry was recently employed on the lamellar Li-birnessite type MnO_2 thin films in $LiClO_4$ and $NaClO_4$. This solid is known to intercalate ions in a wide range of sites with both faradaic and non-faradaic mechanisms for charge storage applications[14]:

i) Non faradaic reaction can take place with an electrochemical adsorption of cations onto the surface according to:

$$(MnO_2)_{surface} + C^+ + e^- = (MnO_2^-C^+)_{surface} \quad (1.18)$$

ii) Faradaic reaction can take place with the intercalation of cations into the interlayer gap (intercalation pseudocapacitance) or onto the surface (redox pseudocapacitance):

$$(MnO_2)_{bulk} + C^+ + e^- = (MnOOC) \quad (1.19)$$

The faradaic contribution is associated with the reduction of metal atoms located either on the surface or in the interlayer lattice planes.[168]

Intercalation of alkali metals was studies by CV and chemical composition analyses.[169] The conclusion was that protons, but not alkali metal cations, are intercalated. With EQCM experiments and MPE calculations, in different alkali cations electrolytes, no calculation matches the equivalent weight considering either H^+ or alkali ions.[170] The authors suggest that both H^+ and alkali cation intercalations play a role in the charge balance. Although this first attempt is "an evolution", the limitations of the technique appear clearly: the global mass response of EQCM could correspond to many hypotheses like ions, ions with solvation shells, free solvent molecules.

Ac-electrogravimetry is an alternative characterization tool that overcomes the limitations of the classical EQCM, and was studied[171] in the case of Li-birnessite type MnO_2 thin films in $LiClO_4$ and $NaClO_4$ aqueous solutions. Pseudocapacitive behavior was detected as it involves Li^+ and Na^+ ions and their respective hydrated ionic species. Both identifications indicate that a part of the hydrated alkali cations lose their hydration shell before the transfer. The counterflux of water molecules was also evidenced. It was possible to estimate the number of water molecules in the hydration shell of cations, the kinetics, resistance value of charged

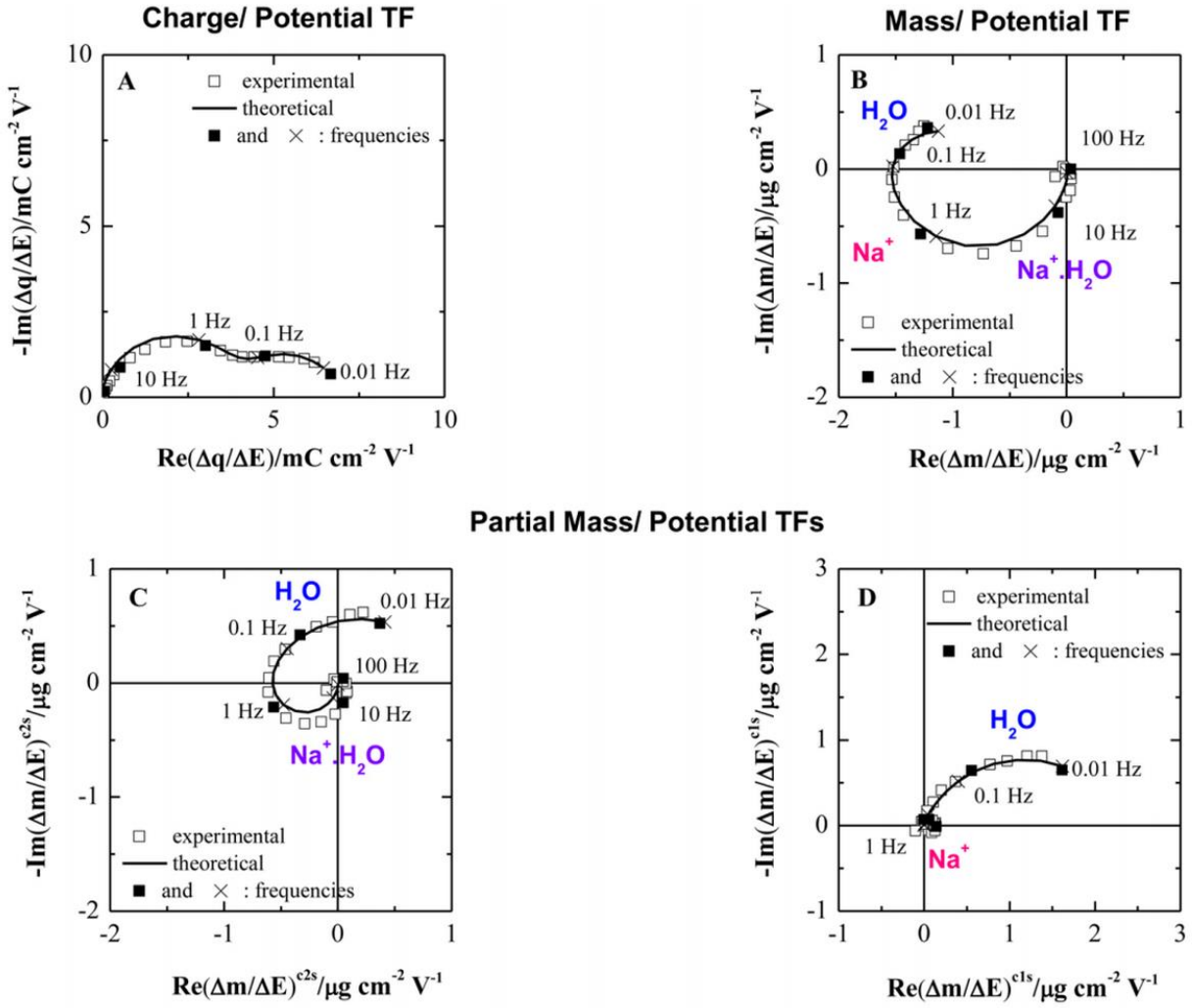

Figure 1.12 : Two main transfer functions (a) $\Delta q/\Delta E(\omega)$ and (b) $\Delta m/\Delta E(\omega)$, and two partial transfer functions (c) $\Delta m/\Delta E^{c1s}(\omega)$ and (d) $\Delta m/\Delta E^{c2s}(\omega)$ involving three species, specifically Na^+, $Na^+.H_2O$ and H_2O (both experimental and theoretical curves are given)[171]

and uncharged species transferred at the electrode/electrolyte interfaces. There are two proposed models: (i) the partial desolvation of hydrated cations are expelled from the film so that partially hydrated cations can access to less attainable sites, (ii) water molecules liberate space for cations.

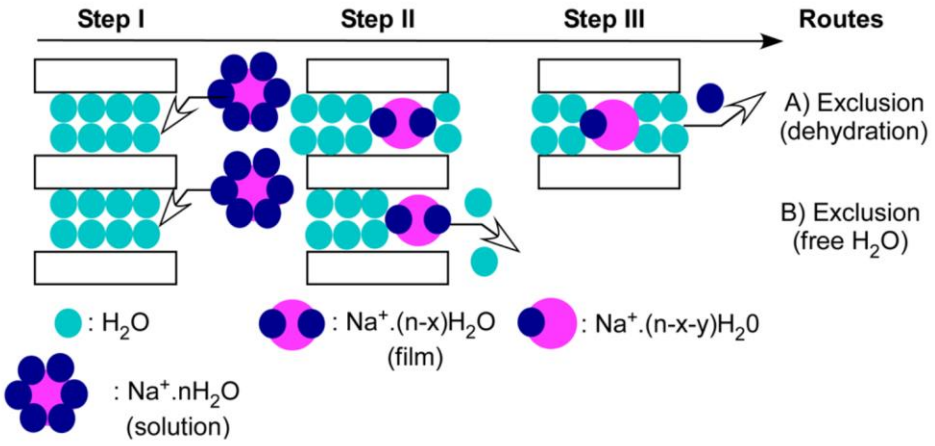

Figure 1.13: Schematic representation of sodium ion species transferred at the electrode/electrolyte interface.[171]

Hydrated Na^+ has faster kinetics than Na^+ probably because it does not completely lose its hydration shell. It is the first study that determines the effect of desolvation in porous and/or layered materials, which is not possible in EQCM measurements.

1.7 XRD coupled to electrochemistry

A few articles evidenced the change in the occupation of the interlayer spacing by combining EQCM and XRD analyses. In addition, the structural modification of LDH was investigated before and after cyclic polarization by EQCM and XRD analyses (*ex situ* characterization with XRD) and during polarization in solution (*in situ or operando* characterization with XRD coupled to EQCM).

1.7.1 *Ex situ* measurements with XRD

XRD enables to follow the interlayer spacing whose distance is a marker of a change in the intercalated species. Coupling EQCM and XRD analyses enables to confirm the nature of the inserted species.

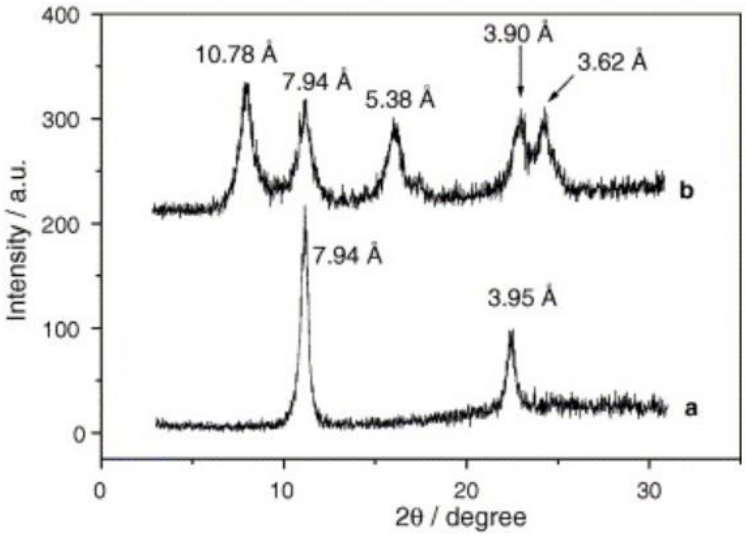

Figure 1.14: XRD pattern of Ni/Al-Cl-LDH film deposited on a glass slide, (a) before and (b) after the film had been soaked overnight in 0.1mM $[Fe(CN)_6]^{4-}$ solution.[164]

For freshly synthesized Ni/Al-Cl-LDH, XRD evidences an interlayer distance of 7.94 Angstöms that is characteristic of Cl^- (Fig. 1.14a). In Ni/Al-Cl-LDH immersed in 0.1 M potassium acetate, the addition of 0.1mM $[Fe(CN)_6]^{4-}$ causes a sharp mass increase attributed to the exchange of Cl^- from the LDH interlayer space by $[Fe(CN)_6]^{4-}$ following the equation:[164]

$$2[Ni_6Al_2(OH)_{16}]Cl_{2(s)} + [Fe(CN)_6]^{4-}_{(aq)} \rightarrow 2[Ni_6Al_2(OH)_{16}]_2[Fe(CN)_6]_{(s)} + 4Cl^-_{(aq).} \quad (1.20)$$

with an ion exchange performance of 85% suggesting that the quadrivalent anion has more affinity than Cl^-. After exchange,[164] XRD confirms this hypothesis with the characteristic two peaks due to the intercalation of Cl^- and $[Fe(CN)_6]^{4-}$ (Fig. 1.14b). After the exchange, EQCM study at 0.1mV/s in 0.1 M sodium,[164] potassium acetate and magnesium acetate containing 0.1 mM $[Fe(CN)_6]^{4-}$ shows the oxidation and reduction of the intercalated $[Fe(CN)_6]^{4-/3-}$, centered at 460mV vs. Ag/AgCl. The film undergoes a mass depletion during $[Fe(CN)_6]^{4-/3-}$ oxidation and a mass increase to the initial value during reduction, which confirms the intercalation of this species.

At synchrotron (beamline CRISTAL at Synchrotron Soleil, France), Taviot-Gueho *et al.*[161] could evidence the structural modification of three Co/Al−NO_3 samples recorded by *ex situ* X-ray diffraction signal (*i.e.* dried, in the absence of polarization):

- without immersion in KOH and without polarization,
- *ex situ* sample, *i.e. C*o/Al−NO_3(ox)-LDH recovered after oxidation in KOH at a potential of 0.8 V/SCE

- *Ex situ* sample, *i.e.* Co/Al−NO_3(ox/red)-LDH submitted to the oxidation in KOH at a potential of 0.8 V/SCE followed by a reduction at a potential of 0V/SCE.

The position of the (00l) diffraction peaks is shifted toward higher 2θ values for treated phases demonstrating a decrease of the interlayer distance from ~9.04 Å for Co/Al−NO_3 to 7.67 Å for Co/Al−NO_3(ox) and Co/Al−NO_3(ox/red). The authors attributed the change to the replacement of nitrate anions by OH^- anions in the interlayer space, which occurs quickly after immersion in KOH electrolyte solution or most likely because CO_3^{2-} anions replace the OH^- after the solids have been separated from the liquid phase, washed with water, and air-dried. Indeed, the interlayer distance of 7.67 Å is very close to that expected for carbonate-containing LDH. The exchange with CO_3^{2-} is further confirmed by FTIR. After the electrochemical treatments, the NO_3^- vibration band disappears and is replaced by a broad absorption band at 1360 cm^{-1} corresponding to the ν_3 vibration of CO_3^{2-}.

XRD, FTIR and EDX analyses were also realized on powder Ni/Al-NO_3.[135] After one night exchange in 0.1M NaOH, KOH and LiOH, *ex situ* analysis by XRD shows only a shift of the (0 0 l) diffraction peaks to lower 2θ, demonstrating a decrease of the interlamellar distance (d spacing) from 0.86 to 0.77nm, consistent with an exchange reaction of nitrate by carbonate anions in the interlamellar space, which is further confirmed by the carbonate band at 1400 cm^{-1} observed on FTIR spectra. The authors suggest that such exchange may have occurred after removing the solid from the solution in contact with atmospheric CO_2. Similarly, before and after the electrolysis of Ni/Al–NO_3 suspension at 1V vs. SCE for 1 h in highly basic conditions, an exchange reaction takes place. In all cases, the (110) diffraction line reflecting the intralayer organization remains unchanged indicating that the LDH layer structure was not modified upon neither the exchange process nor the oxidation of some of the LDH Ni^{2+} sites.

The same conclusion is reported for another Ni/Al–CO_3-LDH phase confirming the good stability of Ni/Al-LDH structure upon oxidative cycling in basic medium. EDX analyses were realized on thin films of Ni/Al–NO_3-LDH deposited on platinum electrodes before and after electrochemical oxidation in different C^+OH^- electrolyte solutions. EDX analyses conducted in two regions of each sample, one near the edge and one near the center of the coating, evaluate the Ni/Al ratio to be around 2. After the electrochemical treatment:

-The Ni and Al contents of the LDH layer were not affected.

- No nitrogen element is detected in any of the samples after oxidation. (The authors assume that the intercalated NO_3^- is exchanged by CO_3^{2-} anions *ex situ* when in contact with air as indicated by the XRD measurements).

- The incorporation of alkali ions after oxidation is observed with C^+/Ni molar ratio of 0.04 for K^+ and 0.20 with Na^+ (Li^+ cannot be measured by this method) only at the edge of the film. The authors suggest that the oxidation phenomenon starts from the edge of the sample coating and propagates to the center of the Ni/Al-LDH thin films.

1.7.2 *Operando* XRD measurements

Operando XRD measurements were carried out using a laboratory-made electrochemical flow cell especially developed for synchrotron measurements with a 0.1M KOH electrolyte solution introduced at a flow rate of 1.25 mL/min.[161] Upon contact with the KOH electrolyte, the interlayer distance of the Co/Al−NO_3 thin film electrode quickly decreased from ~9.03 to ~7.58Å, in agreement with *ex situ* measurements. The authors assign this to the exchange of NO_3^- by OH^-. From the beginning of the polarization, a net increase of the intensity of (00l) diffraction peaks (003), ~7.58 Å and (006) ~3.73 Å is a marker of the improvement of the cristallinity. Taviot-Gueho *et al.* relate this to a migration of OH^- species enhanced by an increase of the positive charge of the hydroxide layers resulting from the oxidation of Co^{2+}. Then, the crystallinity decreases continuously and the (00l) peaks gradually split into two peaks leading to two interlayer distances at 3.72 × 2 = 7.44 Å attributed to a OH^--containing LDH phase and at 3.87 × 2 = 7.74 Å. The origin of the latter distance is uncertain and it was not observed in *ex situ* experiments. Many hypotheses are excluded by the authors: the formation of carbonate-containing LDH is excluded as the measurements were carried out in an airtight cell. Nor is it the β-$Co(OH)_2$ or γ-$Co_{1-x}Al_xOOH_{14}$ displaying characteristic interlayer distances of 4.6 and 6.89 Å, respectively. The formation of α-$Co(OH)_2$ phase incorporating NO_3^-/OH^- interlayer anions as a side product of the oxidation process cannot be ruled out.

XRD coupled to electrochemistry highlight more particularly the transfer phenomena that take place in the interlayer domain. The disadvantage of *ex situ* XRD is that the LDH has to be removed from the solution and dried in air, which may modify the nature of the intercalated. *Operando* measurements necessitate a synchrotron X-ray beam to get a signal in the aqueous media. The position of the (00l) peaks that are a marker of the basal distance of the LDH should be further investigated and coupled to the quartz crystal microbalance to record simultaneously the mass of the film and the basal distance of the LDH. This will be explained in the chapter 3 in order to understand which species play a role in the redox process.

1.8 Conclusion

In this chapter, during the reversible oxidation of the electroactive sites within the LDH, some assume the entry of OH-, other groups assume the expulsion of H+. Another hypothesis is that this transfer is influenced by the nature of the cations that compose the electrolyte. Some also hypothesize a transfer of cations. In this Ph.D thesis, we aim at establishing the mechanisms of transfer of the cationic and anionic species between the electrolyte and the LDH *i.e.* the nature of the involved charged and uncharged species and the specific sites of interaction onto/into the material (adsorption or intercalation). This study will enable to resolve this issue. We also aim to establish the kinetics running the redox process and the motion of the species transferred between the electrolyte and the LDH with the electrochemical measurements coupled with electrogravimetric measurements and *operando* XRD at synchrotron.

In this Ph.D. thesis we knock down the technological barriers for the development of an innovating process of capture/liberation of ions assisted by electrolysis.

Firstly, we have to synthesize and characterize the LDH whose chemical structure, crystallinity and morphology make them good candidates for electrochemical measurements, capture and liberation of species with the electrolyte for charge compensation. The deposition has to be optimized onto the surface of the electrode to enhance the electrical charge transfer between the film and the electrode.

Many different LDHs were studied in the literature. Ni-based LDH and Co-based LDH, the most conductive ones, are of interest for a better response, electronic kinetics, and reversibility. Their conductivity is even enhanced for both when combined with Fe. For practical reasons and because we want to essentially study the Faradaic process, we focused on the preparation and study of the Ni/Fe-LDH.

Chapter 2

Materials and methods

Chapter 2 begins with the description of the two LDH sample preparations; one concerning the chemical synthesis and the other concerning electrochemically assisted synthesis. Then, the techniques and methods of morphological and structural characterization of the material are described. Finally, the electrochemical characterization techniques and the coupling to the XRD characterization are presented.

2.1 Preparation procedure of LDH thin films

2.1.1 Preparation procedure of chemically synthesized LDH and thin film formation

2.1.1.1 1st step: Co-precipitation with variable pH

The Ni^{II}/Fe^{III}-CO_3-LDH 3/1 (in chapter 4 and 5) and the Mg^{II}/Fe^{III}-CO_3-LDH 2/1 (Annex A) were chemically synthesized with the varying pH method in air at 35°C.[77] For the synthesis of Ni^{II}/Fe^{III}-CO_3-LDH 3/1, $Ni(NO_3)_2.6H_2O$ and $Fe(NO_3)_3.9H_2O$ salts were dissolved in deionized water to obtain a molar ratio Ni^{II}/Fe^{III} equal to 3. For the synthesis of Mg^{II}/Fe^{III}-CO_3-LDH 2/1 LDH, $Mg(NO_3)_2.6H_2O$ and $Fe(NO_3)_3.9H_2O$ salts were dissolved in deionized water to obtain a molar ratio Ni^{II}/Fe^{III} equal to 2. The metals were precipitated by a basic aqueous solution containing 1 M Na_2CO_3 (99.8% purity) and 2.6 M NaOH (98% purity) and introduced dropwisely at a constant rate by means of a peristaltic pump until it reached a pH of 10. The slurry was then stirred during 24 h at 60°C for maturation. To eliminate impurities, the slurry was then centrifuged at 4000 rpm during 5 minutes. The supernatant was eliminated, and finally the material underwent a dialysis in deionized water for 5 days to remove impurities from the solution.

2.1.1.2 2nd step: Dropcasting of the chemically synthesized LDH

After the dialysis, the slurry was put in suspension in ethanol and deposited on gold-patterned quartz substrates (9 MHz-AWS, Valencia, Spain), for the preparation of working electrodes. The deposition of LDH films was carried out according to the dropcasting method described in the literature[98, 9] onto the gold surface (surface area: 0.20 cm^2) of the gold-patterned quartz substrates. Around 10 µL of the LDH suspension was deposited and dried in air for a few hours. The film thickness was estimated to be around 500 nm (based on FEG-SEM measurements).

The reason for using the gold-patterned quartz substrates of 9 MHz as working electrodes (WE) is twofold: (i) it allows the measurement of the frequency variation of the quartz resonator before and after the deposition of the LDH thin film, which is related to the deposited film mass using Sauerbrey equation (equation 2.2) and (ii) it enables both the measurement of the current and the electrogravimetric measurements by EQCM and *ac*-electrogravimetry. [11,12, 13,14]

Thereafter, EQCM and *ac*-electrogravimetric measurements were realized in aqueous 0.1 M or 1M solutions of LiOH, KOH, CsOH and Na_2CO_3/$NaHCO_3$.

2.1.2 Procedure of electrochemically assisted synthesis of LDH thin films onto the electrode

For the electrochemically assisted synthesis of Ni^{II}/Fe^{III}-NO_3-LDH 3/1, the elec-Ni/Fe-LDH was deposited by means of a 3-electrode electrochemical cell. The counter-electrode was a platinum grid, the reference electrode was an Ag/AgCl electrode and the LDH was deposited onto the working electrode that is a 9MHz-gold patterned quartz substrate. (Fig. 2.1) The electrolyte was an aqueous solution of $Ni(NO_3)_2.6H_2O$ 0.004 M, $Fe(NO_3)_3.9H_2O$ 0.012 M and KNO_3 0.464M. The molar ratio Ni^{II}/Fe^{III} equals 3 and the molar concentration in NO_3^- equals 0.5 M. The pH of the solution was 2.5 according to the presence of Fe^{3+} that is a Lewis acid. The LDH deposition was realized in a few seconds via a potentiostatic method with the application of a potential of -0.7V/SHE in deaerated solution with Argon while stirring.

After the deposition, the patterned quartz substrate coated with the LDH was removed from the solution and rinsed with a KOH solution pH 10, otherwise the acidity of the solution would dissolute the LDH film.

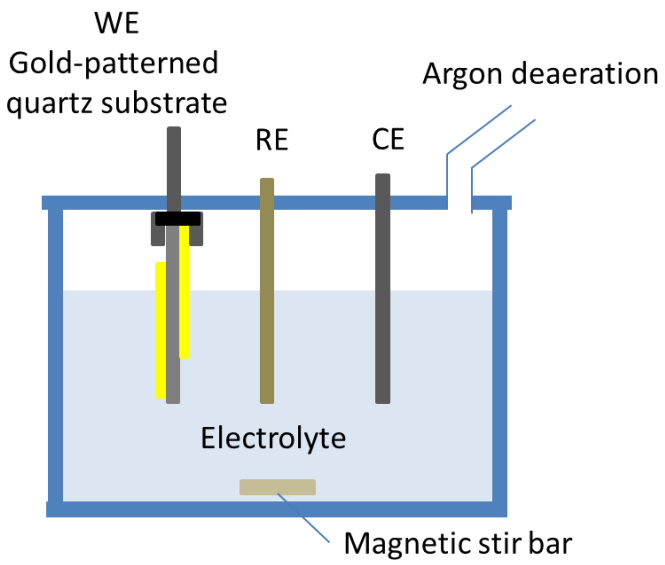

Figure 2.1: Scheme of the electrochemical cell for assisted electrodeposition

2.2 Structural and morphological investigation methods

This section is dedicated to the structural and morphological methods that were used for the characterization of LDH in this thesis. Particularly, the type of instruments and the preparation of the samples for the experiments are described.

2.2.1 Scanning electron microscopy (SEM)

Figure 2.2 shows a schematic description of a SEM set-up. It is composed of the main elements: electron gun, electromagnetic lenses, scanning foils and detectors. The electron gun generates a primary electron beam with energy ranging from 0.2 to 40 keV. The electrons are thermionically emitted from a tungsten filament cathode in vacuum. The beam is then collimated by electromagnetic condenser lenses and focused by an objective lens. With pairs of scanning electromagnetic deflection coils,[172] the electron beam can interact with the sample onto a rectangular surface. Secondary electrons **are emitted** from the sample[173] with lower energy and are selectively attracted towards the secondary electron detector. The latter is a **grid held at a low positive potentia**l with respect to the sample.[174] Secondary electrons are counted per unit time and translated into an electrical signal used for the visualization of the number of collected electron par surface unit. This is in general related to the topology of the surface: from shallow surfaces, few electrons can escape the surface to reach the detector resulting in darker areas, while at the edges or convex surfaces, more electrons can escape and reach the detector resulting in brighter areas.

However, for non-conductive samples, the charge built up on the surface by the primary source of electron cannot be dissipated, resulting in bright images. To prevent this problem, samples can be sputtered with a very thin layer of metals (such as gold, gold/palladium, carbon) as a part of the sample preparation.[172]

There are various types of electron guns. In comparison to thermiooonic electron guns, field emission guns (FEGs) provide enhanced electron brightness (approximately x 100) and longer lifetime. Furthermore, because of the lower electron energy spread (0.3 eV), the chromatic aberration is significantly reduced and probes smaller than 2 nm can be formed, thus, providing much higher resolution for SEM images.

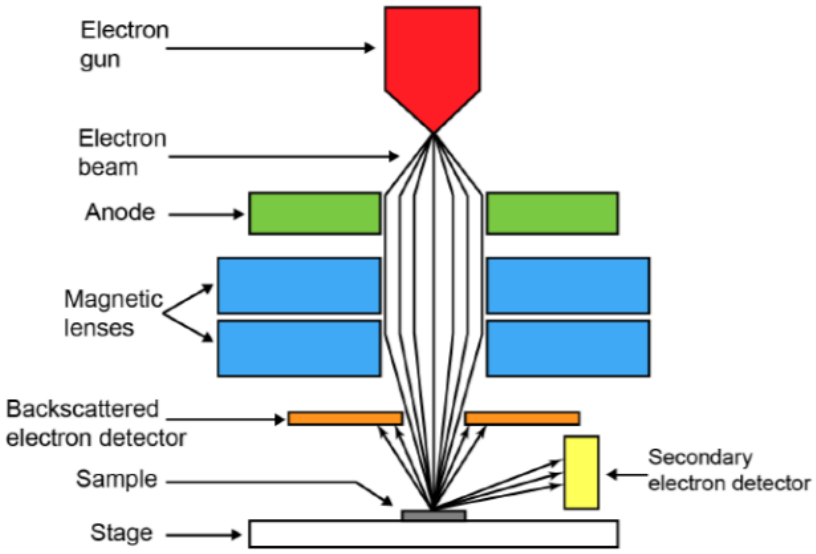

Figure 2.2: Schematic description of a SEM setup[175]

In this Ph.D. thesis, the morphology and thickness of the LDH thin films were investigated by FEG-SEM (Zeiss, Supra 55). Before the analysis, the samples were fixed onto an aluminum stub with a conductive carbon tape and sputter-coated with carbon.

2.2.2 Energy dispersive X-rays (EDX)

EDX is usually associated to SEM. When the primary electron beam reaches the sample (in the top few microns of the surface), it causes the excitation of the electrons of the atoms and the related production of X-ray photons whose energy is characteristic of the atoms. X-ray photons are collected, sorted by energy, counted and translated into electrical signal for display and processing. This technique enables the determination of the different atoms in the sample.

In this Ph.D. thesis, the elemental analysis was performed with an energy dispersive X-ray (EDX) detector associated to the FEG-SEM.

2.2.3 X-Ray diffraction (XRD) coupled to electrochemical techniques

X-ray diffraction is a technique used to characterize crystal structures that consist, ideally, of the infinite repetition of identical structural units in space, which can be either a single atom (such as in copper, silver or gold) or various atoms or molecules.

X-rays are short-wavelength electromagnetic radiations produced either by deceleration of high-energy electrons or by electronic transitions involving electrons in the inner orbitals of atoms. They are produced in a vacuum tube containing both anode and cathode (usually a tungsten filament) electrodes. The cathode is heated to provoke an electron emission and a high voltage is applied between both electrodes for the acceleration of electrons from the cathode to the anode and induce the emission of X-ray radiation from the anode (whose energy depends on the composition of the cathode; copper gives energy of 8 keV).

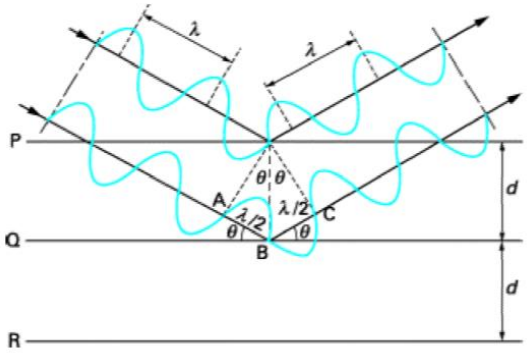

Figure 2.3: Schematic diagram for determining Bragg's law [176]

During the interaction between the X-rays and the surface (Fig. 2.3), positive interference only occurs if the phase shift between two X-rays is a multiple of the wavelength of the X-rays (λ). Since the phase shift is 2dsinθ, with d is the period distance and θ is the incidence angle of X-rays.[177,172,178,179]

The detector counts photons versus angle. The Bragg equation gives the relationship between the angle and the interatomic distance:

$$2dsin(\theta) = n\lambda \qquad (2.1)$$

In this Ph.D. thesis, the crystal structure of the LDH samples was analyzed by using an Empyrean Panalytical X-ray diffractometer (Cu Kα radiation, λ = 1.541 Å). *In situ* XRD measurements under polarization were performed with a home-made setup (Fig. 2.4).

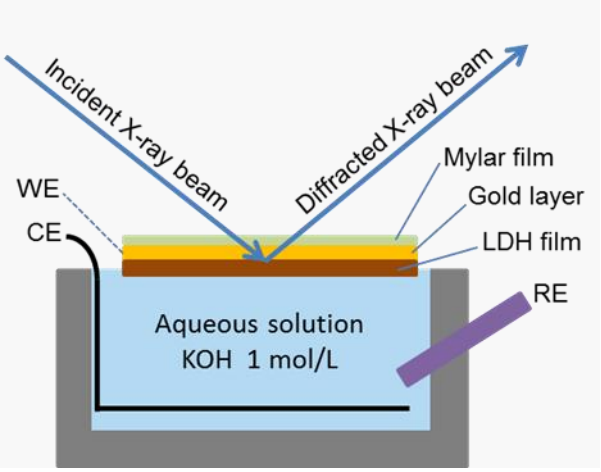

Figure 2.4: Scheme of the setup of *in situ* XRD with electrode (WE) polarization in KOH of a LDH thin film. CE: counter electrode (platinum grid), RE: reference mercury-mercurous sulfate electrode.

The reversible variation of the period of the interlayer distance during the redox reaction of Ni was evaluated by recording *in situ* the XRD characteristic 003-peak of the LDH. A WE made of a mylar film (4.5 µm thickness) coated with a gold layer (100 nm thickness) and a thin film of LDH was immerged in aqueous KOH 1 mol/L solution. This particular WE enables the XRD beam to reach the LDH thin film that is in contact with the electrolyte. In this condition, XRD measurements were recorded with a Panalytical Empyrean diffractometer operating at 45 kV and 40 mA at room temperature, with a Cu Kα radiation (λ = 1.541 Å) passing through a 15 mm mask with 2° slit. The LDH underwent 40 cycles of polarization to be set in the same condition as the experiments conducted with *ac*-electrogravimetry. Scans have been recorded at 0.450 V/SHE (reduced state of LDH) and at 0.710 V/SHE (oxidized state of LDH) from 5° to 31° (2θ) with a step of 0.026° and a counting time of 600 s per step to follow the 003-peak of the LDH and a characteristic peak of mylar taken as reference.

At synchrotron SOLEIL (SIXS line, Saclay, France), a home-made electrochemical cell (Fig. 2.5) was developed to simultaneously record EQCM measurements and the XRD pattern of the material). It consists in a 3-electrode cell (a counter-electrode made of a platinum grid, a sulfate calomel reference electrode, and a 9MHz-gold patterned quartz substrate coated with a film of LDH as working electrode) connected to an Autolab potentiostat-galvanostat electrochemical workstation coupled with a FRA, Solartron 1254 QCM device. The electrochemical cell was filled with three different electrolytes: CsOH 0.1 M (CsOH 1M needed to be diluted 10 times because of the absorbance properties of Cs), KOH 1M, LiOH 1M. Two kapton windows enabled the synchrotron X-ray monochromatic beam to pass through 2 cm of electrolyte to reach the LDH coated sample. The energy required for the photons was 20 keV; only 20 percent of the beam was then transferred. The spot size was 1000×50 μm^2

(horizontally × vertically) reached the quartz at the grazing incidence 0.05 radian and the diffracted beam was recorded in Q-range between 0.5 and 1.1 ($A^{\circ -1}$).

Many parameters were simultaneously recorded under the X-ray beam and under cyclic polarization (between -0.2 V *vs*. SCE and +0.06 V salts were dissolved in deionized water to obtain a molar ratio V *vs.* SCE at 10mV/s and 1mV/s) at room temperature: the current, the frequency shift of the quartz related to the mass variation of the LDH film and the characteristic/details of the (003) Bragg diffraction peak of the LDH pattern. Concerning the latter parameter, scans of the 003-peak were recorded each second. Each peak was fitted with a Lorentzian curve to plot the width, amplitude and position of the peak versus polarization time.

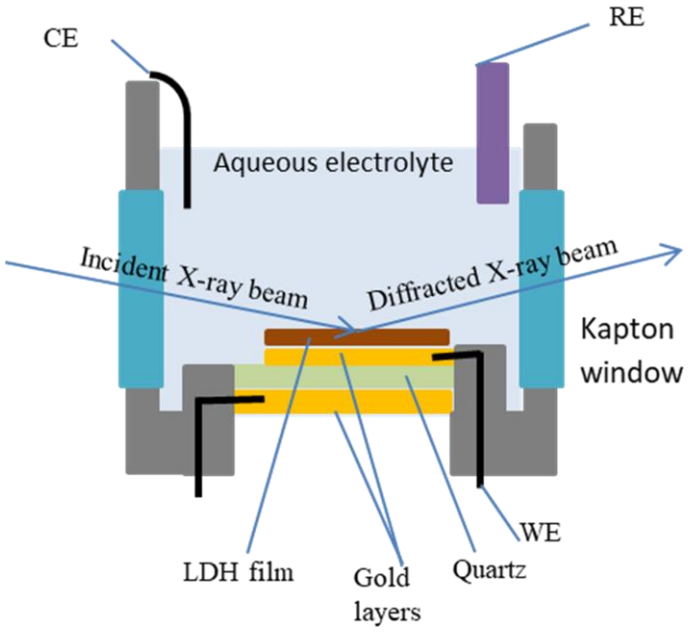

Figure 2.5: Experimental setup of the home-made electrochemical cell used at synchrotron SOLEIL (Saclay, France)

2.2.4 Thermogravimetric analysis (TGA)

Thermogravimetric measurement (TGA) is the measure of the mass variation of a sample over time for a given profile of temperature. This technique enlightens information about physical phenomena (phase transitions, absorption adsorption and desorption of water molecules within the sample) and chemical phenomena (chemisorption, thermal decomposition, solid-gas reactions).

For the determination of the chemical formula of the LDH, TGA enables the quantification of the number of water molecules. By using the scheme of decomposition for chemically synthesized LDH (Fig. 2.6), there are five steps depending on the increase in temperature.

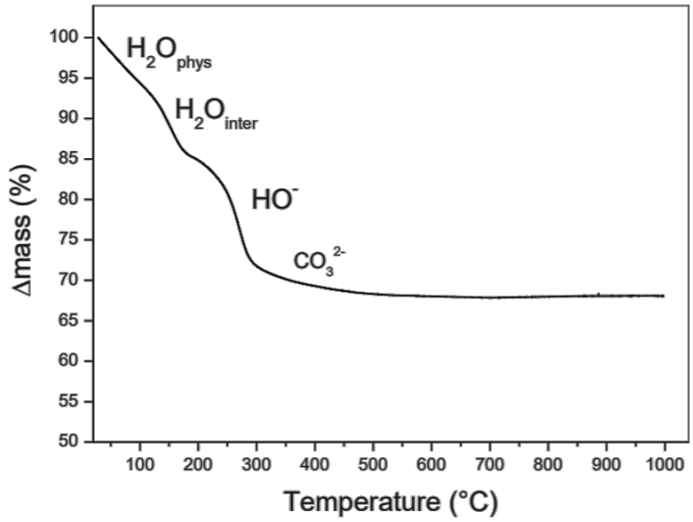

Figure 2.6: TG analysis of chemically synthesized Ni/Fe-LDH

1st step: Release of physisorbed water (H_2O_{phys})

2nd step: Release of interlayered water ((H_2O_{inter})

3rd step: Dehydroxylation of layers and formation of H_2O between 180°C and 300°C

4th step: Decomposition of interlayered anions between 300°C and 600°C

5th step: Formation of oxides and mixed oxides at temperatures above 600°C ($M^{II}O$, $M^{II}M^{III}{}_2O_4$, $M^{III}{}_2O_3$).

2.3 Electrochemical and (electro)gravimetric techniques

2.3.1 Quartz crystal microbalance (QCM)

2.3.1.1 Piezoelectricity

The quartz crystal can convert a mechanical stress into an electrical signal, which can be used to make a transducer or a sensor.[180] The piezoelectric transducer is a device that transforms an interaction at the modified electrode/liquid interface into a measurable electrical signal.[181]

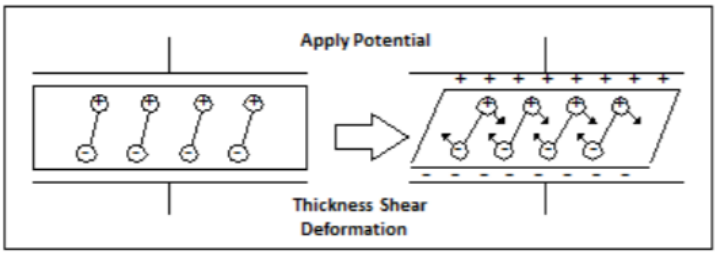

Figure 2.7: Schematic representation of the deformation of a polarized quartz material [182,180]

Microbalance operation is based on the piezoelectric properties of quartz. Piezoelectricity is a property of some materials with no center of symmetry that are electrically charged when a mechanical stress is applied (direct effect). Conversely, the application of a potential creates a reorientation of the dipoles in the acentric material (Fig. 2.7) causing its shear deformation (converse effect).[181,183,182]

Of all the piezoelectric materials existing in nature or made industrially, quartz is one of the most commonly used. It is insoluble in water and resists to temperatures up to 573°C without losing its piezoelectric properties.[184] From its hexagonal prism structure (Fig. 2.8a) with six cap faces at each end, [185] it has trigonal trapezohedral crystal symmetry. Its three axes of symmetries compose an orthogonal coordinate system with Z axis called optic axis, X axis called electrical axis and Y axis called mechanical axis (Fig. 2.8c).[186, 187] The cutting of the quartz crystal in different plane orientation can tune the mode of vibration and its frequency domain. In Figure 2.8b are shown different cuttings BT, CT and DT corresponding to a shear face mode having a resonant frequency around 1 MHz.[181] The main vibration modes include flexion, longitudinal, face shear and thickness shear vibrations. [180] The thickness shear vibration is associated with the AT-cut orientation of 35° 12' with respect to the Z axis and is commonly used for quartz microbalance sensors. The latter is used in this PhD thesis in the form of a thin disk with a diameter of 14mm for quartz crystal microbalance sensing.

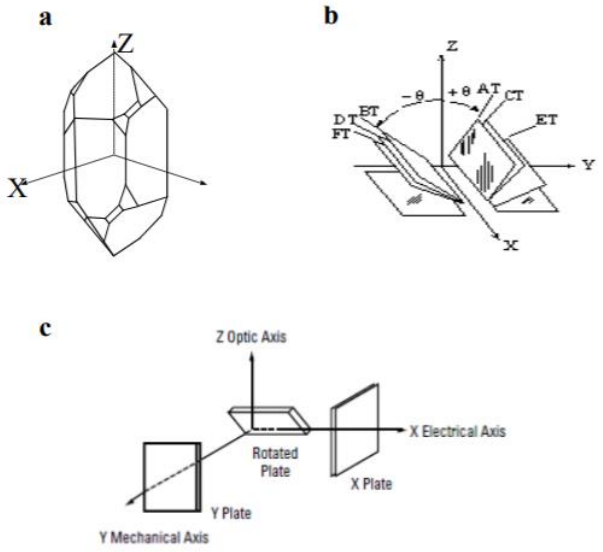

Figure 2.8: Representation of the different sections of a quartz crystal with respect to the principal values

The electrode is composed of a quartz disk on which a gold coating (5mm in diameter) is deposited on each side of the disk by vacuum evaporation and extended by a "leg" for the electrical connection. The thickness of the quartz determines its resonant frequency. For better adhesion between the quartz crystal and the gold electrode (100 nm to 200 nm thickness), a sub-layer of chromium (10 nm thickness) is sandwiched in-between (Fig. 2.9).

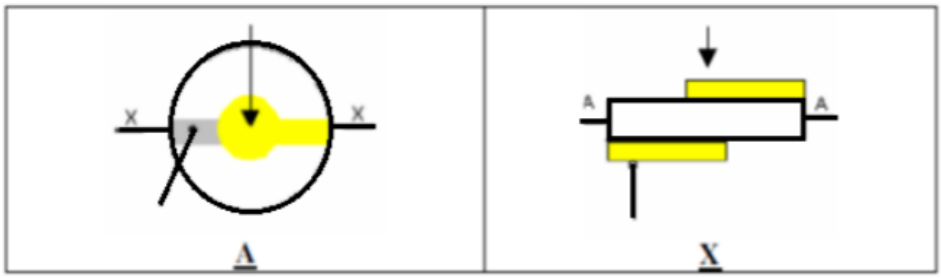

Figure 2.9: Quartz disk face (A) and cross-sectional (X) carrying the two gold electrodes[181]

The piezoelectric effect within the quartz crystal takes place in the active area that is defined by the zone where the two gold electrodes are placed opposite to each other. Under alternating polarization at the pair of gold electrodes, the upper and lower faces of the active zone resonate parallel to each other and a stationary acoustic wave is generated throughout the quartz crystal (Fig. 2.10). The frequency of this wave is called the resonant frequency of the quartz resonator.[181,180]

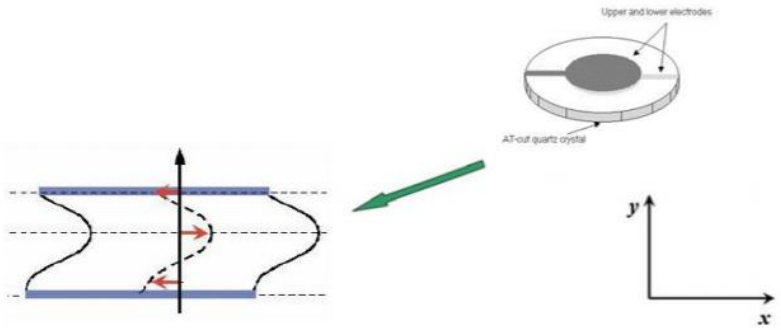

Figure 2.10: Schematic illustration of a thickness shear mode quartz resonator

2.3.1.2 Working principle of QCM

The quartz crystal microbalance, or piezoelectric transducer [188] is an attractive tool for gravimetric measurements. Applications are found in many research fields such as chemical sensors[188,189] and biosensors.[190] The mass sample that is deposited onto the surface of this electrode can be measured through the change of the resonant frequency of the quartz resonator. The relationship between mass and frequency changes [191,182] was established by Sauerbrey[192] for a rigid, purely elastic and electroacoustically thin layer according to:

$$\Delta f_m = -k_s \Delta \mathrm{m} = -\left(\frac{2f_o^2}{Sn\sqrt{\rho_q \mu_q}}\right)\Delta \mathrm{m} \qquad (2.2)$$

where Δf_m is the frequency change of the quartz resonator, Δm is the mass change of the microbalance active surface (g), ρ_q is the quartz density (2.648 g.cm^{-3}), μ_q is the shear modulus of a shear AT quartz crystal (2.947 x 10^{11} g.cm^{-1}.s^{-2}), f_o is the fundamental resonant frequency of the quartz (Hz), S is the active surface on the quartz corresponding to the metal electrode deposited on it (cm^2) and k_s is the theoretical sensitivity factor (Hz.g^{-1}.cm^2). With a QCM operating at 9 MHz, the theoretical sensitivity factor calculated from the Sauerbrey equation is equal to 18.3x10^7 Hz.g^{-1}.cm^2. The applied potential is strong enough to create a vibrational motion of the crystal at its resonant frequency.

The sensitivity factors of quartz crystal operating at 6, 9 and 27 MHz was determined by Bizet et al.[193] by electrodeposition of copper at different electrical current values. For the determination of the experimental k_s^{exp}, a cathodic current is applied to the gold electrode deposited on the quartz crystal in a Cu^{2+} containing solution for the deposition of Cu^{2+} ions to Cu^o and causing a decrease in resonant frequency. The applied current is controlled through a galvanostat and the mass change, Δm, is calculated by assuming that the efficiency of the reduction reaction of copper is equal to 100%.

$$\Delta q = i.\Delta t \quad (2.3)$$

The number of moles of Cu^o is:

$$\Delta m = n_{Cu} M = \frac{i.\Delta t.M}{n_{e-} F} \quad (2.4)$$

Dividing by Δt:

$$\frac{\Delta m}{\Delta t} = \frac{i.M}{n_{e-} F} S \quad (2.5)$$

where j corresponds to the current density ($A.cm^{-2}$), M is the molar mass of copper (63 $g.mol^{-1}$), F is the Faraday's constant (96500 $C.mol^{-1}$), n_{e-} is the electron number. By inserting $\frac{\Delta m}{\Delta t}$ and the experimental $\frac{\Delta f}{\Delta t}$ into the following equation, k_s^{exp} is determined:

$$k_s^{exp} = \frac{\Delta f_m}{\Delta m} S = \frac{\Delta f}{\Delta t} \frac{\Delta t}{\Delta m} S \quad (2.6)$$

At 9 MHz, the experimental mass sensitivity factor is equal to 16.31 (± 0.32)10^7 Hz g^{-1} cm^2 at an imposed current of 0.5 mA, a value which is in fairly good agreement with the theory. This experimental mass sensitivity factor is used throughout the present Ph.D. thesis.

2.3.1.3 Experimental set-up

In this Ph.D. thesis, the set-up used for measuring mass/frequency change of the film onto the electrode is a lab made microbalance developed at the LISE laboratory. A gold-patterned 9 MHz quartz crystal resonator (AWS, Spain) is inserted in an electrochemical cell and connected to a specific electronic circuit, the whole system being called an oscillator. Thus, it is possible to monitor the evolution of microbalance frequency f_m, in real time through the GPES software.

2.3.2 Cyclic electrogravimetry (EQCM)

As mentioned in chapter 1, EQCM, also called cyclic electrogravimetry, is a method based on the coupling between cyclic voltammetry (CV) and gravimetric measurements through a QCM device. Using this method, the mass variations of the thin film coated the Au electrode (calculated from Sauerbrey's equation) is recorded during an electrochemical process.

2.3.2.1 Principle

Electrochemical measurements are carried out in a classical three electrode electrogravimetric cell. A potential is applied between the working (*i.e.* gold electrode of the QCM) and the reference electrode and varies at a constant

rate cyclically between two potentials. The resulting current variation is recorded by means of the counter electrode. Simultaneously, the frequency variation of the quartz changes of the film is measured versus potential. With the Sauerbrey equation,[192] the resonant frequency change is converted into the mass change of the film onto the electrode.

2.3.2.2 Experimental set-up

The experimental set-up (Fig. 2.11) is a 3-electrode electrogravimetric cell (AWS, Spain) composed of a working electrode (a gold electrode deposited on a quartz resonator, 0.5 cm in diameter and an effective surface area of 0.2 cm^2), a reference electrode and a counter electrode, a platinum grid immersed in an electrolyte. The cell is connected to a potentiostatic system (Autolab PG stat 100), a frequency-meter (Yokogawa), the QCM and a computer. These measurements are registered in a central computer. In this Ph.D. thesis, EQCM is utilized to analyze (i) the assisted electrodeposition process of LDH, and (ii) the electroadsorption or intercalation processes of pseudocapacitive electrode materials.

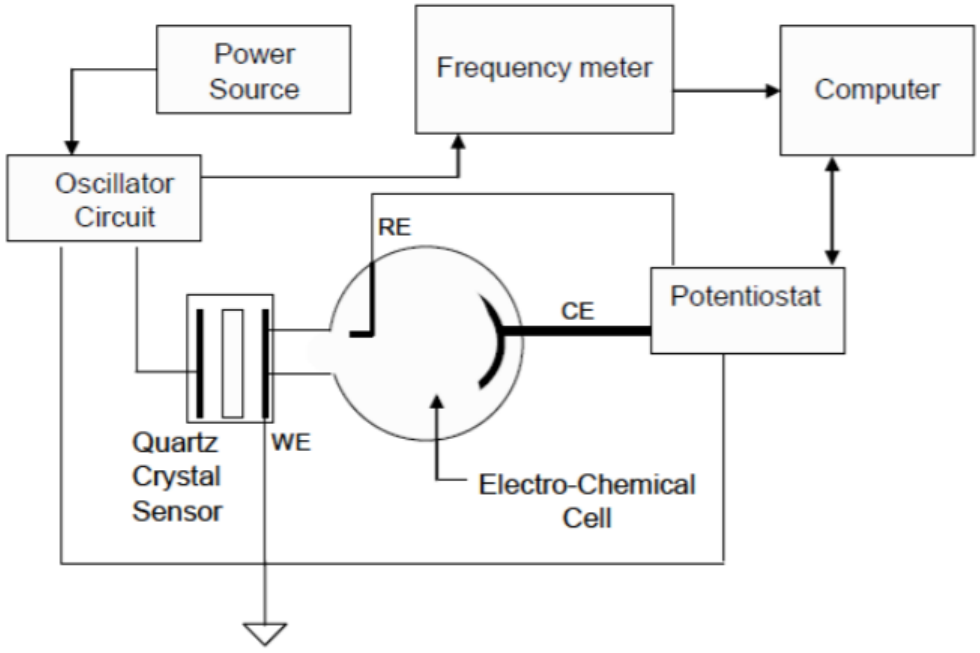

Figure 2.11: Experimental setup of an EQCM[189]

2.3.3 Electrochemical impedance spectroscopy (EIS)

Electrochemical reactions can be composed of several steps, each having different kinetics. EQCM gives a global response of all the steps and does not allow the distinction between the elementary steps. To better understand and study the different steps, electrochemical impedance spectroscopy (EIS) is the appropriate method. It has

been used to study the reaction mechanisms occurring at the electrode/electrolyte interface and has been employed in various domains such as: corrosion,[194] energy[195,196] and biosensors.[188]

The principle of EIS is to apply a sinusoidal potential perturbation ΔV of low amplitude around a stationary potential V_s, at a certain frequency. With low amplitude, the electrochemical system is under stable condition with a low level of disturbance associated with frequency modulation. This helps the separation of the different reactions with different kinetics: fast phenomena occur at high frequencies while the slower phenomena are visible at lower frequencies.[197, 194] The studied response is the variation of current ΔI. In general, electrochemical systems have a nonlinear current voltage I=f(V) characteristic curve. However, working only on a small portion of the so-called Lissajous curve, the relationship between ΔV and ΔI may be considered as linear. Thus, the response of the system ΔI is also probed as a sinusoidal current with low amplitude around a stationary value I_s (Fig. 2.12).

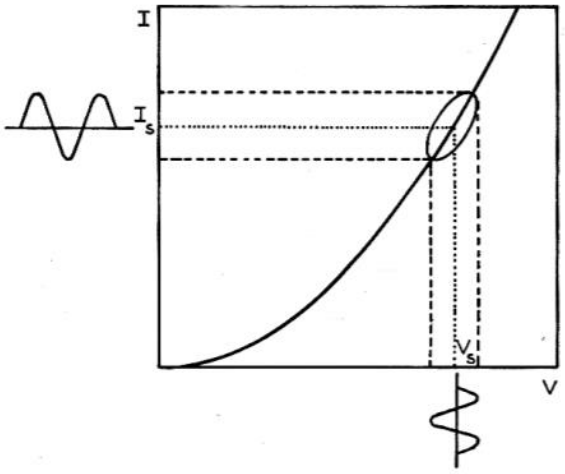

Figure 2.12: Linear current response to a low amplitude sinusoidal perturbation potential around a stationary value

Impedance is a generalization of the concept of resistance and is applicable to the Fourier transform of the sinusoidal functions. The transfer function ΔV/ΔI(ω), called the electrochemical impedance Z(ω) is defined with ω = 2πf corresponding to the pulsation. As a complex number, Z(ω) can be written as:

$$Z(\omega) = |Z|\exp(j\varphi) = Re(Z) + jIm(Z) \quad (2.7)$$

represented in polar coordinates (|Z|,φ), or Cartesian coordinates (Re Z, Im Z). The relationships between these quantities are:

$$|Z|^2 = (Re(Z))^2 + (Im(Z))^2 \quad (2.8)$$

$$\varphi = \arctan\frac{Im(Z)}{Re(Z)} \quad (2.9)$$

$$Re(Z) = |Z|\cos\varphi,\ Im(Z) = |Z|\sin\varphi \quad (2.10)$$

where |Z| is the impedance modulus, ratio of amplitudes between ΔV and ΔI; Re(Z) and Im(Z) are the real and imaginary parts of Z(ω), Φ is the phase angle between ΔV and ΔI, and j is the complex number ($j^2 = -1$).

Two diagrams illustrate the set of points: Nyquist (Fig. 2.13b) and Bode (Fig. 2.13c) diagrams. In the Nyquist diagram, each point corresponds to a certain frequency: the high frequency limit (HF) corresponds to the high-frequency resistance, often equal to the resistance of the electrolyte. The low frequency limit (BF), if obtained, corresponds to the polarization resistance. The Bode plot illustrates separately the module |Z| and φ the phase as a function of the logarithm of the frequency, log *f*, (where $f = \omega/2\pi$).

The response current is the sum of Faraday's current, i_f, and capacitive current i_c. The faradic process characterizes the transfer of electrons at the electrode/electrolyte interface. The capacitive processes characterize the electrical charge at the interface that creates a double layer defined of a certain capacitance C_d. Therefore, the electrochemical cell can be modeled by an equivalent circuit (Fig. 2.13a) comprising a double layer capacitance in parallel with a transfer resistance R_t, and introducing in series an electrolyte with resistance R_e.[181] Consequently, the electrochemical impedance of the equivalent circuit is as follows:

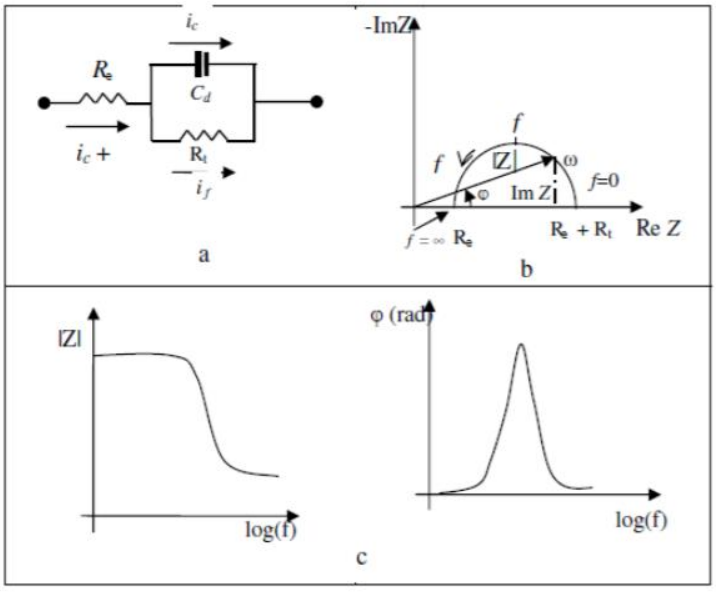

Figure 2.13: (a) Example of an equivalent electrical circuit. Plots of impedance of an electrochemical cell in (b) Nyquist diagram and in (c) Bode diagram

In this Ph.D. thesis, the experimental set-up (Fig. 2.14) consists of:

- A PGSTAT100 (Autolab) potentiostat that works under potentiostatic mode, and imposes a given stationary potential V_s,

- A frequency generator, included in the Frequency Response Analyzer (FRA 1254, Solartron), that delivers the low amplitude sinusoidal perturbation ΔV,

- A three-electrode cell.

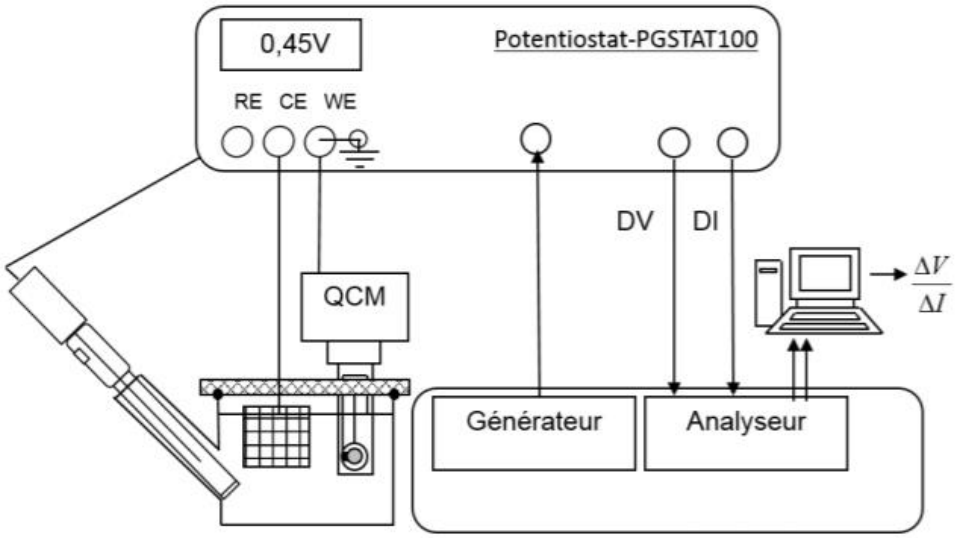

Figure 2.14: Experimental setup for electrochemical impedance measurements

2.3.4 *Ac*-electrogravimetry - A fast electrogravimetric method

Ac-electrogravimetry technique couples EIS measurements with a QCM in dynamic mode. It was first proposed by Gabrielli *et al.*[198] at the LISE laboratory (UMR 8235, Paris, France) to discriminate the activity of the different species involved in the charge transfer during an electrochemical process as well as the transfer of solvent molecules. For each of the charged and uncharged species transferred at the interface between the electrode and the electrolyte, it provides access to the nature (in terms of molar mass), kinetics as well as their relative concentration.

Consequently, more than EIS, *ac*-electrogravimetry appears to be an attractive tool to deconvolute all the charged and uncharged fluxes at the electrode/electrolyte interface.

2.3.4.1 Principle

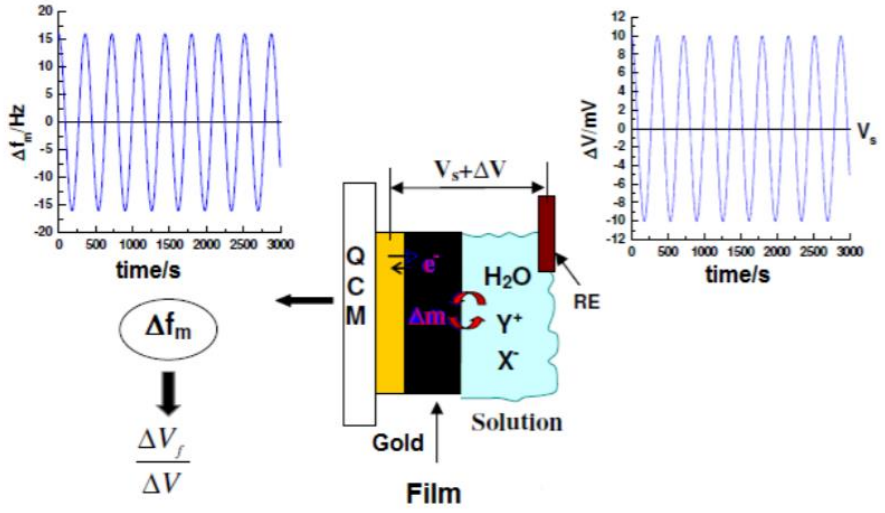

Figure 2.15: Principle of measuring the electrogravimetric transfer function $\Delta V_f/\Delta V$

The principle of *ac*-electrogravimetry is employed in electrochemical systems and is analogous to the principle of electrochemical impedance. A low amplitude sinusoidal perturbation ΔV can lead to changes in the mass of the film coated onto the microbalance surface Δm and in current variations ΔI. Simultaneously, two transfer functions are obtained: the classical electrochemical impedance and an electrogravimetric transfer function[199, 171, 200] also called mass/potential transfer function (Fig. 2.16).

The principle of electrogravimetric transfer function measurements is gathered in Figure 2.15. Measurements are conducted with a three-electrode cell, the working electrode being also a QCM. When the low amplitude sinusoidal perturbation ΔV is applied at a certain frequency to the film deposited onto the gold electrode of the QCM, some of the charged species participate in the charge compensation process within the electroactive material. Their insertion/removal is detected through the microbalance frequency change Δf_m, and the corresponding mass change of the film is calculated using the Sauerbrey equation. Transfer function measurements are controlled by a computer using FRACOM software, a software developed at the LISE laboratory. A multi-channel FRA-Solartron 1254 permits the simultaneous determination of two main transfer functions: the electrochemical impedance $\Delta E/\Delta I(\omega)$ and the frequency/potential function $\Delta f_m/\Delta E(\omega)$ is obtained.

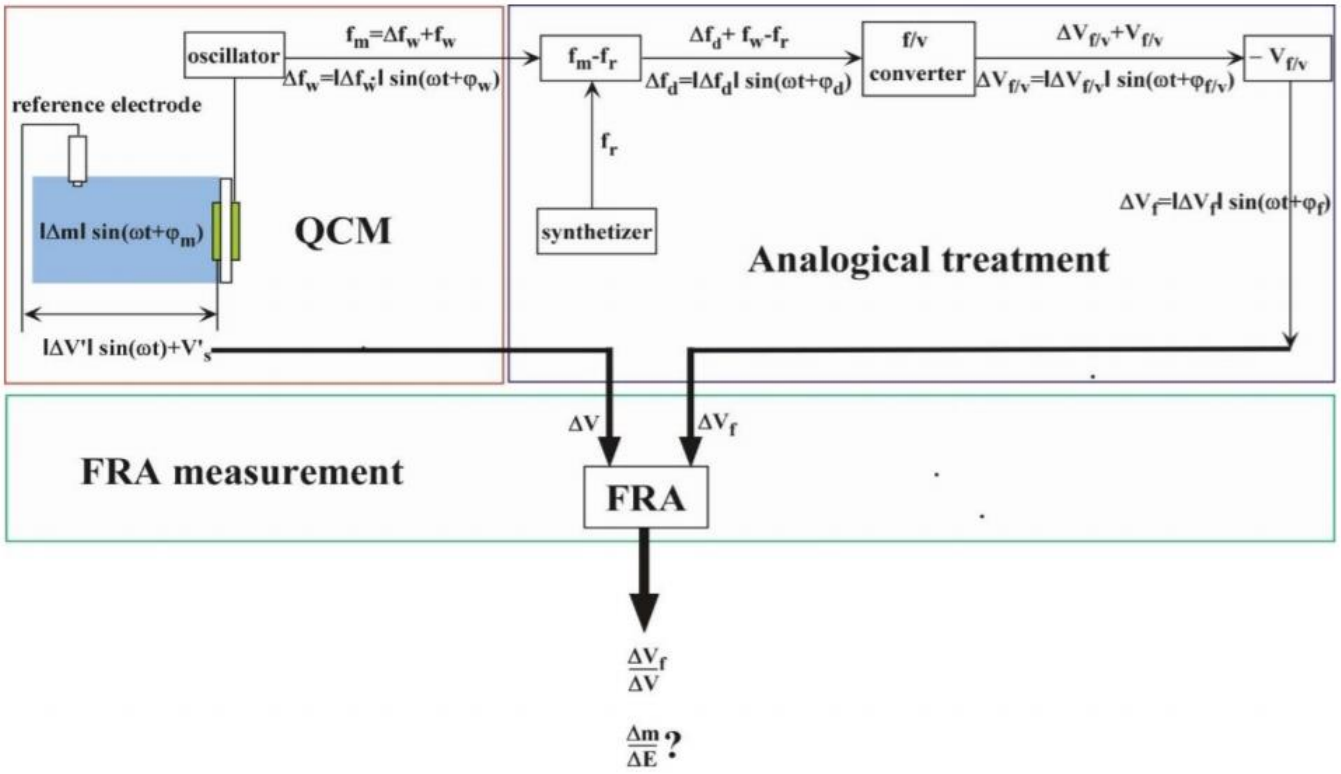

Figure 2.16: Scheme of the principle of electrogravimetric transfer function measurements

In fact, $\Delta f_m/\Delta E(\omega)$ is not directly measurable but needs the measurement step of a third impedance $\Delta V_f/\Delta E(\omega)$. A frequency/voltage converter is in fact used to convert the microbalance frequency signal Δf_m into a measurable voltage signal ΔV_f for the multi-channel FRA-Solartron 1254. However, in order to perform effectively the demodulation frequency of a few Hz on a carrier signal of 9 MHz, the carrier is reduced to a few hundred Hertz to increase accuracy. The differentiation to decrease the carrier to a few hundred Hertz is done with a frequency synthesizer (Marconi-2023) and an electronic module. Then, it is possible to extrapolate Δm from the ΔV_f signal for a given configuration and type of measurement. This is achieved by calibrating the system before the measurement.

2.3.4.2 Experimental method: $\Delta V_f/\Delta V$

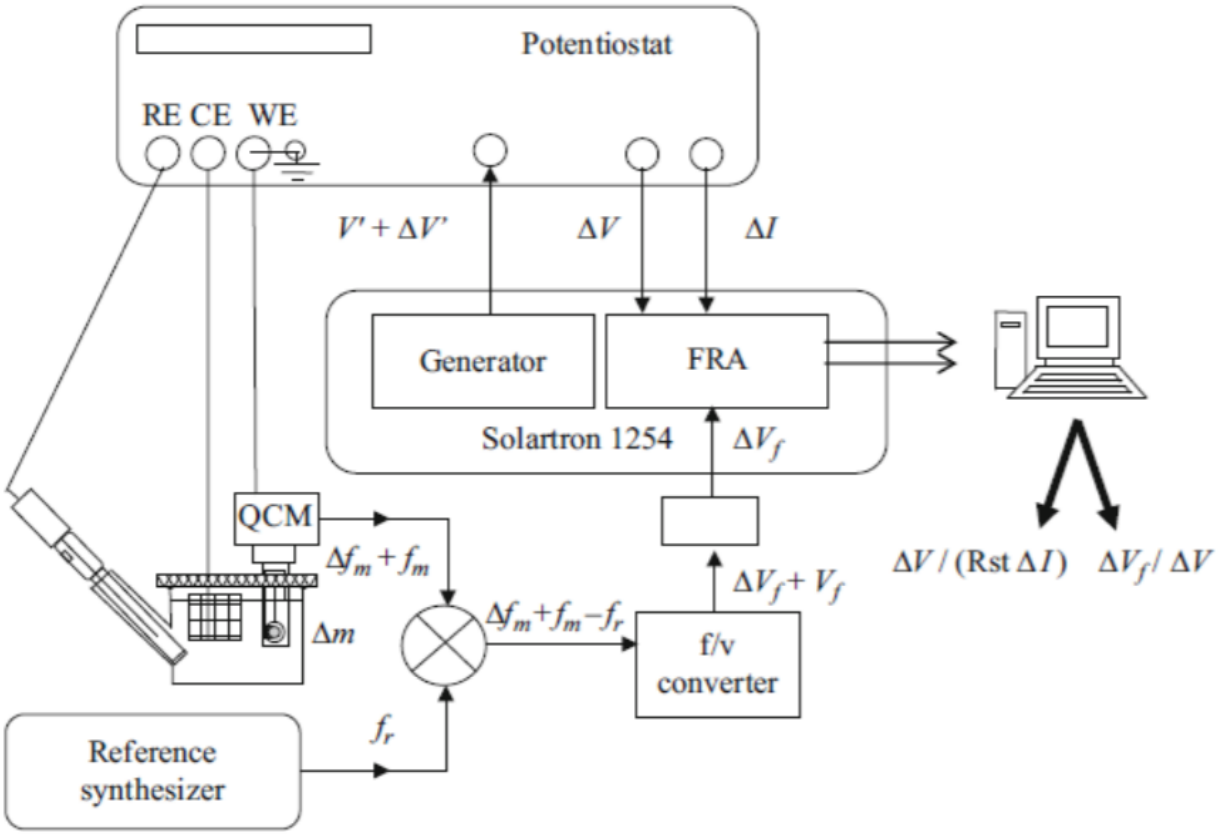

Figure 2.17: *ac*-electrogravimetric setup[201]

The experimental method (Fig. 2.17) consists of:

- An electrochemical cell with three electrodes and the working electrode acting also as a QCM,

- A PG-STAT 100 potentiostat,

- A FRA Solartron 1254, comprising a voltage generator (ΔV'),

- A Marconi 2023 reference frequency synthesizer,

- A frequency/voltage converter developed at the LISE laboratory (UMR 8235, Paris, France).

The working electrode is polarized by the potentiostat at a chosen potential V'_s. Then, the Solartron 1254 generator delivers a low amplitude sinusoidal perturbation ΔV' (superimposed to V') with modulation frequency

f. The signal from the microbalance f_m is detected by means of a lab-made frequency/voltage converter[202, 203] which subtracts a reference signal f_r, close to the frequency of the microbalance issued by the Marconi 2023 frequency synthesizer. Then, the f_m-f_r signal is converted into voltage V_f. If f_m varies, the converter delivers a voltage variation ΔV_f. The resulting signal ΔV_f and the current response ΔI of the working electrode are simultaneously sent to the FRA Solartron 1254, for the calculus of two transfer functions $\Delta V_f/\Delta V(\omega)$ and $\Delta V/R_t\Delta I(\omega)$.

ΔV is the raw potential response which takes into account the electrolyte resistance, and R_t is the resistance in the counter electrode circuit, which allows the current, ΔI to be measured. Usually, a 10^{-2} Hz to 60 kHz frequency range is used to measure these transfer functions.

2.3.4.3 Calibration and corrections of *ac*-electrogravimetry technique

Calibration is schemed in Fig. 2.18. Firstly, the experimental electrochemical impedance is estimated from the raw transfer function $\frac{\Delta V}{R_t \Delta I}(\omega)$ as:

$$\frac{\Delta E}{\Delta I}(\omega) = \left[\frac{\Delta V}{(\Delta I.R_t)} R_t\right] - R_e \qquad (2.11)$$

where R_t is the resistance used in the counter-electrode circuit, incorporated in the potentiostat for measuring the current, and R_e is the electrolyte resistance taken from the high frequency value of $\frac{\Delta V}{\Delta I}(\omega)$. As mentioned previously, the raw transfer function $\frac{\Delta V_f}{\Delta V}(\omega)$ given by the 1254 FRA must be corrected to obtain the final mass/potential transfer function $\frac{\Delta m}{\Delta E}(\omega)$ as:

$$\frac{\Delta m}{\Delta E}(\omega) = \frac{\Delta m}{\Delta f_m}(\omega)\frac{\Delta f_m}{\Delta V_f}(\omega)\frac{\Delta V_f}{\Delta V}(\omega)\frac{\Delta V}{\Delta E}(\omega) \qquad (2.12)$$

Four different transfer functions are distinguished:

- $\frac{\Delta m}{\Delta f_m}(\omega)$ related to the Sauerbrey equation, equals $-\frac{1}{k_s^{theor}}$ or $-\frac{1}{k_s^{exp}}$ where k_s^{exp} is the experimental mass/microbalance frequency factor. At 9 MHz, k^{exp}_s is equal to $16.3*10^{-7}$ Hz g^{-1} cm^2.[193]
- $\frac{\Delta f_m}{\Delta V_f}(\omega)$ is the inverse of the f/v converter sensitivity and is estimated using:

$\frac{\Delta f_m}{\Delta V_f}(\omega) = \frac{\Delta f_m}{\Delta e}(\omega)\frac{\Delta e}{\Delta V_f}(\omega)$, where $\frac{\Delta f_m}{\Delta e}(\omega) = \frac{\Delta f_s}{\Delta e}(\omega)$ is the sensitivity of the reference synthesizer by assuming $\Delta f_m = \Delta f_s$ and $\frac{\Delta e}{\Delta V_f}(\omega)$ is the inverse of the global calibration transfer function $\frac{\Delta V_f}{\Delta e}(\omega)$. It has been observed that the voltage perturbation during a calibration is $\Delta e = |\Delta e|.\sin(\omega t)$.

- $\frac{\Delta V_f}{\Delta V}(\omega)$ is the raw experimental transfer function obtained from the 1254 FRA.

- $\frac{\Delta V}{\Delta E}(\omega)$ allows the Ohmic drop correction by taking into account the electrolyte resistance R_e. The following relation is used by incorporating the experimental electrochemical impedance $\frac{\Delta E}{\Delta I}(\omega)$determined in the equation:

$$\frac{\Delta V}{\Delta E}(\omega) = \frac{R_e}{(\frac{\Delta E}{\Delta I})(\omega)} + 1 \qquad (2.13)$$

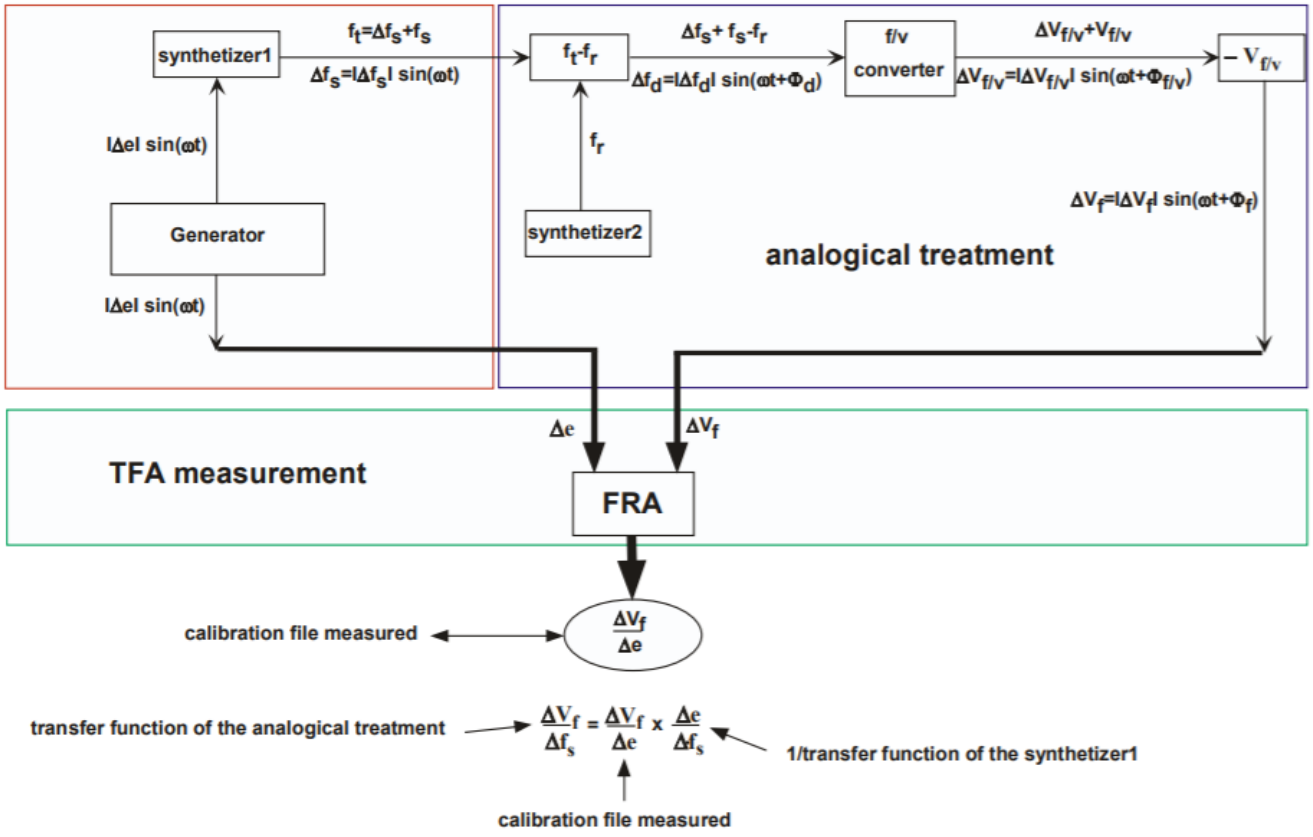

Figure 2.18: Scheme of the calibration of the frequency/voltage converter for determining the transfer function $\frac{\Delta V_f}{\Delta e}$

The Frequency/Voltage transfer function $\frac{\Delta V_f}{\Delta e}(\omega)$ is determined by the frequency synthesizer (Agilent 33205A): the signal Δe coming from the generator FRA 1254 permits the modulation of the frequency of the synthesizer Agilent 33205A and, also, the simulation of the frequency response from the microbalance. The global calibration transfer function $\frac{\Delta V_f}{\Delta e}(\omega)$ has been determined by Gabrielli *et al.* [201] to evaluate the sensitivity of the

frequency/voltage converter, to determine the linear frequency range and also, to measure the calibration file. Figure 2.18 shows the modulus and the phase of the global calibration transfer function $\frac{\Delta V_f}{\Delta e}(\omega)$. At low frequencies, the phase shift of $\frac{\Delta V_f}{\Delta e}(\omega)$is close to 0 and the modulus, $|\Delta V_f/\Delta e|$, is equal to 0.57. This result means that the dynamic sensitivity ($\Delta V_f/\Delta f_s$) dynamic of the system is 29 mV.Hz^{-1}.

The useable frequencies, that is, where the system can be used without any correction, ranges from low frequencies to 1 Hz for this particular configuration. If measurements are expected above 1 Hz, a modulus and phase shift correction is necessary by using calibration curves such as those given in Figure 2.19.

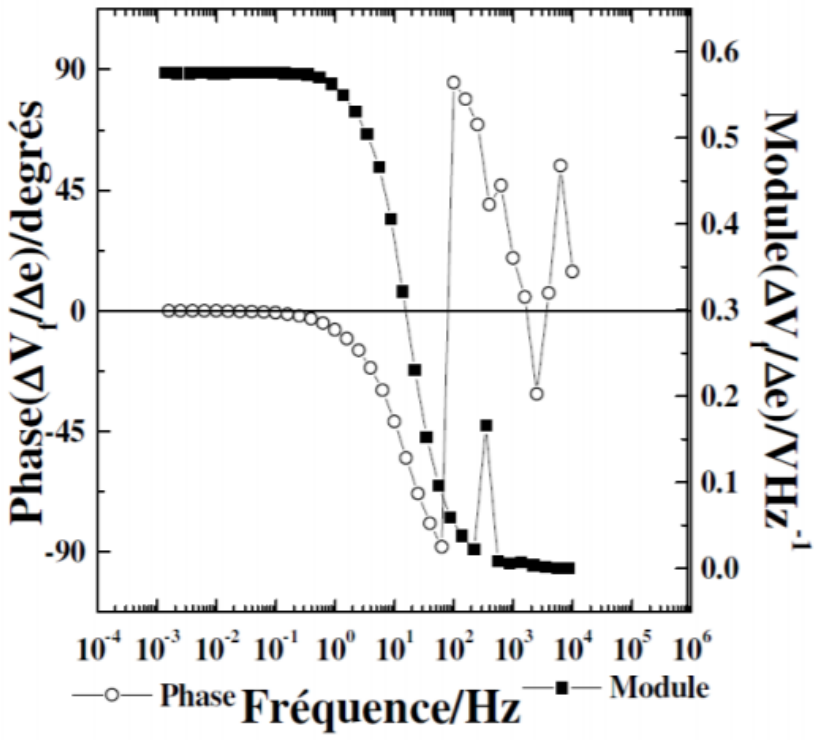

Figure 2.19: Modulus and phase of the global calibration of the frequency/voltage converter[201]

2.3.4.4 Calibration of Synthesizer: $\frac{\Delta f_s}{\Delta e}(\omega)$

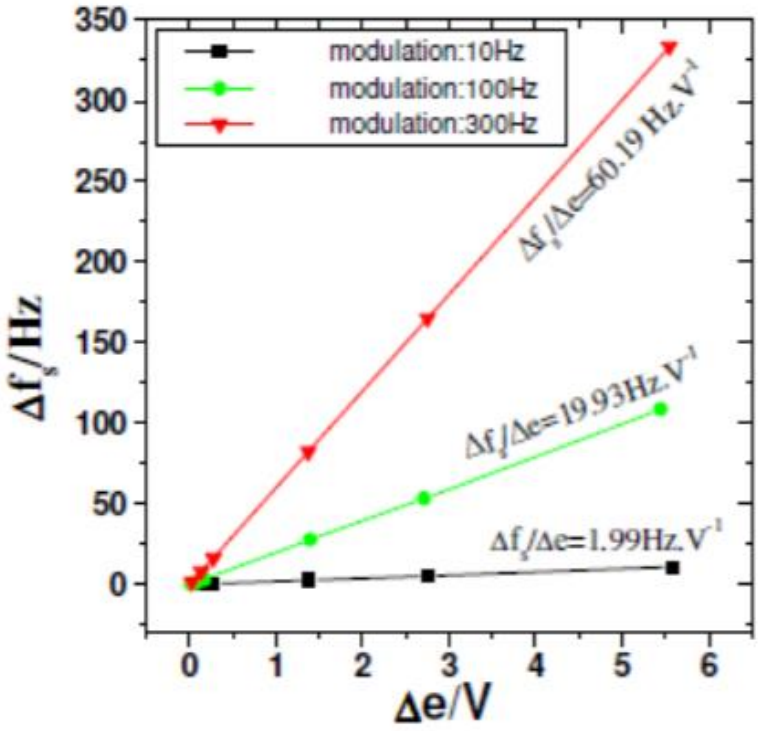

Figure 2.20: Measurements of the transfer function $\frac{\Delta f_s}{\Delta e}$ from the Agilent 33250A-synthesizer for three settings depth modulation (FM): 10 Hz, 100 Hz, 300 Hz

To Thi Kim[181] proposed a method to determine the transfer function $\frac{\Delta f_s}{\Delta e}(\omega)$ of the Agilent 33250A synthesizer used to simulate the QCM during the calibration procedure. To determine the transfer function of the synthesizer, the FRA 1254 generator must impose a fixed sinusoidal perturbation frequency f, in order to vary the amplitude Δe. The Agilent 33250A synthesizer was adjusted to a 9MHz carrier frequency equivalent to the frequency of the QCM used. Then, different tests were performed for three levels of modulation depth around the carrier frequency (FM mode) available on the Agilent 33250A: 10 Hz, 100 Hz and 300 Hz. A plot in Origin® allows the determination of Δe and Δf_s in a precise way at a given frequency modulation and, by selecting the three settings of modulation depth available on the synthesizer, three values for the transfer function $\frac{\Delta f_s}{\Delta e}$ can be obtained.

In this Ph.D thesis, the value $\Delta f_s/\Delta e = 19.93$ Hz.V^{-1} is used and the dynamic sensitivity $(\Delta V_f/\Delta f_s)_{dynamic}$ is calculated as:

$$\frac{\Delta V_f}{\Delta f_s}^{dynamic}_{\omega \to 0} = 0.57 * \frac{1}{19.9} = 28.6\ mV.Hz^{-1} \quad (2.14)$$

2.3.5 Data treatment of *ac*-electrogravimetry

2.3.5.1 Experimental data

From the experimental data, the transfer functions are calculated and taken into account in the fittings. Using the electrochemical impedance, the charge/potential TF is estimated with the function:

$$\left.\frac{\Delta q}{\Delta E}\right|_{exp}(\omega) = \frac{1}{j\omega}\left.\frac{\Delta I}{\Delta E}\right|_{exp} \quad (2.15)$$

The potential disturbance causes charge compensation within the film: species are transferred back and forth at the discretion of the sign (+ or -) of the disturbance signal.

Simultaneously, the reversible transfer of different species at the interface by potential disturbance provokes a sinusoidal variation of resonance frequency (*i.e.* mass variation of the deposited LDH) and enables the calculus of experimental electrogravimetric transfer function. The experimental partial transfer functions are calculated by eliminating the contribution of each of the charged species (an anion or a cation). For example, in a configuration where four species are taken into account: cation 1 (c_1), cation 2 (c_2), anion (a) and solvent (s), the contribution of each of the charged species are successively extracted from the global mass variation and compared with theoretical partial transfer functions. The extraction of the contribution of cation 1 is written as:

$$\left.\frac{\Delta m}{\Delta E}\right|^{c1as}_{exp}(\omega) = \left.\frac{\Delta m}{\Delta E}\right|_{exp} + \frac{m_{c2}}{F}\left.\frac{\Delta q}{\Delta E}\right|_{exp} \quad (2.16)$$

The extraction of the contribution of cation 2 is:

$$\left.\frac{\Delta m}{\Delta E}\right|^{c2as}_{exp}(\omega) = \left.\frac{\Delta m}{\Delta E}\right|_{exp} + \frac{m_{c1}}{F}\left.\frac{\Delta q}{\Delta E}\right|_{exp} \quad (2.17)$$

For the extraction of the anion, it comes:

$$\left.\frac{\Delta m}{\Delta E}\right|^{c1c2s}_{exp}(\omega) = \left.\frac{\Delta m}{\Delta E}\right|_{exp} + \frac{m_a}{F}\left.\frac{\Delta q}{\Delta E}\right|_{exp} \quad (2.18)$$

2.3.5.2 Fitting from Mathcad® simulation data

The fitting of the experimental TFs with the theoretical TFs (which will be described in the following) by using Mathcad® software (PTC Mathcad 15.0) allows the determination of pertinent information on the charge compensation process. The fitting procedure respects the strict criteria that a good agreement between the

experimental and the theoretical function in terms of shape and frequencies was achieved. Specifically, the fitting of the data (at each applied potential perturbation) is performed by calculating the electrochemical impedance, charge/potential transfer function, global and partial mass/potential transfer functions at different modulation frequencies with different parameter values. The parameter values, that are to be determined by fitting, provide relevant information on the ion transfer characterized by the K_i and G_i parameters and identify the nature of the involved species involved in terms of their molar mass m_i. Let us consider the following electroadsorption/desorption mechanism which can intervene in the electrochemical system:

$$< P > + e^- + C^+ \leftrightarrow < P, C^+ > \quad (2.19)$$

$$< P > + A^- \leftrightarrow < P, A^- > + e^- \quad (2.20)$$

where <P> represents a free site within or at the surface of the electroactive film, <P,C^+> is the site occupied with a monovalent cation and <P,A^-> is the site occupied with a monovalent anion. The k_i are related to the transfer kinetic rates. Then, the instantaneous flux of each species J_i can be written as follows:

For a cation:

$$J_c = d_f(k_{c1}(C_{c+,max} - C_{c+})[C^+]_{sol} - k_{c2}(C_{c+} - C_{c+,min})) \quad (2.21)$$

For an anion:

$$J_a = -d_f(k_{a1}(C_{A-,max} - C_{A-})[A^-]_{sol} - k_{a2}(C_{A-} - C_{A-,min})) \quad (2.22)$$

where C_i is the concentration in the film of cations or anions associated to the P sites, $C_{i,max}$ is the maximum concentration of P sites occupied in the film by cations or anions, and $C_{i,min}$ is the minimum concentration of P sites occupied by cations or anions. Under the effect of a sinusoidal potential perturbation, ΔE, imposed at the film/electrolyte interface, sinusoidal concentration fluctuations, ΔC_i and flux J_i are observed (with i = c_1, c_2, a or s) in the following form:

$$\Delta J_i = -d_f \frac{d(\Delta C_i)}{dt} \quad (2.23)$$

where d_f is the film thickness, ΔJ_i is the variation of the flux related to the species i crossing the film/electrolyte interface (mol.m^{-2}.s^{-1}) and ΔC_i is the variation of the concentration in the film (mol.m^{-3}). In dynamic regime, the flux change ΔJ_i is function of the potential E and the concentration of the species ΔC_i can also be written as:

$$\Delta J_i = \frac{\partial J_i}{\partial C_i}\Delta C_i + \frac{\partial J_i}{\partial C_i}\Delta E = K_i \Delta C_i + G_i \Delta E \quad (2.24)$$

Then, the $\left.\frac{\Delta C_i}{\Delta E}\right|_{th}$ transfer function can be calculated using the equations (23) and (24):

$$\left.\frac{\Delta C_i}{\Delta E}\right|_{th}(\omega) = \frac{-G_i}{(j\omega d) + K_i} \quad (2.25)$$

with $K_i = (\frac{\partial J_i}{\partial C_i})$ and $G_i = (\frac{\partial J_i}{\partial E})$ (2.26)

where $\omega = 2\pi f$ is the pulsation, f is the frequency of potential modulation and K_i and G_i are the partial derivatives of the flux with respect to concentration and potential, respectively.

Then, the "virtual" transfer function given in equation (2.25) allows the calculation of all the other measured transfer functions. Thus, the following theoretical expressions have been used to fit all the experimental transfer functions. From the equation (2.25) and considering four species involved in the electrochemical process (i = c_1, c_2, a and s), the following equations can be listed:

$$\frac{\Delta C_{c1}}{\Delta E}\Big|_{th}(\omega) = -\frac{G_{c1}}{(j\omega d_f) + K_{c1}} \quad (2.27)$$

$$\frac{\Delta C_{c2}}{\Delta E}\Big|_{th}(\omega) = -\frac{G_{c2}}{(j\omega d_f) + K_{c2}} \quad (2.28)$$

$$\frac{\Delta C_{a}}{\Delta E}\Big|_{th}(\omega) = -\frac{G_{a}}{(j\omega d_f) + K_{a}} \quad (2.29)$$

$$\frac{\Delta C_{cs}}{\Delta E}\Big|_{th}(\omega) = -\frac{G_{s}}{(j\omega d_f) + K_{s}} \quad (2.30)$$

2.3.5.3 Charge/potential transfer function

The charge/potential transfer function $\frac{\Delta q}{\Delta E}\Big|_{th}(\omega)$ calculated for the adsorption/desorption of two cations c_1 and c_2 and an anion a, using the Faraday number F can be written as follows:

$$\frac{\Delta q}{\Delta E}\Big|_{th}(\omega) = -d_f F(\frac{\Delta C_{c1}}{\Delta E} + \frac{\Delta C_{c2}}{\Delta E} - \frac{\Delta C_{a}}{\Delta E}) \quad (2.31)$$

Replacing the equations (2.25) with the equation (2.31) gives:

$$\frac{\Delta q}{\Delta E}\Big|_{th}(\omega) = d_f F(\frac{G_{c1}}{(j\omega d_f)+K_{c1}} + \frac{G_{c2}}{(j\omega d_f)+K_{c2}} - \frac{G_{a}}{(j\omega d_f)+K_{a}}) \quad (2.32)$$

2.3.5.4 Electrochemical impedance

The theoretical electrochemical impedance can be calculated as follows:

$$\left.\frac{\Delta q}{\Delta E}\right|_{th}(\omega)=\frac{1}{j\omega}\frac{\Delta I}{\Delta E}=d_f F\left(-\frac{\Delta C_{c1}}{\Delta E}-\frac{\Delta C_{c2}}{\Delta E}+\frac{\Delta C_a}{\Delta E}\right) \quad (2.33)$$

Replacing the equation (2.25) with the equation (2.33) gives:

$$\left.\frac{\Delta E}{\Delta E}\right|_{th}(\omega)=\frac{1}{j\omega d_f F\left(\frac{\Delta G_{c1}}{(j\omega d_f)+K_{c1}}+\frac{\Delta G_{c2}}{(j\omega d_f)+K_{c2}}-\frac{\Delta G_a}{(j\omega d_f)+K_a}\right)} \quad (2.34)$$

In theory, if faradic reactions are present, the theoretical Faradaic impedance $Z_F|_{th}(\omega)$ should be taken into account.

2.3.5.5 Electrogravimetric transfer function

The theoretical electrogravimetric transfer function, $\left.\frac{\Delta m}{\Delta E}\right|_{th}$, can be calculated, taking into account the charged/uncharged species contribution:

$$\left.\frac{\Delta m}{\Delta E}\right|_{th}(\omega)=d_f\left(m_{c1}\frac{\Delta C_{c1}}{\Delta E}-m_{c2}\frac{\Delta C_{c2}}{\Delta E}+m_a\frac{\Delta C_a}{\Delta E}+m_s\frac{\Delta C_s}{\Delta E}\right) \quad (2.35)$$

Then, replacing the equation (2.25) with the equation (2.35) results in:

$$\left.\frac{\Delta m}{\Delta E}\right|_{th}(\omega)=d_f\left(m_{c1}\frac{\Delta G_{c1}}{(j\omega d_f)+K_{c1}}-m_{c2}\frac{\Delta G_{c2}}{(j\omega d_f)+K_{c2}}+m_a\frac{\Delta G_a}{(j\omega d_f)+K_a}+m_s\frac{\Delta G_s}{(j\omega d_f)+K_s}\right) \quad (2.36)$$

where m_{c1}, m_{c2}, m_a and m_s are the atomic weight of involved species. From the theoretical overall electrogravimetric transfer function (2.36), it is possible to calculate the theoretical partial transfer functions by removing the c_2 contribution, calculating $\left.\frac{\Delta q}{\Delta E}\right|_{th}^{c1as}(\omega)$ or the c_1 contribution, calculating; $\left.\frac{\Delta q}{\Delta E}\right|_{th}^{c2as}(\omega)$ or the anion contribution, calculating $\left.\frac{\Delta q}{\Delta E}\right|_{th}^{c1c2s}(\omega)$; as shown in the following equations:

$$\left.\frac{\Delta m}{\Delta E}\right|_{th}^{c1as}(\omega)=-d_f\left[(m_{c1}-m_{c2})\frac{\Delta C_{c1}}{\Delta E}+(m_a-m_{c2})\frac{\Delta C_a}{\Delta E}+m_s\frac{\Delta C_s}{\Delta E}\right)] \quad (2.37)$$

$$\left.\frac{\Delta m}{\Delta E}\right|_{th}^{c2as}(\omega)=d_f\left[(m_{c2}-m_{c1})\frac{\Delta C_{c1}}{\Delta E}+(m_a-m_{c1})\frac{\Delta C_a}{\Delta E}+m_s\frac{\Delta C_s}{\Delta E}\right)] \quad (2.38)$$

$$\left.\frac{\Delta m}{\Delta E}\right|_{th}^{c1c2s}(\omega)=d_f\left[(m_{c1}-m_{c2})\frac{\Delta C_{c1}}{\Delta E}+(m_{c2}-m_{c1})\frac{\Delta C_{c2}}{\Delta E}+m_s\frac{\Delta C_s}{\Delta E}\right)] \quad (2.39)$$

Chapter 3

Deepening the insight into the assisted electrodeposition mechanisms of Layered Double Hydroxides by EQCM technique for assisted electrosynthesis and electrochemical behavior investigation of Ni/Fe-based LDH

3.1 Introduction

Layered Double Hydroxides (LDHs) are a class of anionic clays whose structure is based on Brucite ($Mg(OH)_2$)-like layers, in which some of the divalent cations ($M^{(II)}$) were replaced by trivalent ones ($M^{(III)}$), resulting in positively-charged octahedral layers.[204,16] The main properties of LDH compounds are thus directly linked to their composition,[21] structure, and morphology. Indeed, the broad versatility of metallic cations (Fe, Mg, Al, Ni, Co…) in the octahedral layers, combined with a charge density related to the $M^{(II)}/M^{(III)}$ ratio in the Brucite layers[204,16,205] results in anionic clays. These have a large range of Anion Exchange Capacity ($200 < AEC_{meq/100\ g} < 400$) as well as a wide variety of anions in their interlayers.[16,206]

The literature shows several methods for synthesizing a broad range of particle sizes ($1nm<d<10\mu m$) of LDH with various morphologies[16,77,207] leading to a large spectrum of specific surface area values up to ~100 m²/g. For these reasons, LDHs have attracted significant interest for industrial and environmental applications.[208,120,209,210,211,212,213]

Low electronic conductivity LDH is the pivotal obstacle for the development of breakthrough electrochemical processes. The low electronic conductivity of LDHs[214] is claimed to be supplied by preparing thin films of LDH onto a working electrode surfaces (glassy carbon, platinum, gold, indium tin oxide (ITO)…) using different methods like solvent casting, layer-by-layer assembly or electrochemically assisted deposition.[99,161,215,216] For an enhanced adherence and electron transfer onto the electrode, LDH clays can be obtained in an ”indirect electrochemical” manner in the presence of any compound whose electrochemical reduction provides hydroxyl ions (OH^-).[217,218] Reduction of water ($H^{(I)}/H^{(O)}$), dissolved oxygen ($O^{(O)}/O^{(-II)}$), or nitrate ions ($N^{(V)}/N^{(at\ the\ least\ IV)}$)

can supply the required hydroxyls to form these clays, but in practice LDH synthesis essentially takes place via nitrate reduction.

Indira and Kamath in 1994[106] were the first authors to report that kind of electro-assisted deposition method for the synthesis of Co/Al-LDH and Ni/Al-LDH 3:1. The electrochemical reduction of nitrate is nevertheless a complex reaction that can involve different mechanism involving a large number of intermediates and nitrogen compounds. The electrochemical transformation activity and selectivity to the desired products of nitrate are first of all highly dependent on the cathode material. [109,110,111] In most of the publications, LDHs were synthesized under potentiostatic conditions using Pt electrodes. In order to enhance nitrate sorption and limit hydrogen adsorption onto the cathode electrode, the electro-assisted deposition was also performed onto ITO,[113] glassy carbon,[114] gold,[115] FeCrAlloy[116] and Ni metal[117]. Some authors use the deposition of nanomaterials on electrode surface, *i.e.* copper nanoparticles modified gold electrodes, Cu/Pd bimetallic properties modified BDD (boron doped diamond), Cs (solid carbon) nanoparticles and polypyrrole (PP) nanowires modified gold electrodes which increases the sensitivity of the electrode response by maintaining a large and highly active surface area.[112]
Whatever the investigated cathode material and the electrochemical route, the OH^- kinetic production at the interface is a parameter of prime importance.[34] According to low production of OH^-, the LDH should be synthesized onto the electrode in two steps: the first one is the precipitation of the cation having the highest complexation coefficient for hydroxyl and the second is the formation of the LDH from the reaction between the hydroxyde initially formed and this other cation present in the electrolyte. If the production of OH^- is fast, the LDH is formed in one step, with the concomitant precipitation of both metallic cations in the stoechiometric proportions of the synthesis solution. The later conditions is claimed to anable the synthetisis of uniform films of LDHs. For this purpose and for the deposition of pure and well-ordered LDH, the optimization of the applied potentiel, the time deposition, the divalent/trivalent metallic cations ratio, the supporting electrolyte and initial pH value is of a prime importance. For example, as notified by Tonelli's group,[35] tuning the thickness and morphology of the deposited film are controlled by monitoring of the potential and the polarization time. After 60 seconds at -0.66 V/SHE, in a solution with total concentration of $Ni(NO_3)_2$ and $Al(NO_3)_3$ of 0.03 mol/L with different Ni/Al molar ratios and a KNO_3 concentration of 0.3 mol/L, a Pt electrode is fully covered with an homogeneous and dense Ni-Al-LDH film of thickness 150 nm. The sand rose morphology is composed of nanoparticles whose size is lower than 50 nm, connected in a gel-like manner. For longer polarization time, particles have larger size and higher thickness. Otherwise, according to Yarger *et al.*[115] considering Zn/Al-LDH, increasing or decreasing the aluminum concentration in the plating solution resulted in the formation of aluminum or zinc containing impurities respectively, instead of varying aluminum content incorporated into the LDH phase. A more negative potential provokes the deposition of zinc metal or zinc hydroxide, and a less negative potential provokes the deposition of zinc oxide. Increasing the pH destabilizes the formation of the LDH phase, while decreasing pH promotes the deposition of other impurities. It is therefore of prime interest to investigate the

formation mechanism of the LDH during the assisted electrochemical method for further electrochemical applications.

The aim of this chapter is to deepen the insight into the formation mechanism of a Ni/Fe-LDH on gold electrode and to examine all the reactions that take place during imposition of a cathodic potential by cathodic sweep. For this aim, we seek the different steps of reduction/precipitation of the species (nitrates, water and metal cations) by coupling electrochemical and gravimetric techniques (EQCM, *ac*-electrogravimetry) in nitrate and chloride supporting electrolytes. The oxidation state of the metal cations is evidenced. A special attention is paid on the assisted electrodeposition of Ni/Fe-LDH 6/2 that is known to be one of the most conductive LDHs, which enhances oxygen evolution reaction (OER) catalysis and applications in batteries.[99]

3.2 Insights into the understanding of the assisted electrochemical synthesis

3.2.1 Electrolyte preparation and EQCM measurements

To isolate the mechanism of each metallic cation in the presence of nitrates during the electro-assisted deposition, three aqueous electrolytes were prepared:

- Blank solution of KNO_3 $5 \cdot 10^{-1}$ mol/L in which HNO_3 was added to reach pH 2.5
- Electrolyte composed of $Fe(NO_3)_3$ $4 \cdot 10^{-3}$ mol/L and KNO_3 $4.88 \cdot 10^{-1}$ mol/L (pH 2.5), thus containing Fe^{3+} $4 \cdot 10^{-3}$ mol/L, NO_3^- $5 \cdot 10^{-1}$ mol/L, K^+ $4.88 \cdot 10^{-1}$ mol/L and H^+ $3.16 \cdot 10^{-3}$ mol/L
- Electrolyte composed of $Ni(NO_3)_2$ $1.2 \cdot 10^{-2}$ mol/L and KNO_3 $4.76 \cdot 10^{-1}$ mol/L in which HNO_3 was added to reach pH 2.5, thus containing Ni^{2+} $1.2 \cdot 10^{-2}$ mol/L, NO_3^- $5 \cdot 10^{-1}$ mol/L, K^+ $4.76 \cdot 10^{-1}$ mol/L and H^+ $3.16 \cdot 10^{-3}$ mol/L

To understand the formation mechanism of the Ni/Fe-LDH with ratio Ni(II)/Fe(III)=6/2, both metal cations were added in the solution of nitrates with the accurate stoichiometry according to: $Ni(NO_3)_2$ $1.2 \cdot 10^{-2}$ mol/L + $Fe(NO_3)_3$ $4 \cdot 10^{-3}$ mol/L + KNO_3 $4.64 \cdot 10^{-1}$ mol/L (pH 2.5), thus it contains Fe^{3+} $4 \cdot 10^{-3}$ mol/L, Ni^{2+} $1.2 \cdot 10^{-2}$ mol/L, NO_3^- $5 \cdot 10^{-1}$ mol/L, K^+ $4.64 \cdot 10^{-1}$ mol/L.

To understand the effect of nitrates, three other solutions were prepared replacing NO_3^- by Cl^-. HCl was added in chloride-based electrolytes to reach a pH of 2.5 (pH value of solutions containing Fe^{3+}) for a better comparison of data obtained in nitrate and chloride-based electrolytes.

EQCM measurements were conducted in a 3-electrode cell configuration, described in section 2.3.2.2. The reference electrode was mercury-mercurous sulfate electrode, and the potential was compared to SHE electrode. The quartz polarization was conducted from 0.8 V to -1.3 V/SHE at 10 mV/s after electrolyte de-aeration with N_2 gas. The electrochemical and gravimetrical responses were analyzed. The applied potential used to deposit the LDH is lower than the potential of Fe(III) reduction into Fe(II). Let us record that the only specie that reaches the

diffusion layer from the solution is Fe(III). Therefore, depending on the physico-electrochemical conditions at the electrode interface, the Fe species present at the electrode are either Fe(II) or/and Fe(III) ions. That will be discussed thereafter.

3.2.2 PhreeqC simulations

PhreeqC Interactive Version 3.5.0.14000 (released Febr. 14, 2019),[219] a United States Geological Survey (USGS) Computer Program for Speciation, Batch-Reaction, One-Dimensional Transport, and Inverse Geochemical Calculations was used for calculating predominant species concentrations from theoretical speciation at several pH values, as following:

- Predominant Fe(II) speciation in the presence of nitrate *versus* pH values and, for comparison, in the presence of chloride,
- Predominant Ni (II) speciation in the presence of nitrate *versus* pH values and, for comparison, in the presence of chloride,
- Both Fe(II) and Ni (II) speciations in the presence of nitrate *versus* pH values and, for comparison, in the presence of chloride.

The thermodynamic data base used was llnl.dat.

3.2.3 Results and discussion

3.2.3.1 Blank solutions of KCl and KNO_3

Figure 3.1A shows the current-potential (I-V) curves of blank aqueous solutions KCl $5 \cdot 10^{-1}$ mol/L and KNO_3 $5 \cdot 10^{-1}$ mol/L (at pH 2.5) (black and blue curves, respectively). In both solutions a reduction current peak named 1 is noticed.

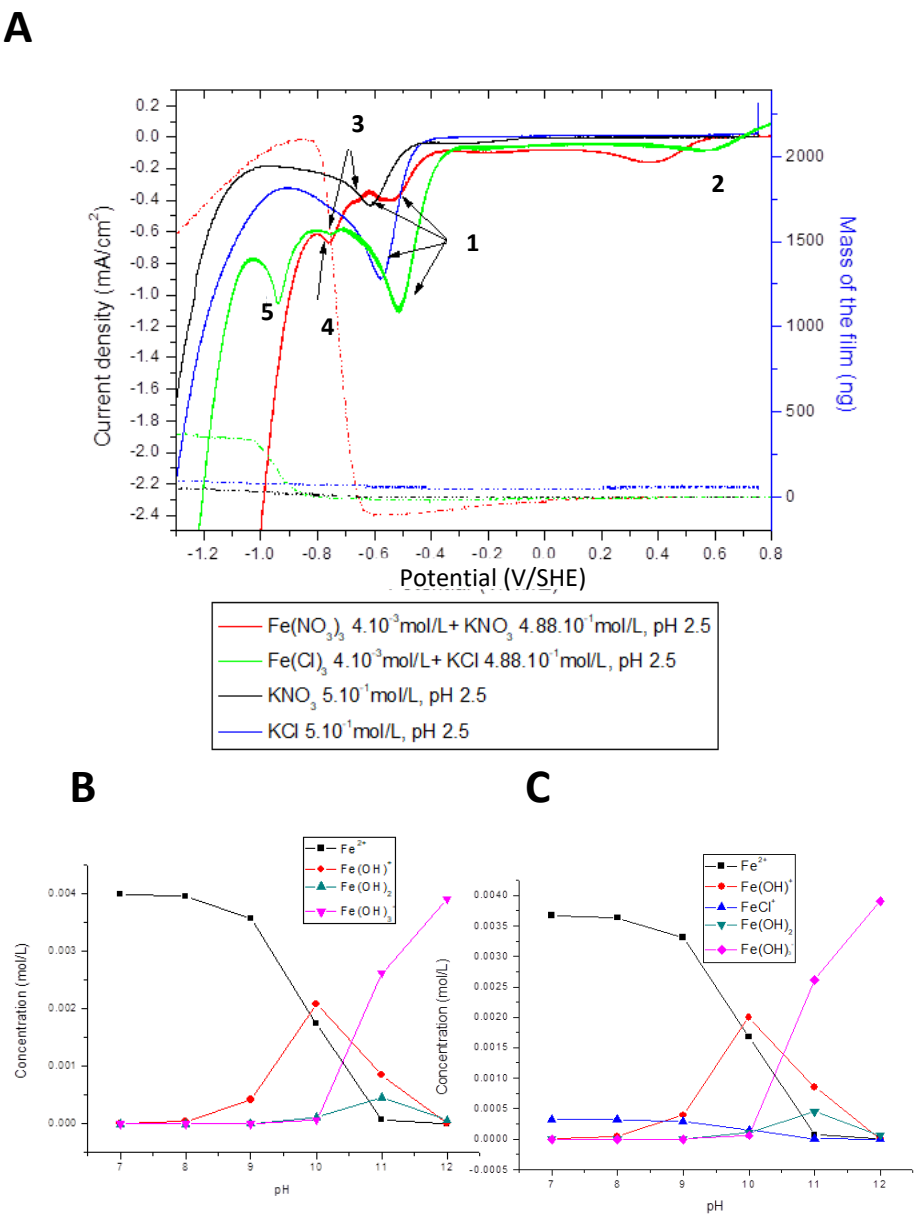

Figure 3.1: (A) I-V curve and m-V curve of Fe(III) solutions with nitrates (red curve) or chlorides (green curve) from 0.8 V/SHE and -1.3 V/SHE. PhreeqC simulations of the (B) speciation of Fe(II) in nitrate *versus* pH and the (C) speciation of Fe(II) in chloride *versus* pH value.

Current peak observed at -0.6V is ascribed to H^+ reduction according to (eq. 3.1), which is asserted as this peak gets more intense when the pH decreases (Fig 3.2).

$2H^+ + 2\ e^- \rightarrow H_2$, $E° = 0.000V/SHE$ (3.1)

It is also noticed that peak 1 is twice more intense in chloride solution than in nitrate solution. This phenomenon should be caused by a more anodic consumption of H^+ in the slow kinetics of nitrate reduction at 0.01V/SHE (eq. 3.2) that decreases the interfacial H^+ concentration.[109,110]

$NO_3^- + H_2O + 2e^- \rightarrow NO_2^- + 2OH^-$ (3.2)

From the potential at peak 1 and for more negative potentials, the pH should increase dramatically in both solutions. The hydrogen evolution reaction (HER) starts at around -1 V in KCl and is more cathodic in the KNO_3 solution as the pH is more basic, due to the nitrate reduction (eq. 3.2).

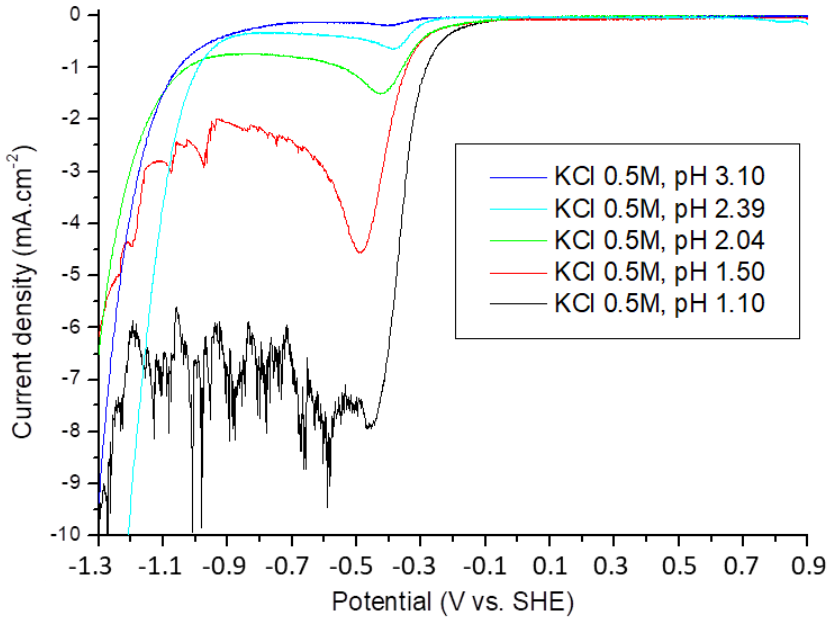

Figure 3.2: Increase of the current peak 1 with the decrease in pH in KCl 0.5 mol/L

3.2.3.2 Aqueous solutions of ferric ions in the presence of NO_3^- or Cl^-

In Fe^{3+} solutions (ferric iron nitrates or chlorides), pH value is 2.5 as Fe^{3+} is a Lewis acid (pKa=9.3-9.5).[220] Figure 3.1A shows the I-V curve in ferric solution $4 \cdot 10^{-3}$mol/L in presence of K^+ $4.88 \cdot 10^{-1}$mol/L and Cl^- (green curve) or NO_3^- $5 \cdot 10^{-1}$mol/L (red curve). In both solutions, H^+ reduction characteristic peak numbered 1 (also visible in the blank solutions) is still noticed. It is nevertheless more anodic in ferric solutions, than in blank solutions. That can be attributed to the diffusion (and thus the reduction) at the interface of the H^+ related to the complexation of Fe^{3+} with H_2O in agreement with the acidity properties of Fe^{3+} (eq. 3.3).

$Fe^{3+} + H_2O \rightarrow Fe(OH)^{2+} + H^+$ (3.3)

Compared to blank solutions, 4 additional cathodic current peaks 2, 3, 4 and 5 (figure 1A, red and green curves) are iron species related. The less cathodic peak, peak 2, between 0.2V and 0.65V/SHE, is observed without any deposition onto the electrode (no mass variation). A fast calculated redox potential $E(Fe^{3+}/Fe^{2+})$ in the experimental conditions using Nernst equation $E = E°(Fe^{3+}/Fe^{2+}) + 0.06 \cdot \log(Fe^{3+})$ is 0.626V/SHE, which is close

to the potential value of peak 2. Thus, this peak is related to the $Fe^{(III)}$ ions at the interface. The presence of nitrate ions in nitrate-based electrolytes shifts peak 3 versus more cathodic potentiels due to the complexation of part of Fe^{3+} in agreement with PhreeqC simulations (eq. 3.4):

$$Fe(OH)^{2+} + H^+ + NO_3^- \rightarrow Fe(NO_3)^{2+} + H_2O \quad (3.4)$$

In agreement with PhreeqC simulations at pH 2.5, the two reduction plateaus observed after peak reduction 2 are characteristics of the Fe^{2+} diffusion plateaus.

Let us now investigate peaks 3, 4 and 5 which are localized more catholically than peak 1. In the electrolytic solution of nitrates, depending on pH value, the produced ferrous ions, Fe^{2+}, at the interface can be complexed with H_2O. PhreeqC simulations clearly show (Fig. 3.1B) that free cation Fe^{2+} is predominant at pH 9 and below. At pH 10, the soluble ferrous complex cationic form $Fe(OH)^+$ is predominant according to the reaction 3.5:

$$Fe^{2+} + H_2O = \mathbf{Fe(OH)}^+ + H^+ \quad (3.5)$$

This reaction can be favored when the potential is more cathodic than the reduction potential of free H^+ (peak 1) at around -0.55V. The generated H^+ (reaction (3.5)) are reduced (peak 3). At pH 11, the soluble ferrous complex anionic form $Fe(OH)_3^-$ becomes predominant according to the reaction with equation (3.6):

$$FeOH^+ + 2H_2O = \mathbf{Fe(OH)_3}^- + 2H^+ \quad (3.6)$$

This reaction produces $2H^+$ that are reduced (peak 4, more intense than peak 3). From pH 9, $Fe(OH)_{2(s)}$ (pK_{sp} = 14.095 at 273.15K) and FeO have reached their saturation level respectively according to reaction (3.7) and (3.8):

$$Fe^{2+} + 2OH^- = \mathbf{Fe(OH)_2} \quad (3.7)$$

$$Fe^{2+} + H_2O = FeO_{(s)} + 2\,H^+ \;;\; \log k = -13.531 \quad (3.8)$$

According to pHreeqC simulations, $Fe(OH)_2$ is also partly soluble at the interface from this pH (and is more than 10^{-4} mol/L from pH 10). Thus, both the Fe(II) hydroxide and oxide can be deposited at the interface as interfacial pH is increasing (as Fe(II) oxy- hydroxide). This pH should be reached from peak 3. That is why the mass of the film starts to increase dramatically at the same potential. It is noticed that the mass of the film becomes constant at a potential close to that of peak 4. The reason is perhaps due to the predominant speciation of ferrous complex anionic form $Fe(OH)_3^-$ at high pH, which prevents the formation of Fe(II) oxy- hydroxide. Moreover, both the increase in cathodic potentials and the increase in pH in agreement with NO_3^- (and H_2O) reduction reaction(s) are responsible for the decrease in the deposited mass in agreement with both Fe(II) oxy- hydroxide redissolution (at

the interface between the coating and the electrolyte) and dehydration (at the interface between the coating and the gold surface, in agreement with bibliography.[218,221] With regard to $FeCl_3$/HCl-based electrolyte, the pH value increase is firstly only responsible for continuous free H^+ reduction that starts from peak 1 when cathodic potential is applied. Thus, the pH value increases more slowly at the interface in the presence of chlorides than in the presence of nitrates. That is the reason why peak 3 associated with H^+ reduction reaction in agreement with eq. 3.5 (and in agreement with $Fe^{(II)}$ speciation in the pH value ranging from 8 < pH<10) is shown at more cathodic potential in chloride-based than in nitrate-based electrolyte. In agreement with PhreeqC simulations, peak reduction 5 is responsible for the reduction of Fe^{+II} to Fe^0 (zero-valent iron), according to reaction 3.9:

$$Fe^{+II} + 2e^- = Fe^0 \quad (3.9)$$

where Fe(+II) represents all soluble species of ferrous iron.

At this potential, the film mass increases and does not reach a plateau. In the same range of potential, but in the presence of nitrates, the ferrous ion species reduction to Fe^0 should also occur but cannot be seen because of the HER. However, the predominant speciation of ferrous complex anionic form $Fe(OH)_3^-$, in the pH range above 12, could minimize/prevents the reduction of Fe(II) to Fe°; *i.e* the $Fe(OH)_3^-$ complex should render Fe(II) reduction more cathodic (i.e Fe(II) reduction should shift towards the more cathodic potentials).

3.2.3.3 Aqueous solutions of Ni^{2+} in the presence of NO_3^- or Cl^-

Ni^{2+} is a Lewis acid (pKa=9.86)[220] (however weaker than Fe^{3+} ; pKa=9.30-9.50). That is why, in Ni^{2+} solutions in the presence of nitrates or chlorides, pH was decreased down to 2.5 by adding HNO_3 or HCl, respectively. Figure 3.3A shows the I-V curve in Ni^{2+} $1.2 \cdot 10^{-2}$mol/L solution in the presence of K^+ $4.76 \cdot 10^{-1}$mol/L and Cl^- (green curve) or NO_3^- $5 \cdot 10^{-1}$mol/L (red curve). In both solutions, peak 1 is characteristic of free H^+ reduction. It is less cathodic in Ni^{2+} solutions than in blank solutions. Compared to the blank solutions, 2 additional cathodic current peaks 6 and 7 (figure 3.3A) are characteristic of the nickel related species.

Below -0.4V/SHE, the interfacial pH increases due to continuous free H^+ reduction (that starts from peak 2). PhreeqC simulation (Fig. 3.3B and 3.3C) shows that free cation Ni^{2+} is predominant at pH 9 and below in the presence of nitrates and chlorides. In nitrates, 23% of the Ni^{2+} is complexed by NO_3^-. In chlorides, only 1.3% of the Ni^{2+} is complexed by Cl^-. From pH 9 to pH 11, the soluble complex cationic form $Ni(OH)^+$ is predominant according to reaction 3.10:

$$Ni^{2+} + H_2O = \mathbf{Ni(OH)^+} + H^+. \quad (3.10)$$

In chloride solution, peak 7 (at -0.6V/SHE) is characteristic of the reduction of the generated H^+. This peak is more cathodic in nitrate solution, probably because it takes more time to increase the interfacial pH due to the speciation with nitrates. This reaction is noticed at -0.65V/SHE.

At pH 12, the soluble complex anionic form $Ni(OH)_3^-$ is predominant according to reaction 3.11:

$$Ni^{2+} + 3H_2O = \mathbf{Ni(OH)_3^-} + 3H^+ \quad (3.11)$$

The three generated H^+ are reduced (peak 7). This event occurs at the same potential for chloride as for nitrate solutions, however with higher intensity in chloride. The production of $Ni(OH)_3^-$ is thus intense.

According to PhreeqC, from pH 8, $Ni(OH)_{2(s)}$ (pK_{sp}= 15.251 at 273.15K) and Bunsenite or $NiO_{(s)}$) (log k = -12.4719) have reached their saturation level according to reactions 3.12 and 3.13:

$$Ni^{2+} + 2OH^- = Ni(OH)_2 \quad (3.12)$$

$$Ni^{2+} + H_2O = NiO_{(s)} + 2H^+, \text{ with } \log k = -12.4719 \quad (3.13)$$

The aqueous soluble form of $Ni(OH)_2$ is also present from pH 11. Thus, both precipitates can be deposited at the interface as interfacial pH is increasing. The large increase in mass from 0.6 to 0.9V/SHE is in agreement with the attainment of the pH value of 11. The high intensity of peak 8 in the presence of chlorides may be the reason why the deposited mass is lower compared to that in nitrate solution. There was probably not enough diffused $Ni^{(II)}$ species present at in the interface to precipitate.

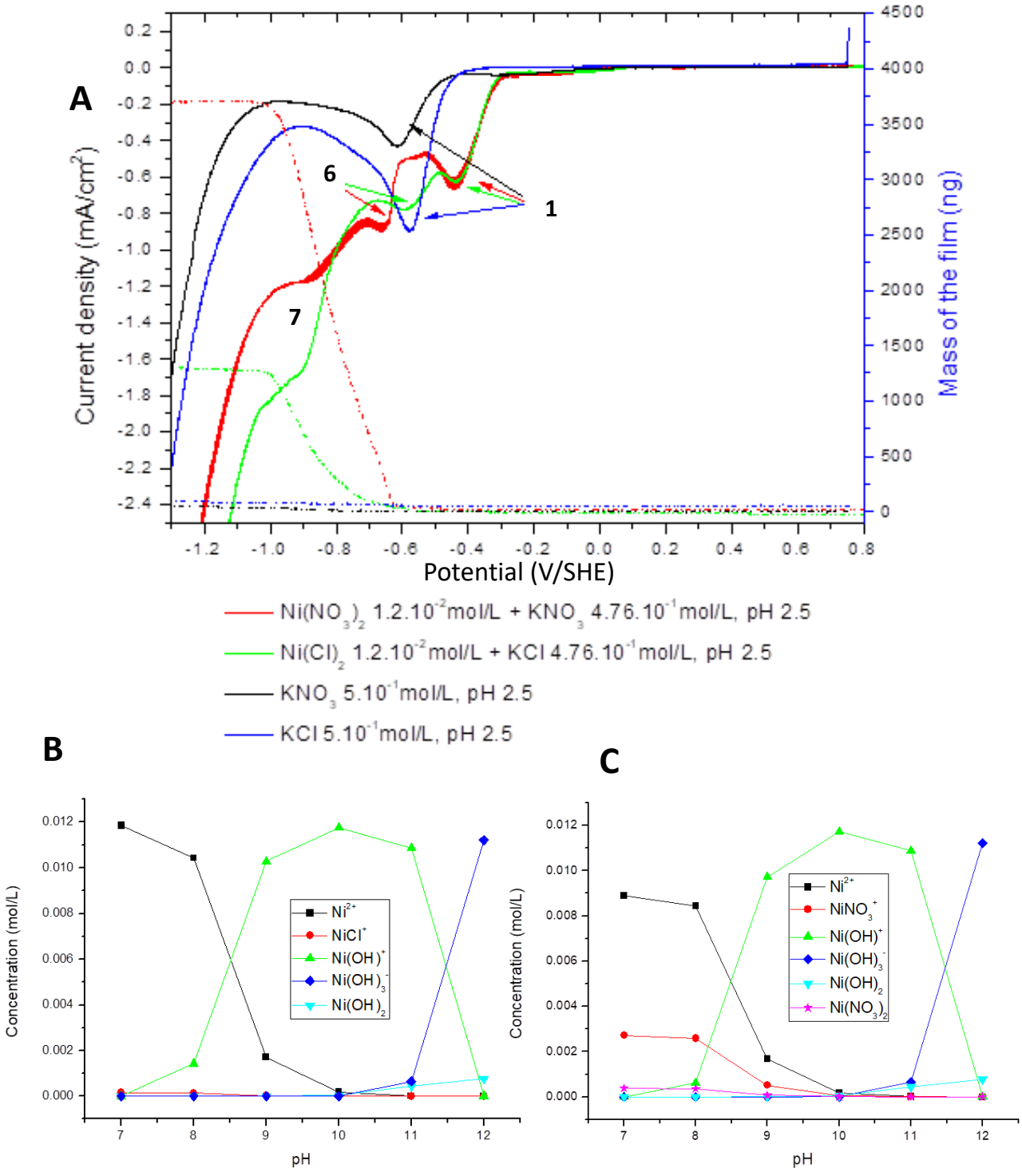

Figure 3.3: (A) I-V and m-V curve of Ni(II) solutions with nitrates (red curve) or chloride (green curve) from 0.8V/SHE and -1.3V/SHE. PhreeqC simulations of the (B) speciation of Ni(II) in chloride versus pH and the (C) speciation of Ni(II) in nitrates versus pH value.

3.2.3.4 Aqueous solutions of Ni^{2+} and Fe^{3+} in the presence of NO_3^- or Cl^-

In mixed Ni^{2+} and Fe^{3+} solutions (composed of nitrates or chlorides), the pH reaches naturally 2.5 due to the presence of the Lewis acid Fe^{3+}. Figure 3.4A shows the I-V curve in Ni^{2+} $1.2 \cdot 10^{-2}$mol/L and Fe^{3+} $4 \cdot 10^{-3}$mol/L in the presence of K^+ $4.64 \cdot 10^{-1}$mol/L and Cl^- (green curve) or NO_3^- 5.10^{-1} mol/L (red curve). Peaks 1 and 2 (accompanied by its diffusion reduction current) are still present, and are characteristic of the reactions that were detected with/for monometallic solutions: Fe^{3+} reduction accompanied with the Fe^{2+} reduction plateau, and free H^+ reduction. In chloride and nitrate solutions, we can also relate the presence of peak 6 to the H^+ reduction from reaction 3.10. It is located at the same potential as in the monometallic Ni^{2+} solution with the same intensity. PhreeqC simulation with both metals, pointed out that the presence of $Ni(OH)^+$ is predominant at pH 9. There are certainly other reactions that may take place, however they are silent regarding the low concentration of other species.

In nitrate solution, peak reduction current 8, at around -0.8 V/SHE, is close to the potential of peaks 4 and 6 related to the reactions 3.10 and 3.12, respectively. Thus, peak 8 should be related to both reactions that are enhanced when pH value reaches 12. It is asserted that the precipitation/co-precipitation of the oxy-hydroxide NiO and Ni(OH)2 takes place simultaneously at the electrode interface. The mass reaches a plateau and remains constant, even at the potential of Fe^{+II} reduction to Fe^0, probably due to the presence of Ni in the film. In chloride solution, peak 9 is located at -0.93 V/SHE, near the potential of peak 5 and 7. In addition, the intensity is almost the sum of the intensities of peaks 5 and 7, related to reactions 3.10 and 3.12 respectively. Peak 8 is more cathodic than peak 9. The increase in pH value is slower in chloride. However, the pH should be also high enough for the deposition or the co-deposition of $Ni(OH)_2$ and $Fe(OH)_2$.

The co-deposition of $Ni(OH)_2$ and $Fe(OH)_2$ is a first step for the LDH formation process, it is necessary that Fe^{III} belongs to the co-deposited/precipitated structure. For this purpose, two hypotheses can be envisaged:

- The progressive reoxydation of Fe(II) within the coating (after the potential was stopped, the electrode was rinsed with oxygenated saturated milliQ water and maintained in a saturated oxygen KOH supporting electrolyte) for the obtainment of probably mixed Fe(II)/Fe(III), Ni(II)-Fe(II)/Fe(III), Ni(II)/Fe(III)-based LDHs.

- The co-precipitation of Ni(II)-Fe(III) on the deposited coating when the coating covered the gold surface and reached a certain thickness. Whatever the supporting electrolyte, the coating does not prevent $H^{(I)}$ reduction at the interface, i.e. it thus does not it does not prevent pH for increasing. It can nevertheless render the metallic elements less mobile at the interface. Moreover, the co-deposited Ni-Fe (oxy-)hydroxide should be non-conductive. Let us record thatFe(III) is still diffusing towards the electrode. The increase in the coating could make some Fe(III) to co-precipitate with Fe(II) and Ni(II) or Fe(III) to

integrate the structure via substitution, more probably, in the presence of nitrate in which pH reaches higher pH values than in the presence of chloride. This is what we investigate at constant pH in section 3.3.

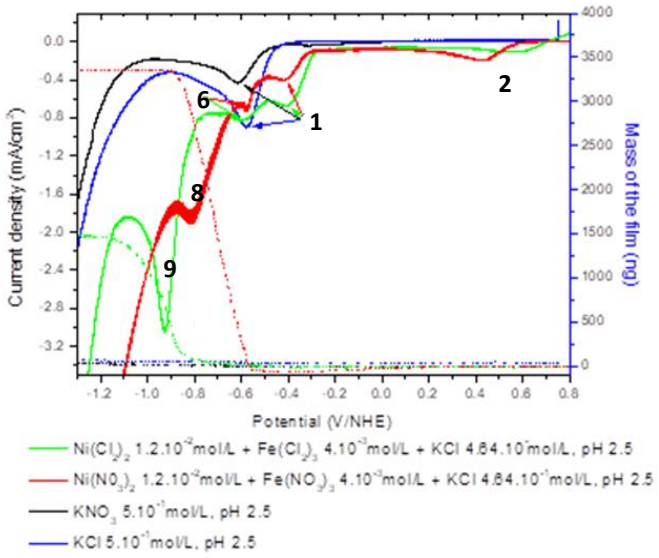

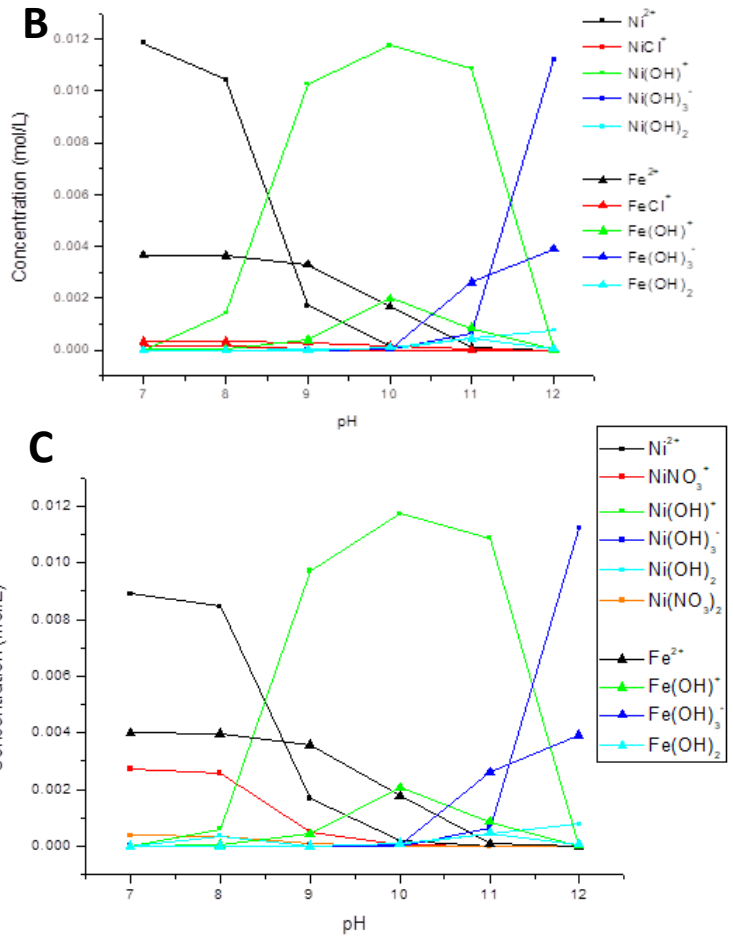

Figure 3.4: (A) I-V and m-V curve of Ni(II) and Fe(III) solutions with nitrates (red curve) or chloride (green curve) from 0.8V/SHE and -1.3V/SHE. PhreeqC simulations of the (B) speciation of Ni(II) and Fe(II) in chloride *versus* pH and the (C) speciation of Ni(II) and Fe(II) in nitrates *versus* pH value

3.3 Electrochemical behavior investigation of Ni/Fe-LDH

3.3.1 Assisted electrodeposition of the LDH and physico-chemical characterization[-]

In agreement with the results provided by the I-V curves, the elec-Ni/Fe-LDH was deposited by means of a 3-electrode electrochemical cell onto a 9MHz-gold patterned quartz substrate as described in section 2.1.2 at -0.7 V/SHE in the nitrate-based electrolyte.

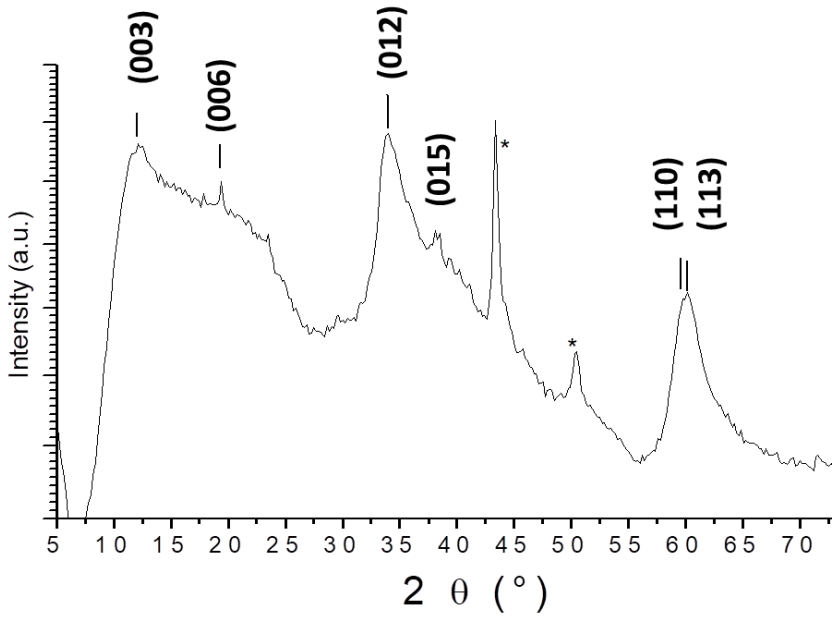

Figure 3.5: PXRD pattern of the electrochemically synthesized LDH whose powder was scraped from 10 samples. Peaks denoted with (*) come from the demagnetized steel.

It was not possible to characterize the structure of the deposited material directly through XRD measurements onto the 9MHz-gold patterned quartz substrate for several reasons: (i) the electrodeposited material is known to have a low crystallinity and is deposited onto a highly crystallized gold and quartz material, (ii) the thickness of the material is of a few hundred nanometers and (iii) the surface area is 0.2 cm^2. Instead, ten samples were electrochemically synthesized and scraped to obtain enough powder.

The XRD pattern (Fig. 3.5) powder evidences a high intensity value of the baseline that should be due to the deposition of an amorphous material. It is also characteristic of the LDH structure. The diffraction peaks were indexed to a hexagonal lattice with rhombohedral 3R symmetry[16] with three reflection groups : (i) a series of basal (00l) reflections that corresponds to the structural stacking along the c-axis and allows determination of basal distance d (here 7.31 Å), which depends on the size of the intercalated anion. [222] The paramater c of the lattice equals 3d(003) (here 21.93 Å), (ii) the position of the (110) reflection that is correlated to the lattice parameter a = 2d(110) (here 3.09 Å), which coincides with the closest M–M distance in the hydrotalcite-like layers, (iii) the positions of the (01l)/(10l) reflections common to hydrotalcite-like compounds which depend on the polytype. These lattice parameters agree well with those reported in the literature.[223]

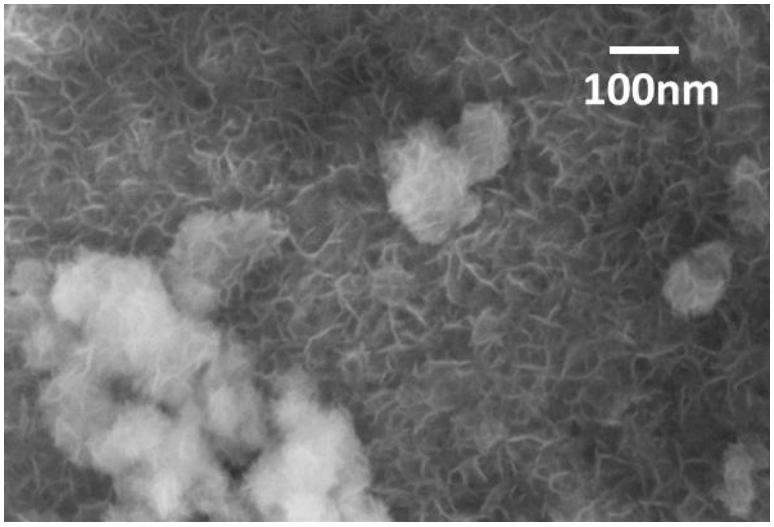

Figure 3.6: SEM micrograph of elec-Ni/Fe-LDH whose morphology is composed of nanowires

SEM micrograph (Fig. 3.6) shows that the electrodeposited LDH is constituted of nanowires, which is in agreement with the literature.[77] By EDX analysis, electro-assisted synthetized LDH has a cationic Ni/Fe ratio evaluated to 73%/27% as expected during the synthesis of LDH (averaged on 3 spots).

3.3.2 Electrochemical and electrogravimetrical investigations of the thin film of LDH by EQCM

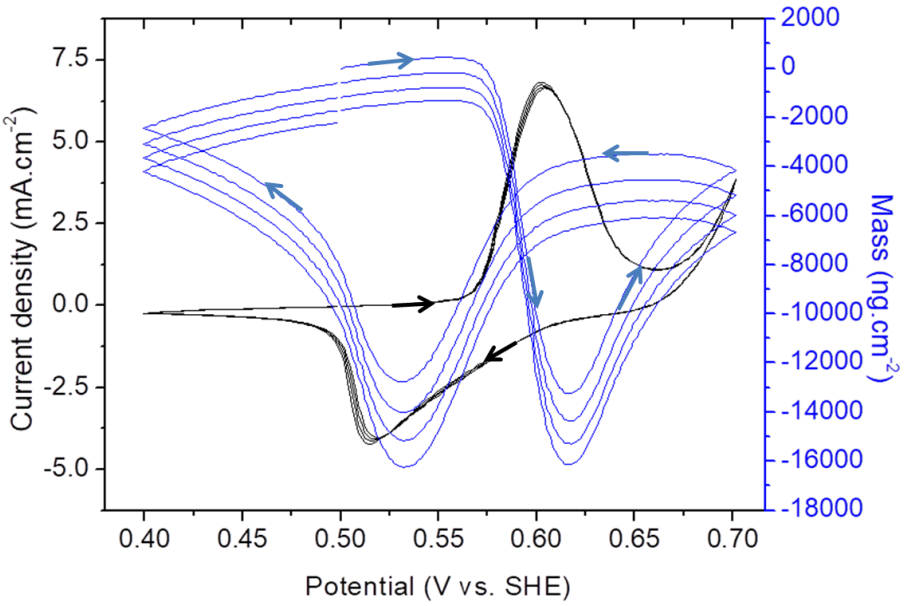

Figure 3.7: EQCM curve of electrochemically assisted route of Ni/Fe-LDH 6/2, during the 4 first cycles in KOH 1 mol/L at 10 mV/s

Films of elec-Ni/Fe-LDH underwent several cycles of polarization in an aqueous solution of KOH 1 mol/L at 10 mV/s while the current and frequency response (I and f vs E curves) were simultaneously recorded. Figure 3.7 shows 4 cycles of elec-Ni/Fe-LDH from which the system already reached a steady state in terms of mass and current. Broad cathodic and anodic peaks with respective potentials at 0.52 V/SHE and at 0.60 V/SHE indicate the reduction and oxidation of Ni sites into the material.[99] The observed high peak separation denotes a charge transfer resistance that can be related to the known electronic transport within the LDH structure due to an electron hopping mechanism between adjacent nickel centers[224] although Fe also plays a role in this hopping process.[99] The OER starts at 0.65 V/SHE and the current is positive from 0.71 V/SHE to 0.65 V/SHE during the cathodic sweep.

The film undergoes a mass depletion followed by a mass increase during the anodic sweep, and a mass depletion followed by a mass increase during the cathodic sweep. In agreement with the electroactivity of the Ni^{3+}/Ni^{2+} redox couple in the LDH structure. During the anodic sweep, a mass increase should be due to both OH^- intercalation into the interlayer spacing and OH^- sorption onto the basal surface of the LDH particles related to an increase of the charges within the layers. In addition, the mass decrease during the anodic sweep should result in the deintercalation of water or desorption of K^+, because of the presence of a positive capacitive current.

However, EQCM only provides an overview of the global transferred mass and cannot give precise information on the nature of the transferred species. It is challenging to deconvolute each species contribution into gravimetric and dynamic components with EQCM results as the global cyclic electrogravimetry response is recorded at a certain potential scan rate (*i.e.* at certain kinetics). Therefore, coupling EQCM and electrochemical impedance spectroscopy techniques (*ac*-electrogravimetry) was performed.

3.3.3 Advanced electrochemical and electrogravimetrical investigation of the thin film of LDH by *ac*-electrogravimetry

3.3.3.1 Elec-Ni/Fe-LDH in aqueous KOH 1 mol/L at a given applied potential (0.66 V/SHE)

After 4 potential cycles from 0.4 V/SHE to 0.71 V/SHE, *ac*-electrogravimetry technique was performed at 0.66 V/SHE in elec-Ni/Fe-LDH to gain insights into the dynamic behavior of each charged/uncharged species transfer at the interface *i.e.* identifying the nature of each transferred species and evaluating their respective concentrations and kinetics as a function of the applied potential. The simulation and fitting of the experimental charge/potential transfer function (TF) $\frac{\Delta q}{\Delta E}(\omega)$ permit the separation of the ionic contributions, however, without any possibility to identify the involved ionic species. Figure 3.9(a) shows two merged loops at intermediate and low frequencies, attributed to any of the ionic species present in the electrolyte.

The kinetic parameter of interfacial transfer (K_i) and the parameter related to the ease of interfacial transfer (G_i) were determined for the two ions by fitting the experimental data with equation equation (2.32) and were used in the ensuing fittings of (2.36). The simulation and fitting of the experimental mass/potential transfer function $\frac{\Delta m}{\Delta E}(\omega)$ confirm that three different species are involved. Figure 3.9(b) evidences two loops at high and intermediate frequencies, and is characteristic of free solvent molecule contributions or anionic contribution in the same flux direction.[167,13] Finally a third contribution appears at low frequency which is characteristic of a cationic contribution or free solvent molecules in the inverse direction. The fitting of the experimental data with the Mathcad software, using equation (2.36) evidences the nature of the three species. H_2O is transferred at high frequencies, OH^- at intermediate frequencies and K^+ at low frequencies, which confirms the configuration of two ions determined by equation (2.32).

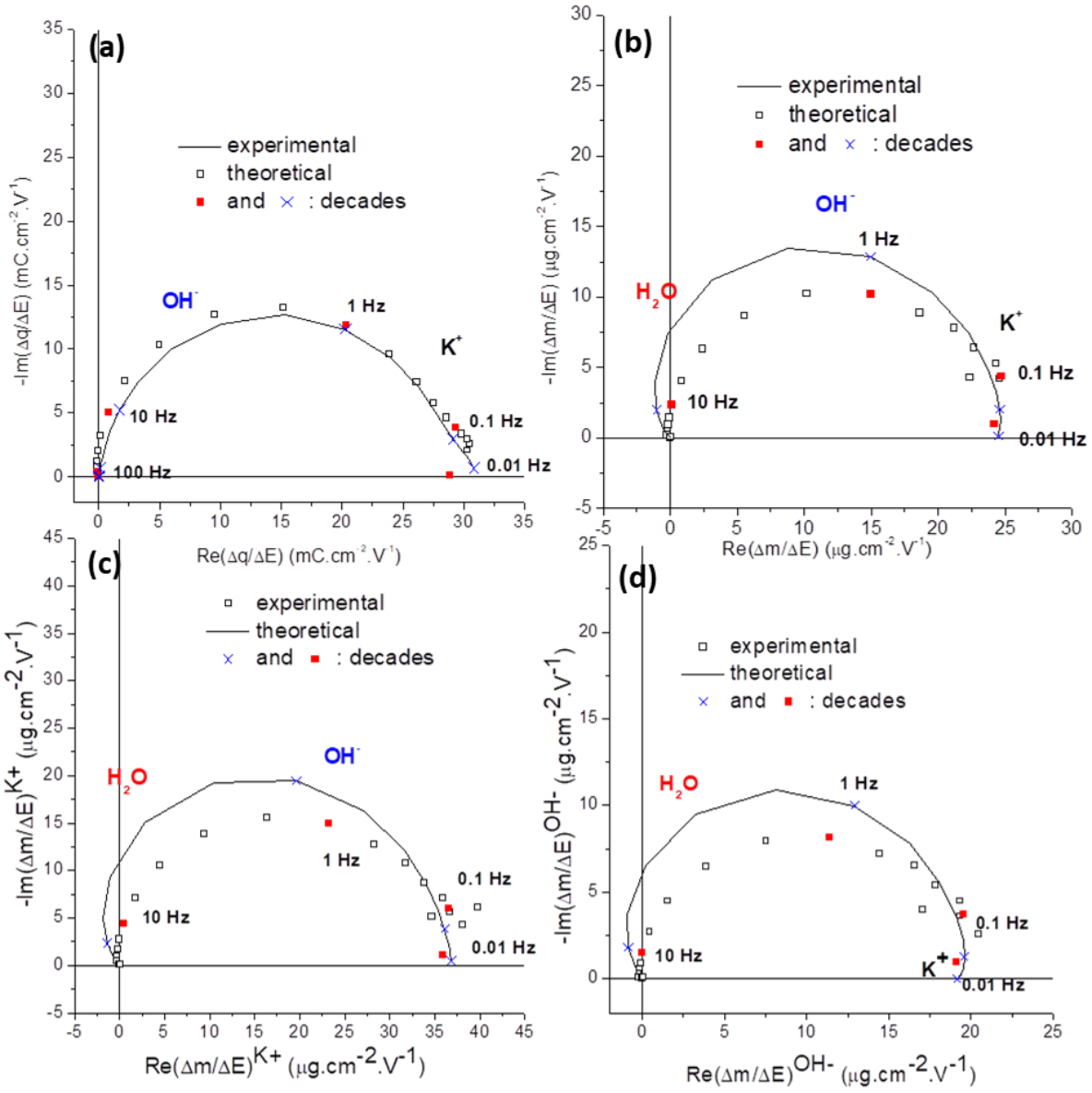

Figure 3.8: Simulation and fitting of the experimental data on a thin film of elec-Ni/Fe-LDH 6/2. (a) ΔqΔE TF, (b) ΔmΔE TF, (c) ΔmΔE partial TFs after removing the contribution of K^+, (d) ΔmΔE partial TFs after removing the contribution of OH^-

Several other configurations were tested using theoretical functions (eq. 2.32 and 2.36). The criteria for attaining a conclusive match between experiment and simulation must be fulfilled for all the TFs and for the so-called partial TFs obtained by removing the contribution of one of the species contribution from the electrogravimetric function, and analyzing the residual response). In the presented model, two theoretical partial functions were

compared to the experimental partial functions and calculated by removing the K^+ contribution (Figure 3.8c, equation 3.14):

$$\left.\frac{\Delta m}{\Delta E}\right|^{K+} = d_f \left[\left.\frac{\Delta C}{\Delta E}\right|^{OH-} (m_{K+} + m_{OH-}) + m_{H2O} \left.\frac{\Delta C}{\Delta E}\right|^{H2O}\right], \quad (3.14)$$

And by removing the OH^- contribution (Figure 3.8d, equation 3.15):

$$\left.\frac{\Delta m}{\Delta E}\right|^{OH-} = d_f \left[\left.\frac{\Delta C}{\Delta E}\right|^{K+} (m_{K+} + m_{OH-}) + m_{H2O} \left.\frac{\Delta C}{\Delta E}\right|^{H2O}\right]. \quad (3.15)$$

In this way, ambiguities concerning various different models of contribution could be excluded.

3.3.3.2 Elec-Ni/Fe-LDH 6/2 in aqueous KOH 1 mol/L as a function of the applied potential

The same fitting procedure and validation control were operated for different applied potentials (0.61 V, 0.635 V and 0.66 V/SHE) corresponding to the potential range where species are transferred from/to the film. The parameters K_i, G_i and $Rt_i = \frac{1}{FG_i}$ were estimated for all of them. Based on the K_i values (Fig. 3.9a), the flux of OH^- ion is faster than the counterflux of K^+ ion at each potential. The flux of free solvent is in the same direction as the flux of OH^-. Water molecules are the slowest species at 0.61 V/SHE and becomes progressively faster to become the fastest species at 0.66 V/SHE.

The calculated Rt_i (Fig. 3.9b) classifies the transfer resistance of each species as follows: Rt_i (K^+) > Rt_i (OH^-) ≥ Rt_i (H_2O). This transfer resistance is the highest for OH^- and its kinetics is the lowest. This information is in good agreement with the intercalation process of OH^- into the interlayer space. K^+ cations are slower and more hardly transferred than OH^- and water, in good agreement with the hypothesis of a less favorable transfer of cations than intercalation/deintercalation of water molecules and free water molecules.

3.3.3.3 Evolution of the relative concentration per volume unit, $C_i - C_o$, and the mass per area unit, $m_i - m_o$.

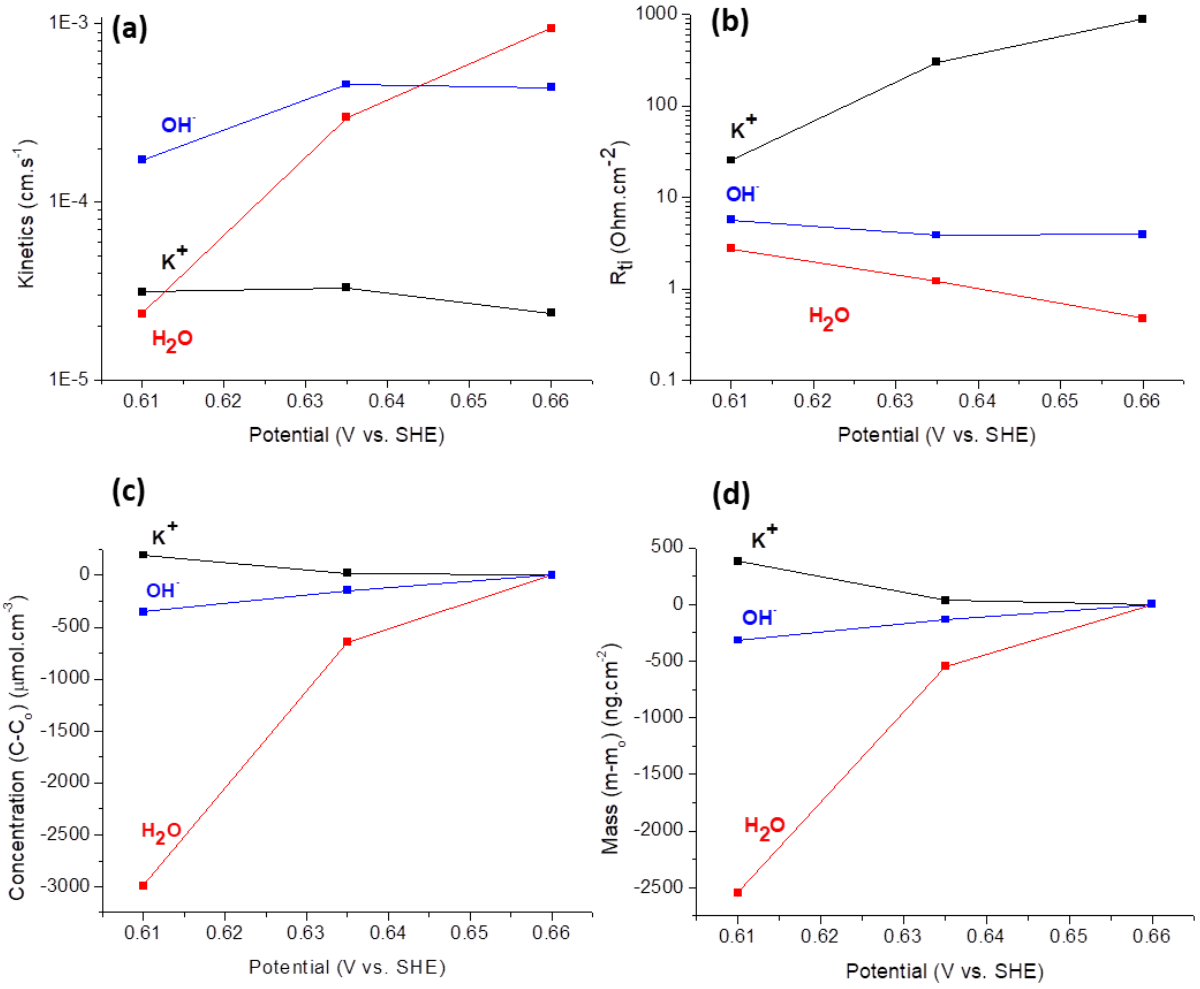

Figure 3.9: (a) Transfer kinetics and (b) transfer resistance of K^+, H_2O and OH^- as a function of the applied potential (c) Relative concentration and (d) Mass variation of K^+, H_2O and OH^- as a function of applied potential at the thin film of elec-Ni/Fe-LDH in KOH 1mol/L aqueous solution.

The variation in concentration (Fig. 3.9c) and variation in mass (Fig. 3.9d) of the transferred species are estimated from the concentration potential transfer function (equation 3.16) at low frequencies:

$$\left|\frac{\Delta C_i}{\Delta E}\right|_{\omega \to 0} = -\frac{G_i}{K_i} \qquad (3.16)$$

and from the relative exchanged mass variation for each species (eq. 3.17):

$$m_i = C_i M_i d_f \qquad (3.17)$$

From 0.61 V to 0.66 V (*i.e.* from more cathodic to more anodic potentials), *ac*-electrogravimetry can deconvolute the concentration and mass variation of all the transferred species. Water molecules are 8.5 times more transferred than OH^- from the electrolyte to the elec-Ni/Fe-LDH whereas K^+ is two times less transferred from the LDH to the electrolyte compared to that of OH^-. However, *ac*-electrogravimetry technique could not be performed for potentials lower than 0.61 V/SHE as the mass was not stable, and thus it was not possible to explain what occurs during the mass depletion of the anodic sweep.

For the confirmation of each determined transferred species (K^+, H_2O and OH^-) and also for a better insight regarding the specific sites of transfer, complementary techniques have to be performed onto the LDH; *i.e.* EDX and XPS analyses and *in situ* XRD under polarization. The low crystallinity and specific morphology of the elec-Ni/Fe-LDH could be responsible for the nature of such transfer of species. Although the *ac*-electrogravimetry technique permits the deconvolution of the species transfer, it does not allow to understand the phenomena that occur more cathodically (in the potential range 0.52 V/SHE to 0.61 V/SHE)

3.4 Conclusion

Free H^+ reduction is mainly responsible for the increase in pH in the considered solutions. The Fe^{III}, Fe^{II} and Ni^{II} cation speciation, when complexed to H_2O, also play a role in the progressive increase in pH value at the interface. The anion has also a role in the pH variation. The speciation between Cl^- and Fe^{II} is facilitated, as well as the speciation between NO_3^- and Ni^{II}, which can prevent the speciation with H_2O and the production of H^+.

Due to nitrate reduction reaction in agreement with eq. 3.2, the presence of nitrates enables the increase in pH at less cathodic potential. This additional reaction enables the formation of LDH at the surface. In monometallic Fe(III) solution containing chlorides, Fe° is deposited. The presence of $Ni^{(II)}$ enables a higher variation in pH for the LDH electro-assisted deposition. However, the deposited mass is lower; probably because the reached pH value is quite smaller than in nitrate-based solutions.

Another remark is the deposition of iron-based LDH with oxidation state (+II) and (+III). Further XPS and XRD analysis under preserved atmosphere just after the synthesis should explain the structural behavior. Experiments via coupled XRD analysis *operando* should help us for further in depth investigation of the coating mechanism.

In depth investigation of the current and mass potential curves led to select the appropriate supporting electrolyte as well as the applied potential for the obtainment of an Ni/Fe-based LDH 6/2 coating.

For the first time, this study investigated all the redox reactions as well as both the related ionic and water transfers using nano-elec-Ni/Fe-LDH 6/2 via electrochemical and electro-gravimetrical characterization.

The reversible Ni(II)/Ni(III) redox reaction was evidenced through I-V response, and a related complex transfer of species was evidenced with EQCM. For the deconvolution of all the transfer mechanisms, *ac*-

electrogravimetry was performed and evidenced that the flux of 1 OH^- is accompanied by a flux of 8.5 H_2O in the same direction and with a faster kinetics and a counterflux of 0.5 H_2O with a slower kinetics. H_2O and OH- are probably intercalated/deintercalated into/from the interlayer spacing, while K^+ should be adsorbed due to a capacitive phenomenon. The latter phenomenon is in agreement with the cationic adsorption that was already observed for Mg/Fe-LDH 4/2 (appendix A), and evidences again the property of mix cation/anion exchanger of the LDH.

Ac-electrogravimetry technique permits the deconvolution of the species transfer from 0.61 V/SHE to 0.66 V/SHE but does not allow to understand the phenomena that occur at lower potentials (in the potential range 0.52 V/SHE to 0.61 V/SHE).

For the confirmation of the intervention of K^+, H_2O and OH^- in the transfer mechanism, and also for a better insight regarding the specific sites of transfer, complementary analyses have to be performed onthe LDH, *i.e.* EDX and XPS analyses and *in situ*/*operando* XRD under polarization. *In situ/operando* XRD under polarization enables to observe the basal distance, however, this observation is complicated onto the elec-Ni/Fe-LDH thin film as it is not well crystallized. Also, the EDX and XPS analyses permit the identification of the adsorbed cations onto the surface, however, it is not possible to assert if cations would be adsorbed onto the LDH or onto impurities within the thin film.

To elude this problem and deepen the characterizations, it is necessary to study the properties of the chemically synthesized Ni/Fe-LDH 6/2 (chem-Ni/Fe-LDH 6/2). Despite the lower electronic charge transfer inherent to the less adherent film onto the LDH, this material has the property to be highly pure and crystallized.

Chapter 4

In situ study of redox reactions and ionic transfer in thin films of Ni/Fe-based layered double hydroxide under polarization in KOH 1 mol/L

4.1 Introduction

In this chapter, we want to solve the low crystallinity issue encountered for elec-Ni/Fe-LDH (chapter 3) that prevents the confirmation of the transfer mechanisms by complementary experimental techniques. To deepen the characterization. To deepen the characterizations, it is necessary to study the properties of the chemically synthesized Ni/Fe-LDH 6/2 (chem-Ni/Fe-LDH 6/2). Despite the lower electronic charge transfer inherent to the less adherent film onto the LDH, this material has the property to be highly pure and crystallized.

For wide applications in terms of energy storage or water treatment, the reversibility of the ion transfers between the electrolyte and the basal spacing needs to be further investigated. A reversible ion transfer is actually controlled by tuning the oxidation state of the metallic sites to reversibly modify the positive charge excess within the layers. This phenomenon depends on the electrochemical accessibility of the redox-active transition cations (ex : Co^{3+}/Co^{2+}, Ni^{3+}/Ni^{2+}, Fe^{3+}/Fe^{2+} etc…) that participates in an electron hopping mechanism.99 The low electronic conductivity performance of the LDHs[214] is promoted by preparing thin films of LDH coated on a working electrode surface (glassy carbon, platinum, gold, indium tin oxide…) by solvent casting, layer-by-layer assembly or electrochemically assisted deposition.[99,161,215,216]

A few studies explored the reversible ion transfer phenomenon related to the cyclic oxidation/reduction of electroactive cations within the layers.[161,10,225,164,226,153] Each of them could evidence the reversible intercalation of anions. Among them, some could also evidence the contribution of cations,[161, 10, 164, 153] and propose some hypotheses concerning the nature of the species. A publication suggests the transfer of electrolytic cations,[164] another one advances anion intercalation/sorption influenced by the electrolytic cations.[161] There is also evidence of a transfer of ion pair[153] as well as the loss of some water molecules from the LDH basal spacing accompanied with a loss of protons from the LDH lattice.[10] The redox reactivity of LDHs remains challenging to characterize probably due to a duality of adsorption surfaces sites in agreement, by analogy, to cationic clay

minerals.[227,228,229,230,231,232,233,234] Indeed, basal surfaces of cationic clay minerals have a permanent negative charge arising from isomorphic cationic substitutions whereas edge surfaces have a variable proton surface charge arising from hydroxyl functional groups. The redox reactions involving the redox-active transition cations lead to the modulation of the electric charge of the layers. For nontronite 2/1, the negative charge increase due to Fe(III) to Fe(II) reduction is balanced by adsorption of cations into the clay interlayers as well as a specific sorption of H^+ from the solution. Prevalence of one compensating mechanism over the other is related to the growing lattice distortion induced by structural Fe(III) reduction. At low reduction levels, interlayered cation adsorption dominates and some of the incorporated protons react with structural hydroxyl groups, leading to a dehydroxylation of the structure.[235]

In addition, the reactivity of edge surfaces is strongly influenced by the net proton surface charge, which depends on pH and ionic strength, with respect to Brønsted–Lowry acid-base theory, through the following reactions:

$$\equiv M\text{-}OH + H^+ \Leftrightarrow \equiv M\text{-}OH_2^+ \quad (4.1)$$

$$\equiv M\text{-}OH \Leftrightarrow \equiv M\text{-}O^- + H^+ \quad (4.2)$$

where M is a metal cation constituting the layered sheets and consequently the clay edge surfaces. It implies the sorption of both cations and anions onto edge surfaces depending on the pH at the clay interface. In agreement with reaction 2, for pH >>> pH_{PZNC} (pH of zero point of net charge (ZPNC)), the species $\equiv M\text{-}O^-$ predominates, leading to the cation sorption on edge surfaces.

By analogy to cationic clay minerals, the redox reactions involving the structural transition cations of LDH should lead to the modulation on the positive electric charge of the layers and thus induce the modulation of the anionic transfer capacity and, to a lesser extent, a desorption of H^+ from structural OH groups to maintain electro-neutrality. The reactivity of the edge surfaces should also be strongly influenced by the net proton surface charge.

To attribute the phenomena postulated by analogy with cationic clay minerals, the modification of the structural charge of the LDH, via oxidation/reduction of a part of redox active cations constituting the layers makes it possible to demonstrate the presence of the anionic exchange sites. The use of a solution having a pH largely superior to pH_{PZNC} should allow to differentiate the anionic transfer into the interlayer space from the external basal sites and the edge surfaces where the cation sorption takes place.

For this purpose, electrochemical techniques appear well suited. Indeed, it allows redox transition of LDH active cations as well as the modulation of the pH value at the solid-surface via electro-catalytic properties of LDHs versus water oxidation/reduction.[236,237,238] In addition, *ac*-electrogravimetry method which couples electrochemical impedance (intensity/potential transfer function) and mass/potential transfer function measurements allows the identification of exchanged species, in terms of anions, cations or neutral species as

well as their molar mass, ease/difficulty of transfer, exchanged concentration and exchanged mass for each species at different potentials. In such a way, this technique has already been validated in studying oxide materials[239] and conductive polymers.[240] This study brings insights on the mechanisms of the interfacial redox reactions by exploiting *ac*-electrogravimetric methodology.

A special attention is paid on Ni/Fe-LDH 6/2 that is known to be one of the most conductive LDH and whose electroactive Ni can be reversibly switched to the (+II) and (+III) oxidation states under polarization.[99] The use of nano-Ni/Fe-LDH 6/2 tends to enhance the number of the transfer sites (i.e intercalation sites and adsorption sites onto both edge and basal surfaces). Since Ni/Fe-LDH has a pH_{PZNC} equal to 8, this work was conducted in KOH 1 mol/L solution whose pH value is higher than pH_{PZNC} to induce the cationic sorption onto the LDH border sites. The catalyzed oxidation reaction of water[157,241,242,243] enabled the modulation of the pH value at the LDH/electrolyte interface.

For the first time, the nature of each reversibly transferred species (anion, cation and water molecules) related to the redox reactions was identified, and the species kinetics were determined. EDX and XPS analyses confirmed the electrosorption of cations, corroborating the pseudo-capacitive properties of a mix cation and anion exchanger. The electro-catalytic properties of the interlayered water molecules were pointed out. In addition, *in situ* XRD under LDH polarization has especially contributed to our current-day understanding of LDH hydration during cyclic oxidation/reduction (to investigate the transfer of water molecules from/to the interlayer space).

4.2 Physical and chemical characterization of chem-Ni/Fe-LDH 6/2 samples

4.2.1 XRD Analysis

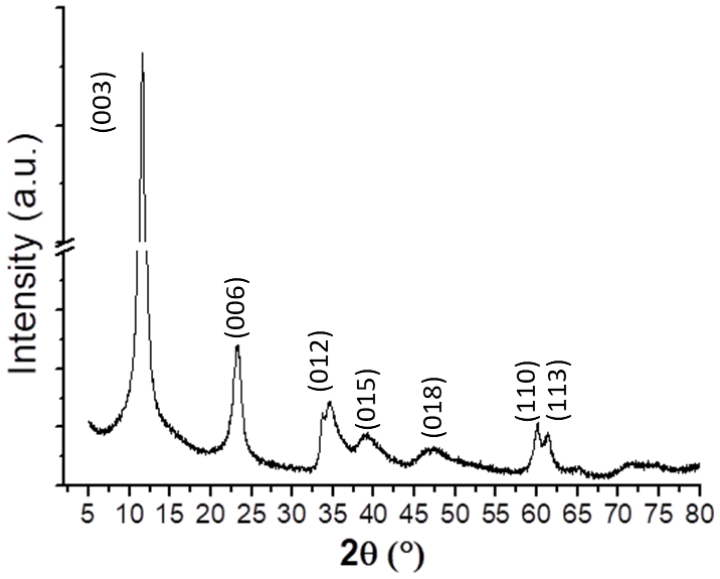

Figure 4.1: Powder XRD pattern of the Ni/Fe-LDH.

The powder XRD pattern of Ni/Fe-LDH (Fig. 4.1) is characteristic of the LDH structure. The diffraction peaks were indexed to a hexagonal lattice with rhombohedral 3R symmetry[16] with three reflection groups: (i) a series of basal (00l) reflections that corresponds to the structural stacking along the c-axis and allows determination of basal distance d (here 7.64 Å) which depends on the size of the intercalated anion.[222] The parameter c of the lattice equals 3d(003) (here 22.92 Å), (ii) the position of the (110) reflection that is correlated to the lattice parameter a = 2d(110) (here 3.08 Å) which coincides with the closest M–M distance in the hydrotalcite-like layers, (iii) the positions of the (01l)/(10l) reflections common to hydrotalcite-like compounds which depend on the polytype. These lattice parameters agree well with those reported in the literature.[223]

4.2.2 FEG-SEM, EDX and XPS analyses

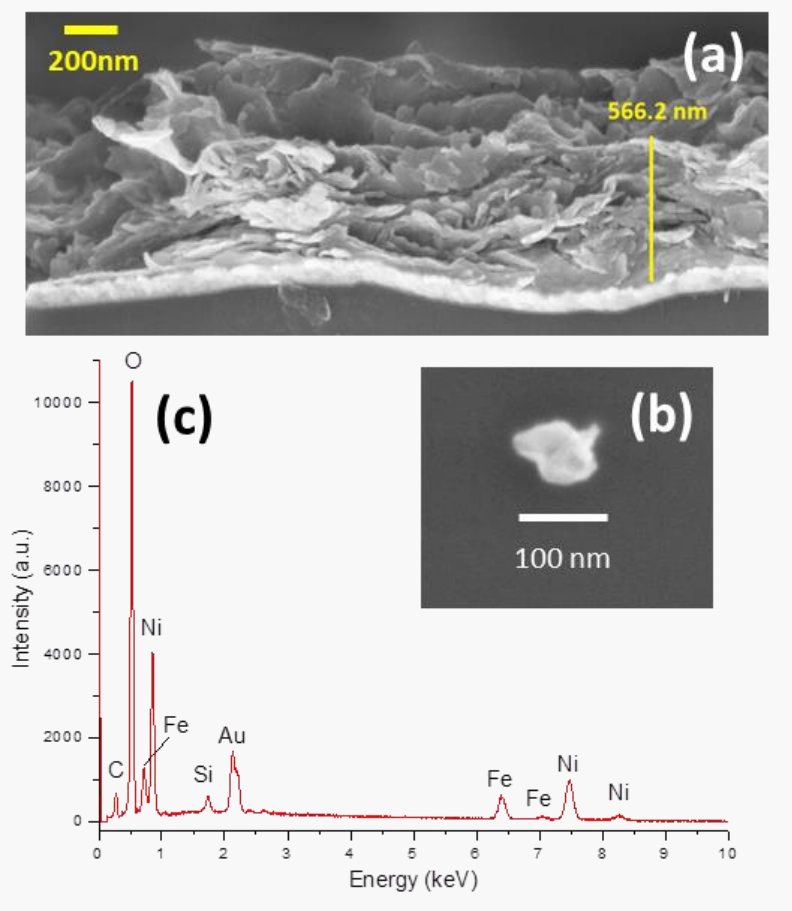

Figure 4.2: (a) FEG-SEM micrograph showing the cross-section of a gold-patterned quartz resonator modified with a thin film of LDH, (b) FEG-SEM micrograph of a nanoplatelet of the Ni/Fe-LDH 6/2 isolated on a silicon wafer, (c) EDX analysis of a thin film of Ni/Fe-LDH 6/2 deposited on the gold electrode of a quartz resonator.

FEG-SEM micrographs show that synthesized LDH is constituted of nanoplatelets with particle size close to 80 nm (Fig. 4.2b) which is in agreement with the literature.[77] The thickness of the film was also measured with FEG-SEM (Fig. 4.2a) and is estimated to be around 500 nm after a deposition of 24.51 µg on a 0.2 cm^2 gold electrode.

Calibrated EDX analysis (Fig. 4.2c) was performed on a thin film of LDH dried on quartz coated with gold. The Ni/Fe cationic ratio equals 76%/24% as expected during the synthesis of the LDH.

XPS survey spectrum (see Fig. 4.3) shows that no contribution around 400 eV is detected (N1s photopeak) confirming that nitrate ions are no present in the LDH film.

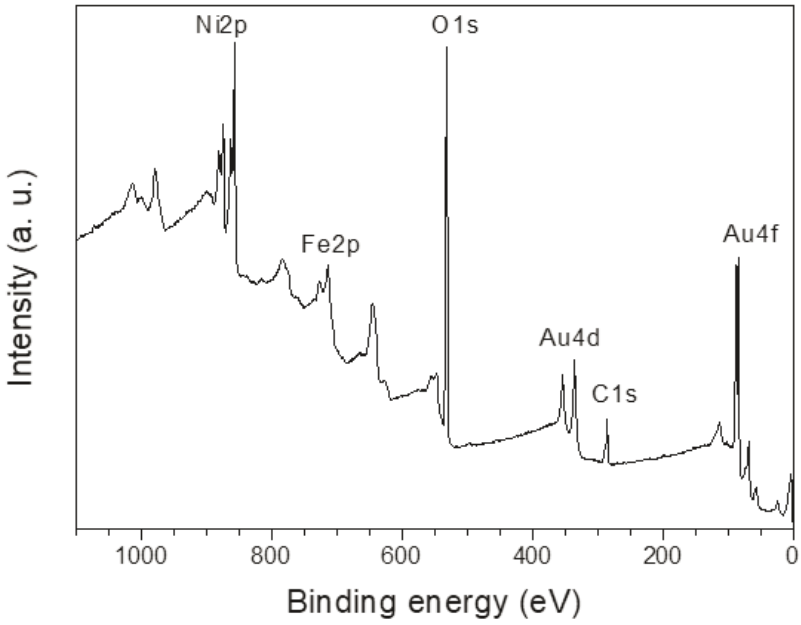

Figure 4.3: XPS spectrum of the gold electrode coated with chem-Ni/Fe-LDH

4.2.3 Thermogravimetric analysis

The number of water molecules present in the interlayer spacing was estimated by TG analysis (Fig. 4.4). It enables the determination of the chemical formula of the LDH as $[Ni^{II}_{0.76}Fe^{III}_{0.24}(OH)_2(CO_3^{2-})_{0.12}]$. 0.5 H_2O. Therefore, a deposition of a LDH thin film of 24.51 µg on the quartz coated with gold was made by drop casting. This mass corresponds to 0.227 10^{-6} mol of LDH and therefore to 1.04 10^{17} Ni sites and the anodic charge necessary to oxidize all the Ni(II) into Ni(III) is 16.6 mC.

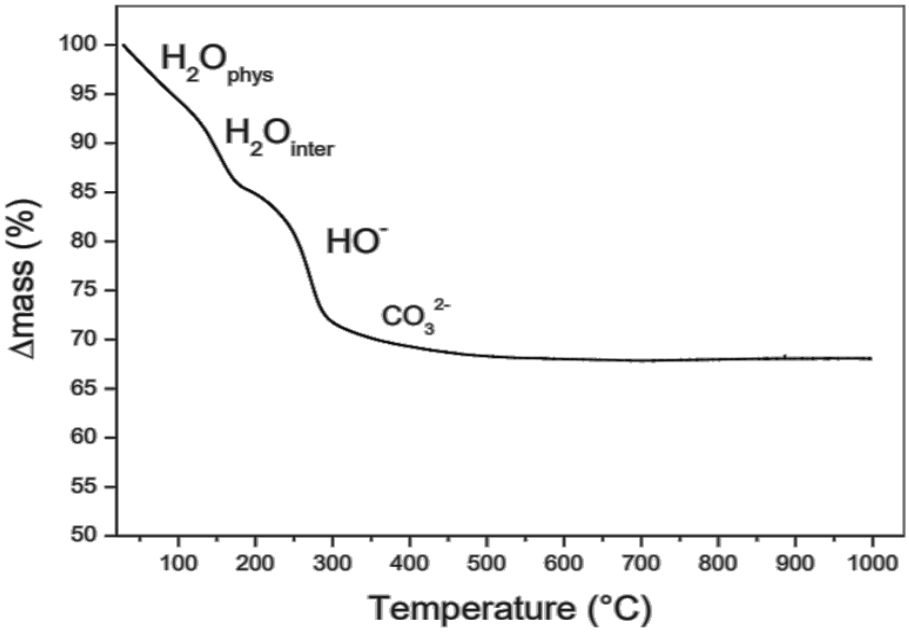

Figure 4.4: TGA analysis of the chem-Ni/Fe-LDH sample

4.3 EQCM investigations

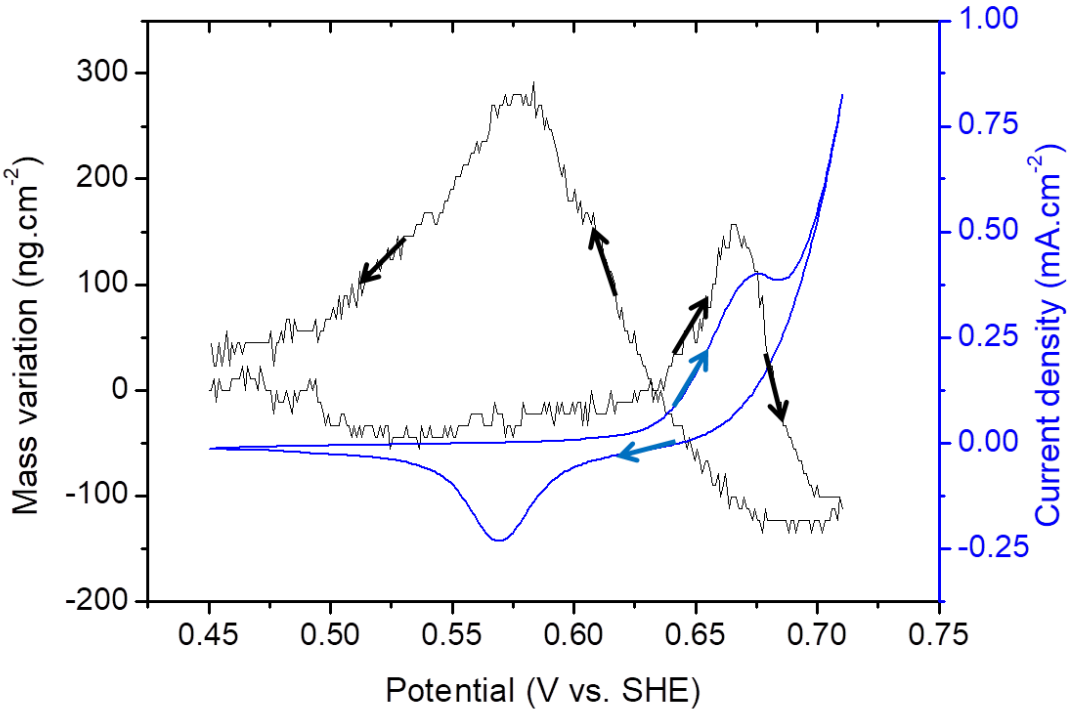

Figure 4.5: EQCM response during the 40th potential scan for a Ni/Fe-LDH coated quartz resonator in KOH 1 mol/L, at a scan rate of 10 mV/s.

Thin films of Ni/Fe-LDH underwent 50 cycles of polarization in an aqueous solution of KOH 1 mol/L at 10 mV/s (Fig. 4.6), while the current response (I vs. E curves) and the mass response (m vs. E curves) were simultaneously recorded. The oxidation and reduction current peaks increased with the number of cycles indicating a rise in the number of redox active Ni sites, probably owing to a higher conductivity of some irreversibly oxidized $Ni^{(+III)}$ clusters that enhance the conductivity.[149, 150,151,152]

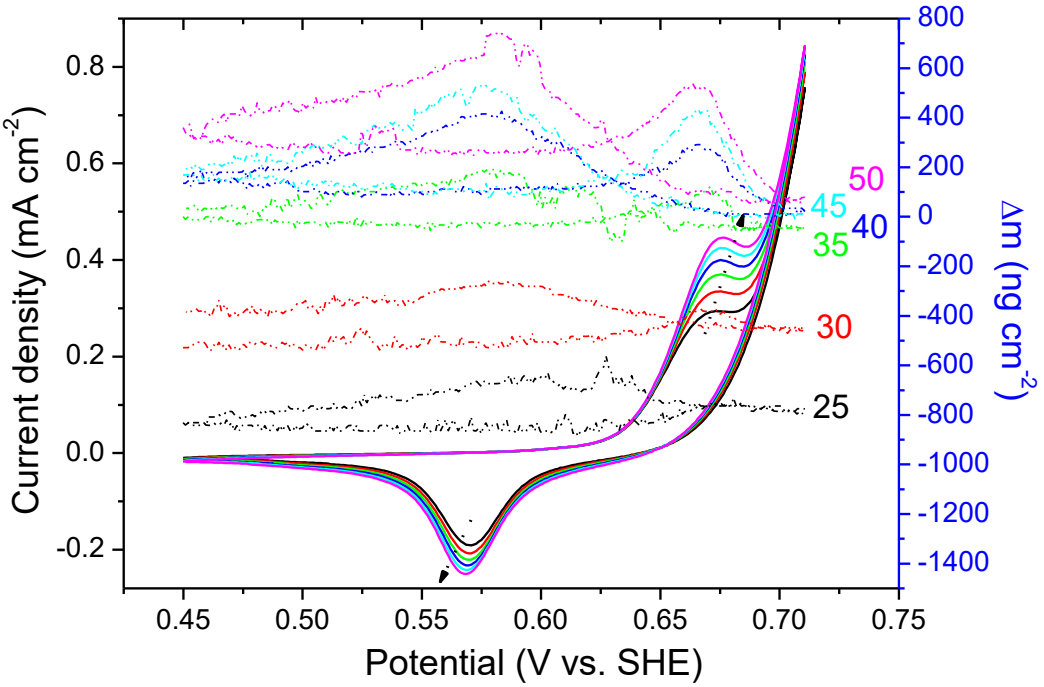

Figure 4.6: By EQCM, chem-Ni/Fe-LDH underwent 50 cycles of polarization in an aqueous solution of KOH 1 mol/L at 10 mV/s

Figure 4.5 shows the 40th cycle from which the system reached a steady state regarding both current and mass versus applied potential. A broad cathodic peak (at 0.575 V/SHE) and a broad anodic peak (at 0.681 V/SHE) indicate the reduction and the oxidation of Ni sites into the material, respectively.[99, 5]

The peak separation is 106 mV comparable to the 98 mV value found in literature[99] on platinum electrode coated with Ni/Fe-LDH 6/2 which denotes a slow charge transfer. This phenomenon can be related to the known electronic transport within the LDH structure due to an electron hopping mechanism between adjacent nickel centers[224] although Fe also plays a role in this hopping process[99].

The low percentage of activated Ni sites is confirmed with the low charge transfer. From potential cycle number 40, the charge is estimated from the integration of the cathodic peak to be equal to 0.27 mC corresponding to 1.685 10^{15} electroactive Ni atoms, which corresponds to 1.62 % of the Ni sites. Regarding the anodic peak, the concomitant Ni(II) and H_2O oxidation reactions do not allow an accurate determination of the percentage of Ni(III) sites.

The Ni/Fe-LDH 6/2 film undergoes a mass increase followed by a mass depletion during the anodic sweep, and a mass increase followed by a mass depletion during the cathodic sweep (Fig. 4.5). In agreement with Ni(II) oxidation to Ni(III) within the LDH structure, the resulting modification in the redox state should induce OH^- intercalation into the interlayer spacing. In addition and in agreement with the electrocatalytic behavior of the coated LDH for H_2O oxidation, the resulting pH variations at the interface, from above pH_{ZPNC} to pH_{ZPNC} (*i.e.* from $pH >> pH_{ZPNC}$ to $pH \approx pH_{ZPNC}$), should result in modification of the charge sign at edge surfaces (Reaction (4.2)) and consequently in the electrodesorption/electrosorption of K^+ at edge surfaces of the LDH nanosheets.

However, EQCM only provides an overview of the global transferred mass and cannot give precise information on the nature of the transferred species. It is challenging to deconvolute each species contribution into gravimetric and dynamic components with EQCM results as the global cyclic electrogravimetry response is recorded at a certain scan rate (*i.e.* at certain kinetics of transfer).[12, 171, 244] Therefore, *ac*-electrogravimetry study which couples EQCM and electrochemical impedance spectroscopy was conducted.

4.4 *Ac*-electrogravimetric investigations

4.4.1 Ni/Fe-LDH 6/2 in aqueous KOH 1 mol/L at a given applied potential

After 50 potential cycles from +0.45 V to +0.71 V, *ac*-electrogravimetry was performed at different potentials to gain insights into the (i) dynamic behavior of each charged and uncharged species transfer at the interface, (ii) identifying the nature of each transferred species and (iii) evaluating their respective concentration variation and kinetics as a function of the applied potential.

The fitting of the experimental charge/potential transfer function (Eq. 2.31) permits the separation of the ionic contributions, however, without any possibility to identify the involved ionic species. Fig. 4.7a shows two loops, one at high frequencies and the other at low frequencies. They are attributed to the interfacial transfer of two different ionic species present in the electrolyte. Their kinetics of transfer is not sufficiently different from each other to appear as completely separate loops.

However, the kinetic parameter of interfacial transfer (K_i) and the parameter related to the ease/difficulty of interfacial transfer (G_i) were determined for the two ions by fitting the experimental data with (equ. 2.31) and were used in the fittings of mass/potential transfer function $\frac{\Delta \mathbf{m}}{\Delta \mathbf{E}}(\boldsymbol{\omega})$ (eq. 2.36)). This fitting shows that three different species are involved. This transfer function permits the identification of the ionic species and also solvent molecule if there is any. Fig. 4.7b evidences a first loop appearing in the third quadrant at high frequency. It is noted that the loops in the third quadrant are characteristic of cation contribution or free solvent molecules in the same flux direction.[167,13] Another contribution also appears at intermediate frequencies in the third quadrant

highlighting the challenge in the exact identification of species. Although small, a third contribution appears in the fourth quadrant at low frequency. Contributions in the fourth quadrant are characteristic of an anion contribution or free solvent molecules in the same direction than the anions. The fitting of the experimental data in Fig. 4.7b with (eq. 2.36) evidences the nature of the three species. K^+ (Ion 1 Fig. 4.7a) is transferred at high frequencies and OH^- (Ion 2 Fig. 4.7a) at low frequencies which confirms the configuration of two ions determined by the $\frac{\Delta \mathbf{q}}{\Delta \mathbf{E}}(\boldsymbol{\omega})$ TF (Fig. 4.7a, fitting of charge/potential transfer function using (eq. 2.31), water molecules are transferred in the same direction than the cations.

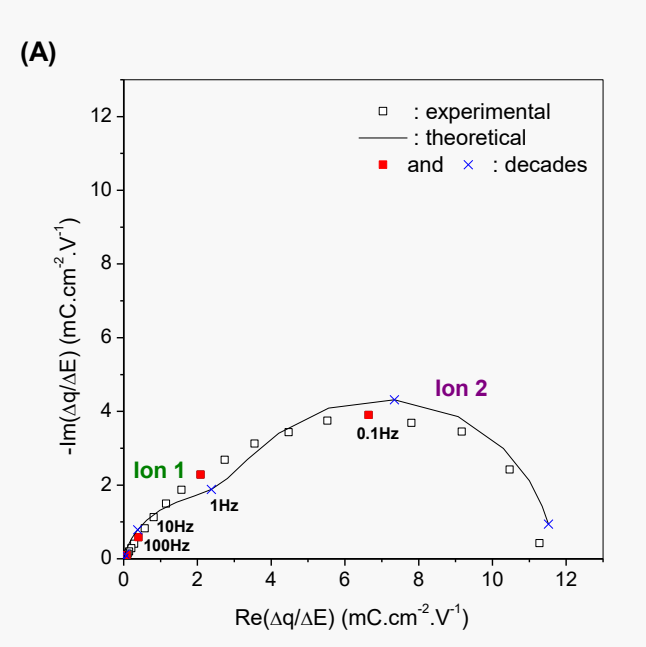

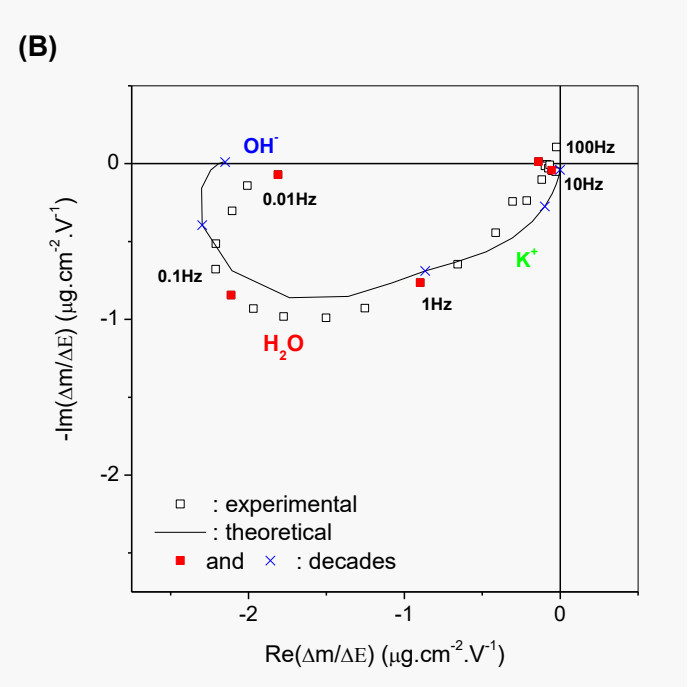
(B)
OH-
100Hz
10Hz
0.01Hz
0.1Hz
1Hz
K+
H2O
: experimental
: theoretical
and : decades
-Im(Δm/ΔE) (µg.cm-2.V-1)
Re(Δm/ΔE) (µg.cm-2.V-1)

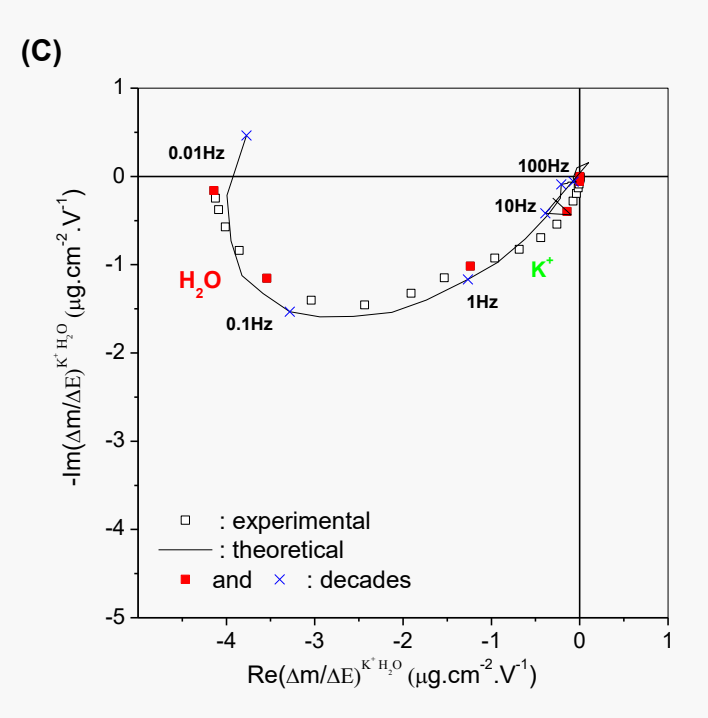
(C)
0.01Hz
100Hz
10Hz
H2O
K+
1Hz
0.1Hz
: experimental
: theoretical
and : decades
-Im(Δm/ΔE)K+H2O (µg.cm-2.V-1)
Re(Δm/ΔE)K+H2O (µg.cm-2.V-1)

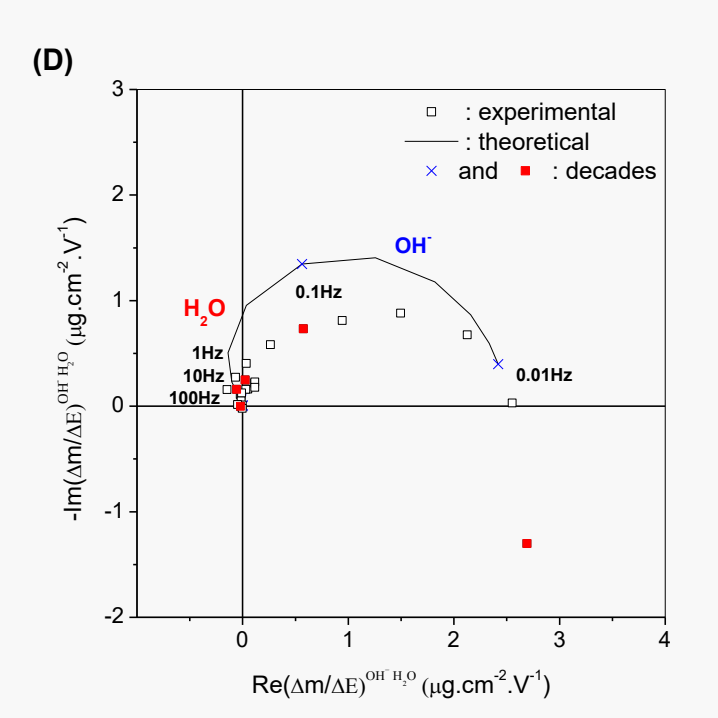

Figure 4.7: Fitting of the experimental data of a thin film of nano-Ni/Fe-LDH 6/2. (A) Δq/ΔE TF, (B) Δm/ΔE TF, (C) Δm/ΔE cation + water partial TFs (after removing the contribution of OH^-), (D) Δm/ΔE anion + water partial TFs (after removing the contribution of K^+).

Several other configurations were tested in the fitting of the experimental data using the theoretical functions in Eq. (2.32) and (2.36). The criteria for attaining a conclusive match between experiment and fitting must be fulfilled for all the TFs and for the so-called partial TFs obtained by removing the contribution of one of the species contribution from the electrogravimetric function, and analyzing the residual response.

In the presented model, two theoretical partial functions (Eq. 4.3 and 4.4) were compared to the experimental partial functions. One was calculated by removing the OH^- contribution (Fig. 4.7c):

$$\left.\frac{\Delta m}{\Delta E}\right|^{K^+ \text{ and } H2O} = d_f\left[(m_{K+} + m_{OH-})\left.\frac{\Delta C}{\Delta E}\right|^{K^+} + m_{H2O}\left.\frac{\Delta C}{\Delta E}\right|^{H2O}\right] \quad (4.3)$$

And the other by removing the K^+ contribution (Fig. 4.7d):

$$\left.\frac{\Delta m}{\Delta E}\right|^{OH^- \text{ and } H2O} = d_f\left[(m_{OH-} + m_{K+})\left.\frac{\Delta C}{\Delta E}\right|^{OH^-} + m_{H2O}\left.\frac{\Delta C}{\Delta E}\right|^{H2O}\right] \quad (4.4)$$

In this way, ambiguities concerning various models of contribution could be excluded.

4.4.2 Ni/Fe-LDH 6/2 in aqueous KOH 1 mol/L at different potentials

The same fitting procedure and validation control were operated for all the studied potentials from +0.575 V to +0.675 V corresponding to the potential range where species are transferred from/to the LDH film. The parameters K_i, G_i and $\mathrm{Rt_i} = \frac{1}{\mathrm{FG_i}}$ were estimated for all of them. Based on the K_i values (Fig. 4.8a), the K^+ ion is the fastest of the three species exchanged at each potential, followed by H_2O and OH^-. The calculated Rt_i (Fig. 4.8b) classify the transfer resistance of each species as follows: Rt_i (OH^-) > Rt_i (H_2O) ⩾ Rt_i (K^+). This resistance of transfer is the highest for OH^- and its kinetics is the lowest. This information is in good agreement with the intercalation process of OH^- into the interlayer space. K^+ cations are faster and more easily transferred especially at more anodic potentials (more than 0.625 V/SHE), in good agreement with the hypothesis of electroadsorption onto more accessible sites like LDH edge surfaces. Adsorbed K^+ desorb once the interfacial pH decreases and tends to the pH_{PZNC} value during the anodic sweep. That will be discussed thereafter.

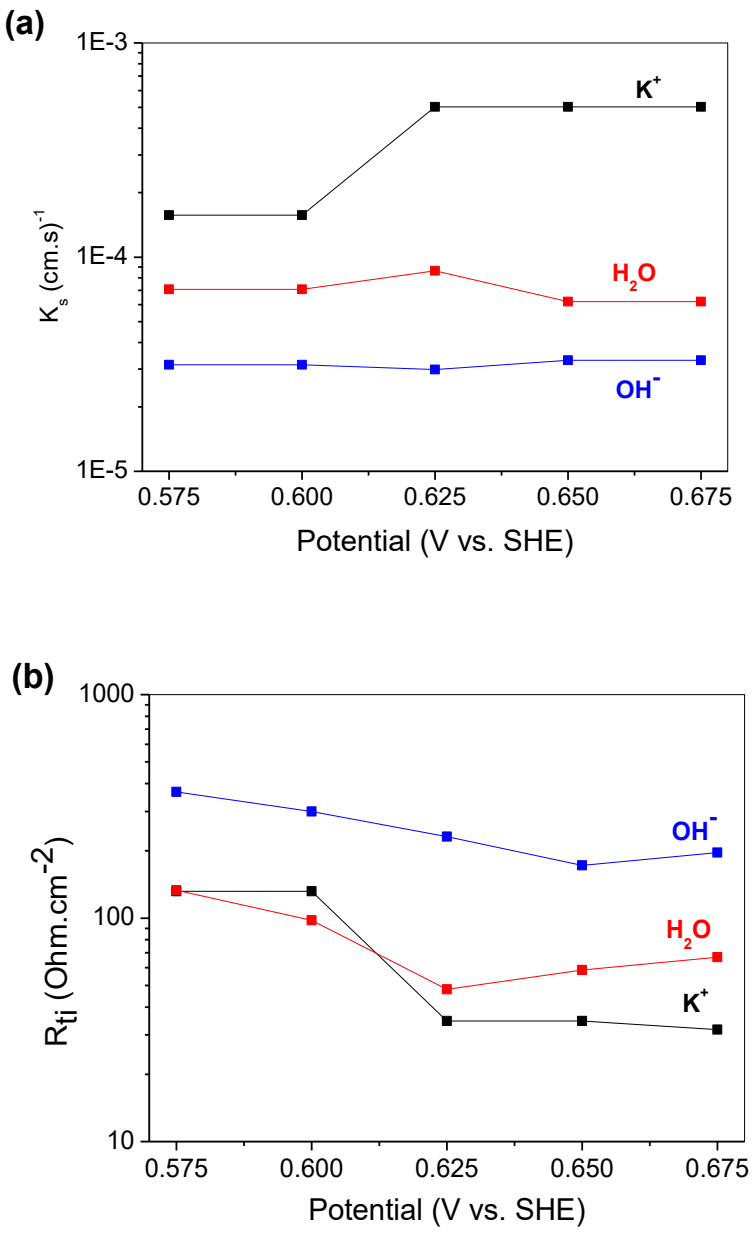

Figure 4.8: (a) Transfer kinetics and (b) transfer resistance of K^+, H_2O and OH^- as a function of applied potential at the interface between the thin film of Ni/Fe-LDH and KOH 1 mol/L solution.

The evolutions of the relative concentration per volume unit, $C_i - C_o$, and the mass per area unit, m_i - m_o are determined. The variation in concentration of the transferred species (Fig. 6a) is estimated from the concentration/potential transfer function at low frequencies[12] $\left|\frac{\Delta C_i}{\Delta E}\right|_{\omega \to 0} = \int_{E0}^{Ei} -\frac{G_i}{K_i}\, dE$.

From 0.575 V to 0.675 V/SHE, K^+ and water molecules are transferred from the LDH to the electrolyte whereas OH^- is transferred from the electrolyte to the LDH when the material is oxidized.

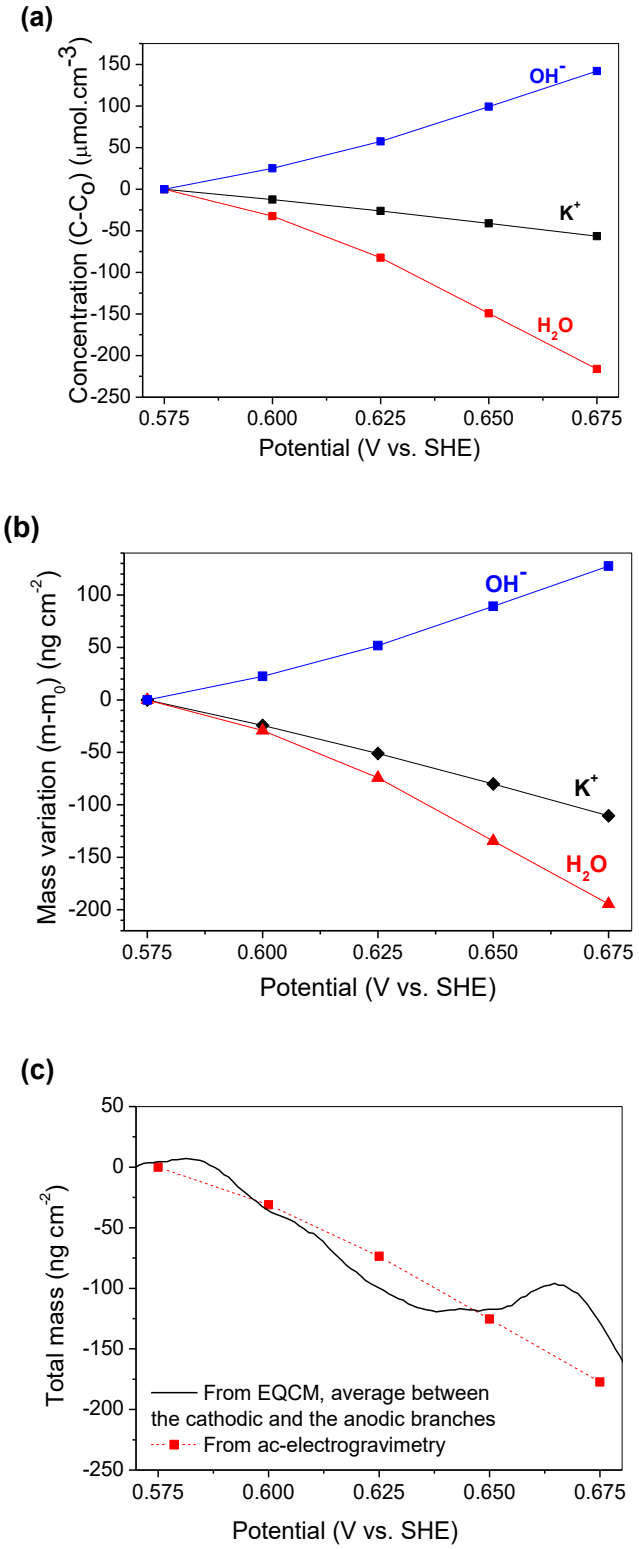

Figure 4.9: (a) Relative concentration and (b) mass variation of K^+, H_2O and OH^- as a function of applied potential at the interface between the thin film of Ni/Fe-LDH and KOH 1 mol/L, (c) comparison between the mass variation estimated with the *ac*-electrogravimetry and that obtained from EQCM (10 mV/s).

The relative exchanged mass variation for each species is obtained with equation (4.5):

$$m_i - m_o = (C_i - C_o)M_i d_f \quad (4.5)$$

and is represented in Fig. 4.9b. Both mass variations in the cathodic and anodic branches of EQCM were averaged and compared to the total exchanged mass found with the *ac*-electrogravimetry technique (Fig. 4.9c). Both mass variations plotted in Fig. 4.9c present the same slope from 0.575 V to 0.650 V which evidences the accuracy of the developed model, at least for the studied potential range.

However, the rising mass of the EQCM data from 0.650 V to 0.675 V does not perfectly fit with the *ac*-electrogravimetry data, which could be attributed to the occurrence of possible non-reversible reactions. The most probable one is the interlayered oxygen evolution reaction in the potential range [0.650; 0.675] V. The assumption is that interlayered water molecules are oxidized leading to the generation of O_2 molecules and H^+ that are released from the interlayer space. Once the oxygen evolution reaction is stopped, water molecules return into the interlayer space by diffusion.

The two concomitant mechanisms of intercalation/deintercalation of water and probable oxidation catalysis of water molecules into the interlayer spacing will be explained in the discussion section.

For a better insight regarding the specific sites of each determined transferred species (K^+, H_2O and OH^-), complementary techniques were performed on the sample; *i.e.* EDX, XPS analyses and *in situ* XRD under LDH film polarization.

4.5 EDX and XPS analyses

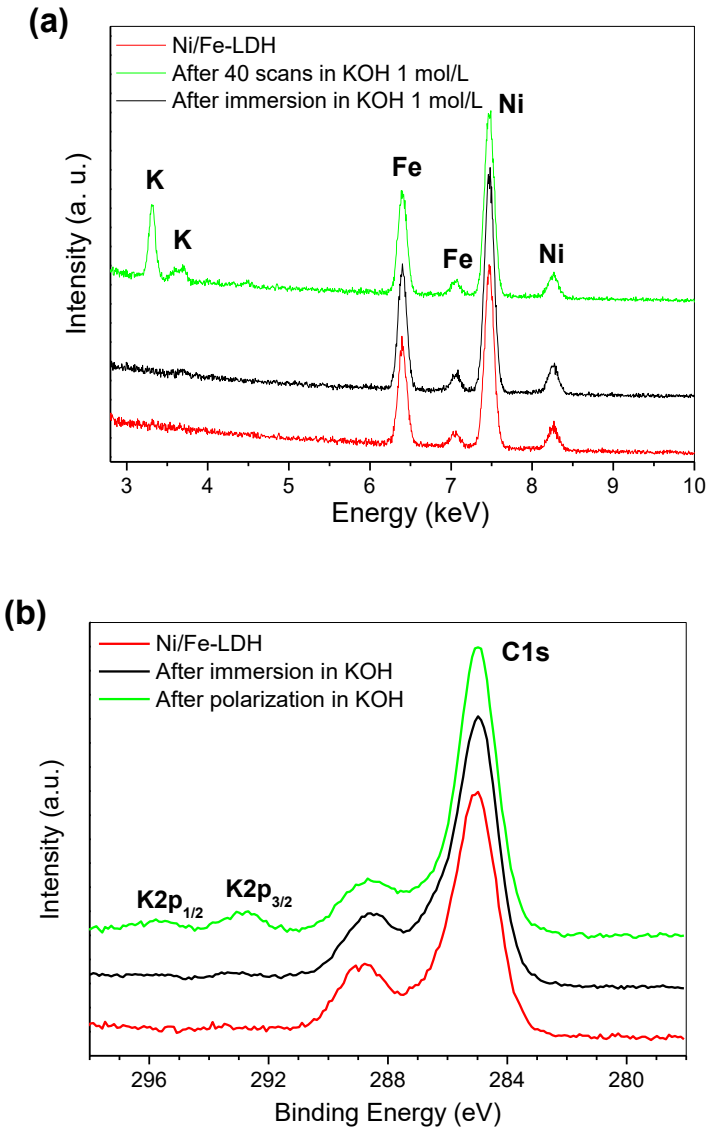

Figure 4.10: EDX measurements of the presence of potassium, nickel and Iron, (b) XPS measurement of $K2p_{1/2}$ and $K2p_{3/2}$ peaks of a thin film of dried LDH before immersion in KOH 1 mol/L, after immersion in KOH 1 mol/L and after immersion and polarization in KOH 1 mol/L.

It is noted that both anions and cations are detected in the electrogravimetric study which were tentatively attributed to the species contributing to charge compensate a redox process and a capacitive process. Therefore, to confirm the electroadsorption of cations (capacitive process) onto the LDH nanosheets, EDX and XPS analyses were performed on a thin film of LDH deposited on the gold electrode of a quartz resonator (i) before any experiment, (ii) after the immersion in KOH 1 mol/L for 40 minutes and (iii) after 40 cycles of polarization from

0.45 V/SHE to 0.72 V/SHE at 10 mV/s in KOH 1 mol/L. Before analyses, LDH films that were in contact with KOH 1 mol/L were rinsed in NaOH 10^{-4} M to eliminate the excess of KOH. The EDX and XPS spectra shown in Fig. 4.10 do not evidence the presence of potassium ions in LDH thin film neither before immersion nor after a simple immersion (40 min) in KOH 1 mol/L. On the contrary, potassium was detected in the film having undergone 40 cycles of Ni oxidation/reduction in KOH 1 mol/L by both EDX and XPS analyses; *i.e.* both (i) down into the LDH bulk material and (ii) onto the surface (10 nm) of the LDH film. These findings evidence the electro-adsorption of potassium cations onto the nano-porous material.

4.6 *In situ* XRD analysis

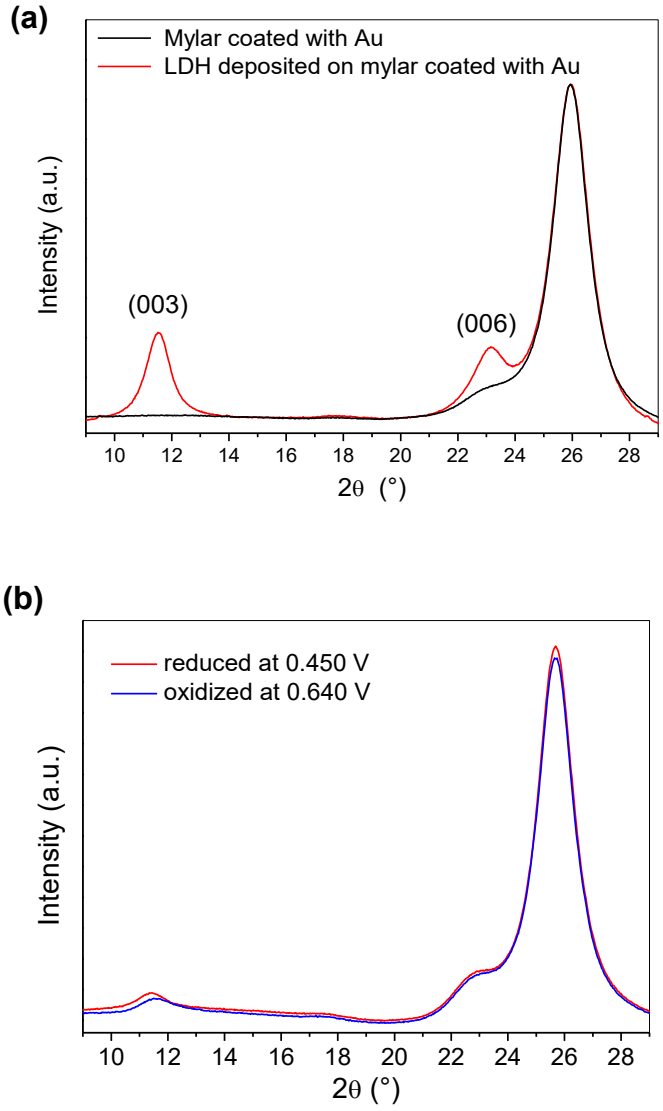

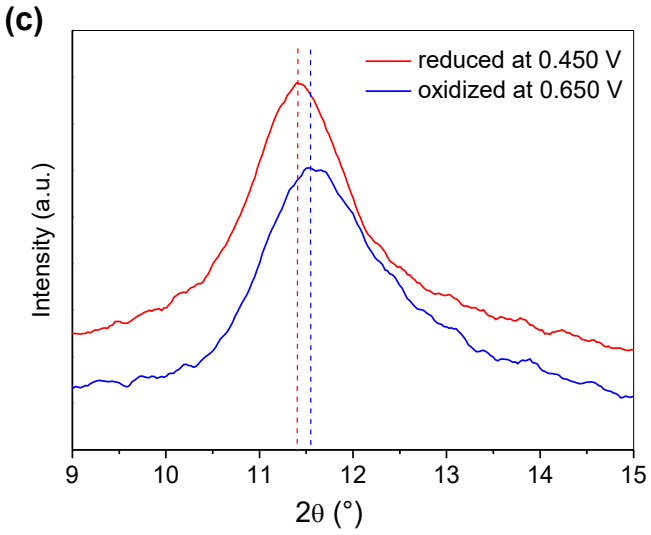

Figure 4.11: (a) XRD pattern of a mylar film coated with gold without and with a thin film of Ni/Fe-LDH. (b) *In situ* XRD patterns of a mylar film coated with gold and LDH under two different polarizations: 0.450 V (red curve) and 0.640 V (black curve). The position of the (003) peak of LDH and mylar are respectively located at 11° and 26°. (c) Magnification of the position of the (003) peak under two polarizations. A shift can be observed.

For a better insight of the influence of the electrochemical treatment undergone by LDH particles in aqueous KOH 1 mol/L (*i.e.* cyclic oxidation and reduction of Ni and induced intercalated species), XRD analyses were performed on LDH particles deposited on a gold-based electrode (see section 2.2.3, Fig.2.4 and Fig. 4.11) which consists in a gold-coated mylar film. Experiments were realized in the range from 9 to 29° in 2θ.

Analyses were first conducted on (i) gold-coated mylar film (Fig. 4.11a, black line) and (ii) dried LDH particles deposited on gold-coated mylar film (Fig. 4.11a, red line). The faced-center cubic[245] gold is illustrated by the small broad band at 2θ = 23° and the diffraction peaks at 2θ = 26°. The position of (003) and (006) peaks of the LDH can be clearly evidenced around 11.5° and 23° (2θ), respectively.

Analyses were then conducted in KOH 1 mol/L solution after 40 cycles of polarization, successively (i) at 0.640 V (oxidation of some Ni(II) sites, Fig. 4.11b, blue line) and (ii) 0.450 V (reduction of Ni(III), Fig. 4.11b, red line). Analyses were performed five times. In the range from 22° to 24° in 2θ, the (006) peaks present a rather low signal to noise ratio due to the substrate (Fig. 4.11a). The gold characteristic diffraction peak at 2θ = 26° remained at the same position whatever the potential imposed. Thus, it was used as an internal reference to investigate the (003) LDH diffraction peak behavior; *i.e.* to investigate the basal distance evolution versus the applied potential.

Fig. 4.11c shows a zoom view of the XRD range between 9° and 15° in 2θ. The evaluation of the 003-period variation in solution is possible through the shift in position of (003) peak of LDH (Fig. 4.11c). Table 1 shows the shift in position of the 003-period for 5 successive experiments.

Experiment number	Applied potential (V)	Period (Å)	Error (Å)	Period variation (Å)
1	0.450	7.4280	0.0239	---
2	0.640	7.3619	0.0444	-0.0661
3	0.450	7.4426	0.0250	0.0807
4	0.640	7.3855	0.0449	-0.0571
5	0.450	7.4532	0.0270	0.0677

Table 4.2: Period obtained during 5 successive polarizations at 0.450 V (Ni reduction) and at 0.640 V (Ni oxidation in KOH 1 mol/L.

The Ni oxidation at 0.640 V (experiments 2 and 4 in Table 4.2) leads to the 003-period decrease, whereas the Ni reduction at 0.450 V (experiments 3 and 5) lead to the 003-period increase. The redox reactions involve a local withdrawal/expansion of d-spacing from the average value.

4.7 Discussion

The investigation of the *ac*-electrogravimetric behavior of nano-Ni/Fe-LDH 6/2 particles in KOH 1 mol/L indicates LDH pseudocapacitive properties of a mix cation and anion exchanger. Indeed, two different ionic species with different kinetics were detected, their contribution was attributed to two different processes (redox and capacitive). The layer positive charge increases due to oxidation of Ni(II) to Ni(III), it is balanced by intercalation of OH^- anions in the LDH interlayers. The intercalation of one OH^- anion follows the expulsion of two interlayered water molecules (Fig. 4.9a) according to the following equation (4.6):

$$[Ni^{II}_{6}Fe^{III}_{2}(OH)_{16-c}(OK)_c]^{2+}[(OH)_2]^{2-},4H_2O + x\ OH \Leftrightarrow \quad (4.6)$$
$$[Ni^{II}_{6-x}Ni^{III}_{x}Fe^{III}_{2}(OH)_{16-c}(OK)_c]^{(2+x)+}[(OH)_{2+x}]^{(2+x)-},(4-2x)H_2O + 2xH_2O + xe\text{-}$$

This phenomenon can be related to the free water transfer owing to conformational movements of electroactive film,[11] leading to the LDH layer contraction. Indeed, EXAFS analysis of polarized Ni/Fe-LDH 6/2 electrodes indicates that both Ni–O and Fe–O distances decrease to ~1.9 Å (from d(Ni–O) = 2.06 Å and d(Fe–O) = 2.01 Å in the unpolarized electrode).[246] The Ni–O bond shortening is consistent with the increase in Ni oxidation state.[5] Fe bond contraction is rather explained because of the lattice contraction that accompanies Ni oxidation imposes a stronger ligand field on the Fe(III) centers, thereby inducing crossover from a high-spin electronic structure to a low-spin state.[247] Fe–O distances of ~1.9 Å are consistent with low-spin Fe(III).[248] Moreover, by analogy to cationic clay minerals, the nature and the strength of forces that a water molecule experiences depend on its position within the pore space, that is here the distance to the LDH surfaces.[72] In clay minerals, crystalline swelling is controlled by a balance between strong forces of attraction and repulsion[74,73] and is more easily modeled by considering potential energies of attraction and repulsion.[75] By analogy to cationic clay minerals, the attraction potential energy should be electrostatic and dominantly arises from the Coulombic attraction between the positive surface charge sites caused by isomorphous substitution and the negative charge of the interlayer anions. Van der Waals interactions between adjacent layers may also contribute to the total potential energy of attraction. The potential energy of repulsion comes from the partial hydration potential energy of the interlayer anions and to a lesser extent the partial hydration potential energy of the positive surface charge sites. By analogy to swelling stages investigated by Lal and Shukla,[76] the charge increase due to Ni(II) to Ni(III) oxidation generates reinforced Coulombian charges which leads to a stronger osmotic pressure between the layers owing to expulsion of interlayered water molecules; i.e. the H_2O deintercalation is opposed by the electrostatic attraction between anions and positively charged layers of the LDH. During the cathodic sweep, the hydration of the anions is more important than the electroactive attraction between the anion and the positively charge layer. In this way, *ac*-electrogravimetric measurements are in good agreement with *in situ* XRD under polarization. The redox reactions are responsible for local withdrawal/expansion phenomena in agreement with the successive exclusion and insertion of interlayered water molecules in d-spacing. By analogy to cationic clay minerals, these results are in good agreement with those provided by Stucki et al.[249, 250,251]

In situ XRD under polarization has especially contributed to our current-day understanding of LDH hydration during cyclic oxidation/reduction. In addition, let us note that, EQCM revealed an irreversible redox reaction that was attributed to the O_2 evolution reaction according to the following equation (4.7):

$$[Ni^{II}_{6-x}Ni^{III}_{x}Fe^{III}_{2}(OH)_{16-c}(OK)_c]^{(2+x)+}[(OH)_{2+x}]^{(2+x)-},(4-2x)H_2O \rightarrow [Ni^{II}_{6-x}Ni^{III}_{x}Fe^{III}_{2}(OH)_{16-c}(OK)_c]^{(2+x)+}[(OH)_{2+x}]^{(2+x)-},(4-2x-z)H_2O + z/2\ O_2 + 2z\ H^+ + 2z\ e^- \quad (4.7)$$

The produced oxygen can be whether totally expulsed or partly sorbed into the macroporosity of the nanomaterial.

Concomitantly during the anodic sweep, the catalyzed oxygen evolution reaction leads to a decrease of the interfacial pH and allowed cation desorption from the negatively charged external surfaces. During the backward cathodic scan, when the current canceled, oxygen evolution reaction stopped. The interfacial pH became equal to the one of the bulk solution and allowed cation sorption on the external negatively charged surfaces. This phenomenon was evidenced by EDX and XPS analyses (K detection), in agreement with the following equation (4.8):

$$[Ni^{II}_{6-x}Ni^{III}_{x}Fe^{III}_{2}(OH)_{16-c}(OK)_{c}]^{(2+x)+}[(OH)_{2+x}]^{(2+x)-},(4-2x-z)H_2O + 2z\ H^+ \leftrightarrows$$
$$[Ni^{II}_{6-x}Ni^{III}_{x}Fe^{III}_{2}(OH)_{16-c}(OH)_{c}]^{(2+x)+}[(OH)_{2+x}]^{(2+x)-},(4-2x-z)H_2O + c\ K^+ + (2z-c)\ H^+ \quad (4.8)$$

When the oxygen evolution reaction stops, water molecules should diffuse into the interlayer space again, in agreement with the comparison between the EQCM and *ac*-electrogravimetry data.

Related to cation transfer, K^+ cations were demonstrated to be faster and more easily transferred especially at more anodic potentials (more than 0.625 V), in good agreement with the hypothesis of electroadsorption onto more accessible sites like edge surfaces once the pH decreases and tends to the pH_{PZNC} value during the anodic sweep. Compared to cationic clay minerals whose edge surface can be reversibly deprotonated[233, 252], the positively charged LDH basal surface should render the H of the ≡M-OH group more labile. Its lability should be amplified by the oxidation of the basal Ni(II). Thus, in the case of LDH, both edge surfaces and external basal surface sites are both cation sorption sites. The whole mechanism is summed up in Fig. 4.12.

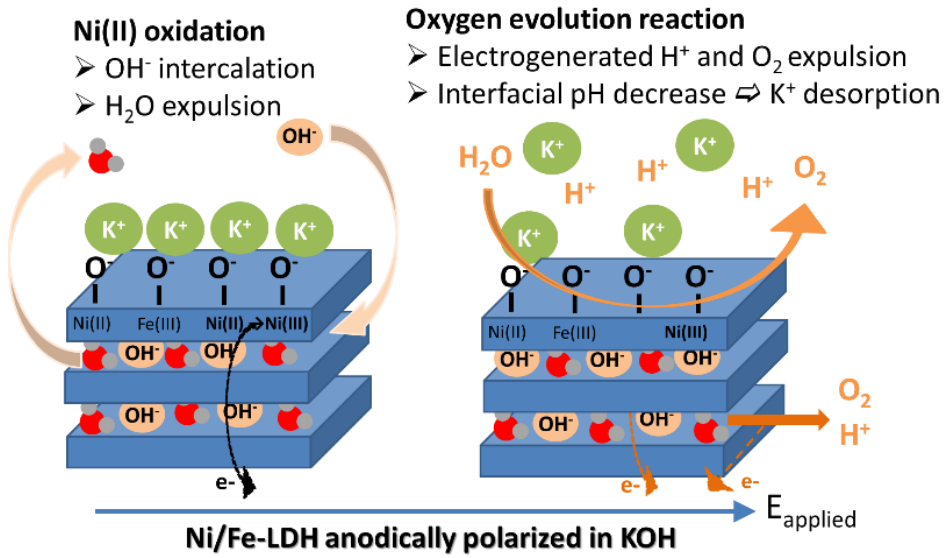

Figure 4.12: Scheme of the mechanism of the ionic and solvent transfers between the chem-Ni/Fe-LDH and the KOH 1 mol/L electrolyte and during redox reaction of Ni.

4.8 Conclusion

For the first time, this study investigates electrochemical reactions as well as both the related ionic and water transfers using of Ni/Fe-LDH 6/2 via electro-gravimetrical characterization. Experiments were specifically conducted under polarization in KOH 1 mol/L to differentiate the associated specific transfer sites (i.e. adsorption sites onto both edge and external basal surfaces, and intercalation sites). For a better insight, complementary techniques were performed by EDX and XPS analyses and *in situ* XRD under polarization.

Reversible Ni oxidation and reduction was observed using EQCM with a slow charge transfer. After 40 cycles, the film mass variation was reversible however complex.

Ac-electrogravimetry methodology allows identification of the nature of the charged and uncharged species as well as the kinetics ($K(K^+) > K(H_2O) > K(OH^-)$) and easiness of transfer, exchanged concentration and exchanged mass for each species at different polarizations. It led to demonstrate the nano-Ni/Fe-LDH pseudocapacitive properties of mix cation (K^+) and anion (OH^-) exchanger. It also led to demonstrate the water molecule transfer during the reversible redox reaction i.e. Ni oxidation generates reinforced Coulombian charges which leads to a stronger osmotic pressure between the layers owing to the expulsion of interlayered water molecules. The intercalation of one OH^- anion results from the expulsion/intercalation of two interlayered water molecules. This mechanism was further evidenced by *in situ* XRD analyses. The advanced electrogravimetric analysis led to demonstrate the existence of an irreversible oxidation reaction that was attributed to the O_2 evolution reaction

within the interlayer space. Concomitantly, the electrochemical control of pH variation at the coated interface, using catalyzed oxygen evolution reaction, allowed cation electroadsorption/desorption onto the external surfaces in agreement with the pH of zero point of net charge of the nano-Ni/Fe-LDHs. This phenomenon was further evidenced by EDX and XPS analyses.

For a better insight, we have to further investigate the mechanisms of the electroadsorption of different cations as well as the electrocatalytic properties of the interlayered water molecules and structural stability of the LDH while cycling. To do so, chapter 5 presents *operando* technique was developed and applied for the first time, at synchrotron SOLEIL (Saclay, France), by coupling EQCM measurements and structural characterization with a synchrotron XRD beam (20KeV) under polarization, in real time.

Chapter 5

Operando XRD coupled to electrogravimetric measurements for understanding the species transfer in Ni/Fe-LDH in basic electrolytes

5.1 Introduction

Layered double hydroxides (LDHs) are lamellar inorganic solids with a brucite-like structure ($Mg(OH)_2$), in which the partial substitution of trivalent $M^{(III)}$ for divalent $M^{(II)}$ metallic cations results in an excess of positive charges in the octahedral layers. This excess of positive charges is compensated by the presence of exchangeable hydrated anions in the interlayer space of the solid.[253] This leads to the general formula: $[M^{(II)}_{1-x}N^{(III)}_{x}(OH)_2]^{x+}(A^{n-}_{x/n}).mH_2O$, providing LDHs high capacity for anion exchange (2-3 meq/g).[254,16,255] Moreover, the synthesis of LDHs bearing electroactive metal cations within their structure enables reversible electrochemical oxidation and reduction[99, 214,161,215,216] making it possible to control ions and water molecules exchanges capacity (annex A, chapter 4) and thus to envisage breakthrough electrolysis processes for the capture and release of ions (energy storage, water treatment, industrial effluent treatment…). Indeed, for the first time, the investigation of the LDH electrochemical behavior confirmed the pseudo-capacitance properties of mix cation and anion exchanger. It also led to demonstrate the water molecules transfer during the reversible redox reaction involving the electroactive metal cations constituting the brucitic layers. This work was conducted using Ni/Fe-LDH 6/2 coated electrode (pH_{PZNC} equal to 8) in KOH 1M. This electrolyte ($pH = 14 >>> pH_{PZNC}$) was selected to envisage cationic sorption on the LDHs edge sites in agreement with Eq (5.1):

$$\equiv M\text{-}OH + C^+ \Leftrightarrow \equiv M\text{-}O^- + H^+ + C^+ \Leftrightarrow \equiv M\text{-}O^-C + H^+ \quad (5.1)$$

where M is a metal cation constituting the layered sheets and C^+ a cation adsorbed onto the surface.

Reversible oxidation/reduction reaction of the couple Ni(II)/Ni(III) was observed using EQCM with a slow charge transfer. The coupling of the electrochemical (EQCM and *ac*-electrogravimety) combined to the results of complementary physical techniques (EDX and XPS and *in situ* XRD) determined and

confirmed the nature of the transferred species. *Ac*-electrogravimetry identified the nature, in terms of molar mass, and related kinetics and concentration variation of each of the reversibly transferred species associated with the redox reactions involving Ni. These mechanisms are summed up in equation (5.2):

$$[Ni^{II}_{6}Fe^{III}_{2}(OH)_{16-c}(OK)_{c}]^{2+}[(OH)_{2}]^{2-},0.5H_2O + xOH^- \Leftrightarrow \quad (5.2)$$
$$[Ni^{II}_{6-x}Ni^{III}_{x}Fe^{III}_{2}(OH)_{16-c}(OK)_{c}]^{(2+x)+}[(OH)_{2+x}]^{(2+x)-},(4-2x)H_2O + 2xH_2O + xe^-$$

Ac-electrogravimety evidenced reversible anion intercalation/deintercalation into the interlayer spacing in agreement with the redox reactions leading to modulate the electric charge of the layers. Concomitantly, the electric charge modulation enabled the reversible transfer of water molecules by tuning the Coulombian interactions within the layers. This phenomenon was confirmed by *in situ* XRD under polarization. In addition, the induced electrochemical modification of the pH at the coated interface via catalyzed oxygen evolution reaction (OER) allowed cation electro-desorption onto the LDH external surfaces in agreement with the pH of zero point of net charge of the nano-Ni/Fe-LDHs (Eq. 5.3):

$$[Ni^{II}_{6-x}Ni^{III}_{x}Fe^{III}_{2}(OH)_{16-c}(O\mathbf{K})_{c}]^{(2+x)+}[(OH)_{2+x}]^{(2+x)-},(4-2x)\mathbf{H_2O} + \mathbf{cH^+} \Leftrightarrow \quad (5.3)$$
$$[Ni^{II}_{6-x}Ni^{III}_{x}Fe^{III}_{2}\ (OH)_{16-c}(O\mathbf{H})_{c}]^{(2+x)+}[(OH)_{2+x}]^{(2+x)-},(4-2x-\mathbf{z})\mathbf{H_2O + cK^+}$$

Then adsorption is reversibly obtained in agreement with the pH value increase when OER stopped during the cathodic sweep.

This phenomenon was evidenced by combining EDX/XPS analyses. Finally, the comparison between EQCM and *ac*-electrogravimetry postulated the electrocatalytic properties of interlayered water molecules.

In this chapter, we investigated further the mechanisms of electroadsorption of cations as well as the electrocatalytic properties of the interlayered water molecules. Concerning electroadsorption of cations, electrochemical and electrogravimetrical techniques compared the influence of the cation nature on current and mass. Three monovalent cations were investigated in the following electrolytes: LiOH, KOH and CsOH. For a better insight, *ac*-electrogravimetry technique couples electrochemical impedance and mass/potential transfer functions measurements at different polarizations. In agreement with reversible redox reactions, it allowed identification of transferred species and determination of associated transfer kinetics. It also determines easiness of transfer and concentration variation of transferred cations to investigate the influence of the nature of the electrolytic cation on the intercalation/deintercalation of both anions and water, in agreement with the redox reactions involving Ni(III)/Ni(II) within the Ni/Fe-LDH 6/2.

To investigate the electrocatalytic properties of the interlayered water molecules, an *operando* technique was developed and applied for the first time, at synchrotron SOLEIL (Saclay, France), by

coupling EQCM measurements and structural characterization with a synchrotron XRD beam (20KeV) under polarization. In real time, under polarization of chem-Ni/Fe-LDH coated film, we recorded current, frequency related to mass, and parameters of the 003-peak of the XRD pattern simultaneously. Measurements enabled to differentiate water deintercalation, caused reinforced Coulombian interactions in agreement with OH^- intercalation, from the oxidation of water into the interlayer spacing by OER.

5.2 *Coupled* electrochemical and gravimetric measurements

5.2.1 Global mass variation within one cyclic polarization

A series of polarization cycles was performed during 4900 s between 0.440 V/SHE and a potential depending on the supporting electrolyte: 0.710 V/SHE for KOH and LiOH 1 mol/L, 0.730 V/SHE for LiOH 1 mol/L, 0.840 V/SHE for CsOH 0.1 mol/L. The current and frequency variation related to the mass of the film were recorded for each of the electrolytes KOH, CsOH, LiOH 1 mol/L and CsOH 0.1 mol/L. Table 5.1 (pp 145-146) summarizes the characteristics of the investigated electrolytes (activity coefficient, calculated pH and measured pH). For each electrolyte, the activity coefficient is dependent on the electrolytic cation.[148] The initial pH was measured and calculated by the pHreeqC software using Thermoddem® database. The pH value differed slightly from one electrolyte to another (table 1) following pH(CsOH 1 mol/L) > pH(KOH 1 mol/L) > pH(LiOH 1 mol/L) >> pH(CsOH 0.1 mol/L). For each investigated electrolyte, Ni/Fe-LDH presents a characteristic electrogravimetric behavior. Figure 5.1 illustrates the electro-gravimetrical characteristic response obtained during the last cycle at 4900 seconds for each of the electrolytes.

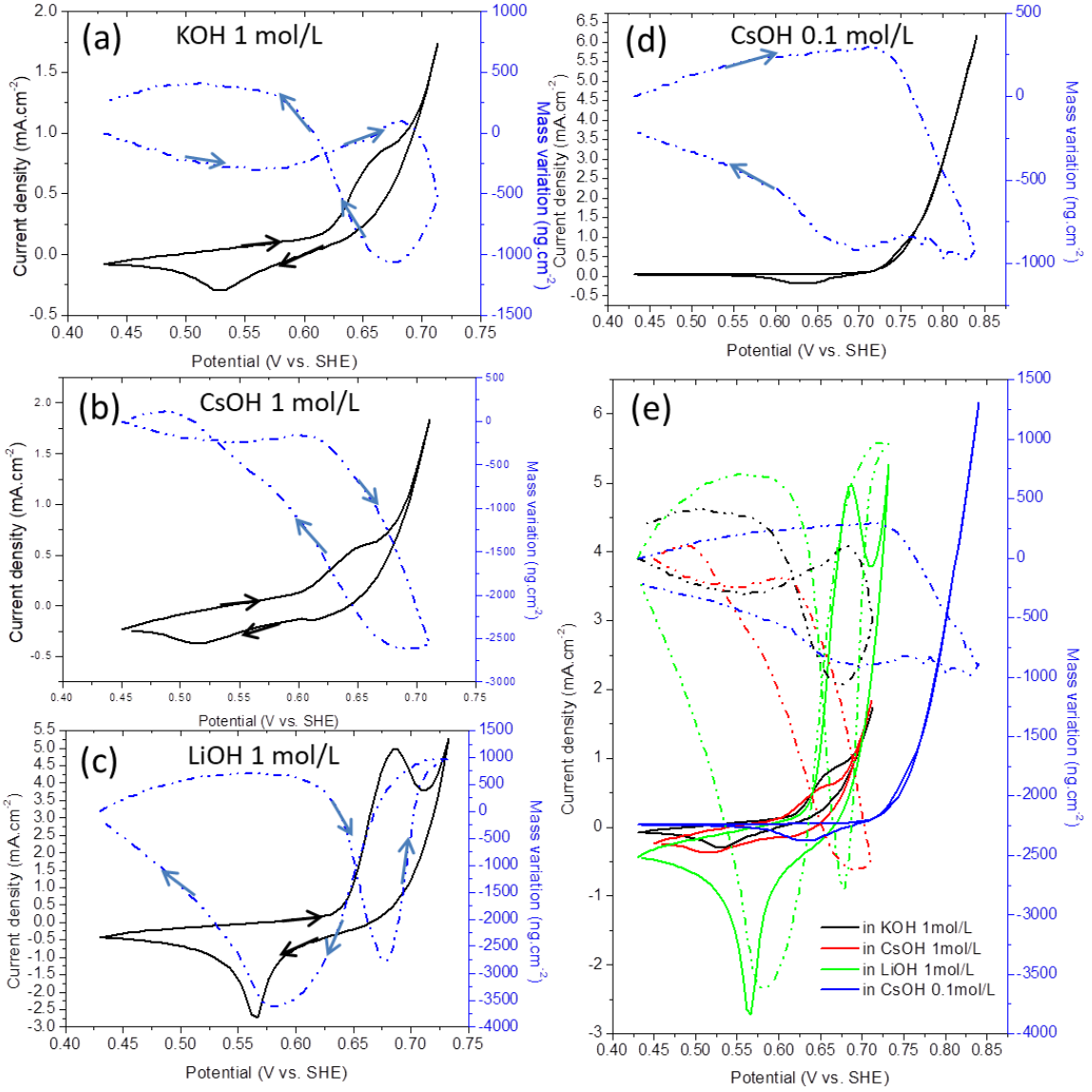

Figure 5.1: Current and mass variation curves obtained from Ni/Fe-LDH for cycle number 60 under cyclic polarization between 0.440 V/SHE and a potential depending on the supporting electrolyte (0.710 V/SHE for KOH and LiOH 1 mol/L, 0.730 V/SHE for LiOH 1 mol/L, 0.84V/SHE for CsOH 0.1 mol/L).

As previously studied for Ni/Fe-LDH in KOH 1mol/L, (chapter 4) during the anodic sweep (Fig. 5.1a), Ni(II) redox active sites were oxidized to Ni(III)[99,5] and oxygen evolution reaction (OER) was started in agreement with the electro-catalytic properties of Ni/Fe-LDHs.[241,157,242] During the cathodic sweep, oxidized Ni(III) sites were reduced to Ni(II). The same behavior is observed for other electrolytes (Fig. 5.1b, c, d). Ni(III)/Ni(II) redox peaks appear at different potentials depending on the investigated electrolyte. For 1 mol/L electrolytes, it is situated in the same range of potentials, however slightly shifted to the anodic potential according to: $E_{Ni(III)/Ni(II)}$ (LiOH 1 mol/L) = 0.63 V/SHE

> $E_{Ni(III)/Ni(II)}$ (KOH 1 mol/L) = 0.60 V/SHE > $E_{Ni(III)/Ni(II)}$ (CsOH 1 mol/L) = 0.58 V/SHE, following the pH value of the supporting electrolytes according to: pH (CsOH 1 mol/L) > pH (KOH 1 mol/L) > pH (LiOH 1 mol/L). For CsOH 0.1 mol/L, it is approximately 60 mV shifted to more anodic potential ($E_{Ni(III)/Ni(II)\ CsOH\ 0.1M}$= 0.69 V/SHE) compared to that of CsOH 1 mol/L. This leads to $E_{Ni(III)/Ni(II)\text{-}Ni/Fe\ 6/2\ LDH}$ (V/SHE) ≈ -0.08×pH +1.8 in the investigated pH range.

The shape of the mass response also depends on the electrolyte. As previously studied for chem-Ni/Fe-LDH in KOH 1 mol/L (chapter 4), different species are simultaneously involved. During the anodic sweep, the global mass increase (slope 1) highlights the OH^- intercalation, simultaneously with Ni(II) oxidation. The subsequent mass decrease (slope 2) is concomitant to the OER. From previous *ac*-electrogravimetric study (chapter 4), it was modeled that the decrease in the interfacial pH value enables the electrodesorption of K^+ onto the external basal surfaces. It was also concluded that H_2O molecules are driven out from the interlayer space as the OH^- species are intercalated when some Ni(II) are oxidized. During the cathodic sweep, the counterflux of these species was expected. The mass increase (slope 3) is concomitant to the electroadsorption of K^+ as the interfacial pH increases as well as the intercalation of the water molecules. Finally, the mass decrease (slope 4) is due to the deintercalation of OH^- during Ni(III) reduction.

In LiOH 1 mol/L, the anodic sweep shows a mass gain (slope 1) followed by a mass loss (slope 2). The competition of the different phenomena seen above with KOH 1 mol/L solution could be responsible for the inversion of slopes compared to that of KOH 1 mol/L. A possible explanation is supported by the different kinetics transfer for OH^- and Li^+, due to the lower pH of the LiOH 1 mol/L solution, or an easier desorption of Li^+ than that of Cs^+ and K^+.

In CsOH 1 mol/L and 0.1 mol/L, the global mass variation shape shows principally a mass loss during the anodic sweep (slope 1), and a mass gain during the cathodic sweep (slope 2). We assume that the entry of OH^- having a low molar mass is hidden by the loss of Cs^+ whose molar mass is about 8 times higher. In CsOH 0.1 mol/L, except for Ni(III) reduction peak, the current density is positive even during the cathodic sweep. These phenomena could be attributed to the remarkable Cs^+ properties for which, in the case of cationic clay minerals, the adsorption is assumed to clearly increase when the ionic strength decreases.[256, 257,258] Indeed, during the cathodic sweep, and below the Ni(III) reduction peak, the positive current accompanied by the slow increase in mass is characteristic of a capacitive current associated to the adsorption of Cs^+. During the anodic sweep between 0.440 V and 0.740 V/SHE, the same phenomenon pursues with a capacitive current density of 20 to 40 µA/cm^2 (10 mV/s).

EQCM technique only provides an overview of the global transferred mass and cannot give precise information on the nature and kinetics of the transferred species. It is challenging to deconvolute each

species contribution into gravimetric and dynamic components with EQCM results as the global cyclic electrogravimetry response is recorded at a certain scan rate (*i.e.* at certain kinetics). Therefore, coupling both QCM and electrochemical impedance spectroscopy techniques (*ac*-electrogravimetry) was performed. It allowed comparing the kinetics and concentration variation of the species in the different electrolytes.

The nature and kinetics of ions and water molecules transfers in each of the supporting electrolytes cannot be concluded regarding EQCM, as the mass variation is a global mass transfer of potentially several species, thus *ac*-electrogravimetry is needed and the results are discussed thereafter.

5.2.2 Ac-electrogravimetry

Ac-electrogravimetry was investigated for Ni/Fe-LDH in CsOH and LiOH 1 mol/L (Fig. 5.2) and in KOH 1 mol/L (Fig. 4.7). (Ni/Fe-LDH *ac*-electrogravimetry behavior was not investigated in 0.1 M supporting electrolyte; this concentration prevents the obtainment of a significant signal. Phenomena recorded in KOH 1 mol/L have already been discussed in Chapter 4. Here, the *ac*-electrogravimetry simulation (Fig. 5.2) at 0.650 V/SHE shows that whatever the investigated electrolyte, the same species are reversibly transferred: a flux of anions (OH^-) and, a counterflux of dehydrated cations (Cs^+, K^+, Li^+) and free water molecules.

The simulation of the results obtained by *ac*-electrogravimetry at different potentials enabled to determine the transferred concentrations (Fig. 5.3) of each of the species contributions in the different electrolytes. This shows the transfer of cations to the LDH during oxidation, as well as the counterflux of OH^- and H_2O. It has been proved in another study on Ni/Fe-LDH in KOH (chapter 4) that cations are electrosorbed/desorbed onto the external surfaces following equation (5.4):

$[Ni^{II}_6Fe^{III}_2(OH)_{14}(OC)_2]$, $[OH]_2$,(4-y) $H_2O + 2yH^+ \leftrightarrows [Ni^{II}_6Fe^{III}_2(OH)_{14}(OH)_2]$, $[OH]_2$,(4-y) $H_2O + (2y-2)H^+ + 2C^+$ (5.40)

where C^+ is a cation (K^+, Cs^+, Li^+).

OH^- anions are transferred from the electrolyte to the interlayer space during the anodic sweep. This is in agreement with other studies demonstrating the intercalation of OH^- while Ni is oxidized to preserve electroneutrality. For the three electrolytes used in this study, free water molecules are also reversibly transferred from the interlayer space to the electrolyte during the anodic sweep (Eq. 5.5).

$[Ni^{II}_6Fe^{III}_2(OH)_{14}(OH)_2]$, $[OH]_2$,(4-y) $H_2O + xOH^- \leftrightarrows [Ni^{II}_6Ni^{III}_xFe^{III}_2(OH)_{14}(OH)_2]$, $[OH]_{2+x}$,(4-y) $H_2O + xe^-$ (5.5)

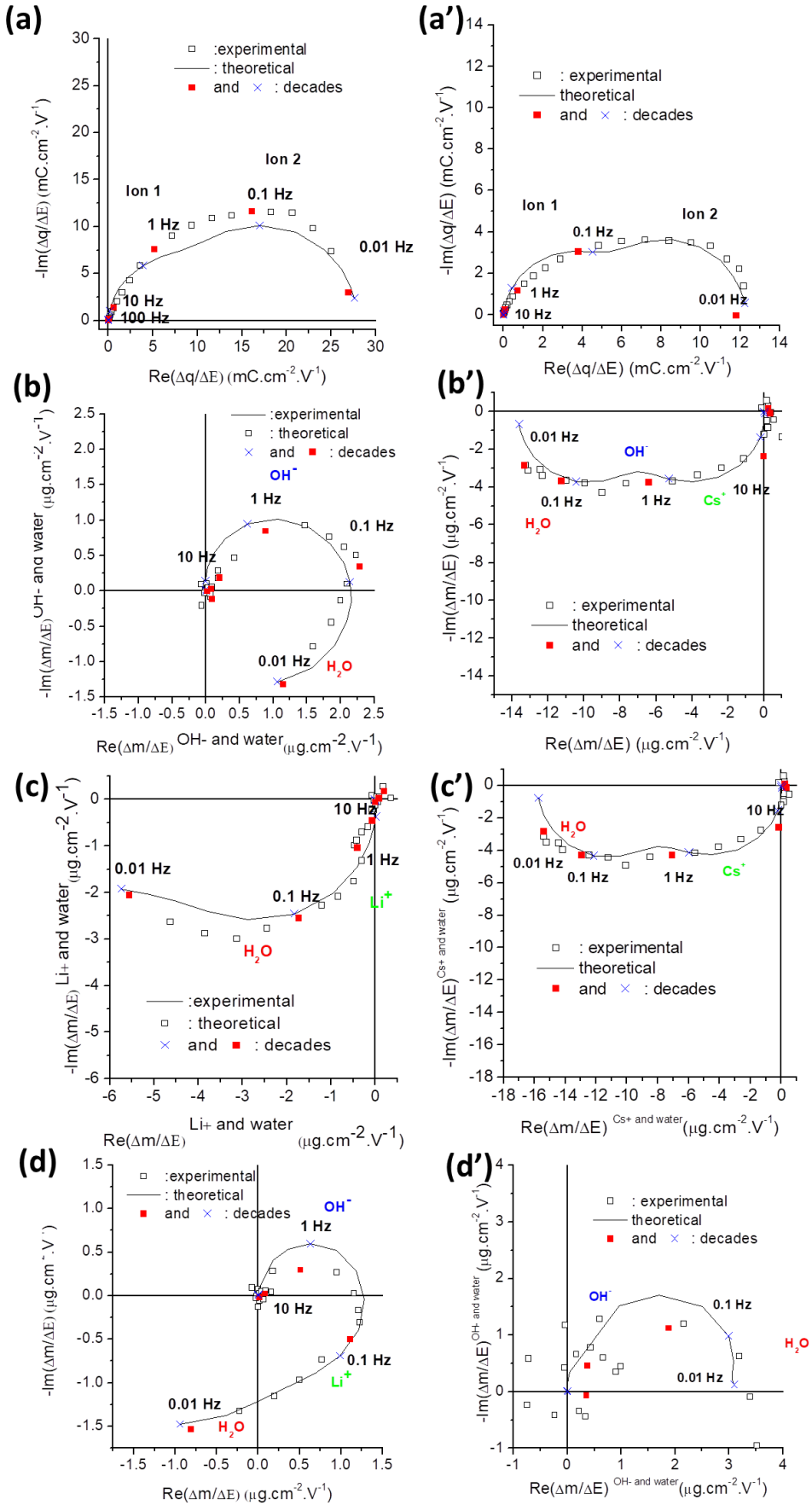
(a)
:experimental
: theoretical
and : decades
Ion 1
Ion 2
1 Hz
0.1 Hz
0.01 Hz
10 Hz
100 Hz
-Im(Δq/ΔE) (mC.cm-2.V-1)
Re(Δq/ΔE) (mC.cm-2.V-1)
(a')
: experimental
theoretical
and : decades
Ion 1
Ion 2
0.1 Hz
1 Hz
10 Hz
0.01 Hz
-Im(Δq/ΔE) (mC.cm-2.V-1)
Re(Δq/ΔE) (mC.cm-2.V-1)
(b)
:experimental
: theoretical
and : decades
OH-
1 Hz
0.1 Hz
10 Hz
0.01 Hz
H2O
-Im(Δm/ΔE) OH- and water (μg.cm-2.V-1)
Re(Δm/ΔE) OH- and water (μg.cm-2.V-1)
(b')
0.01 Hz
OH-
0.1 Hz
1 Hz
Cs+
10 Hz
H2O
: experimental
theoretical
and : decades
-Im(Δm/ΔE) (μg.cm-2.V-1)
Re(Δm/ΔE) (μg.cm-2.V-1)
(c)
10 Hz
1 Hz
0.01 Hz
0.1 Hz
Li+
H2O
:experimental
: theoretical
and : decades
-Im(Δm/ΔE) Li+ and water (μg.cm-2.V-1)
Re(Δm/ΔE) Li+ and water (μg.cm-2.V-1)
(c')
10 Hz
H2O
0.01 Hz
0.1 Hz
1 Hz
Cs+
: experimental
theoretical
and : decades
-Im(Δm/ΔE) Cs+ and water (μg.cm-2.V-1)
Re(Δm/ΔE) Cs+ and water (μg.cm-2.V-1)
(d)
:experimental
: theoretical
and : decades
OH-
1 Hz
10 Hz
0.1 Hz
Li+
0.01 Hz
H2O
-Im(Δm/ΔE) (μg.cm-2.V-1)
Re(Δm/ΔE) (μg.cm-2.V-1)
(d')
: experimental
theoretical
and : decades
OH-
0.1 Hz
0.01 Hz
H2O
-Im(Δm/ΔE) OH- and water (μg.cm-2.V-1)
Re(Δm/ΔE) OH- and water (μg.cm-2.V-1)

Figure 5.2: Fitting of the experimental data of a thin film of nano-Ni/Fe-LDH 6/2 in LiOH 1M (a) Δq/ΔE TF, (b) Δm/ΔE TF, (c) Δm/ΔE cation + water partial TFs (after removing the contribution of OH^-), (d) Δm/ΔE anion + water partial TFs (after removing the contribution of Li^+). Fitting of the experimental data of a thin film of nano-Ni/Fe-LDH 6/2 in CsOH 1M (a) Δq/ΔE TF, (b) Δm/ΔE TF, (c) Δm/ΔE cation + water partial TFs (after removing the contribution of OH^-), (d) Δm/ΔE anion + water partial TFs (after removing the contribution of Cs^+).

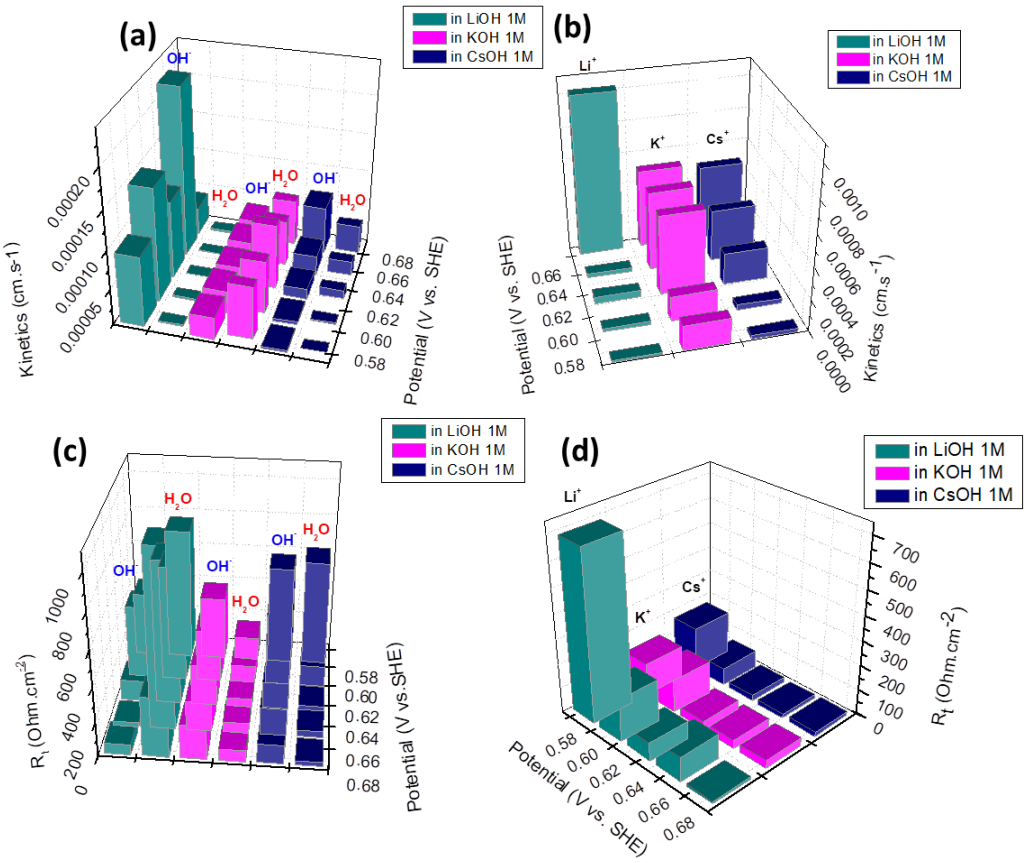

Figure 5.3: *ac*-electrogravimetric results of Ni/Fe-LDH electrodes in three aqueous electrolytes (LiOH, KOH and CsOH 1M). Evolution of the kinetic parameters, K_i ($cm.s^{-1}$) is shown, for intercalated water molecules and anions (a) and cations (b). Evolution of the transfer resistance values, Rt_i is shown, for intercalated water molecules and anions (c) and cations (d).

By comparing kinetics of OH^- in different supporting electrolytes (Fig. 5.3a), it is observed that OH^- is slower than H_2O in KOH 1 mol/L, but faster than H_2O in LiOH and CsOH 1 mol/L. OH^- has the fastest transfer kinetics in LiOH 1 mol/L (10^{-4}cm/s), followed by KOH 1 mol/L (2 10^{-5} cm/s) and CsOH 1 mol/L (from 4 10^{-6} to 5 10^{-5} cm/s), probably because of the intense charge for the oxidation of Ni(II) to Ni(III) sites.

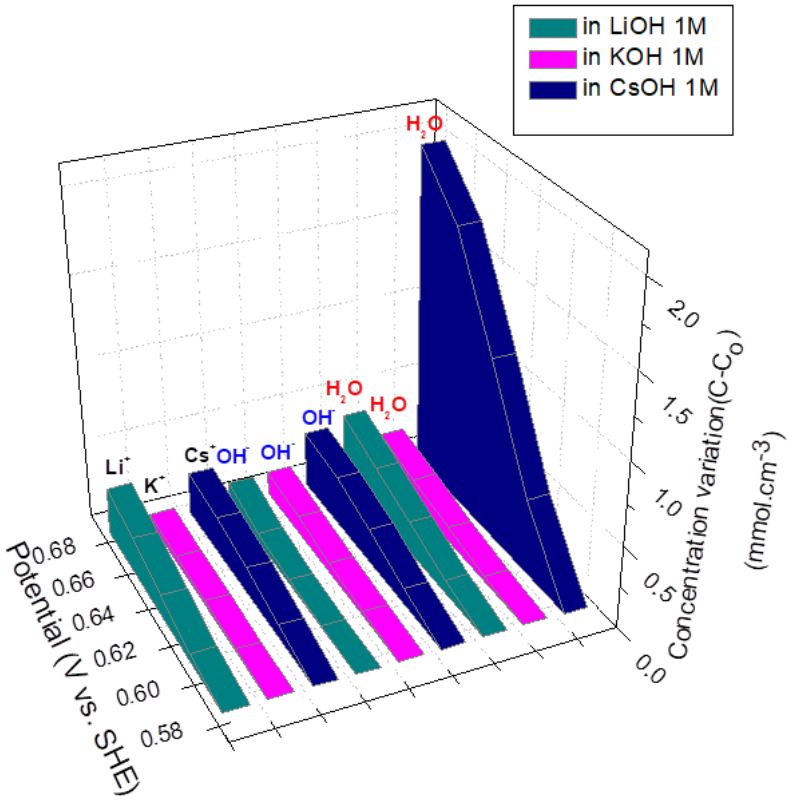

Figure 5.4: Evolution of the relative concentration, $C_i - C_O$, of each species, over the potential range [0.575 V; 0.675 V], considering three aqueous electrolytes (LiOH, KOH and CsOH 1M).

The highest transferred OH^- concentration (Fig. 5.4) is calculated in CsOH 1 mol/L (300 µmol/cm^3), followed by KOH 1 mol/L (150 µmol/cm^3) and LiOH 1 mol/L (140 µmol/cm^3). In LiOH 1 mol/L, OH^- is only intercalated at the highest potentials (*i.e.* 0.65V and 0.675V vs. SHE), contrarily to KOH and CsOH solution where OH^- is intercalated from 0.575V to 0.675V. That can be explained due to the anodic shift of the Ni oxidation peak in LiOH 1M (which also means that the concentration of OH^- is lower at the interface).

Regarding the behavior of reversibly transferred H_2O, it has the lowest transfer kinetics (Fig. 5.3a) in LiOH 1 mol/L (4 10^{-6}cm/s) followed by KOH 1 mol/L (7 10^{-4}cm/s) and CsOH 1 mol/L (2 10^{-5}cm/s for the most anodic potential).

Deintercalation of water molecules is the highest (Fig. 5.4) in CsOH 1 mol/L (2000 µmol.cm^{-3}). This can be explained because the highest concentration of intercalated OH^- is also found in CsOH 1 mol/L. There is around six times more reversibly deintercalated H_2O than intercalated OH^- in CsOH 1 mol/L. In both electrolytes KOH 1 mol/L and LiOH 1 mol/L, both concentrations of intercalated OH^- are

similar. However, with regard to intercalated OH^-, there is three times more deintercalated H_2O in LiOH (with low kinetics) and two times more deintercalated H_2O in KOH 1M (with high kinetics).

Comparing the cation behavior, K^+ is slightly faster than Cs^+ at 0.675 V/SHE (≈4 10^{-4}cm/s) (Fig. 5.3b). In comparison, Li^+ is 2.5 faster (1 10^{-3}cm/s). This comparison can be related to the known diffusion coefficient in bulk (table 5.1) whose values are comparable in terms of scale $d(Cs^+) < d(K^+) < d(Li^+)$. The lowest transfer kinetics was calculated for CsOH 1M, for the more cathodic potential (2.375 10^{-5}). This value is in good agreement with the capacitive phenomenon observed in CsOH 0.1M in which the transfer kinetics should be even lower.

These results enable to understand the global mass variation *versus* applied potential reported in Fig. 5.1. In CsOH and KOH 1 mol/L, the transfer kinetics of cations, anions and water molecules is comparable. This is the reason why the shape of the mass *vs.* E curve is quite similar. The differences are only localized in the highest concentration of reversibly transferred OH^-, H_2O and cations in CsOH 1 mol/L. Compared to the gravimetric curve shape obtained in KOH 1 mol/L, the one obtained in CsOH highlighted the contribution of the Cs^+ cations in agreement with their molar mass that is almost 8 times higher than that of OH^- (Fig. 5.4).

The electrogravimetrical curve obtained in LiOH 1 mol/L (Fig. 5.1c) can be differentiated from the others. During the anodic sweep, a huge decrease in mass is observed in the range [0.625; 0.700] V/SHE followed by a huge increase in mass in the range [0.700; 0.740] V/SHE. In comparison with data acquired in KOH (Fig. 5.1a) or CsOH 1 mol/L (Fig. 5.1b), the differences are localized in both kinetics and concentration of reversibly transferred species. The phenomenon related to the mass increase in range [0.700V; 0.740] V/SHE was not investigated by *ac*-electrogravimetry due to water oxidation reaction. Nevertheless, the global gravimetric decrease during the anodic sweep can be explained by the reversible intercalation of OH^- while 3 times more H_2O are deintercalated and Li^+ is desorbed. In the range [0.700V; 0.740] V/SHE, the only way to explain this high increase is the transfer of species towards whose global mass is positive *i.e.* the sum of masses from which OH^- intercalation dominates compared to the deintercalation of water molecules and desorption of cations.

5.2.3 Global mass variation *versus* incremented polarization cycle

In each investigated supporting electrolyte, the electrogravimetrical behavior of Ni/Fe-LDH during the linear potential cycling is presented versus time in Fig. 5.5.

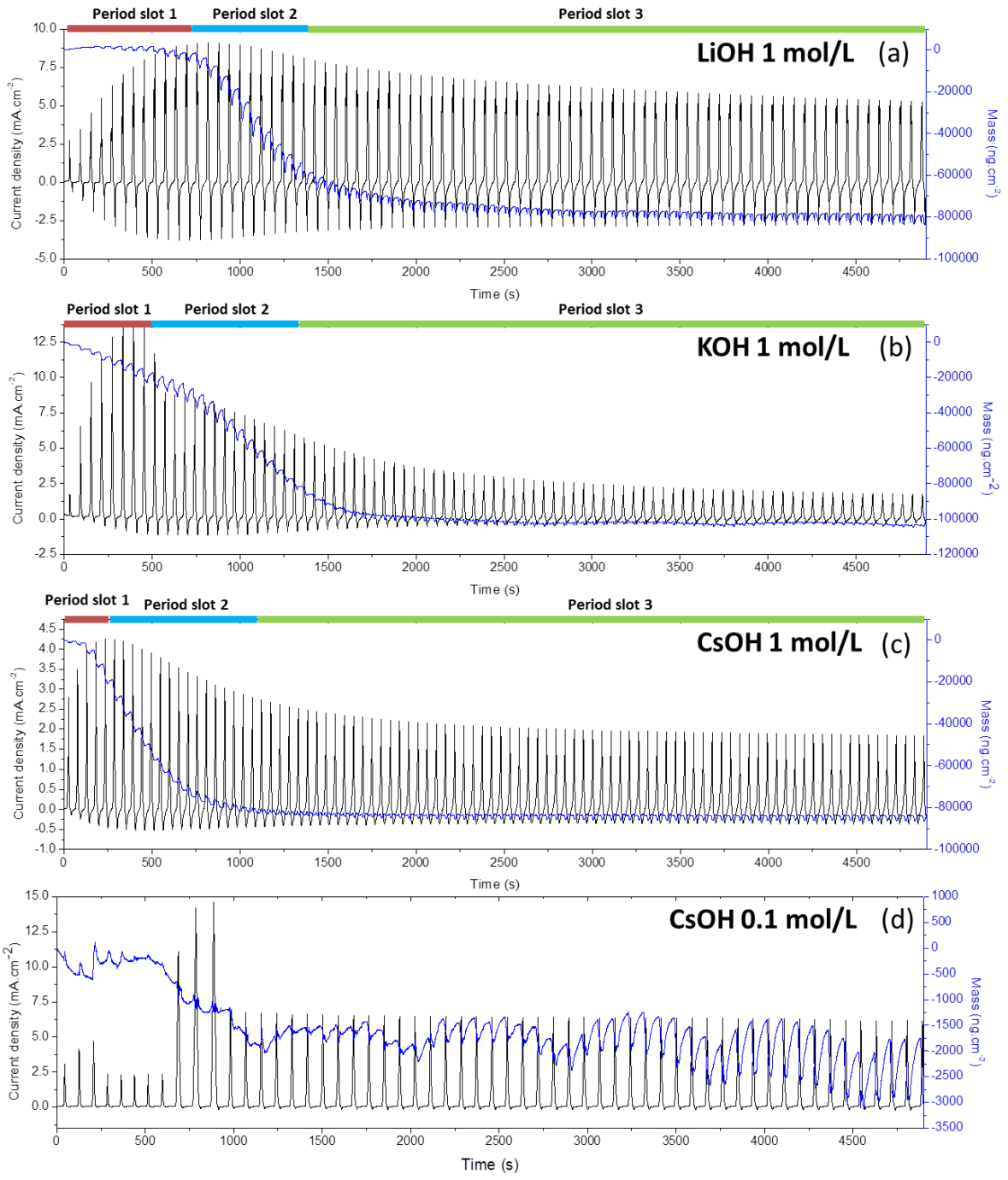

Figure 5.5: Current and mass variation obtained from Ni/Fe-LDH versus time under cyclic polarization between 0.44V/SHE and a potential depending on the supporting electrolyte (0.710 V/SHE for CsOH 1 mol/L (c) and KOH 1 mol/L (b), 0.73V/SHE for LiOH 1 mol/L (a), 0.840 V/SHE for CsOH 0.1 mol/L (d), the scan rate is 10 mV/s

The maximum positive current density is related to the OER whereas the maximum negative current density is related to redox active Ni(III) reduction peak. Table 5.1 summarizes exhaustively the electro-gravimetrical performances of Ni/Fe-LDH *i.e.* the potential of Ni(III)/Ni(II) peaks, OER was determined from the maximum intensity at the most anodic potential, intensity of Ni(III) reduction peak and OER peak and mass variation until the last cycle.

Table 5.1: Physical and chemical characteristics of CsOH, KOH and LiOH 1 mol/L and CsOH 0.1 mol/L.

Electrolyte	**Activity coefficient of the electrolyte**	**Calculated pH (pHreeqC)**	**Measured pH**	**Ion diffusion coefficients in bulk solution D_{bulk} x 10^{-10} m^2/s [144,145]**	**Potential of the Ni reduction and oxidation peaks (V/SHE)**	**Intensity of the Ni peak (red) (mA/cm^2)**	**Intensity of the highest OER peak (mA/cm^2)**	**Variation from highest OER peak intensity to peak at 4900sec**	**Mass variation from initial to final 5000s (ng/cm^2)**	**Ionic and water transfer kinetics at the LDH interface (cm/s) (simulation)**
CsOH 1M	0.966	13.87	14	22 ± 1	0.55V (red) and difficult to say (ox)	7^{th} cycle	**4.25** 5^{th} cycle **Maybe not the same limit**	-56.7%	86299	
KOH 1 mol/L	0.968	13.77	13.8	21 ± 4	0.54V (red) and 0.65V (ox) Difference: 0.12V	**13^{th} cycle**	8^{th} cycle **14.78**	-88.3%	104395	K^+ 1.57E-4 to 5.03E-4 H_2O 6.21E-5 to 8.64E-5

										OH^- 2.99E-5 to 3.30E-5
LiOH 1 mol/L	0.973	13.61	13.62	10 ± 1	0.57V (red) and 0.69V (ox) Difference: 0.12V	15^{th} cycle **1.47E-3**	**9.098** 14^{th} cycle	-42.2%	-83525	Li^+ 2.3419E-5 to 4.72-5
CsOH 0.1 mol/L	0.997	12.89	12.70	22 ± 1	0.63V (red) and difficult to say (ox)	The last peak is the most intense	**14.63** 11^{th} cycle **Maybe not the same limit**	-58%	3019	Cs^+ 2.38E-5 to 4.76E-4 H_2O 9.43E-7 to 3.96E-5 OH^- 5.09E-6 to 6.55E-5

In 1 mol/L electrolytes (Fig. 5.5A, B, C), the electrogravimetrical behavior of Ni/Fe-LDH can be divided into three distinct periods. During the first period slot (Fig. 5.5, period slot 1), the current density of the Ni(III) reduction reaction increases versus incremented cycles and is shifted towards more cathodic potentials with incremented cycles. The same phenomenon occurs with Ni(II) oxidation reaction (however it is not visible in Fig. 5.5). These enhanced reactions are in agreement with the increase in some irreversibly oxidized Ni(III) clusters that enhance the conductivity of the Ni/Fe-LDH[151,149,150,152,259] (chapter 4). The maximum current density of Ni(III)/Ni(II) peaks is reached after 15 cycles in LiOH 1 mol/L, 13 cycles in KOH 1 mol/L and 7 cycles in CsOH 1 mol/L (Fig. 5.6) and should be correlated to the highest conductivity of the material. This hypothesis is corroborated as the increase in Ni(II) oxidation current density during the whole first period slot conducts to an enhanced catalysis of the OER *i.e.* the intensity of the OER increases and is progressively shifted to lower potential. The maximum intensity of OER is reached after 14 cycles in LiOH 1 mol/L, 8 cycles in KOH 1 mol/L and 5 cycles in CsOH 1 mol/L. Simultaneously to the increase in conductivity and in the catalysis of OER, the mass of the film remains constant from one cycle to another which highlights the stability of the film even under OER. It is to be noted that for KOH 1 mol/L, the experimental optimization of the anodic scanning potential within this first period increased the OER which enhances a premature mass decrease that is explained in the next paragraph.

During the second period slot, (Fig. 5.5, period slot 2) the current densities due to both H_2O oxidation and Ni(III)/Ni(II) system decrease versus incremented cycles and are slightly shifted towards more anodic potentials. Those concomitant phenomena in agreement with those previously described during the first slot period clearly highlight the duality between conductivity and interfacial pH. The increase in conductivity drastically enhances OER which is responsible for the progressive and continuous decrease in the interfacial pH value versus incremented cycles. This renders water oxidation potential, more anodic. Depending on the supporting electrolyte, the OER current density decreases sharply (table 5.1) following the order: KOH 1 mol/L (-88%) > CsOH 1 mol/L (-58%) > LiOH 1 mol/L (-42%). The interfacial pH dramatic decrease is responsible for the anodic shift and decrease in Ni(III)/Ni(II) redox peaks as OH^- anions are less available at the interface. Thus, the kinetics of the reaction (equation (5.6), adapted from equation (5.1) (chapter 4) is slower:

$$[Ni^{II}_6Fe^{III}_2(OH)_{16-c}(OC)_c]^{2+}[(OH)_2]^{2-},4H_2O + xOH^- \leftrightarrows \quad (5.6)$$
$$Ni^{II}_{6-x}Ni^{III}_xFe^{III}_2[(OH)_{16-c}(OC)_c]^{(2+x)+}[(OH)_{2+x}]^{(2+x)-},(4-2x)H_2O + 2xH_2O + xe^-$$

where C^+ is the investigated cation. Once the Ni(II)/Ni(III) peaks and OER shift and become less intense, the mass value decreases sharply compared to the initial value (table 5.1). The decrease in mass is aggravated for CsOH 1M, followed by LiOH 1M and KOH 1M. This phenomenon will substantially be discussed thereafter.

In the third period slot (Fig. 5.5, period slot 3), only the mass response reaches a plateau in both electrolytes, indicating a stationary evolution of the mass transfer. In the meantime, the catalysis of OER is still becoming more and more anodic, indicating progressive and continuous decrease of the interfacial pH value.

Regarding CsOH 0.1 mol/L electrolyte, Fig. 5.5D shows the electrogravimetrical behavior of Ni/Fe-LDH. In comparison with 1 mol/L supporting electrolytes, pH is largely inferior. The investigated potential range is thus larger to observe the reactions of interest. Let us first note that, as in KOH 1M, the optimization of the anodic scanning enhanced dehydration phenomenon. This phenomenon was intentionally caused between 0 and 1000 seconds such as to comfort premature dehydration in agreement with OER. A priori, the electrogravimetrical curves do not present phenomenon as remarkable as those observed in the 1 M supporting electrolytes. Ni oxidation-reduction current peaks increase slowly and do not reach any maximum during the 4900 seconds of cycling. From 1000s, the current density of the OER decreases softly versus time with the slight mass decrease. The mass variation reaches a first plateau during the range [1500-3000] s. Let us remember that for CsOH 0.1M the variation of pH value is one unit lower than that in the 1M supporting electrolytes, and the investigated potential range is quite larger in comparison with those carried out in the other supporting electrolytes. Thus, the low decrease in mass and in OER intensity should be attributed to the larger scanning range that leads to the reversible increase in pH value at the interface when the OER is stopped.

Regarding this preview analysis, the aim is to understand further the mechanisms of transfer that are at the origin of the difference in behavior for the investigated electrolytes. *Ac*-electrogravimetry enabled to determine the nature (in terms of molar mass), kinetics and concentration of the reversible transfer of charged and uncharged species. To investigate further the non-reversible reaction of water oxidation within interlayer spacing, it was necessary to analyze the basal distance during the cyclic polarization. Consequently, *operando* XRD coupled to EQCM measurements are developed in the next section.

5.3 *Operando* XRD coupled to EQCM measurements

5.3.1 Principle

A home-made electrochemical cell (Fig. 2.5) was developed to simultaneously record EQCM measurements and the XRD pattern of the material at synchrotron SOLEIL (SIXS line). The whole setup is described in section 2.2.3.

Several parameters were simultaneously recorded under XRD and cyclic polarization at room temperature: current, frequency shift of the quartz related to the mass variation of the LDH film and characteristic/details of the (003)-peaks of the LDH pattern. Concerning the latter parameter, one scan of the 003-peak was recorded at each second. Each peak was then fitted with a Lorentzian curve to plot the width, intensity and position of the peak versus time.

For a better insight into the structural stability of the Ni/Fe-LDH under potential cycling and for a further investigation of the species transfer into the interlayer space, *operando* XRD coupled to electrogravimetric

measurements were performed in KOH 1M, LiOH 1M and CsOH 0.1M solutions. The experiment could not be conducted in CsOH 1M as the X-ray synchrotron beam was mainly adsorbed by the electrolyte leading to too low signal that could not be interpreted. The 003-peak of the LDH diffractogram was recorded *versus* time, successively, in the absence of any polarization (4900 seconds) and against under polarization (potential cycling for 4900 seconds). The 003-peak was fitted with a Lorentzian curve to determine its Full width at half the maximum intensity (FWHM) and its position *versus* time and applied potential. The variation of the peak intensity can be related either to the change in electronic density or to the change in the electronic density distribution in the c-axis. The analysis of only one (00l) peak does not allow determining the relevant phenomenon, thus the peak intensity is not shown and discussed thereafter. The width of the peak is an indicator of the de-organization level of the layers within a sheet. The position of the 003-peak (in Q-range) was converted to obtain the LDH basal distance.

The monitoring of the position of the coated Ni/Fe-LDH 6/2 003-peak was conducted for 4900 seconds without polarization in the investigated supporting electrolytes. It was then conducted under polarization. Figure 5.6 illustrates the data acquired for Ni/Fe-LDH 6/2 in LiOH 1M.

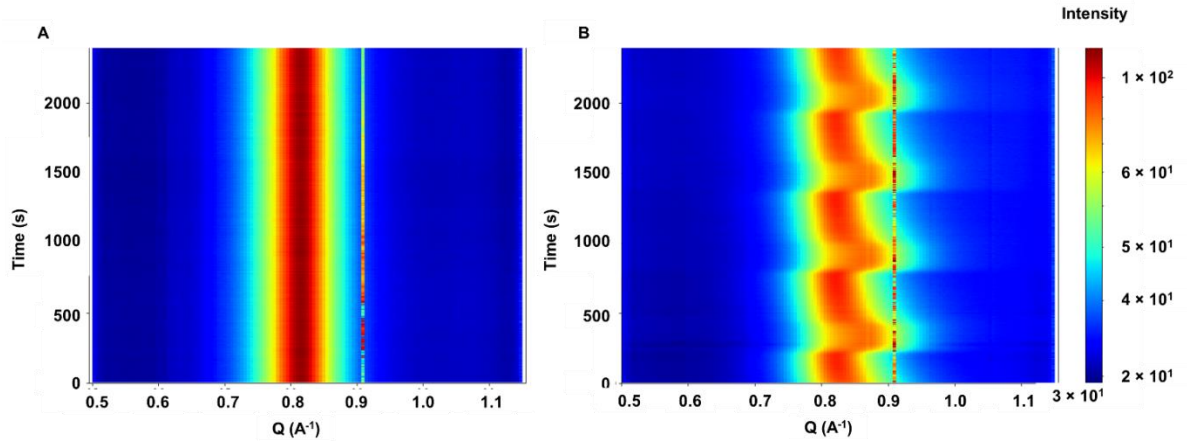

Figure 5.6: ***Evolution of the*** **003-peak of the Ni/Fe-LDH in LiOH 1 M (A) in the absence of any polarization and (B)** ***under cyclic polarization between 0.440 V/SHE and 0.710 V/SHE, at 1mV/s***

Without polarization, the 003-peak position, intensity and width remained constant *versus* time. This result clearly demonstrated that the chemical anionic exchange between interlayered CO_3^{2-} and OH^- anions coming from the 1 and 0.1M bulk solutions was done.

5.3.2 Versus incremented polarization cycle

Figure 5.7 shows *operando* XRD data acquired in KOH, LiOH 1 mol/L and CsOH 0.1 mol/L. It shows the electrogravimetric behavior of Ni/Fe-LDH 6/2 under cyclic polarization in agreement with the evolution of the LDH basal distance via the monitoring of the 003-peak.

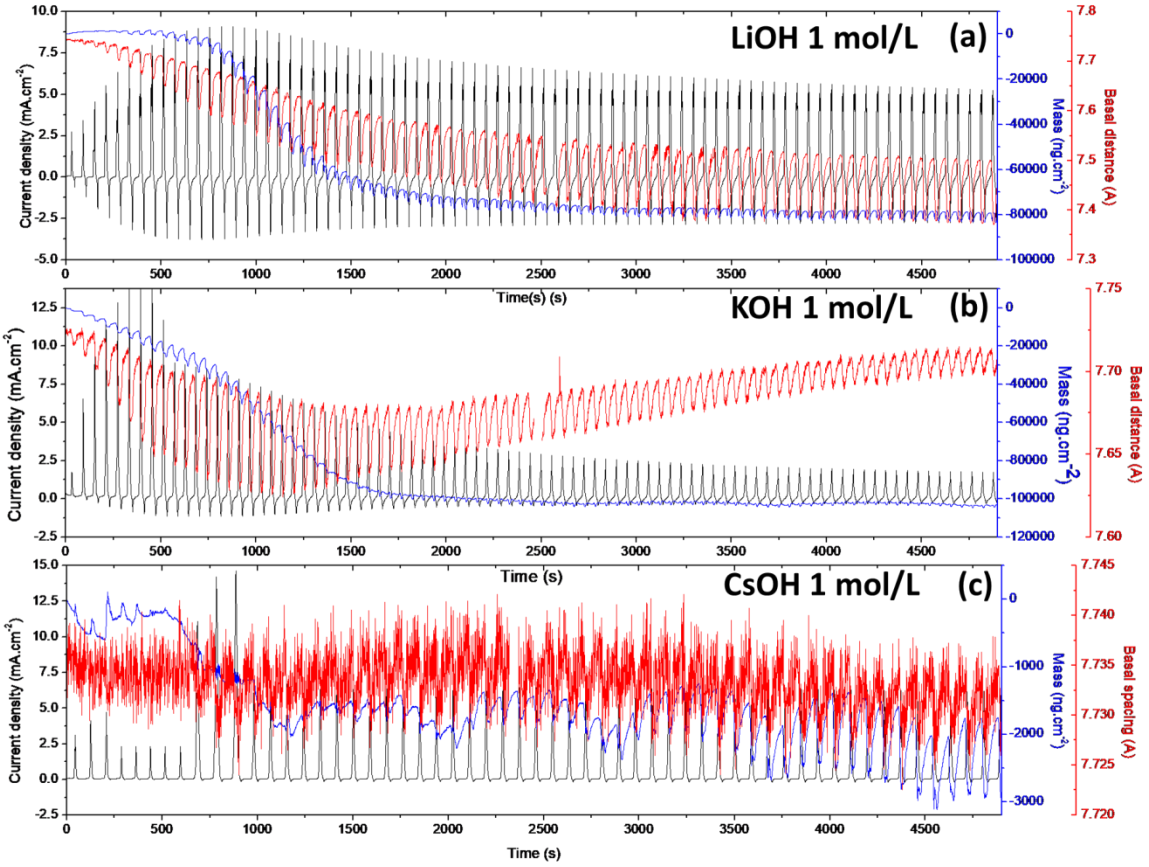

Figure 5.7: *Operando* XRD in LiOH 1 mol/L (a), KOH 1 mol/L (b) and CsOH 0.1 mol/L (c).

Whatever the investigated supporting electrolyte, the 003-peak is observed over the whole cycling experiment which demonstrates that the LDH structure is conserved *versus* time and applied potential. Under polarization cycle, both full width at half maximum (FWHM) and basal distance vary. Nevertheless, they vary anticorelatively and with a similar percentage of variation which indicates, in agreement with the Scherrer equation, that the number of stacked layers within a sheet remains globally constant (in the range 8-10 layers). This result clearly highlights the conservation of crystallographic structure of the Ni/Fe-LDH and specifically the number of stacked layers in each particle *versus* polarization and time. This result, associated to the constant mass response in period slot 3 (see Fig. 5.7), is related to the absence of any dissolution, dissolution/reprecipitation or crystallization of the LDH material.

For LiOH 1mol/L solution, the basal distance decreases during period slot 1 (Fig 5.7), while the mass of the film remains constant and the conductivity and OER are enhanced. In a first approach, this is consistent with the increase of some irreversibly oxidized Ni(III) clusters within the lattice. Indeed, this is responsible for the increase in the distortion in the lattice due to the irreversible shortening of Ni–O and Fe–O distances decrease to ~1.9 Å (from d(Ni–O) = 2.1 Å and d(Fe–O) = 2.0 Å[246]). This distortion progressively and irreversibly prevents deintercalated water to reversibly intercalate within the Ni/Fe-LDH layers. This phenomenon aggravates the electrostatic attraction between anions and positively charged layers. Both concomitant phenomena are responsible for progressively collapse the Ni/Fe-LDH particle layers. At the same time, the mass oscillation around a stationary value is explained by a mass balance between interlayered species intercalation/deintercalation and external species adsorption/desorption while Ni-Fe-LDH dehydrates.

During period slot 2 in LiOH 1mol/L (Fig. 5.7), the basal distance continues to decrease. This phenomenon is observed while the LDH reached its highest conductivity as already discussed. At the same time, the gravimetric curve shows a drastic decrease. Alone, the increase of Ni(III) clusters within the lattice (leading LDH layers to collapse) does not explain those concomitant evolutions. Together, they clearly highlight another one concomitant phenomenon. The only way to explain both gravimetric and basal distance decrease during period slot 2 is the catalysis of the interlayered H_2O, in agreement with the OER enhancement and the demonstrated constant characteristic structure of the Ni/Fe-LDH *versus* polarization and time. Those concomitant phenomena are then responsible for the progressive decrease in the intensity of OER and Ni(II) oxidation peak which potential shifts anodically in consequence of a decrease of the interfacial pH.

An OER may oxidize the interlayered H_2O molecules, the resulting products are O_2 gas and H^+ that should diffuse to the bulk of the solution according to reaction (5.7):

$$[Ni^{II}_6Fe^{III}_2(OH)_{14}(OLi)_2][OH]_2,4H_2O \rightarrow [Ni^{II}_6Fe^{III}_2(OH)_{14}(OLi)_2][OH]_2,(4-y)\ H_2O + 2y\ e^- + y/2\ O_2 + 2y\ H^+ \quad (5.7)$$

H^+ is probably either expulsed to the solution bulk or is bonded to an interlayer OH^- (and this event may be followed by the intercalation of another OH^-). During the cathodic sweep, when the current reaches zero, H_2O molecules should be reversibly reintercalated.

This reaction is not reversible, thus H^+ and O_2 transfers cannot be observed by the *ac*-electrogravimetry technique. It is to be noted that for KOH 1 mol/L in the first period slot, the experimental optimization of the anodic scanning potential increased the OER and enhanced a dehydration phenomenon which generated the premature mass decrease.

During period slot 3, the basal spacing oscillated around a stationary value (Fig. 5.7a). In that case, the constant oscillation is essentially attributed to the reversible intercalation/deintercalation of H_2O in agreement with equation 1. This steady state could be due to the competition between an equivalent mass

gain and a mass loss. The mass gain is caused by a constant diffusion of water due to the slowdown of the water oxidation at low pH. The mass loss is caused by OER still active although slowed down.

Like in LiOH 1 mol/L, in the presence of KOH 1 mol/L (Fig. 5.7b), the basal spacing behaves similarly during period slots 1 and 2 to reach its minimum value at the end of period slot 2. However, during period slot 3, the basal spacing oscillated with an increase of the mean value as the mass of the film reached a plateau and OER intensity decreases sharply by 86%. This huge decrease in intensity is in agreement with:

- a much lower pH at the interface (and less available OH^-) as in LiOH 1 mol/L, that allows to rehydrate the anions in the interlayer space

- the chemical reduction of Ni(III) sites (in agreement with $E_{Ni(III)/Ni(II)\text{-}Ni/Fe\ 6/2\ LDH} > E_{O2/H2O}$) that prevents the conductivity to be enhanced and is responsible for the drastic decrease in the intensity of the oxidation-reduction peaks. OH^- is irreversibly deintercalated.

The mass oscillation around a stationary value is explained by a mass balance between interlayer species intercalation/deintercalation and external surface species adsorption/desorption while globaly OH^- deintercalate, K^+ desorbs and Ni/Fe-LDH rehydrates. This is in agreement with the mass constancy, the decrease in pH at the interface and the decrease in the distortion in the lattice, the bondings Ni–O and Fe–O distances increase from ~1.9 Å to d(Ni–O) = 2.1 Å and d(Fe–O) = 2.0 Å.[246] By analogy, it is in agreement with the data acquired on structural properties of smectites bearing Fe(II)/Fe(III) iron.[251]

In CsOH 0.1 mol/L, the basal spacing oscillated around a "stationary" value *versus* incremented polarization cycles, which denotes a stability of the interlayer distance. By the end of the experiment, the intensity of the OER only decreased by 58% (and the majority of the decrease occurs between the 11^{th} and 12^{th} cycle during the optimization of the potential range). Within the whole cycling, the intentional enhancement of the dehydration phenomenon caused by OER did not sufficiently affect the basal spacing because *ac*-electrogravimetry demonstrated that for the reversible redox reaction according to equation (5.1), Ni(III)/Ni(II) redox active couple within the Ni/Fe-LDH lattice (in KOH 0.1 mol/L) is able to reversibly deintercalate 6 H_2O for each OH^- intercalated in agreement with equation (5.1). The *operando* XRD conducted in CsOH 0.1 mol/L is in quite good agreement with such a water hydration.

5.3.3 Within one cycle in LiOH 1M

For a better illustration of the hydration phenomenon, Fig. 5.8 shows the electrogravimetrical curve and the interlayered spacing variation *versus* the cyclic potential variation obtained by *operando XRD* in LiOH 1 mol/L.

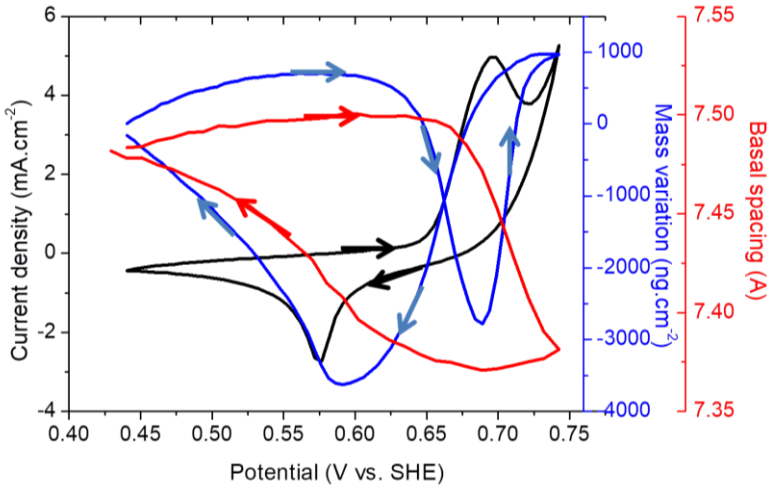

Figure 5.8: Electrogravimetrical curve (in blue) and interlayered spacing variation (in red) and current (in black) *versus* the applied potential obtained *operando* XRD in LiOH 1 mol/L, scan rate at 1 mV/s.

In an I-V cycle in LiOH 1 mol/L, during the cathodic sweep (Fig. 5.8), as long as the current density is positive, the basal spacing value is at its minimum. At the zero current and just below the zero current, there is a slight increase in the period value. The slope of the basal spacing curve is sharper at the Ni(III) reduction peak. After the Ni(III) reduction peak, the current density is still negative. During the anodic sweep, it is still negative as the basal spacing continues to increase slightly. Once the current value becomes positive, the period is constant and decreases sharply from the Ni(II) oxidation peak to reach its minimum value.

The positive current (corresponding to both Ni and water oxidation reactions) is responsible for a first decrease in mass, followed by an increase and finally a 2nd decrease in mass in EQCM, owing to a loss of Li^+ at the surface, a gain of OH^- in the interlayer space, and finally a loss of H_2O in the interlayer space. The decrease of the basal spacing is related to water swelling which was demonstrated by EQCM measurement, *ac*-electrogravimetry and *operando* XRD under cyclic polarization.

5.4 Conclusion

Previous investigation of the electrochemical behavior of nano-Ni/Fe-LDH in KOH 1 mol/L confirmed the pseudo-capacitance properties of mix cation and anion exchanger. It led to demonstrate the water molecule transfer during the reversible redox reaction involving the metal cation constituting the brucitic structure. It also led to postulate the electrocatalytic properties of interlayered water molecules. In this study, we investigated further the mechanisms of electroadsorption of three cations (Li^+, K^+, Cs^+) as well as the electrocatalytic properties of the interlayered water molecules by *operando* XRD coupled to electrogravimetric measurements.

Electrochemical and electrogravimetrical techniques (EQCM) allowed us to compare the influence of the cation nature on current density and mass variation. For a better insight, *ac*-electrogravimetry technique was employed for the identification of transferred species and the determination of associated transfer kinetics. It also allowed to determine the easiness of transfer and the concentration variation of the transferred cations.

Under the investigated conditions, the current density of H_2O oxidation and Ni(III)/Ni(II) redox reactions are intimately linked. Whatever the electrolyte, the same species are reversibly transferred: anions (OH^-), dehydrated cations (Cs^+, K^+, Li^+) and water molecules. Ni(II) oxidation generates reinforced Coulombian charges between the layers owing to the expulsion of interlayered water molecules. The intercalation of one OH^- anion is correlated/linked with the expulsion of water molecules. The H_2O to OH^- ratio depends on the nature of the investigated electrolyte. Concomitantly, the electrochemical modification of the pH at the coated interface correlated with catalyzed oxygen evolution reaction, allowed cations electroadsorption/desorption onto the external surfaces in agreement with the pH of zero point of net charge of the nano-Ni/Fe-LDH. Each of these species is transferred with its own kinetics and concentration depending on the potential and the supporting electrolyte. Regarding interlayered water molecules, electrochemical irreversible transfer occurs during the OER that depends on the interfacial pH and the applied potential.

In CsOH and KOH 1 mol/L, the transfer kinetics of cations, anions and water molecules are comparable. This is the reason why the shape of the electrogravimetrical curve is quite similar. The differences are only localized in the highest concentration of reversibly transferred OH^-, H_2O and cations in CsOH 1 mol/L. Compared to the gravimetric curve shape obtained in KOH 1 mol/L, the one obtained in CsOH highlighted the contribution of the Cs^+ cations in agreement with its molar mass that is almost 8 times higher than that of OH^-.

The electrogravimetrical response obtained in LiOH 1 mol/L is different from the others. In comparison with data acquired in KOH and CsOH, the differences are localized in both kinetics and concentration of reversibly transferred species. The consecutive huge catalysis of the interlayered H_2O, in agreement with the OER enhancement and the slow downed but continuous OER ($I_{OER}LiOH >> I_{OER}KOH$) let to appreciate the OH^- intercalation/deintercalation by gravimetry.

An *operando* technique was developed and applied at synchrotron SOLEIL (Saclay, France), by coupling EQCM measurements and structural characterization under polarization to investigate the electrocatalytic properties of the interlayered water molecules. In real time, under polarization, current, mass of Ni/Fe-LDH coated film, LDH basal spacing, electronic density along the c axis and organization level of the layers were recorded simultaneously. Measurements enabled to differentiate water deintercalation caused reinforced Coulombian interactions in agreement with OH^- intercalation, from the oxidation of water into the interlayer spacing by OER.

Whatever the investigated supporting electrolyte, the 003-peak is observed over the whole cycling experiments during 4900s which demonstrates the LDH structure is conserved *versus* time and applied

potential. Both FWHM and basal distance vary with time. Nevertheless, they vary anticorelatively and with a similar percentage of variation which indicates that the number of stacked layers within a particle remains globally constant in agreement with the Scherrer equation. This result clearly highlights the constant characteristic structure of the Ni/Fe-LDH *versus* polarization and time. This finding, associated to the constant mass response in period slot 3, is related to the absence of any dissolution, dissolution/reprecipitation or crystallization of the LDH material.

The presence of some irreversibly oxidized Ni(III) clusters within the lattice is responsible for the increase in the distortion in the lattice which progressively and irreversibly prevent deintercalated water. This phenomenon aggravates the electrostatic attraction between anions and positively charged layers, in agreement with the progressively collapsing of the Ni/Fe-LDH particle layers. Concomitantly, the interlayered oxygen evolution reaction occurs.

Reversible water "swelling" caused by the reversible redox reactions involving Ni(III)/Ni(II) within the Ni/Fe-LDH and concomitantly by the electrocatalysis of the H_2O interlayered water was demonstrated by EQCM measurement, *ac*-electrogravimetry and *operando* XRD under cyclic polarization. This phenomenon appeared reversible: the decrease in OER as well as the reversible chemical oxidation of the Ni(III) clusters within the lattice allowed Ni/Fe-LDH to rehydrate.

Under the investigation conditions, the monitoring of the 003-peak by *operando* XRD and electrochemical measurement clearly highlighted H_2O swelling behavior within the nano-Ni/Fe-LDH. For a better insight into the change in electronic density and/or into the change in the electronic density distribution in the c-axis, new *operando* measurements will be conducted on different (00l) peaks to determine more relevant phenomena

General conclusions and outlook

In this Ph.D thesis, thin films of nano-Ni/Fe-LDH 6/2 coated onto electrode were prepared by chemical or assisted electrochemical routes to investigate the ions and water molecules transfers at the interface between the LDH and the electrolyte under polarization.

Special attention was paid to the Ni/Fe-LDH 6/2 because it is known to be one of the most conductive LDH and electroactive Ni can be reversibly switched between the (+II) and (+III) oxidation states under polarization. Nano-Ni/Fe-LDH 6/2 was investigated to enhance the number of transfer sites (*i.e* intercalation sites and adsorption sites onto both edge and basal surfaces). For a better insight in the associated transferred species (anions, cations and water molecules), experiments were conducted in different supporting electrolytes (LiOH, KOH and CsOH) whose pH value was higher than Ni/Fe-LDH 6/2 pH of zero point of net charge (for Ni/Fe-LDH 6/2, pH_{PZNC} equals 8).

Each LDH synthesis route has specific advantages and drawbacks in terms of crystallinity, morphology of LDH and charge transfer level. The choice of synthesis route has also a consequence on the employed investigation techniques and on the mechanism of charge transfer and side reactions.

Based on the state of the art of assisted electrochemical synthesis route of LDH, the insight into the different reactions that play a role in the synthesis route of Ni/Fe-LDH 6/2 was deepened through EQCM measurements. The cathodic potential for deposition was evaluated in order to deposit a thin film of LDH onto the electrode by assisted electrochemistry.

Through EQCM measurements in KOH 1 mol/L, reversible Ni(II)/Ni(III) redox reaction was observed correlated to a reversible complex mass variation of the LDH film. The transfer mechanisms and kinetics of ions and water molecules were specifically studied by *ac*-electrogravimetry. For the first time, this study investigated all the redox reactions as well as both the related ionic and water transfers using nano-elec-Ni/Fe-LDH 6/2 via electrochemical and electro-gravimetrical characterizations. During Ni(II) oxidation a flux of K^+ and a counterflux of OH^- and free water were evidenced. It led to demonstrate the nano-Ni/Fe-LDH pseudocapacitance properties of mix cations (K^+) and anions (OH^-) exchanger. However, the low crystallinity of the material prevented XRD advanced analyses from being performed which further limits in depth physico-electrochemical investigations for pointing out the specific sites where each reaction takes place.

For the confirmation of the intervention of K^+, H_2O and OH^- in the transfer mechanism, and also for a better insight regarding the specific sites of transfer, complementary analyses have to be performed on the LDH, *i.e.* EDX and XPS analyses and *in situ*/*operando* XRD under polarization. *In situ/operando* XRD under polarization enables to observe the basal distance, however, this observation is complicated onto the elec-

Ni/Fe-LDH thin film as it is not well crystallized. Also, the EDX and XPS analyses permit the identification of the adsorbed cations onto the surface, however, it is not possible to assert if cations would be adsorbed onto the LDH or onto impurities within the thin film.

To elude this problem and deepen the characterizations, it is necessary to study the properties of the chemically synthesized Ni/Fe-LDH 6/2 (chem-Ni/Fe-LDH 6/2). Despite the lower electronic charge transfer inherent to the less adherent film onto the LDH, this material has the property to be highly pure and crystallized.

For a better insight, EQCM and *ac*-electrogravimetry methodology were thus performed on chemically synthesized nano-Ni/Fe-LDH in KOH 1 mol/L. It allowed identification of the nature of the charged and uncharged transferred species as well as the kinetics ($K(K^+) > K(H_2O) > K(OH^-)$), easiness of transfer, transferred concentration and mass for each species at different polarizations. As previously mentioned for the electro-assisted deposited LDH, the nano-Ni/Fe-LDH pseudocapacitance properties of mix cations (K^+) and anions (OH^-) exchanger was demonstrated.

The positive charge layer increase related to oxidation of Ni(II) to Ni(III) is balanced by intercalation of OH^- anions in the LDH interlayer space. The intercalation of one OH^- anion follows the expulsion of two intercalated water molecules in agreement with the following equation:

$$[Ni^{II}_{6}Fe^{III}_{2}(OH)_{16-c}(OK)_c]^{2+}[(OH)_2]^{2-},4H_2O + x\ OH \Leftrightarrow$$

$$[Ni^{II}_{6-x}Ni^{III}_{x}Fe^{III}_{2}(OH)_{16-c}(OK)_c]^{(2+x)+}[(OH)_{2+x}]^{(2+x)-},(4-2x)H_2O + 2xH_2O + xe-$$

This mechanism was further evidenced by *in situ* XRD analyses and it was demonstrated that it is an intercalation/deintercalation process. The water molecule transfer during the reversible redox reaction *i.e.* Ni(II) oxidation generates reinforced Coulombian charges which leads to the expulsion of intercalated water molecules.

Concomitantly, the electrochemical variation of the pH at the electrolyte/LDH interface, via catalyzed oxygen evolution reaction, allowed cation electroadsorption/desorption onto the external surfaces of the LDH particles in agreement with the pH of zero point of net charge of Ni/Fe-LDH. This phenomenon was confirmed by EDX and XPS analyses, in agreement with the following equation:

$$[Ni^{II}_{6-x}Ni^{III}_{x}Fe^{III}_{2}(OH)_{16-c}(OK)_c]^{(2+x)+}[(OH)_{2+x}]^{(2+x)-},(4-2x-z)H_2O + 2z\ H^+ \leftrightarrows$$

$$[Ni^{II}_{6-x}Ni^{III}_{x}Fe^{III}_{2}(OH)_{16-c}(OH)_c]^{(2+x)+}[(OH)_{2+x}]^{(2+x)-},(4-2x-z)H_2O + c\ K^+ + (2z-c)\ H^+$$

Experiments led to postulate the existence of an irreversible oxidation reaction attributed to water oxidation, with O_2 evolution reaction at the interlayer space.

The study was deepened by investigating further the mechanisms of electroadsorption of cations in the presence of different supporting electrolytes (LiOH, KOH and CsOH) as well as the electrocatalytic properties of the intercalated water molecules by *operando* XRD coupled to electrogravimetric measurements. *Ac*-electrogravimetry technique allowed identification of transferred species and determination of associated transfer kinetics. It also determined easiness of transfer and concentration variation of transferred cations. Whatever the electrolyte, the same species are reversibly transferred: anions (OH^-), dehydrated cations (Cs^+, K^+, Li^+) and free water molecules, however with own kinetics and concentration depending on the applied potential and the nature of the cations present in the supporting electrolyte. For a better insight into the electrochemical induced phenomena, *operando* technique was developed and implemented at synchrotron SOLEIL (Saclay, France), by coupling EQCM measurements and structural characterization under polarization to investigate the electrocatalytic properties of the interlayered water molecules. Reversible water swelling caused by the reversible redox reactions involving Ni(II)/Ni(III) within the Ni/Fe-LDH and concomitantly by the electrocatalysis of the H_2O intercalated water was demonstrated by EQCM measurement, *ac*-electrogravimetry and *operando* XRD under cyclic polarization. This phenomenon appeared reversible: the decrease in OER as well as the reversible chemical oxidation of the Ni(III) within the lattice allowed Ni/Fe-LDH to rehydrate. The (003)-peak is observed over the whole cycling experiment during 4900 s demonstrating that the LDH structure is conserved *versus* time and applied potential. Both full width at half maximum and basal distance varied *versus* time. Nevertheless, they varied anticorelatively and with a similar percentage of variation which indicated that the quantity of stacked layers within a sheet remained constant in agreement with the Scherrer equation. This result clearly highlighted the maintained characteristic structure of the Ni/Fe LDH *versus* polarization and time and the absence of any dissolution, dissolution/reprecipitation or crystallization of the material.

New *operando* measurements should be conducted on different (00l) peaks for a better insight into the change in electronic density and/or into the change in the electronic density distribution in the c-axis.

These results pave the way to large perspectives for layered double hydroxides. LDHs could be used as "universal material" and optimized for the development of toxic, strategic or expendable cations and anions capture/release processes.

Contrary to Ni-based LDH with enhanced faradaic properties, Co-based LDH are known to have less faradaic properties and enhanced capacitive properties. Thus, it could be particularly interesting to compare and evaluate the difference in terms of electrochemical behavior: definition of a standards $Co^{(III)}/Co^{(II)}$-Co-based-LDHs redox potential, nature, kinetics, and concentration of adsorbed, intercalated and transferred species, OER and hydrogen evolution reaction (HER) performances. [260]

Another way could be the synthesis of Ni-Co-based LDH hybrid materials such as to define and compare the electrochemical behavior.

For particular applications, *i.e.* “selective” anion capture/release processes, and for lower energy cost, a solution could be the synthesis of an LDH with (a) redox-active element(s) whose potential is far from the OER or HER. For this purpose, the investigation of Mn-based LDH could be of great interest.

Finally, the investigation of the transfers between LDHs and electrolytes containing other supporting anions is also of great interest to determine and compare their specific kinetics and concentrations. It could be valuable to build an electrochemical affinity scale for applications in terms of water treatment, as many pollutants, strategic or expendable species are anionic (arsenates, vanadates, nitrates, sulfates…).

Annex A

Tuning redox state and ionic transfers of nano-Mg/Fe-(2:1) layered double hydroxide by electrochemical and electrogravimetric methods

Elise Duquesne[a,b], Stéphanie Betelu[b*], Alain Seron[b], Ioannis Ignatiadis[b], Catherine Debiemme-Chouvy[a*], Hubert Perrot[a], Ozlem Sel[a]

[a] Sorbonne Université, CNRS, Laboratoire Interfaces et Systèmes Électrochimiques, 4 place Jussieu, 75005 Paris, France

[b] BRGM, French Geological Survey, 3 Avenue Claude Guillemin, 45060 Orléans Cedex 02, France

Abstract

Studying the electrogravimetric behavior of nano-Mg/Fe layered double hydroxide particles with an Electrochemical Quartz Crystal Microbalance demonstrates its pseudocapacitance properties of mix cation and anion exchanger. The electrochemical control of the oxidation state of iron constituting the layered sheets allowed anion intercalation/deintercalation into the layered double hydroxide interlayer space. Concomitantly, in agreement with the pH of zero point of net charge of the nano-Mg/Fe-LDHs, the electrochemical control of the pH at the coated interface, via catalyzed hydrogen evolution reaction, allowed cation electroadsorption/desorption onto the external surfaces.

Keywords

Layered double hydroxide (LDH), Electrochemical Quartz Crystal Microbalance (EQCM), redox reactions, ionic exchanges, Zero point of net charge (ZPNC).

1. Introduction

Layered double hydroxide (LDH) materials consist in a stacking of positively charged brucite-like layers, due to the substitution of some divalent cations M(II) by trivalent cations M(III). The charge compensation is managed by anions A^{n-} intercalated into the interlayer space. This leads to the general formula: $[M(II)_{1-x}M(III)_x(OH)_2]^{x+}(A^{n-}_{x/n}).mH_2O$, providing a high capacity for anion exchange.[254]

It is well established[161] that a reversible ion transfer between the interlayer spacing and the electrolyte is induced by tuning the redox state of nano-LDH layered sheets according to:

$$n[\mathrm{LDH} - M^{II}] + A^{n-} \leftrightarrow \mathrm{n}[LDH - M^{III}]^{n+}[A^{n-}] + e^{-},$$

with an electron displaced within the layer via a hopping mechanism. Thus, the ion uptake/release occurring during redox processes can be monitored with suitable *in-situ* coupled methods, *i.e.* combining structural, electrochemical and electrogravimetric methods.

For progress in broad applications where layered materials are employed, for instance in water treatment[21] or energy storage[261], the reversibility of the ion transfer between the electrolyte and the material merits further investigation. Only a few studies[161,262,11] have explored the ion transfer phenomenon and its reversibility related to the repetitive oxidation/reduction of electroactive cations within the layers for the most conducting LDH (Co/Ni-LDH, Ni/Al-LDH, Mg/Al/Fe-LDH, Fe/Fe-LDH …) by probing the mass variation with electrochemical quartz crystal microbalance (EQCM). To the best of our knowledge, no study has been conducted yet on Mg/Fe-LDH.

This letter reports on a study conducted for the first time to investigate the ion transfer phenomena of nano-Mg/Fe-LDH 2:1. Through a fine EQCM analysis, it has been demonstrated that Fe sites are reversibly switched, under polarization, to the (+III) or (+II) oxidation state inducing anion intercalation or deintercalation. The variation of the pH of the zero point of net charge[60], pH_{ZPNC} (pH resulting from the cancellation of the positive charge originating from the chemical composition of the LDH and the variable charge resulting from the protonation/deprotonation of the LDH layers) and the pH tuning at the interface due to formation of hydroxyl ions by electrochemical water reduction play a key role on the electroadsorption process of cations.

2. Experimental

2.1 Preparation of thin films of nano-Mg/Fe-LDH onto a gold electrode

LDH particle synthesis consists in co-precipitation of Mg/Fe from nitrates solution by increasing pH, thermal maturation and purification via centrifugation and carbonate exchange via dialysis in a carbonated solution[77]. The resulting suspension (15g/L) was dropcasted (10µL) onto the gold electrode of a quartz resonator (operating at 9MHz, AWS Sensors, Spain) and dried at room temperature.

2.2 Electrogravimetric characterization with EQCM

EQCM measurements were conducted in a 3-electrodes cell configuration using an Autolab potentiostat (PGSTAT302) coupled with a laboratory-made QCM device. A gold patterned quartz substrate coated with the thin film of LDH was employed as working electrode, a Pt grid as a counter electrode and a silver chloride electrode with KCl 3mol/L (Ag/Ag^+) as a reference electrode. The aqueous electrolyte was deaerated with nitrogen gas. Frequency change, Δf, of the quartz crystal resonator was monitored during cyclic voltammetry measurements. Then, Δf is converted into mass change, Δm, by using the Sauerbrey equation:

$$\Delta f = -k_s \, \Delta m$$

where k_s is the sensitivity factor (experimental value[193]: $16.31 \cdot 10^7$ $Hz.g^{-1}.cm^2$ for 9MHz).

The LDH was characterized by X-ray powder diffraction (Panalytical Empyrean), using a Cu Kα radiation (λ=1.541Å) at room temperature after drying the slurry at 70°C for 48h. Scans were recorded from 4° to 84°

(2θ) at a counting time of 1200s per step of 0.026°. The morphology of the film dried onto gold was examined under a field emission gun scanning electron microscope (FEG-SEM) Ultra55 Zeiss.

3. Results and Discussion

3.1 Structural and morphological characterization of the LDH

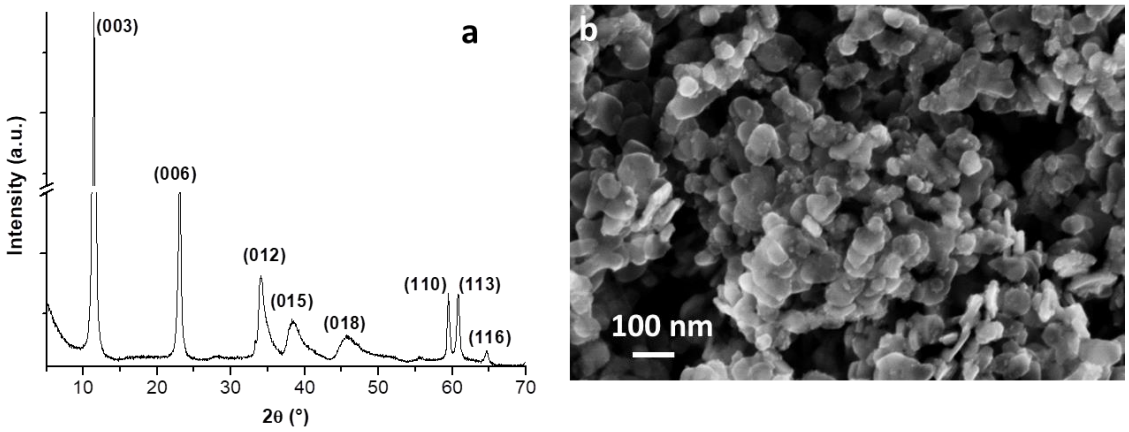

Figure 1: (a) X-ray powder diffraction pattern of the nano-Mg/Fe-LDH, (b) FEG-SEM micrograph of the nano-Mg/Fe-LDH thin film.

The powder X-ray diffraction pattern (Fig. 1a) shows a characteristic LDH structure[16]. A series of basal (00l) reflections corresponds to the basal distance *d*=7.74Å which depends on the size of the intercalated anion and its degree/level of hydration. The *c* parameter equals 3d(003)=23.21Å.

FEG-SEM micrographs (Fig. 1b) revealed that the LDH is made of nanoplatelets whose size is close to 80 nm implying a high surface-to-volume ratio. The expected molar ratio Mg/Fe=2 was confirmed with atomic absorption spectroscopy.

2.2. Polarization induced ionic transfers

EQCM was conducted on the gold electrode of quartz resonators uncoated and coated with a thin film of nano-Mg/Fe-LDH. The measurements were recorded at 25 $mV \cdot s^{-1}$ in an aqueous buffer solution of $Na_2CO_3/NaHCO_3$ 0.1mol/L at pH=10.8 that is slightly superior to the pH_{ZPNC} of the initial film that was calculated to be 10.6.[60]

The behavior of the nano-Mg/Fe-CO_3^{2-} thin film was successively investigated in three different potential ranges, *i.e.* [-1.8; -0.3]V, [-1.2; -0.3]V and [-1.5; -0.3]V, to prove the H_2O reduction in the intercalated spacing. The electrode was finally rinsed with distilled water, dried at room temperature, and investigated again in the initial potential range [-1.8; -0.3]V. Results were compared to the behavior of a bare gold-

patterned resonator.

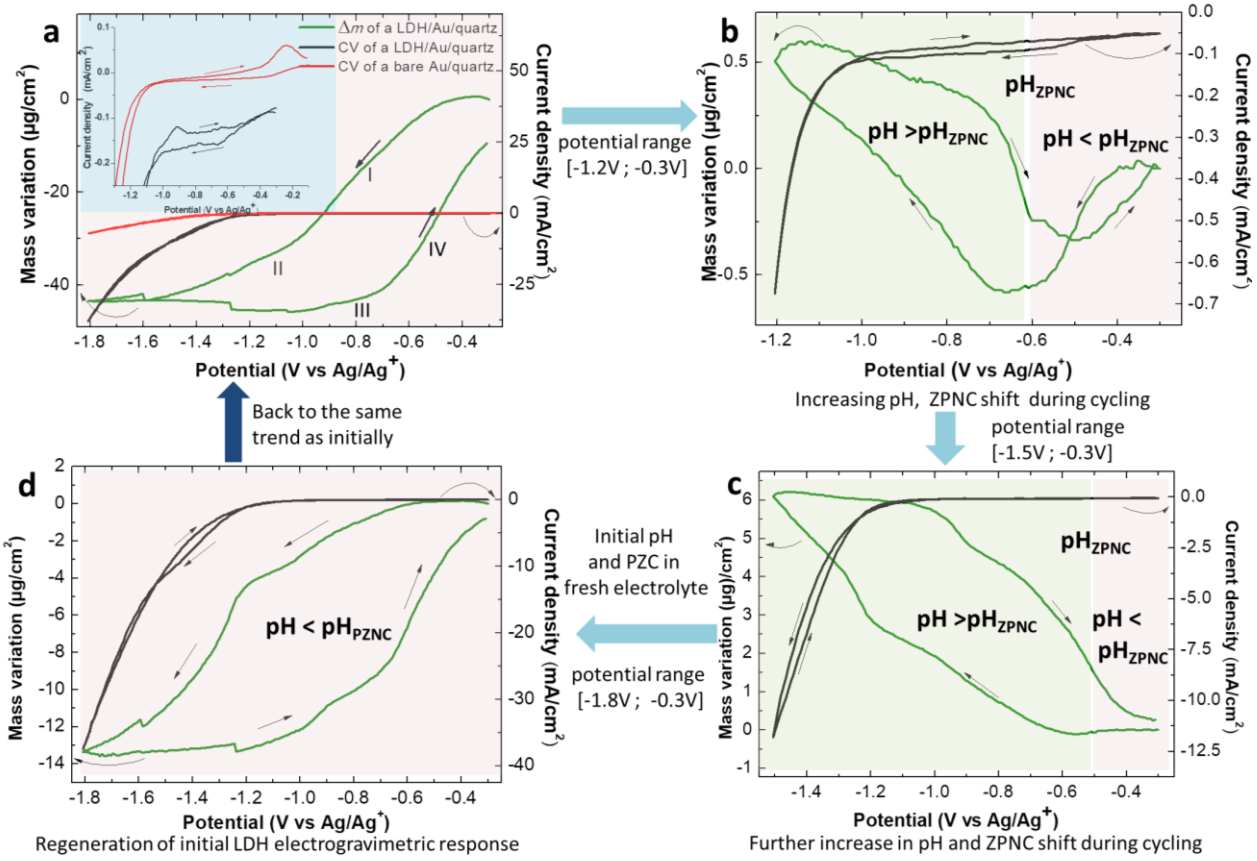

Figure 2: Representative EQCM measurements of a gold electrode coated with LDH successively cycled in different potential ranges: (a) [-1.8; -0.3]V, (b) [-1.2;-0.3]V, (c) [-1.5;-0.3]V, (d) [-1.8; -0.3]V after drying it in air for 12 hours.

2.2.1. EQCM in the [-1.8; -0.3]V range

Fig. 2a shows the I-V curve (in red) of a bare gold-patterned resonator in the range [-1.8; -0.3]V where the reduction of the H_2O starts below -1.2V.

In comparison, below -1.2V on the LDH-coated electrode, the higher negative current reveals the catalysis of the reduction of H_2O from the bulk of the solution. In addition, between -0.3V and -1V (Fig. 2a, inset), the negative current both during the cathodic and anodic sweep and especially the pseudo-plateau below -0.6V validates necessarily a diffusion-limited reaction that can only be water reduction, probably intercalated water. The simultaneous mass loss (slope I) during the cathodic sweep (from -0.6V to -1V) confirms this hypothesis and is attributed to the repulsion of the electrochemically generated OH^- from the interlayer space due to negative charges in excess. Inversely, during the anodic sweep (slope IV, from -0.7V to -0.3V) the mass gain should be due to the lower kinetics of the H_2O reduction compared to that of the water re-intercalation by diffusion.

The electrochemical oxidation and reduction of the Fe^{III}/Fe^{II} redox couple are observed around -0.95V and -1.05V respectively, the latter being masked by the continuous water reduction. The Fe^{III} reduction decreases the charge of the layers and is responsible for anion deintercalation from the interlayer space. This phenomenon is confirmed by the mass loss from -1.0V to -1.6V (slope II). Inversely, the mass gain

between -1.0V and -0.7V (slope III) is induced by the Fe^{II} oxidation and is most likely due to the intercalation of CO_3^{2-} which has the strongest affinity for LDH[263] following:

$$Mg^{II}_4Fe^{III}_2[(OH)_{16}]^{(2)+}[CO_3]^{(2)-}, 4H_2O + (x+y)e^- \Leftrightarrow Mg^{II}_4Fe^{III}_{2-x}Fe^{II}_x[(OH)_{16}]^{(2-x)+}[(CO_3)_{2-0.5x}]^{(2-x)-}, (4-y)H_2O + 0.5xCO_3^{2-} + 0.5yH_2 + yOH^-$$

2.2.2. EQCM in the [-1.2; -0.3]V range

In order to eliminate the hydrogen evolution reaction of the bulk and investigate the water reduction phenomenon from the interlayer space, the potential range of cycling was reduced to [-1.2;-0.3]V after the 7th cycle, during 16 cycles (Fig. 2b). As described previously between -0.3V and -0.60V, the cathodic mass loss and anodic mass gain are in agreement with the dehydration/hydration of the LDH interlayer space. Between -0.6V and -1.2V, the mass variations, increasing at each incremented cycle, are attributed to a phenomenon that becomes preponderant. The continuous hydrogen evolution reaction, while cycling, increases the OH^- amount at the vicinity of the coated electrode. This pH increase is responsible for the deprotonation of the Metal-OH function of the external layers once the pH_{ZPNC} is reached. The H_2O reduction in the intercalated space is sufficient to drive the cation electroadsorption/desorption (probably Na^+) during the cathodic/anodic sweep.

2.2.3. EQCM in the [-1.5; -0.3]V range

Continuing the electrochemical cycling in the potential range [-1.5;-0.3]V during 9 cycles (Fig. 2c) reactivates the hydrogen evolution reaction from the bulk. The interfacial pH increase leads to an enhanced deprotonation and reversible cation electroadsoption onto the LDH surface in higher quantity than previously observed in the range [-1.2; -0.3]V (Fig. 2b). Under these conditions, cation electroadsorption/desorption dominates the LDH electrogravimetric response following:

$$Mg^{II}_4Fe^{III}_{2-x}Fe^{II}_x[(OH)_{16}]^{(2-x)+}[(CO3)_{2-0.5x}]^{(2-x)-}, (4-y)H_2O + yOH^- + zNa^+ \Leftrightarrow Mg^{II}_4Fe^{III}_{2-x}Fe^{II}_x[(OH)_{16-z}[(ONa)_z]^{(2-x)+}[(CO3)_{2-0.5x}]^{(2-x)-}, (4-y)H_2O + (y-z)OH^- + zH_2O$$

2.2.4. EQCM in the [-1.8; -0.3]V range – regeneration of the initial LDH

The electrode was then rinsed with bi-distilled water and dried at room temperature. The electrode was reused in a fresh electrolyte under the same initial conditions, *i.e.*, in the range [-1.8; -0.3]V (Fig. 2d). A similar electrogravimetric response is observed (Fig. 2a) because of the restoration of the initial pH at the interface, the decrease in mass variation is probably owing to ageing of the structure

4. Conclusion

The ionic exchanges occurring in response to the tuning of the redox state of a thin film of a nano-Mg/Fe-LDH were investigated by EQCM and demonstrate pseudocapacitance properties of mix cation and anion exchanger. The concomitant electrochemical control of (i) the physical and the chemical conditions at the interface and (ii) the oxidation state of the cations constituting the layered sheets of nano-LDHs and (iii) the zero point of net charge allowed anion intercalation/deintercalation into the interlayer space and cation sorption/desorption onto the external sheets at the interface. For a better insight, further structural and electrogravimetric investigations will be conducted by coupling EQCM and X-ray diffraction.

Conflict of interest

None

Acknowledgment

The French Geological Survey (BRGM) and the Cluster of Excellence LABEX MATISSE led by Sorbonne Université, France supported this work.

Annex B

List of oral communications and posters

Posters

March 2017	La 6ème Journée Des Doctorants du BRGM, Orléans, France.
May 2017	La Journée de l'Ecole Doctorale 388, Paris, France.
Nov. 2017	La journée scientifique de la Division Chimie-Physique, Paris, France.
April 2018	La 7ème Journée Des Doctorants du BRGM, Orléans, France.
May 2018	The 8th international conference on Electrochemistry and Nanosciences, Nancy, France.
July 2019	The international conference on clay science and technology, Paris, France

Oral communications

Sept. 2018	The 69th annual meeting of the International Society of Electrochemistry (ISE).
July 2019	The international conference on clay science and technology, Paris, France.

Tuning redox state and ionic transfers of nano-Mg/Fe-layered double hydroxides using electrochemical and gravimetrical techniques.

Elise Duquesne[1,2], Stéphanie Betelu[2], Alain Seron[2], Ioannis Ignatiadis[2], Hubert Perrot[1], Ozlem Sel[1], Catherine Debiemme-Chouvy[1]

[1] Laboratoire Interfaces et Systèmes Electrochimiques, LISE UMR 8235, Sorbonne Université, CNRS, 4 place Jussieu, 75005 Paris, France

[2] BRGM, French Geological Survey, 3 Avenue Claude Guillemin, 45000 Orléans, France

Layered double hydroxides (LDHs)

LDHs bearing electroactive metal cations within their sheets:
(≡Me: Fe, Co, Ni…)

→ $M^{(III)}/M^{(III)}$ reversible redox reaction
- Anion intercalation/deintercalation

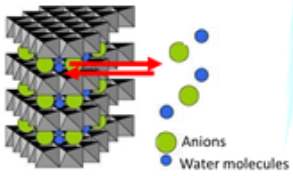

Catalyzed oxygen evolution reaction (OER)

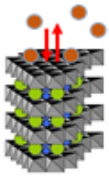

→ Interfacial pH control : sorption/desoprtion of
- cations
  ≡MeOH ⇔ ≡MeO^- + H^+ , for pH >>pH^*_{PZNC}
- anions
  ≡Me-OH + H^+ ⇔ ≡$Me-OH_2^+$, for pH<<pH^*_{PZNC}

pH^*_{ZPNC} : pH of zero point of net charge

Mg/Fe-CO_3 synthesis and characterisations

Synthesis: co-precipitation method
- Dissolved Co^{II} / Fe^{III} 6/2
- pH increase using alkaline solution: NaOH + Na_2CO_3
- Thermal maturation
- Dialysis : nitrates are exchanged by carbonates
  LDH suspension at 15 g/L

Nano Crystalline $Mg_6Fe_2(OH)_{16}(CO_3).4H_2O$ / pH of (pH_{ZPNC}) : **10.6**

SEM photography of Co/Fe LDH

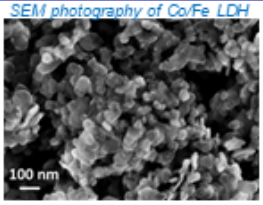

PXRD pattern of Mg/Fe-CO_3 LDH

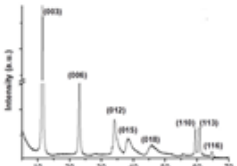

Electrochemistry coupled with quartz cristal microbalance (EQCM)

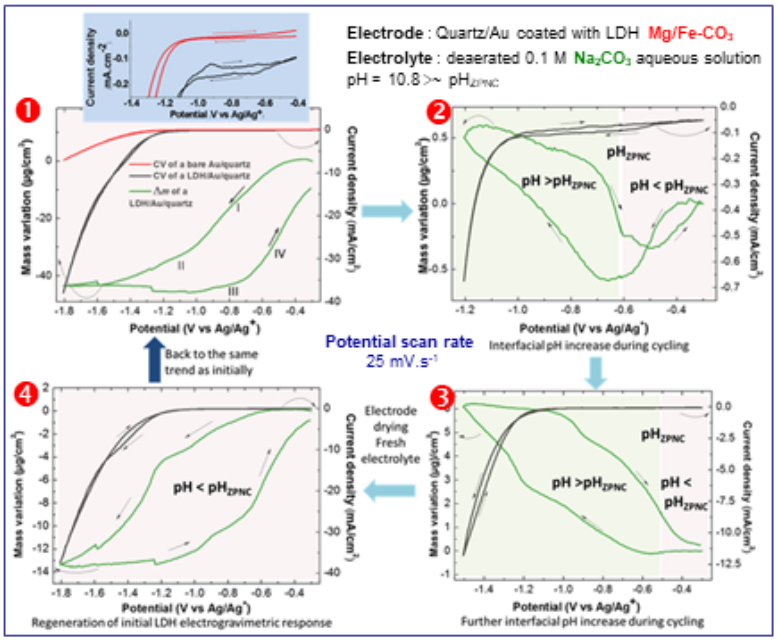

Mg/Fe-LDH suspension was dropcasted (10 µL) onto the gold electrode of a quartz resonator (9 MHz) ⇨ **working electrode**

LDH-coated electrode

Main parameter : Interfacial pH / pH_{ZPNC}

❶ EQCM in the [-1.8; -0.3]V range

Below -1.2V : catalysis H_2O reduction from the bulk solution

Between -0.3V and -1V
- Pseudo-plateau below -0.6V : diffusion-limited reaction / electrochemical reduction of physisorbed H_2O → osmotic pressure variation between the external and the internal lamelar sheets → interlayered H_2O deintercalation → interlayered H_2O electroreduction catalysis in agreement with the huge mass decrease
  Reversible H_2O interlayered intercalation
- Fe^{III}/Fe^{II}-LDH redox couple : -0.95/-1.05V
  → CO_3^{2-} reversible intercalation/deintercalation

❷ EQCM in the [-1.2; -0.3]V range
- Dehydration/hydration of the LDH interlayer space
  → Continuous hydrogen evolution reaction
  → interfacial pH increase → reversible deprotonation of the Metal-OH function of the external layers once pH >> pH_{PZNC}
- **Catalytic H_2O reduction in the intercalated space is sufficient to drive the cation lectroadsorption/desorption (probably Na+) during the cathodic/anodic sweep**

❸ EQCM in the [-1.5; -0.3]V range

The interfacial pH increase leads to a further enhanced deprotonation and reversible cation electroadsoption onto the LDH

❹ Reuse of the LDH coated electrode after rinsing and drying at room temperature for 12 hours

$Mg^{II}_4Fe^{III}_2[(OH)_{16}][CO_3]$, $4H_2O$ + (x+y)e^- ⇔ $Mg^{II}_4Fe^{III}_{2-x}Fe^{II}_x[(OH)_{16}][(CO_3)_{2-0.5x}]$, (4-y)$H_2O$ + 0.5xCO_3^{2-} + 0.5yH_2 + yOH^-

$Mg^{II}_4Fe^{III}_{2-x}Fe^{II}_x[(OH)_{16}][(CO3)_{2-0.5x}]$, (4-y)$H_2O$ + yOH^- + zNa^+ ⇔ $Mg^{II}_4Fe^{III}_{2-x}Fe^{II}_x[(OH)_{16-z}[(ONa)_z][(CO3)_{2-0.5x}]$,(4-y)$H_2O$ + (y-z)OH^- + zH_2O

The ionic exchanges occurring in response to the tuning of the redox state of a thin film formed by Mg/Fe-LDH nanoplatelets were investigated by EQCM and **demonstrate pseudocapacitance properties of mix cation and anion exchanger**. The concomitant electrochemical control of (i) the physical and the chemical conditions at the interface and (ii) the oxidation state of the cations constituting the layered sheets of the LDH and (iii) the zero point of net charge allowed anion intercalation/deintercalation into the interlayer space and cation sorption/desorption onto the external sheets at the interface. For a better insight, electrogravimetric and structural investigations by coupling EQCM and in situ X-ray diffraction are in progress.

Exploration Into the Ionic Exchanges in the Ni/Fe Lamellar Double Hydroxide by *in situ* Techniques under Polarization

Elise Duquesne[1,2], Ozlem Sel[1], Hubert Perrot[1], Alain Seron[2], Stéphanie Betelu[2], Ioannis Ignatiadis[2], Catherine Debiemme-Chouvy[1]

[1] *Sorbonne Université, CNRS, Laboratoire des Interfaces et Systèmes Electrochimiques, LISE, UMR 8235, 4, Place Jussieu, 75005 Paris, France*

[2] *D3E, Bureau de Recherches Géologiques et Minières, 3 Avenue Claude Guillemin, 45100 Orléans, France.*

Lamellar Double Hydroxides (LDHs)

$[M(II)_{1-x}M(III)_x(OH)_2]^{x+}(A^{n-}_{x/n}).mH_2O$

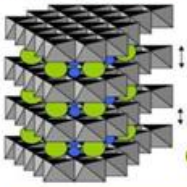

- **Structure**
  - Positively charged brucitic layers due to the substitution of divalent cations with trivalent cations.
  - Anions inserted into the interlayer spacing for charge compensation.

- **Sélectivity for anions**
  - Different affinity for anions : $CO_3^{2-}>SO_4^{2-}>OH^->F^->Cl^->Br^->NO_3^-$ (Miyata, 1983).
  - The cationic composition of the brucitif layers has an influence on the affinity for the anionic species.[1]

Aim

Study of the mecanisms and kinetics related to oxidation and reduction of the electroactive components of the LDHs

Choice of the Ni/Fe 6/2 LDH

- Ni is an electroactive element
- One of the most conductive LDHs

Comparison between two synthesis routes and characterization of LDHs

1) **Electrochemical-assisted synthesis :**
Electrochemical reduction of nitrate ions leads to local incease of the pH
⇨ precipitation of the cations (Ni(II) and Fe(III))
Chemical synthesis :
Coprecipitation by pH variation of the solution

2) **Characterization of the physico-chemical properties of the LDH**
- Determination of crystalline phases (DRX)
- Morphology (SEM)
- Nature of the anionic species (IR-FT)
- Cationic ratio (EDX)

3) **Study of the electrogravimetrical properties (by *ac*-électrogravimetry[2])**

Study of the electrochemical and gravimetric responses versus the electrode potential in a 3-electrode electrochemical cell.

Chemical synthesis of the Ni/Fe 6/2 LDH

Physico-chemical properties of the LDH

Morphology in sand rose of the Ni/Fe LDH observed by SEM

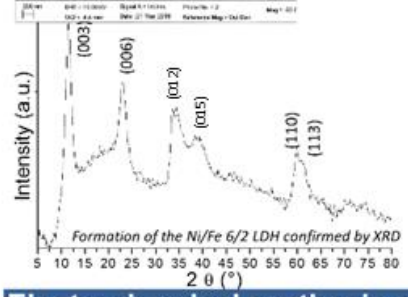

Electrogravimetric response

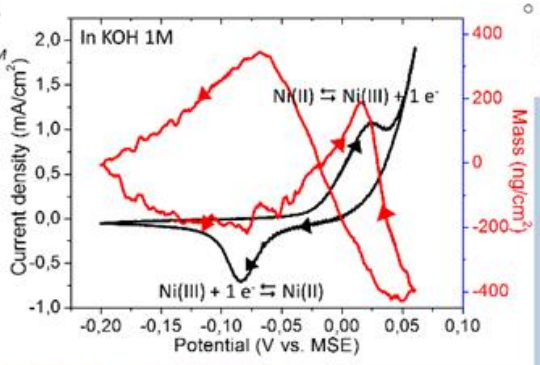

- High crystallinity of the LDH
- Exchanges of different species during Ni oxidation/reduction confirmed by QCM

Setup of the electrochemical cell and QCM

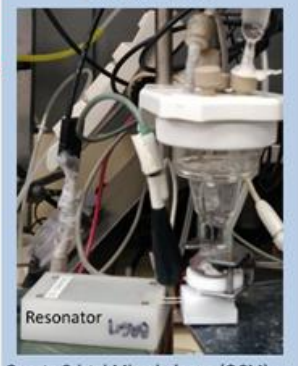

Quartz Cristal Microbalance (QCM): Relation between frequency variation (Δf) and deposited mass (Δm)
$\Delta f = k\,\Delta m$ (Sauerbray equation)

Electrochemical synthesis of the Ni/Fe 6/2 LDH

Physico-chemical properties of the LDH

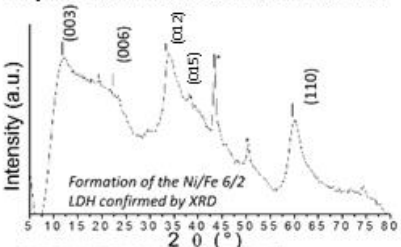

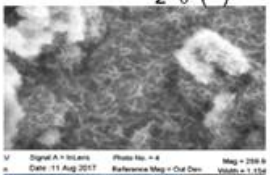

Morphology in sand rose of the Ni/Fe LDH observed by SEM
➔ *Higher specific area for enhanced anionic exchanges.*

Electrogravimetric response

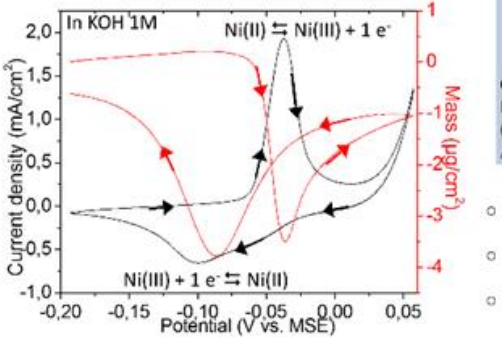

- Lower crystallinity of the LDH with the electrochemical-assisted synthesis.
- Higher charge transfert for the electrochemical synthesis.
- During Ni oxidation/reduction, different competition of the species according to the synthesis route.

Conclusion Using electrogravimetric studies brings to light different species exchanges and competitions for two synthesis routes of the Ni/Fe LDH. This study will be completed by other in situ techniques (ac-électrogravimétry, XRD) to identify the nature of the exchanged species.

References

1. Delorme, F.; Seron, A.; Vergnaud, B.; Galle-Cavalloni, P.; Jean-Prost, V.; Manguin, J., *Journal of Materials Science* **2013,** *48* (15), 5273-5279.
2. Agrisuelas, J.; Delgado, C.; Gabrielli, C.; Garcia-Jareno, J. J.; Perrot, H.; Sel, O.; Vicente, F., *Journal of Solid State Electrochemistry* **2015,** *19* (9), 2555-2564.

References

1. Zhao, Y.; Li, F.; Zhang, R.; Evans, D. G.; Duan, X., Preparation of layered double-hydroxide nanomaterials with a uniform crystallite size using a new method involving separate nucleation and aging steps. *Chemistry of Materials* **2002,** *14* (10), 4286-4291.
2. Evans, D. G.; Duan, X., Preparation of layered double hydroxides and their applications as additives in polymers, as precursors to magnetic materials and in biology and medicine. *Chemical Communications* **2006,** (5), 485-496.
3. Williams, G. R.; O'Hare, D., Towards understanding, control and application of layered double hydroxide chemistry. *Journal of Materials Chemistry* **2006,** *16* (30), 3065-3074.
4. Zhang, C.; Shao, M. F.; Zhou, L.; Li, Z. H.; Xiao, K. M.; Wei, M., Hierarchical NiFe Layered Double Hydroxide Hollow Microspheres with Highly-Efficient Behavior toward Oxygen Evolution Reaction. *Acs Applied Materials & Interfaces* **2016,** *8* (49), 33697-33703.
5. Friebel, D.; Louie, M. W.; Bajdich, M.; Sanwald, K. E.; Cai, Y.; Wise, A. M.; Cheng, M. J.; Sokaras, D.; Weng, T. C.; Alonso-Mori, R.; Davis, R. C.; Bargar, J. R.; Norskov, J. K.; Nilsson, A.; Bell, A. T., Identification of Highly Active Fe Sites in (Ni,Fe)OOH for Electrocatalytic Water Splitting. *Journal of the American Chemical Society* **2015,** *137* (3), 1305-1313.
6. Lee, S. H.; Yi, C. W.; Kim, K., Characteristics and Electrochemical Performance of the TiO2-Coated ZnO Anode for Ni-Zn Secondary Batteries. *Journal of Physical Chemistry C* **2011,** *115* (5), 2572-2577.
7. Simon, P.; Gogotsi, Y., Materials for electrochemical capacitors. *Nature Materials* **2008,** *7* (11), 845-854.
8. Chen, H.; Hu, L. F.; Chen, M.; Yan, Y.; Wu, L. M., Nickel- Cobalt Layered Double Hydroxide Nanosheets for High- performance Supercapacitor Electrode Materials. *Advanced Functional Materials* **2014,** *24* (7), 934-942.
9. Roto, R.; Villemure, G., Cyclic voltammetry of metal bipyridyl cations at redox active Ni-Al-Cl layered double hydroxide films. *Journal of Electroanalytical Chemistry* **2007,** *601* (1-2), 112-118.
10. Roto, R.; Yamagishi, A.; Villemure, G., Electrochemical quartz crystal microbalance study of mass transport in thin film of a redox active Ni-Al-Cl layered double hydroxide. *Journal of Electroanalytical Chemistry* **2004,** *572* (1), 101-108.
11. Agrisuelas, J.; Gabrielli, C.; Garcia-Jareno, J. J.; Perrot, H.; Sel, O.; Vicente, F., Polymer dynamics in thin p-type conducting films investigated by ac-electrogravimetry. Kinetics aspects on anion exclusion, free solvent transfer, and conformational changes in poly(o-toluidine). *Electrochimica Acta* **2015,** *153*, 33-43.
12. Escobar-Teran, F.; Arnau, A.; Garcia, J. V.; Jimenez, Y.; Perrot, H.; Sel, O., Gravimetric and dynamic deconvolution of global EQCM response of carbon nanotube based electrodes by Ac-electrogravimetry. *Electrochemistry Communications* **2016,** *70*, 73-77.
13. Gabrielli, C.; Garcia-Jareno, J. J.; Keddam, M.; Perrot, H.; Vicente, F., Ac-electrogravimetry study of electroactive thin films. II. Application to polypyrrole. *Journal of Physical Chemistry B* **2002,** *106* (12), 3192-3201.
14. Toupin, M.; Brousse, T.; Belanger, D., Charge storage mechanism of MnO2 electrode used in aqueous electrochemical capacitor. *Chemistry of Materials* **2004,** *16* (16), 3184-3190.
15. Benicio, L. P. F.; Silva, R. A.; Lopes, J. A.; Eulalio, D.; dos Santos, R. M. M.; de Aquino, L. A.; Vergutz, L.; Novais, R. F.; da Costa, L. M.; Pinto, F. G.; Tronto, J., LAYERED DOUBLE HYDROXIDES: NANOMATERIALS FOR APPLICATIONS IN AGRICULTURE. *Revista Brasileira De Ciencia Do Solo* **2015,** *39* (1), 1-13.
16. Cavani, F.; Trifiro, F.; Vaccari, A., HYDROTALCITE-TYPE ANIONIC CLAYS: PREPARATION, PROPERTIES AND APPLICATIONS. *Catalysis Today* **1991,** *11* (2), 173-301.
17. Evans, D. G.; Slade, R. C. T., Structural aspects of layered double hydroxides. In *Layered Double Hydroxides*, Duan, X.; Evans, D. G., Eds. Springer-Verlag Berlin: Berlin, 2006; Vol. 119, pp 1-87.

18. Britto, S.; Kamath, P. V., Polytypism in the Lithium-Aluminum Layered Double Hydroxides: The LiAl2(OH)(6) (+) Layer as a Structural Synthon. *Inorganic Chemistry* **2011,** *50* (12), 5619-5627.
19. Shao, M. F.; Han, J. B.; Wei, M.; Evans, D. G.; Duan, X., The synthesis of hierarchical Zn-Ti layered double hydroxide for efficient visible-light photocatalysis. *Chemical Engineering Journal* **2011,** *168* (2), 519-524.
20. Gu, Y. H.; Lu, Z. Y.; Chang, Z.; Liu, J. F.; Lei, X. D.; Li, Y. P.; Sun, X. M., NiTi layered double hydroxide thin films for advanced pseudocapacitor electrodes. *Journal of Materials Chemistry A* **2013,** *1* (36), 10655-10661.
21. Delorme, F.; Seron, A.; Vergnaud, B.; Galle-Cavalloni, P.; Jean-Prost, V.; Manguin, J., Evidence of the influence of the cationic composition on the anionic affinity of layered double hydroxides. *Journal of Materials Science* **2013,** *48* (15), 5273-5279.
22. Leroux, F.; Taviot-Gueho, C., Fine tuning between organic and inorganic host structure: new trends in layered double hydroxide hybrid assemblies. *Journal of Materials Chemistry* **2005,** *15* (35-36), 3628-3642.
23. Goh, K. H.; Lim, T. T.; Banas, A.; Dong, Z. L., Sorption characteristics and mechanisms of oxyanions and oxyhalides having different molecular properties on Mg/Al layered double hydroxide nanoparticles. *Journal of Hazardous Materials* **2010,** *179* (1-3), 818-827.
24. Abdolmohammad-Zadeh, H.; Rezvani, Z.; Sadeghi, G. H.; Zorufi, E., Layered double hydroxides: A novel nano-sorbent for solid-phase extraction. *Analytica Chimica Acta* **2011,** *685* (2), 212-219.
25. Violante, A.; Pucci, M.; Cozzolino, V.; Zhu, J.; Pigna, M., Sorption/desorption of arsenate on/from Mg-Al layered double hydroxides: Influence of phosphate. *Journal of Colloid and Interface Science* **2009,** *333* (1), 63-70.
26. Constantino, V. R. L.; Pinnavaia, T. J., STRUCTURE-REACTIVITY RELATIONSHIPS FOR BASIC CATALYSTS DERIVED FROM A MG(2+)/AL(3+)/CO(3)(2-) LAYERED DOUBLE HYDROXIDE. *Catalysis Letters* **1994,** *23* (3-4), 361-367.
27. Beres, A.; Palinko, I.; Kiricsi, I.; Nagy, J. B.; Kiyozumi, Y.; Mizukami, F., Layered double hydroxides and their pillared derivatives - materials for solid base catalysis; synthesis and characterization. *Applied Catalysis a-General* **1999,** *182* (2), 237-247.
28. Basile, F.; Benito, P.; Fornasari, G.; Rosetti, V.; Scavetta, E.; Tonelli, D.; Vaccari, A., Electrochemical synthesis of novel structured catalysts for H-2 production. *Applied Catalysis B-Environmental* **2009,** *91* (1-2), 563-572.
29. Del Hoyo, C., Layered double hydroxides and human health: An overview. *Applied Clay Science* **2007,** *36* (1-3), 103-121.
30. Trikeriotis, M.; Ghanotakis, D. F., Intercalation of hydrophilic and hydrophobic antibiotics in layered double hydroxides. *International Journal of Pharmaceutics* **2007,** *332* (1-2), 176-184.
31. Choy, J. H.; Jung, J. S.; Oh, J. M.; Park, M.; Jeong, J.; Kang, Y. K.; Han, O. J., Layered double hydroxide as an efficient drug reservoir for folate derivatives. *Biomaterials* **2004,** *25* (15), 3059-3064.
32. Li, B. X.; He, J.; Evans, D. G.; Duan, X., Inorganic layered double hydroxides as a drug delivery system - intercalation and in vitro release of fenbufen. *Applied Clay Science* **2004,** *27* (3-4), 199-207.
33. Perioli, L.; Posati, T.; Nocchetti, M.; Bellezza, F.; Costantino, U.; Cipiciani, A., Intercalation and release of antiinflammatory drug diclofenac into nanosized ZnAl hydrotalcite-like compound. *Applied Clay Science* **2011,** *53* (3), 374-378.
34. Gualandi, I.; Monti, M.; Scavetta, E.; Tonelli, D.; Prevot, V.; Mousty, C., Electrodeposition of Layered Double Hydroxides on platinum: Insights into the reactions sequence. *Electrochimica Acta* **2015,** *152*, 75-83.
35. Scavetta, E.; Mignani, A.; Prandstraller, D.; Tonelli, D., Electrosynthesis of thin films of Ni, Al hydrotalcite like compounds. *Chemistry of Materials* **2007,** *19* (18), 4523-4529.
36. Lovric, M.; Scholz, F., A model for the propagation of a redox reaction through microcrystals. *Journal of Solid State Electrochemistry* **1997,** *1* (1), 108-113.
37. Prevot, V.; Tokudome, Y., 3D hierarchical and porous layered double hydroxide structures: an overview of synthesis methods and applications. *Journal of Materials Science* **2017,** *52* (19), 11229-11250.
38. Goh, K. H.; Lim, T. T.; Dong, Z., Application of layered double hydroxides for removal of oxyanions: A review. *Water Research* **2008,** *42* (6-7), 1343-1368.

39. Liang, X. F.; Zang, Y. B.; Xu, Y. M.; Tan, X.; Hou, W. G.; Wang, L.; Sun, Y. B., Sorption of metal cations on layered double hydroxides. *Colloids and Surfaces a-Physicochemical and Engineering Aspects* **2013,** *433*, 122-131.
40. Jobbagy, M.; Regazzoni, A. E., Dissolution of nano-size Mg-Al-Cl hydrotalcite in aqueous media. *Applied Clay Science* **2011,** *51* (3), 366-369.
41. Rojas, R., Effect of particle size on copper removal by layered double hydroxides. *Chemical Engineering Journal* **2016,** *303*, 331-337.
42. Marappa, S.; Kamath, P. V., Water Molecules in Hydrotalcite-like Layered Double Hydroxides: Interplay between the Hydration of the Anions and the Metal Hydroxide Layer. *Zeitschrift Fur Anorganische Und Allgemeine Chemie* **2015,** *641* (5), 927-934.
43. Wang, Y. F.; Gao, H. Z., Compositional and structural control on anion sorption capability of layered double hydroxides (LDHs). *Journal of Colloid and Interface Science* **2006,** *301* (1), 19-26.
44. Miyata, S., PHYSICOCHEMICAL PROPERTIES OF SYNTHETIC HYDROTALCITES IN RELATION TO COMPOSITION. *Clays and Clay Minerals* **1980,** *28* (1), 50-56.
45. Costa, D. G.; Rocha, A. B.; Souza, W. F.; Chiaro, S. S. X.; Leitao, A. A., Comparative Structural, thermodynamic and electronic analyses of Zn-Al-A(n-) hydrotalcite-like compounds (A(n-)=Cl-, F-, Br-, OH-, CO32- or NO3-): An ab initio study. *Applied Clay Science* **2012,** *56*, 16-22.
46. Delorme, F.; Seron, A.; Gautier, A.; Crouzet, C., Comparison of the fluoride, arsenate and nitrate anions water depollution potential of a calcined quintinite, a layered double hydroxide compound. *Journal of Materials Science* **2007,** *42* (14), 5799-5804.
47. Tezuka, S.; Chitrakar, R.; Sonoda, A.; Ooi, K.; Tomida, T., Nitrate ion-sieve properties of layered double hydroxides. *Chemistry Letters* **2003,** *32* (8), 722-723.
48. Tezuka, S.; Chitrakar, R.; Sonoda, A.; Ooi, K.; Tomida, T., Studies on selective adsorbents for oxo-anions. Nitrate ion-exchange properties of layered double hydroxides with different metal atoms. *Green Chemistry* **2004,** *6* (2), 104-109.
49. Hibino, T., Anion Selectivity of Layered Double Hydroxides: Effects of Crystallinity and Charge Density. *European Journal of Inorganic Chemistry* **2018,** (6), 722-730.
50. Murayama , N.; Sakamoto , D.; Shibata, J.; Valix, M., Removal of Harmful Anions in Aqueous Solution with Various Layered Double Hydroxides. *Resources Processing* **2013,** *60* (3), 131-137.
51. Liang, X. F.; Hou, W. G.; Xu, Y. M.; Sun, G. H.; Wang, L.; Sun, Y.; Qin, X., Sorption of lead ion by layered double hydroxide intercalated with diethylenetriaminepentaacetic acid. *Colloids and Surfaces a-Physicochemical and Engineering Aspects* **2010,** *366* (1-3), 50-57.
52. Kameda, T.; Saito, S.; Umetsu, Y., Mg-Al layered double hydroxide intercalated with ethylene-diaminetetraacetate anion: Synthesis and application to the uptake of heavy metal ions from an aqueous solution. *Separation and Purification Technology* **2005,** *47* (1-2), 20-26.
53. Fujii, S.; Sugie, Y.; Kobune, M.; Touno, A.; Touji, J., UPTAKES OF CU2+, PH2+ AND ZN2+ ON SYNTHETIC HYDROTALCITE IN AQUEOUS-SOLUTION. *Nippon Kagaku Kaishi* **1992,** (12), 1504-1507.
54. Marani, D.; Macchi, G.; Pagano, M., LEAD PRECIPITATION IN THE PRESENCE OF SULFATE AND CARBONATE - TESTING OF THERMODYNAMIC PREDICTIONS. *Water Research* **1995,** *29* (4), 1085-1092.
55. Zhao, D. L.; Sheng, G. D.; Hu, J.; Chen, C. L.; Wang, X. K., The adsorption of Pb(II) on Mg2Al layered double hydroxide. *Chemical Engineering Journal* **2011,** *171* (1), 167-174.
56. Richardson, M. C.; Braterman, P. S., Cation exchange by anion-exchanging clays: the effects of particle aging. *Journal of Materials Chemistry* **2009,** *19* (42), 7965-7975.
57. Kameda, T.; Yoshioka, T., Hybrid Inorganic-organic Composites of Layered Double Hydroxides Intercalated with Organic Acid Anions for the Uptake of Hazardous Substances from Aqueous Solution. In *Metal, Ceramic and Polymeric Composites for Various Uses*, Cuppoletti, J., Ed. Intech Europe: Rijeka, 2011; pp 123-148.
58. Byrne, R. H., Inorganic speciation of dissolved elements in seawater: the influence of pH on concentration ratios. *Geochemical Transactions* **2002,** *3*, 11-16.
59. Buffle, J., Complexation Reactions in Aquatic Systems; Analytical Approach. *Acta Hydrochimica et hydrobiologica* **1988,** *17* (2).

60. Hu, W. G.; Su, Y. L.; Sun, D. J.; Zhang, C. G., Studies on zero point of charge and permanent charge density of Mg-Fe hydrotalcite-like compounds. *Langmuir* **2001,** *17* (6), 1885-1888.
61. Elmoubarki, R.; Mahjoubi, F. Z.; Elhalil, A.; Tounsadi, H.; Abdennouri, M.; Sadiq, M.; Qourzal, S.; Zouhri, A.; Barka, N., Ni/Fe and Mg/Fe layered double hydroxides and their calcined derivatives: preparation, characterization and application on textile dyes removal. *Journal of Materials Research and Technology-Jmr&T* **2017,** *6* (3), 271-283.
62. Liu, Y. T.; Wang, M. K.; Chen, T. Y.; Chiang, P. N.; Huang, P. M.; Lee, J. F., Arsenate sorption on lithium/aluminum layered double hydroxide intercalated by chloride and on gibbsite: Sorption isotherms, envelopes, and spectroscopic studies. *Environmental Science & Technology* **2006,** *40* (24), 7784-7789.
63. Yang, L.; Shahrivari, Z.; Liu, P. K. T.; Sahimi, M.; Tsotsis, T. T., Removal of trace levels of arsenic and selenium from aqueous solutions by calcined and uncalcined layered double hydroxides (LDH). *Industrial & Engineering Chemistry Research* **2005,** *44* (17), 6804-6815.
64. Das, D. P.; Das, J.; Parida, K., Physicochemical characterization and adsorption behavior of calcined Zn/Al hydrotalcite-like compound (HTlc) towards removal of fluoride from aqueous solution. *Journal of Colloid and Interface Science* **2003,** *261* (2), 213-220.
65. Manju, G. N.; Gigi, M. C.; Anirudhan, T. S., Hydrotalcite as adsorbent for the removal of chromium (VI) from aqueous media: Equilibrium studies. *Indian Journal of Chemical Technology* **1999,** *6* (3), 134-141.
66. Terry, P. A., Characterization of Cr ion exchange with hydrotalcite. *Chemosphere* **2004,** *57* (7), 541-546.
67. Kameda, T.; Takeuchi, H.; Yoshioka, T., Kinetics of uptake of Cu2+ and Cd2+ by Mg-Al layered double hydroxides intercalated with citrate, malate, and tartrate. *Colloids and Surfaces a-Physicochemical and Engineering Aspects* **2010,** *355* (1-3), 172-177.
68. Das, J.; Das, D.; Dash, G. P.; Parida, K. M., Studies on Mg/Fe hydrotalcite-like-compound (HTlc) - I. Removal of inorganic selenite (SeO32-) from aqueous medium. *Journal of Colloid and Interface Science* **2002,** *251* (1), 26-32.
69. Chitrakar, R.; Tezuka, S.; Sonoda, A.; Sakane, K.; Ooi, K.; Hirotsu, T., Adsorption of phosphate from seawater on calcined MgMn-layered double hydroxides. *Journal of Colloid and Interface Science* **2005,** *290* (1), 45-51.
70. Tezuka, S.; Chitrakar, R.; Sonoda, A.; Ooi, K.; Tomida, T., Studies on selective adsorbents for oxo-anions. NO3- adsorptive properties of Ni-Fe layered double hydroxide in seawater. *Adsorption-Journal of the International Adsorption Society* **2005,** *11*, 751-755.
71. Chen, M.; Shen, W.; Lu, X. C.; Zhu, R.; He, H. P.; Zhu, J. X., Jumping Diffusion of Water Intercalated in Layered Double Hydroxides. *Journal of Physical Chemistry C* **2016,** *120* (23), 12924-12931.
72. Likos, W. J.; Lu, N., Pore-scale analysis of bulk volume change from crystalline interlayer swelling in Na+- and Ca2+-smectite. *Clays and Clay Minerals* **2006,** *54* (4), 515-528.
73. Norrish, K., THE SWELLING OF MONTMORILLONITE. *Discussions of the Faraday Society* **1954,** (18), 120-134.
74. Kittrick, J. A., INTERLAYER FORCES IN MONTMORILLONITE AND VERMICULITE. *Soil Science Society of America Proceedings* **1969,** *33* (2), 217-&.
75. Laird, D. A., Model for crystalline swelling of 2:1 phyllosilicates. *Clays and Clay Minerals* **1996,** *44* (4), 553-559.
76. Rattan, L.; K., S. M., *Principle of soil Physics*. Marcel Dekker: New York, 2004.
77. Seron, A.; Delorme, F., Synthesis of layered double hydroxides (LDHs) with varying pH: A valuable contribution to the study of Mg/Al LDH formation mechanism. *Journal of Physics and Chemistry of Solids* **2008,** *69* (5-6), 1088-1090.
78. Miyata, S., SYNTHESES OF HYDROTALCITE-LIKE COMPOUNDS AND THEIR STRUCTURES AND PHYSICOCHEMICAL PROPERTIES .1. SYSTEMS MG2+-AL3+-NO-3,MG2+-AL3+-CL-,MG2+-AL3+-CLO-4,NI2P-AL3+-CL- AND ZN2+-AL3+-CL. *Clays and Clay Minerals* **1975,** *23* (5), 369-&.
79. Carja, G.; Nakamura, R.; Aida, T.; Niiyama, H., Textural properties of layered double hydroxides: effect of magnesium substitution by copper or iron. *Microporous and Mesoporous Materials* **2001,** *47* (2-3), 275-284.

80. Ni, X. M.; Kuang, K. Q.; Jin, X.; Xiao, X. K.; Liao, G. X., Large scale synthesis of porous microspheres of Mg-Al-layerd double hydroxide with improved fire suppression effectiveness. *Solid State Sciences* **2010,** *12* (4), 546-551.
81. Costa, D. G.; Rocha, A. B.; Diniz, R.; Souza, W. F.; Chiaro, S. S. X.; Leitao, A. A., Structural Model Proposition and Thermodynamic and Vibrational Analysis of Hydrotalcite-Like Compounds by DFT Calculations. *Journal of Physical Chemistry C* **2010,** *114* (33), 14133-14140.
82. Xiao, T.; Tang, Y. W.; Jia, Z. Y.; Li, D. W.; Hu, X. Y.; Li, B. H.; Luo, L. J., Self-assembled 3D flower-like Ni2+-Fe3+ layered double hydroxides and their calcined products. *Nanotechnology* **2009,** *20* (47), 7.
83. Gu, T. H.; Gunjakar, J. L.; Kim, I. Y.; Patil, S. B.; Lee, J. M.; Jin, X.; Lee, N. S.; Hwang, S. J., Porous Hybrid Network of Graphene and Metal Oxide Nanosheets as Useful Matrix for Improving the Electrode Performance of Layered Double Hydroxides. *Small* **2015,** *11* (32), 3921-3931.
84. Xu, Z. P.; Zeng, H. C., A new approach for design and synthesis of Co-II and Co-II,Co-III hydroxide materials. *International Journal of Inorganic Materials* **2000,** *2* (2-3), 187-196.
85. Ma, R.; Takada, K.; Fukuda, K.; Iyi, N.; Bando, Y.; Sasaki, T., Phase transitions - Topochemical synthesis of monometallic (Co2+-CO3+) layered double hydroxide and its exfoliation into positively charged Co(OH)2 nanosheets. *Angewandte Chemie-International Edition* **2008,** *47* (1), 86-89.
86. Xu, Z. P.; Stevenson, G.; Lu, C. Q.; Lu, G. Q., Dispersion and size control of layered double hydroxide nanoparticles in aqueous solutions. *Journal of Physical Chemistry B* **2006,** *110* (34), 16923-16929.
87. Chen, L. B.; Li, C. C.; Wei, Y. H.; Zhou, G.; Pan, A. Q.; Wei, W. F.; Huang, B. Y., Hollow LDH nanowires as excellent adsorbents for organic dye. *Journal of Alloys and Compounds* **2016,** *687*, 499-505.
88. Faour, A.; Mousty, C.; Prevot, V.; Devouard, B.; De Roy, A.; Bordet, P.; Elkaim, E.; Taviot-Gueho, C., Correlation among Structure, Microstructure, and Electrochemical Properties of NiAl-CO3 Layered Double Hydroxide Thin Films. *Journal of Physical Chemistry C* **2012,** *116* (29), 15646-15659.
89. Prevot, V.; Szczepaniak, C.; Jaber, M., Aerosol-assisted self-assembly of hybrid Layered Double Hydroxide particles into spherical architectures. *Journal of Colloid and Interface Science* **2011,** *356* (2), 566-572.
90. Wang, Y. C.; Zhang, F. Z.; Xu, S. L.; Wang, X. Y.; Evans, D. G.; Duan, X., Preparation of layered double hydroxide microspheres by spray drying. *Industrial & Engineering Chemistry Research* **2008,** *47* (15), 5746-5750.
91. Soler-illia, G. J. D.; Sanchez, C.; Lebeau, B.; Patarin, J., Chemical strategies to design textured materials: From microporous and mesoporous oxides to nanonetworks and hierarchical structures. *Chemical Reviews* **2002,** *102* (11), 4093-4138.
92. Torchilin, V. P., Micellar nanocarriers: Pharmaceutical perspectives. *Pharmaceutical Research* **2007,** *24* (1), 1-16.
93. Tarutani, N.; Tokudome, Y.; Jobbagy, M.; Viva, F. A.; Soler-Illia, G.; Takahashi, M., Single-Nanometer-Sized Low-Valence Metal Hydroxide Crystals: Synthesis via Epoxide-Mediated Alkalinization and Assembly toward Functional Mesoporous Materials. *Chemistry of Materials* **2016,** *28* (16), 5606-5610.
94. Gunawan, P.; Xu, R., Synthesis of unusual coral-like layered double hydroxide microspheres in a nonaqueous polar solvent/surfactant system. *Journal of Materials Chemistry* **2008,** *18* (18), 2112-2120.
95. Zhang, J.; Xie, X. L.; Li, C. J.; Wang, H.; Wang, L. J., The role of soft colloidal templates in the shape evolution of flower-like MgAl-LDH hierarchical microstructures. *Rsc Advances* **2015,** *5* (38), 29757-29765.
96. Sun, H. X.; Chu, Z. Y.; Hong, D. H.; Zhang, G.; Xie, Y.; Li, L.; Shi, K. Y., Three-dimensional hierarchical flower-like Mg-Al-layered double hydroxides: Fabrication, characterization and enhanced sensing properties to NOx at room temperature. *Journal of Alloys and Compounds* **2016,** *658*, 561-568.
97. Shao, M. F.; Ning, F. Y.; Zhao, J. W.; Wei, M.; Evans, D. G.; Duan, X., Hierarchical Layered Double Hydroxide Microspheres with Largely Enhanced Performance for Ethanol Electrooxidation. *Advanced Functional Materials* **2013,** *23* (28), 3513-3518.
98. Vialat, P.; Leroux, F.; Mousty, C., Hybrid Co2Al-ABTS/reduced graphene oxide Layered Double Hydroxide: Towards O-2 biocathode development. *Electrochimica Acta* **2015,** *158*, 113-120.
99. Scavetta, E.; Vlamidis, Y.; Posati, T.; Nocchetti, M.; Tonelli, D., Effect of the Synthesis Route and Fe Presence on the Redox Activity of Ni in Layered Double Hydroxides. *Chemelectrochem* **2016,** *3* (9), 1320-1328.

100. Valarezo, E.; Tammaro, L.; Gonzalez, S.; Malagon, O.; Vittoria, V., Fabrication and sustained release properties of poly(epsilon-caprolactone) electrospun fibers loaded with layered double hydroxide nanoparticles intercalated with amoxicillin. *Applied Clay Science* **2013,** *72*, 104-109.
101. Zhang, F. Z.; Sun, M.; Xu, S. L. L.; Zhao, L. L.; Zhang, B. W., Fabrication of oriented layered double hydroxide films by spin coating and their use in corrosion protection. *Chemical Engineering Journal* **2008,** *141* (1-3), 362-367.
102. Wang, Y.; Dou, H.; Wang, J.; Ding, B.; Xu, Y. L.; Chang, Z.; Hao, X. D., Three-dimensional porous MXene/layered double hydroxide composite for high performance supercapacitors. *Journal of Power Sources* **2016,** *327*, 221-228.
103. Huang, S.; Zhu, G. N.; Zhang, C.; Tjiu, W. W.; Xia, Y. Y.; Liu, T. X., Immobilization of Co-Al Layered Double Hydroxides on Graphene Oxide Nanosheets: Growth Mechanism and Supercapacitor Studies. *Acs Applied Materials & Interfaces* **2012,** *4* (4), 2242-2249.
104. Guo, X. X.; Xu, S. L.; Zhao, L. L.; Lu, W.; Zhang, F. Z.; Evans, D. G.; Duan, X., One-Step Hydrothermal Crystallization of a Layered Double Hydroxide/Alumina Bilayer Film on Aluminum and Its Corrosion Resistance Properties. *Langmuir* **2009,** *25* (17), 9894-9897.
105. Szekeres, M.; Szechenyi, A.; Stepan, K.; Haraszti, T.; Dekany, I., Layer-by-layer self-assembly preparation of layered double hydroxide/polyelectrolyte nanofilms monitored by surface plasmon resonance spectroscopy. *Colloid and Polymer Science* **2005,** *283* (9), 937-945.
106. Indira, L.; Kamath, P. V., ELECTROGENERATION OF BASE BY CATHODIC REDUCTION OF ANIONS - NOVEL ONE-STEP ROUTE TO UNARY AND LAYERED DOUBLE HYDROXIDES (LDHS). *Journal of Materials Chemistry* **1994,** *4* (9), 1487-1490.
107. Perez-Gallent, E.; Figueiredo, M. C.; Katsounaros, I.; Koper, M. T. M., Electrocatalytic reduction of Nitrate on Copper single crystals in acidic and alkaline solutions. *Electrochimica Acta* **2017,** *227*, 77-84.
108. Cai, Y.; Anderson, A. B., The reversible hydrogen electrode: Potential-dependent activation energies over platinum from quantum theory. *Journal of Physical Chemistry B* **2004,** *108* (28), 9829-9833.
109. Dima, G. E.; de Vooys, A. C. A.; Koper, M. T. M., Electrocatalytic reduction of nitrate at low concentration on coinage and transition-metal electrodes in acid solutions. *Journal of Electroanalytical Chemistry* **2003,** *554*, 15-23.
110. Davis, J.; Moorcroft, M. J.; Wilkins, S. J.; Compton, R. G.; Cardosi, M. F., Electrochemical detection of nitrate and nitrite at a copper modified electrode. *Analyst* **2000,** *125* (4), 737-741.
111. Hu, J. F.; Sun, J. Z.; Bian, C.; Tong, J. H.; Zia, S. H., Three-dimensional nano-structured silver on gold interdigitated microband array electrode for nitrate determination. *Indian Journal of Chemical Technology* **2012,** *19* (6), 414-419.
112. Solak, A. O.; Cekirdek, P., Square wave voltammetric determination of nitrate at a freshly copper plated glassy carbon electrode. *Analytical Letters* **2005,** *38* (2), 271-280.
113. Mignani, A.; Ballarin, B.; Giorgetti, M.; Scavetta, E.; Tonelli, D.; Boanini, E.; Prevot, V.; Mousty, C.; Iadecola, A., Heterostructure of Au Nanoparticles-NiAl Layered Double Hydroxide: Electrosynthesis, Characterization, and Electrocatalytic Properties. *Journal of Physical Chemistry C* **2013,** *117* (31), 16221-16230.
114. Scavetta, E.; Ballarin, B.; Giorgetti, M.; Carpani, I.; Cogo, F.; Tonelli, D., Electrodes modified by one-step electrosynthesis of Ni/Al-NO3 double layered hydroxide. *Journal of New Materials for Electrochemical Systems* **2004,** *7* (1), 43-50.
115. Yarger, M. S.; Steinmiller, E. M. P.; Choi, K. S., Electrochemical synthesis of Zn-Al layered double hydroxide (LDH) films. *Inorganic Chemistry* **2008,** *47* (13), 5859-5865.
116. Monti, M.; Benito, P.; Basile, F.; Fornasari, G.; Gazzano, M.; Scavetta, E.; Tonelli, D.; Vaccari, A., Electrosynthesis of Ni/Al and Mg/Al Layered Double Hydroxides on Pt and FeCrAlloy supports: Study and control of the pH near the electrode surface. *Electrochimica Acta* **2013,** *108*, 596-604.
117. Obayashi, C.; Ishizaka, M.; Konishi, T.; Yamada, H.; Katakura, K., Preparation of the Electrochemically Precipitated Mn-Al LDHs and Their Electrochemical Behaviors. *Electrochemistry* **2012,** *80* (11), 879-882.
118. Lovric, M.; Hermes, M.; Scholz, F., The effect of the electrolyte concentration in the solution on the voltammetric response of insertion electrodes. *Journal of Solid State Electrochemistry* **1998,** *2* (6), 401-404.

119. Schroder, U.; Oldham, K. B.; Myland, J. C.; Mahon, P. J.; Scholz, F., Modelling of solid state voltammetry of immobilized microcrystals assuming an initiation of the electrochemical reaction at a three-phase junction. *Journal of Solid State Electrochemistry* **2000,** *4* (6), 314-324.
120. Mousty, C.; Leroux, F., LDHs as Electrode Materials for Electrochemical Detection and Energy Storage: Supercapacitor, Battery and (Bio)-Sensor. *Recent Patents on Nanotechnology* **2012,** *6* (3), 174-192.
121. Mousty, C.; Prevot, V., Hybrid and biohybrid layered double hydroxides for electrochemical analysis. *Analytical and Bioanalytical Chemistry* **2013,** *405* (11), 3513-3523.
122. Mousty, C.; Therias, S.; Forano, C.; Besse, J. P., ANION-EXCHANGING CLAY-MODIFIED ELECTRODES - SYNTHETIC LAYERED DOUBLE HYDROXIDES INTERCALATED WITH ELECTROACTIVE ORGANIC-ANIONS. *Journal of Electroanalytical Chemistry* **1994,** *374* (1-2), 63-69.
123. Therias, S.; Mousty, C.; Forano, C.; Besse, J. P., Electrochemical transfer at anionic clay modified electrodes. Case of 2,2'-azinobis(3-ethylbenzothiazoline-6-sulfonate). *Langmuir* **1996,** *12* (20), 4914-4920.
124. Therias, S.; Lacroix, B.; Schollhorn, B.; Mousty, C.; Palvadeau, P., Electrochemical study of ferrocene and nitroxide derivatives intercalated in Zn-Cr and Zn-Al layered double hydroxides. *Journal of Electroanalytical Chemistry* **1998,** *454* (1-2), 91-97.
125. Gaillon, L.; Bedioui, F.; Devynck, J.; Battioni, P., ELECTROCHEMICAL CHARACTERIZATION OF MANGANESE PORPHYRINS FIXED ONTO SILICA AND LAYERED DIHYDROXIDE MATRICES. *Journal of Electroanalytical Chemistry* **1993,** *347* (1-2), 435-442.
126. Yao, K.; Taniguchi, M.; Nakata, M.; Shimazu, K.; Takahashi, M.; Yamagishi, A., Mass transport on an anionic clay-modified electrode as studied by a quartz crystal microbalance. *Journal of Electroanalytical Chemistry* **1998,** *457* (1-2), 119-128.
127. Mousty, C.; Forano, C.; Fleutot, S.; Dupin, J. C., Electrochemical Study of Anionic Ferrocene Derivatives Intercalated in Layered Double Hydroxides: Application to Glucose Amperometric Biosensors. *Electroanalysis* **2009,** *21* (3-5), 399-408.
128. Ahmed, A. A. A.; Talib, Z. A.; bin Hussein, M. Z., Thermal, optical and dielectric properties of Zn-Al layered double hydroxide. *Applied Clay Science* **2012,** *56*, 68-76.
129. *Chemical Thermodynamics of Nickel*. Elsevier Science: 2005.
130. Bard, A. J.; Parsons, R.; Jordan, J., Standard Potentials in Aqueous Solution. CRC Press: 1985.
131. Vialat, P.; Leroux, F.; Mousty, C., Electrochemical properties of layered double hydroxides containing 3d metal cations. *Journal of Solid State Electrochemistry* **2015,** *19* (7), 1975-1983.
132. Conway, B. E.; Birss, V.; Wojtowicz, J., The role and utilization of pseudocapacitance for energy storage by supercapacitors. *Journal of Power Sources* **1997,** *66* (1-2), 1-14.
133. Scavetta, E.; Tonelli, D.; Giorgetti, A.; Nobili, F.; Marassi, R.; Berrettoni, M., AC impedance study of a synthetic hydrotalcite-like compound modified electrode in aqueous solution. *Electrochimica Acta* **2003,** *48* (10), 1347-1355.
134. Gao, Z.; Wang, J.; Li, Z. S.; Yang, W. L.; Wang, B.; Hou, M. J.; He, Y.; Liu, Q.; Mann, T.; Yang, P. P.; Zhang, M. L.; Liu, L. H., Graphene Nanosheet/Ni2+/Al3+ Layered Double-Hydroxide Composite as a Novel Electrode for a Supercapacitor. *Chemistry of Materials* **2011,** *23* (15), 3509-3516.
135. Vialat, P.; Leroux, F.; Taviot-Gueho, C.; Villemure, G.; Mousty, C., Insights into the electrochemistry of (CoxNi(1-x))(2)Al-NO3 Layered Double Hydroxides. *Electrochimica Acta* **2013,** *107*, 599-610.
136. Depauli, C. P.; Trasatti, S., ELECTROCHEMICAL SURFACE CHARACTERIZATION OF IRO2+SNO2 MIXED-OXIDE ELECTROCATALYSTS. *Journal of Electroanalytical Chemistry* **1995,** *396* (1-2), 161-168.
137. Roto, R.; Villemure, G., Electrochemical impedance spectroscopy of electrodes modified with thin films of Ni-Al-Cl layered double hydroxides. *Journal of Electroanalytical Chemistry* **2002,** *527* (1-2), 123-130.
138. Rodrigues, S.; Munichandraiah, N.; Shukla, A. K., Kinetics of hydrogen evolution reaction on Zr0.5Ti0.5V0.6Cr0.2Ni1.2 alloy in KOH electrolyte. *Bulletin of Materials Science* **2000,** *23* (5), 383-391.
139. Barral, G.; Maximovitch, S.; NjanjoEyoke, F., Study of electrochemically formed Ni(OH)(2) layers by EIS. *Electrochimica Acta* **1996,** *41* (7-8), 1305-1311.
140. Sluytersrehbach, M., IMPEDANCES OF ELECTROCHEMICAL SYSTEMS - TERMINOLOGY, NOMENCLATURE AND REPRESENTATION .1. CELLS WITH METAL-ELECTRODES AND LIQUID SOLUTIONS (IUPAC RECOMMENDATIONS 1994). *Pure and Applied Chemistry* **1994,** *66* (9), 1831-1891.

141. Barral, G.; Njanjoeyoke, F.; Maximovitch, S., CHARACTERIZATION OF THE PASSIVE LAYER AND OF HYDROXIDE DEPOSITS OF NICKEL BY IMPEDANCE SPECTROSCOPY. *Electrochimica Acta* **1995,** *40* (17), 2815-2828.
142. Macarthur, D. M., HYDRATED NICKEL HYDROXIDE ELECTRODE POTENTIAL SWEEP EXPERIMENTS. *Journal of the Electrochemical Society* **1970,** *117* (4), 422-+.
143. Hu, M.; Ji, X. D.; Lei, L. X.; Lu, X. W., The effect of cobalt on the electrochemical performances of Ni-Al layered double hydroxides used in Ni-M(H) battery. *Journal of Alloys and Compounds* **2013,** *578*, 17-25.
144. Li, Y. H.; Gregory, S., DIFFUSION OF IONS IN SEA-WATER AND IN DEEP-SEA SEDIMENTS. *Geochimica Et Cosmochimica Acta* **1974,** *38* (5), 703-714.
145. Flury, M.; Gimmi, T., Part 4, Physical Methods. In *Methods of Soil Analysis*, Soil Science Society of America: Madison, Wisconsin, USA, 2002.
146. Bostick, B. C.; Vairavamurthy, M. A.; Karthikeyan, K. G.; Chorover, J., Cesium adsorption on clay minerals: An EXAFS spectroscopic investigation. *Environmental Science & Technology* **2002,** *36* (12), 2670-2676.
147. Kim, Y.; Kirkpatrick, R. J., Na-23 and Cs-133 NMR study of cation adsorption on mineral surfaces: Local environments, dynamics, and effects of mixed cations. *Geochimica Et Cosmochimica Acta* **1997,** *61* (24), 5199-5208.
148. Debye, P.; Huckel, E., The theory of electrolytes I. The lowering of the freezing point and related occurrences. *Physikalische Zeitschrift* **1923,** *24*, 185-206.
149. Qiu, J. B.; Villemure, G., ANIONIC CLAY-MODIFIED ELECTRODES - ELECTROCHEMICAL ACTIVITY OF NICKEL(II) SITES IN LAYERED DOUBLE HYDROXIDE FILMS. *Journal of Electroanalytical Chemistry* **1995,** *395* (1-2), 159-166.
150. Qiu, J. B.; Villemure, G., Anionic clay modified electrodes: Electron transfer mediated by electroactive nickel, cobalt or manganese sites in layered double hydroxide films. *Journal of Electroanalytical Chemistry* **1997,** *428* (1-2), 165-172.
151. Corrigan, D. A.; Bendert, R. M., EFFECT OF COPRECIPITATED METAL-IONS ON THE ELECTROCHEMISTRY OF NICKEL-HYDROXIDE THIN-FILMS - CYCLIC VOLTAMMETRY IN 1M KOH. *Journal of the Electrochemical Society* **1989,** *136* (3), 723-728.
152. Song, F.; Hu, X. L., Exfoliation of layered double hydroxides for enhanced oxygen evolution catalysis. *Nature Communications* **2014,** *5*, 9.
153. Su, L. H.; Zhang, X. G.; Mi, C. H.; Liu, Y., Insights into the electrochemistry of layered double hydroxide containing cobalt and aluminum elements in lithium hydroxide aqueous solution. *Journal of Power Sources* **2008,** *179* (1), 388-394.
154. Ballarin, B.; Seeber, R.; Tonelli, D.; Vaccari, A., Electrocatalytic properties of nickel(II) hydrotalcite-type anionic clay: application to methanol and ethanol oxidation. *Journal of Electroanalytical Chemistry* **1999,** *463* (1), 123-127.
155. Lyons, M. E. G.; Brandon, M. P., Redox switching and oxygen evolution electrocatalysis in polymeric iron oxyhydroxide films. *Physical Chemistry Chemical Physics* **2009,** *11* (13), 2203-2217.
156. Oliver-Tolentino, M. A.; Vazquez-Samperio, J.; Manzo-Robledo, A.; Gonzalez-Huerta, R. D.; Flores-Moreno, J. L.; Ramirez-Rosales, D.; Guzman-Vargas, A., An Approach to Understanding the Electrocatalytic Activity Enhancement by Superexchange Interaction toward OER in Alkaline Media of Ni-Fe LDH. *Journal of Physical Chemistry C* **2014,** *118* (39), 22432-22438.
157. Trotochaud, L.; Young, S. L.; Ranney, J. K.; Boettcher, S. W., Nickel-Iron Oxyhydroxide Oxygen-Evolution Electrocatalysts: The Role of Intentional and Incidental Iron Incorporation. *Journal of the American Chemical Society* **2014,** *136* (18), 6744-6753.
158. Ruby, C.; Upadhyay, C.; Gehin, A.; Ona-Nguema, G.; Genin, J. M. R., In situ redox flexibility of FeII-III oxyhydroxycarbonate green rust and fougerite. *Environmental Science & Technology* **2006,** *40* (15), 4696-4702.
159. Antony, H.; Labrit, A.; Rouchaud, J. C.; Legrand, L.; Chausse, A., Study of Fe-II/Fe-III ratio in thin films of carbonate or sulphate green rusts obtained by potentiostatic electrosynthesis. *Electrochimica Acta* **2008,** *53* (24), 7173-7181.

160. Vialat, P.; Mousty, C.; Taviot-Gueho, C.; Renaudin, G.; Martinez, H.; Dupin, J. C.; Elkaim, E.; Leroux, F., High-Performing Monometallic Cobalt Layered Double Hydroxide Supercapacitor with Defined Local Structure. *Advanced Functional Materials* **2014,** *24* (30), 4831-4842.
161. Taviot-Gueho, C.; Vialat, P.; Leroux, F.; Razzaghi, F.; Perrot, H.; Sel, O.; Jensen, N. D.; Nielsen, U. G.; Peulon, S.; Elkaim, E.; Mousty, C., Dynamic Characterization of Inter- and Intralamellar Domains of Cobalt-Based Layered Double Hydroxides upon Electrochemical Oxidation. *Chemistry of Materials* **2016,** *28* (21), 7793-7806.
162. Zhang, L. J.; Zhang, X. G.; Shen, L. F.; Gao, B.; Hao, L.; Lu, X. J.; Zhang, F.; Ding, B.; Yuan, C. Z., Enhanced high-current capacitive behavior of graphene/CoAl-layered double hydroxide composites as electrode material for supercapacitors. *Journal of Power Sources* **2012,** *199*, 395-401.
163. Su, L. H.; Zhang, X. G.; Mi, C. H.; Gao, B.; Liu, Y., Improvement of the capacitive performances for Co-Al layered double hydroxide by adding hexacyanoferrate into the electrolyte. *Physical Chemistry Chemical Physics* **2009,** *11* (13), 2195-2202.
164. Roto, R.; Villemure, G., Mass transport in thin films of Fe(CN)(6) (4-) exchanged Ni-Al layered double hydroxide monitored with an electrochemical quartz crystal microbalance. *Journal of Electroanalytical Chemistry* **2006,** *588* (1), 140-146.
165. Mo, Y. B.; Hwang, E.; Scherson, D. A., In situ quartz crystal microbalance studies of nickel hydrous oxide films in alkaline electrolytes. *Journal of the Electrochemical Society* **1996,** *143* (1), 37-43.
166. Ohligschlager, T.; Schwitzgebel, G., EQCM contributions to the reactions of the nickel oxide electrode. *Physical Chemistry Chemical Physics* **2001,** *3* (23), 5290-5296.
167. Gabrielli, C.; Garcia-Jareno, J. J.; Keddam, M.; Perrot, H.; Vicente, F., Ac-electrogravimetry study of electroactive thin films. I. Application to Prussian Blue. *Journal of Physical Chemistry B* **2002,** *106* (12), 3182-3191.
168. Brezesinski, K.; Wang, J.; Haetge, J.; Reitz, C.; Steinmueller, S. O.; Tolbert, S. H.; Smarsly, B. M.; Dunn, B.; Brezesinski, T., Pseudocapacitive Contributions to Charge Storage in Highly Ordered Mesoporous Group V Transition Metal Oxides with Iso-Oriented Layered Nanocrystalline Domains. *Journal of the American Chemical Society* **2010,** *132* (20), 6982-6990.
169. Kanoh, H.; Tang, W. P.; Makita, Y.; Ooi, K., Electrochemical intercalation of alkali-metal ions into birnessite-type manganese oxide in aqueous solution. *Langmuir* **1997,** *13* (25), 6845-6849.
170. Kuo, S. L.; Wu, N. L., Investigation of pseudocapacitive charge-storage reaction of MnO2.nH(2)O supercapacitors in aqueous electrolytes. *Journal of the Electrochemical Society* **2006,** *153* (7), A1317-A1324.
171. Arias, C. R.; Debiemme-Chouvy, C.; Gabrielli, C.; Laberty-Robert, C.; Pailleret, A.; Perrot, H.; Sel, O., New Insights into Pseudocapacitive Charge-Storage Mechanisms in Li-Birnessite Type MnO2 Monitored by Fast Quartz Crystal Microbalance Methods. *Journal of Physical Chemistry C* **2014,** *118* (46), 26551-26559.
172. O, S. Hierarchical meso- and micropore architectures by liquid crystlline and polymer colloid templating. Universität Potsdam, 2006.
173. W., Z.; R., A.; Z., W.; D., J., *Scanning Microscopy for Nanotechnology*. Springer: New York, 2007.
174. Zhou; W.; Apkarian, R.; Wang, Z.; Joy, D., *Scanning Microscopy for Nanotechnology*. Springer: New York, 2007.
175. M., M. Electrical Properties of Single-Walled Carbon Nanotube Networks Produced by Langmuir-Blodgett Deposition Durham University, 2013.
176. L, B. Elaboration et caractérisation de poudres nanostructurées de MnO2 et de polypyrrole : Application comme matériaux d'électrodes dans des dispositifs de stockage de l'énergie. Université Pierre Marie Curie, 2014.
177. Howard, J. A. K.; Batsanov, A. S., Encyclopedia of Inorganic and Bioinorganic Chemistry. John Wiley & Sons, Ltd: 2011.
178. Fundamentals of Powder Diffraction and Structural Characterization of Materials. Springer US: 2009; pp 133-149.
179. B.D., C.; S.R, S., *Elements of X-Ray Diffraction, third edition*. 2001.
180. H., P., Chemical Sensors and Biosensors. John Wiley & Sons, Inc.: 2012; pp 71-91.
181. L., T. T. K. Etude de films électroactifs par couplage de techniques électrochimique et

gravimétrique. Application à la caractérisation de membranes à conduction protonique. Université Pierre et Marie Curie, 2009.
182. Buttry, D. A.; Ward, M. D., MEASUREMENT OF INTERFACIAL PROCESSES AT ELECTRODE SURFACES WITH THE ELECTROCHEMICAL QUARTZ CRYSTAL MICROBALANCE. *Chemical Reviews* **1992,** *92* (6), 1355-1379.
183. T.A., T. AlN piezoelectric films for sensing and actuation. Technische Universiteit Delft, 2014.
184. G.G., G., Methods and Phenomena. A.W, L. U. C. C., Ed. Elsevier: 1984; Vol. 7, pp 251- 280.
185. A, G. Ultrasensitive quartz crystal microbalance integrated with carbon nanotubes. The Pennsylvania State University, 2006.
186. G., T. Etude et développement d'une plateforme de détection chimique à ondes acoustiques de surface pour environnement sévère haute temperature. Université de Bordeaux, 2009.
187. D., J. MODELIZACION DE LA ELECTRODISOLUCION DEL CINC EN MEDIO ACIDO. Universitat de Valencia, 2004.
188. Bănică, F. G., *Chemical Sensors and Biosensors*. John Wiley & Sons, Ltd: 2012.
189. E., C.; K., K.; H., P.; Y., J., Piezoelectric Transducers and Applications. Vives, A., Ed. Springer Berlin Heidelberg: 2008; pp 307-330.
190. S., S.; E., C., Piezoelectric Transducers and Applications. Vives, A., Ed. Springer Berlin Heidelberg: 2008; pp 259-270.
191. Ostrom, G. S.; Buttry, D. A., QUARTZ CRYSTAL MICROBALANCE STUDIES OF DEPOSITION AND DISSOLUTION MECHANISMS OF ELECTROCHROMIC FILMS OF DIHEPTYLVIOLOGEN BROMIDE. *Journal of Electroanalytical Chemistry* **1988,** *256* (2), 411-431.
192. Sauerbrey, G., VERWENDUNG VON SCHWINGQUARZEN ZUR WAGUNG DUNNER SCHICHTEN UND ZUR MIKROWAGUNG. *Zeitschrift Fur Physik* **1959,** *155* (2), 206-222.
193. Bizet, K.; Gabrielli, C.; Perrot, H., Immunodetection by quartz crystal microbalance - A new approach for direct detection of rabbit IgG and peroxidase. *Applied Biochemistry and Biotechnology* **2000,** *89* (2-3), 139-149.
194. M.E., O.; B., T., *Electrochemical Impedance Spectroscopy*. John Wiley & Sons, Inc.: 2008.
195. Portet, C.; Taberna, P. L.; Simon, P.; Flahaut, E.; Laberty-Robert, C., High power density electrodes for carbon supercapacitor applications. *Electrochimica Acta* **2005,** *50* (20), 4174-4181.
196. Portet, C.; Taberna, P. L.; Simon, P.; Flahaut, E., Influence of carbon nanotubes addition on carbon-carbon supercapacitor performances in organic electrolyte. *Journal of Power Sources* **2005,** *139* (1-2), 371-378.
197. J., C. Caractérisation électrochimique de matériaux à insertion de Li pour supercondensateurs hybrides à haute densité d'énergie. Université de Toulouse, 2012.
198. Bourkane, S.; Gabrielli, C.; Keddam, M., KINETIC-STUDY OF ELECTRODE PROCESSES BY AC QUARTZ ELECTROGRAVIMETRY. *Journal of Electroanalytical Chemistry* **1988,** *256* (2), 471-475.
199. Gabrielli, C.; Garcia-Jareno, J. J.; Perrot, H., Charge compensation process in polypyrrole studied by ac electrogravimetry. *Electrochimica Acta* **2001,** *46* (26-27), 4095-4103.
200. Gabrielli, C.; Perrot, H.; Rose, D.; Rubin, A.; Toque, J. P.; Pham, M. C.; Piro, B., New frequency/voltage converters for ac-electrogravimetric measurements based on fast quartz crystal microbalance. *Review of Scientific Instruments* **2007,** *78* (7), 6.
201. C., G.; H., P., Modern Aspects of Electrochemistry. Schlesinger, M., Ed. Springer New York: 2009; Vol. 44, pp 151-238.
202. Torres, R.; Arnau, A.; Perrot, H.; Garcia, J.; Gabrielli, C., Analogue-digital phase-locked loop for alternating current quartz electrogravimetry. *Electronics Letters* **2006,** *42* (22), 1272-1273.
203. Yang, H.; Kwak, J., Mass transport investigated with the electrochemical and electrogravimetric impedance techniques .1. Water transport in PPy/CuPTS films. *Journal of Physical Chemistry B* **1997,** *101* (5), 774-781.
204. Basile, F.; Fornasari, G.; Gazzano, M.; Vaccari, A., Synthesis and thermal evolution of hydrotalcite-type compounds containing noble metals. *Applied Clay Science* **2000,** *16* (3-4), 185-200.
205. Giovannelli, F.; Zaghrioui, M.; Autret-Lambert, C.; Delorme, F.; Seron, A.; Chartier, T.; Pignon, B., Magnetic properties of Ni(II)-Mn(III) LDHs. *Materials Chemistry and Physics* **2012,** *137* (1), 55-60.

206. Miyata, S., Anion exchange properties of hydrotalcite-like compounds. *Clays and Clay Minerals* **1983,** *31* (4), 305-311.
207. Giovannelli, F.; Chartier, T.; Autret-Lambert, C.; Delorme, F.; Zaghrioui, M.; Seron, A., A fast route to obtain manganese spinel nanoparticles by reduction of K-birnessite. *Journal of Solid State Chemistry* **2009,** *182* (5), 1021-1026.
208. Wang, Q.; O'Hare, D., Recent Advances in the Synthesis and Application of Layered Double Hydroxide (LDH) Nanosheets. *Chemical Reviews* **2012,** *112* (7), 4124-4155.
209. Shao, M. F.; Zhang, R. K.; Li, Z. H.; Wei, M.; Evans, D. G.; Duan, X., Layered double hydroxides toward electrochemical energy storage and conversion: design, synthesis and applications. *Chemical Communications* **2015,** *51* (88), 15880-15893.
210. Wang, J.; Wang, L.; Chen, X.; Lu, Y. L.; Yang, W. S., Chemical power source based on layered double hydroxides. *Journal of Solid State Electrochemistry* **2015,** *19* (7), 1933-1948.
211. del Arco, M.; Gutierrez, S.; Martin, C.; Rives, V.; Rocha, J., Synthesis and characterization of layered double hydroxides (LDH) intercalated with non-steroidal anti-inflammatory drugs (NSAID). *Journal of Solid State Chemistry* **2004,** *177* (11), 3954-3962.
212. Ookubo, A.; Ooi, K.; Hayashi, H., HYDROTALCITES AS POTENTIAL ADSORBENTS OF INTESTINAL PHOSPHATE. *Journal of Pharmaceutical Sciences* **1992,** *81* (11), 1139-1140.
213. Mousty, C., Sensors and biosensors based on clay-modified electrodes - new trends. *Applied Clay Science* **2004,** *27* (3-4), 159-177.
214. Lal, M.; Howe, A. T., STUDIES OF ZINC-CHROMIUM HYDROXY SALTS .2. COMPOSITE ANION CONDUCTORS OF PRESSED DISKS OF ZN2CR(OH)6X-NH2O, WHERE X-= F-,CL-,BR-,L-,NO3- AND 1/2CO3/2-). *Journal of Solid State Chemistry* **1981,** *39* (3), 377-386.
215. Xu, L.; Lin, Y. Q.; Chen, X.; Lu, Y. L.; Yang, W. S., Electrodeposition of Platinum Nanoparticles on MgAl-layered Double Hydroxide Modified Indium Tin Oxide Electrode for Electrochemical Glucose Biosensor. *Chemical Journal of Chinese Universities-Chinese* **2016,** *37* (3), 442-447.
216. Desigaux, L.; Ben Belkacem, M.; Richard, P.; Cellier, J.; Leone, P.; Cario, L.; Leroux, F.; Taviot-Gueho, C.; Pitard, B., Self-assembly and characterization of layered double hydroxide/DNA hybrids. *Nano Letters* **2006,** *6* (2), 199-204.
217. Warren, J. L.; Geballe, T. H., RESEARCH OPPORTUNITIES IN NEW ENERGY-RELATED MATERIALS. *Materials Science and Engineering* **1981,** *50* (2), 149-198.
218. Rao, C. N. R., CHEMICAL SYNTHESIS OF SOLID INORGANIC MATERIALS. *Materials Science and Engineering B-Solid State Materials for Advanced Technology* **1993,** *18* (1), 1-21.
219. Parkhurst, D. L.; Appelo, C. A. J., User's guide to PHREEQC (Version 2) - A computer program for speciation, batch-reaction, one-dimensional transport, and inverse geochemichal calculations, Water-ressources investigations report 99-4259, 1999.
220. Sturm, W.; James, M. J., Aquatic Chemistry: Chemical Equilibria and Rates in Natural Waters, 3rd Edition. 1995.
221. Betelu, S.; Rodrigues, R.; Seron, A.; Chauvet, F.; Ignatiadis, I.; Tzedakis, T., Linear sweep voltammetry coupled to a quartz crystal microbalance for investigating the catalytic activity of the Mg-(II)-water electrochemical system and managing the Mg oxy-hydroxide hydration state. *Electrochemistry Communications* **2017,** *84*, 45-49.
222. Hunter, B.; Winkler, J.; Gray, H.; Mueller, A., Effect of interlayer anions on NiFe -LDH nanosheet water oxidation activity. *Abstracts of Papers of the American Chemical Society* **2016,** *251*, 1.
223. Bookin, A. S.; Cherkashin, V. I.; Drits, V. A., REINTERPRETATION OF THE X-RAY-DIFFRACTION PATTERNS OF STICHTITE AND REEVESITE. *Clays and Clay Minerals* **1993,** *41* (5), 631-634.
224. Scavetta, E.; Berrettoni, M.; Giorgetti, M.; Tonelli, D., Electrochemical characterisation of Ni/Al-X hydrotalcites and their electrocatalytic behaviour. *Electrochimica Acta* **2002,** *47* (15), 2451-2461.
225. Scavetta, E.; Ballarin, B.; Corticelli, C.; Gualandi, I.; Tonelli, D.; Prevot, V.; Forano, C.; Mousty, C., An insight into the electrochemical behavior of Co/Al layered double hydroxide thin films prepared by electrodeposition. *Journal of Power Sources* **2012,** *201*, 360-367.
226. Guo, X. X.; Zhang, F. Z.; Evans, D. G.; Duan, X., Layered double hydroxide films: synthesis, properties and applications. *Chemical Communications* **2010,** *46* (29), 5197-5210.

227. Bradbury, M. H.; Baeyens, B., A mechanistic description of Ni and Zn sorption on Na-montmorillonite .2. Modelling. *Journal of Contaminant Hydrology* **1997,** *27* (3-4), 223-248.
228. Bradbury, M. H.; Baeyens, B., Modelling the sorption of Zn and Ni on Ca-montmorillonite. *Geochimica Et Cosmochimica Acta* **1999,** *63* (3-4), 325-336.
229. Avena, M. J.; De Pauli, C. P., Proton adsorption and electrokinetics of an Argentinean montmorillonite. *Journal of Colloid and Interface Science* **1998,** *202* (1), 195-204.
230. Tombacz, E.; Szekeres, M., Colloidal behavior of aqueous montmorillonite suspensions: the specific role of pH in the presence of indifferent electrolytes. *Applied Clay Science* **2004,** *27* (1-2), 75-94.
231. Tournassat, C.; Ferrage, E.; Poinsignon, C.; Charlet, L., The titration of clay minerals II. Structure-based model and implications for clay reactivity. *Journal of Colloid and Interface Science* **2004,** *273* (1), 234-246.
232. Tournassat, C.; Neaman, A.; Villieras, F.; Bosbach, D.; Charlet, L., Nanomorphology of montmorillonite particles: Estimation of the clay edge sorption site density by low-pressure gas adsorption and AFM observations. *American Mineralogist* **2003,** *88* (11-12), 1989-1995.
233. Tournassat, C.; Davis, J. A.; Chiaberge, C.; Grangeon, S.; Bourg, I. C., Modeling the Acid-Base Properties of Montmorillonite Edge Surfaces. *Environmental Science & Technology* **2016,** *50* (24), 13436-13445.
234. Tournassat, C.; Bizi, M.; Braibant, G.; Crouzet, C., Influence of montmorillonite tactoid size on Na-Ca cation exchange reactions. *Journal of Colloid and Interface Science* **2011,** *364* (2), 443-454.
235. Hadi, J.; Tournassat, C.; Ignatiadis, I.; Greneche, J. M.; Charlet, L., Modelling CEC variations versus structural iron reduction levels in dioctahedral smectites. Existing approaches, new data and model refinements. *Journal of Colloid and Interface Science* **2013,** *407*, 397-409.
236. Lee, Y.; Choi, J. H.; Jeon, H. J.; Choi, K. M.; Lee, J. W.; Kang, J. K., Titanium-embedded layered double hydroxides as highly efficient water oxidation photocatalysts under visible light. *Energy & Environmental Science* **2011,** *4* (3), 914-920.
237. Morales-Guio, C. G.; Mayer, M. T.; Yella, A.; Tilley, S. D.; Gratzel, M.; Hu, X. L., An Optically Transparent Iron Nickel Oxide Catalyst for Solar Water Splitting. *Journal of the American Chemical Society* **2015,** *137* (31), 9927-9936.
238. Hunter, B. M.; Blakemore, J. D.; Deimund, M.; Gray, H. B.; Winkler, J. R.; Muller, A. M., Highly Active Mixed-Metal Nanosheet Water Oxidation Catalysts Made by Pulsed-Laser Ablation in Liquids. *Journal of the American Chemical Society* **2014,** *136* (38), 13118-13121.
239. Benmouhoub, C.; Agrisuelas, J.; Benbrahim, N.; Pillier, F.; Gabrielli, C.; Kadri, A.; Pailleret, A.; Perrot, H.; Sel, O., Influence of the Incorporation of CeO2 Nanoparticles on the Ion Exchange Behavior of Dodecylsulfate Doped Polypyrrole Films: Ac-Electrogravimetry Investigations. *Electrochimica Acta* **2014,** *145*, 270-280.
240. Gao, W. L.; Sel, O.; Perrot, H., Electrochemical and viscoelastic evolution of dodecyl sulfate-doped polypyrrole films during electrochemical cycling. *Electrochimica Acta* **2017,** *233*, 262-273.
241. Corrigan, D. A., THE CATALYSIS OF THE OXYGEN EVOLUTION REACTION BY IRON IMPURITIES IN THIN-FILM NICKEL-OXIDE ELECTRODES. *Journal of the Electrochemical Society* **1987,** *134* (2), 377-384.
242. Stevens, M. B.; Trang, C. D. M.; Enman, L. J.; Deng, J.; Boettcher, S. W., Reactive Fe-Sites in Ni/Fe (Oxy)hydroxide Are Responsible for Exceptional Oxygen Electrocatalysis Activity. *Journal of the American Chemical Society* **2017,** *139* (33), 11361-11364.
243. Gao, X. Y.; Pan, X. Y.; Long, X.; Yi, Z. G., Room-Temperature Synthesis FeNiCo Layered Double Hydroxide as an Excellent Electrochemical Water Oxidation Catalyst. *Journal of the Electrochemical Society* **2017,** *164* (12), II755-II759.
244. Goubaa, H.; Escobar-Teran, F.; Ressam, I.; Gao, W.; El Kadib, A.; Lucas, I. T.; Raihane, M.; Lahcini, M.; Perrot, H.; Sel, O., Dynamic Resolution of Ion Transfer in Electrochemically Reduced Graphene Oxides Revealed by Electrogravimetric Impedance. *Journal of Physical Chemistry C* **2017,** *121* (17), 9370-9380.
245. Jaffee, R. I.; Smith, E. M.; Gonser, B. W., THE CONSTITUTION OF THE GOLD-GERMANIUM SYSTEM. *Transactions of the American Institute of Mining and Metallurgical Engineers* **1945,** *161*, 366-372.

246. Mansour, A. N.; Melendres, C. A.; Wong, J., In situ X-ray absorption spectroscopic study of electrodeposited nickel oxide films during redox reactions. *Journal of the Electrochemical Society* **1998,** *145* (4), 1121-1125.
247. Sanson, A.; Kantor, I.; Cerantola, V.; Irifune, T.; Carnera, A.; Pascarelli, S., Local structure and spin transition in Fe2O3 hematite at high pressure. *Physical Review B* **2016,** *94* (1), 7.
248. Hunter, B. M.; Winkler, J. R.; Gray, H. B., Iron Is the Active Site in Nickel/Iron Water Oxidation Electrocatalysts. *Molecules* **2018,** *23* (4), 7.
249. Stucki, J. W.; Low, P. F.; Roth, C. B.; Golden, D. C., EFFECTS OF OXIDATION-STATE OF OCTAHEDRAL IRON ON CLAY SWELLING. *Clays and Clay Minerals* **1984,** *32* (5), 357-362.
250. Wu, J.; Low, P. F.; Roth, C. B., EFFECTS OF OCTAHEDRAL-IRON REDUCTION AND SWELLING PRESSURE ON INTERLAYER DISTANCES IN NA-NONTRONITE. *Clays and Clay Minerals* **1989,** *37* (3), 211-218.
251. Stucki, J. W.; Lee, K.; Zhang, L. Z.; Larson, R. A., Effects of iron oxidation state on the surface and structural properties of smectites. *Pure and Applied Chemistry* **2002,** *74* (11), 2145-2158.
252. Secor, R. B.; Radke, C. J., SPILLOVER OF THE DIFFUSE DOUBLE-LAYER ON MONTMORILLONITE PARTICLES. *Journal of Colloid and Interface Science* **1985,** *103* (1), 237-244.
253. Taviot-Guého, C.; Vialat, P.; Leroux, F.; Razzaghi, F.; Perrot, P.; Sel, O.; Daugaard Jensen, N.; Gro Nielsen, U.; Peulon, S.; Elkaim, E.; Mousty, C., Dynamic characterization of inter- and intralamellar domains of cobalt-based layered double hydroxides upon electrochemical oxidation. *Chem. Mater.* **2016,** *28* (21), 7793–7806.
254. Bish, D. L., ANION-EXCHANGE IN TAKOVITE - APPLICATIONS TO OTHER HYDROXIDE MINERALS. *Bulletin De Mineralogie* **1980,** *103* (2), 170-175.
255. Vaccari, A., Preparation and catalytic properties of cationic and anionic clays. *Catalysis Today* **1998,** *41* (1-3), 53-71.
256. Nar-Yosef, B.; Kafkafi, U.; Rosenberg, R.; Sposito, G., Phosphorus adsorption by kaolinite and montmorillonite. I. Effect of time, ionic strength, and pH. *Soil Science Society of America Journal* **1988**.
257. Satmark, B.; Albinsson, Y., SORPTION OF FISSION-PRODUCTS ON COLLOIDS MADE OF NATURALLY-OCCURRING MINERALS AND THE STABILITY OF THESE COLLOIDS. *Radiochimica Acta* **1992,** *58-9*, 155-161.
258. Gutierrez, M.; Fuentes, H. R., A mechanistic modeling of montmorillonite contamination by cesium sorption. *Applied Clay Science* **1996,** *11* (1), 11-24.
259. Sun, P. Z.; Ma, R. Z.; Bai, X. Y.; Wang, K. L.; Zhu, H. W.; Sasaki, T., Single-layer nanosheets with exceptionally high and anisotropic hydroxyl ion conductivity. *Science Advances* **2017,** *3* (4), 8.
260. Yang, R.; Zhou, Y. M.; Xing, Y. Y.; Li, D.; Jiang, D. L.; Chen, M.; Shi, W. D.; Yuan, S. Q., Synergistic coupling of CoFe-LDH arrays with NiFe-LDH nanosheet for highly efficient overall water splitting in alkaline media. *Applied Catalysis B-Environmental* **2019,** *253*, 131-139.
261. Kim, H.; Hong, J.; Park, K. Y.; Kim, S. W.; Kang, K., Aqueous Rechargeable Li and Na Ion Batteries. *Chemical Reviews* **2014,** *114* (23), 11788-11827.
262. Antony, H.; Legrand, L.; Chausse, A., Carbonate and sulphate green rusts - Mechanisms of oxidation and reduction. *Electrochimica Acta* **2008,** *53* (24), 7146-7156.
263. Miyata, S., ANION-EXCHANGE PROPERTIES OF HYDROTALCITE-LIKE COMPOUNDS. *Clays and Clay Minerals* **1983,** *31* (4), 305-311.